PhD-FSTC-2018-42
The Faculty of Sciences, Technology and Communication

DISSERTATION

Defence held on 15/05/2018 in Luxembourg

to obtain the degree of

DOCTEUR DE L'UNIVERSITÉ DU LUXEMBOURG

EN BIOLOGIE

by

Javier Martin JARAZO
Born on 15 July 1985 in Buenos Aires (Argentina)

THE PARKINSON'S DISEASE ASSOCIATED PINK1-PARKIN PATHWAY IN PATHOLOGY AND DEVELOPMENT

Dissertation defence committee

Dr Jens Schwamborn, dissertation supervisor
Professor, Université du Luxembourg

Dr Liliana Bernardino
Health Sciences Research Center, Covilhã
Associate professor, University of Beira Interior

Dr Philip Seibler
Institute of Neurogenetics, Lübeck
Professor, University of Lübeck

Dr Anne Grünewald, Chairman
Associate professor, Université du Luxembourg


uni.lu
UNIVERSITÉ DU
LUXEMBOURG


LCSB


Fonds National de la
Recherche Luxembourg
AFR


SysMedPD


Fondation du Pélican

“We live on one level of existence, but there are others.

These hidden dimensions of reality are everywhere.

Far away, across the light years.

Beneath our feet.

And even inside you and me.”

Neil deGrasse Tyson

Table of Contents

Abbreviations

ATP	Adenosine triphosphate
Cas9	CRISPR associated protein 9
CLEAR	Coordinated lysosomal expression and regulation
CRISPR	Cluster regularly interspaced short palindromic
DNA	Deoxyribonucleic acid
DSB	Double strand break
ER	endoplasmic reticulum
ESCs	Embryonic stem cells
FACE	FACS-Assisted CRISPR/Cas9 genome editing
GABAergic	γ-aminobutyric acid producing neurons
GFP	Green fluorescent protein
gRNA	Guide RNA
GSH	Glutathione
GWAS	Genome-wide association study
HDR	Homologous directed repair
hiPSCs	Human induced pluripotent stem cells
HP-β-CD	2-hydroxypropil-β-cyclodextrin
IMM	Inner mitochondrial membrane
ITR	Inverted terminal repeats
mbDA	Midbrain dopaminergic neurons
MDVs	Mitochondria derived vesicles
MPTP	1-methyl-4-phenyl-1,2,3,6-tetra-hydropyridine
mRNA	Messenger RNA
NADPH	Nicotinamide adenine dinucleotide phosphate

NESCS	Neuroepithelial stem cells
NHEJ	non-homologous end joining
NPCs	Neuroprecursor cells
NPD	Niemman-Pick's disease
OMM	Outer mitochondrial membrane
OMMAD	Outer mitochondrial membrane associated degradation
PAM	Protospacer adjacent motif
PD	Parkinson's disease
PMA	Purmorphamine
RNA	Ribonucleic acid
ROS	Reactive oxygen species
SCNT	Somatic cell nuclear transfer
SGZ	Subgranullar zone
SNP	Single nucleotide polymorphism
SVZ	Subventricular zone
TALEN	Transcription activator like effector nucleases
TH	Tyrosine hydroxylase
ZFN	Zinc-finger nuclease

Summary

Parkinson's disease (PD) has an aetiology not completely understood. One of the hypothesis in the field is that many neurodegenerative diseases are influenced by developmental disorders. The underlying concept is that already during brain development some processes are deregulated producing a higher degree of susceptibility for neurodegeneration during aging. Two hereditary early onset forms of PD are caused by recessive mutations in PTEN-induced putative kinase 1 (PINK1) and Parkin genes that regulate mitochondrial function and morphology, quarantining damaged mitochondria before their degradation as well as triggering the process of mitophagy. Our hypothesis is that alterations of the Pink1-Parkin pathway have an impact in mitochondrial physiology tempering the differentiation ability of neuroepithelial stem cells into dopaminergic neurons. For evaluating this hypothesis we reprogramed patients' fibroblasts carrying PINK1 mutations, as well as from healthy individuals, to human induced pluripotent stem cells. We developed a streamlined technique of gene editing (FACE) by using the CRISPR/Cas9 system combined with a composite of fluorescent proteins in the donor template for biallelic gene targeting. Isogenic controls were generated using this technique that allowed us to analyze the contribution of corrected patients' mutations in the cellular defects observed. Human iPSCs were differentiated into a neuroepithelial stem cell state (NESC) from where the cells were further differentiated into neurons. We established different algorithms for pattern recognition and applied them for image analysis of different features such as mitochondrial morphology, proliferation capacity, apoptosis and differentiation. Patient's derived cells presented an impaired differentiation efficiency into dopaminergic neurons as well as an imbalanced cell renewal that can be linked to the mitochondrial differences. Using 3D cultures, such as microfluidics and organoids, we were able to recapitulate this differentiation impairment in a system that mimics better the context of an in vivo environment. We evaluated the energetic capabilities of the NESCs and the firing activity of differentiated neurons, which also showed a dysregulation in patient cells. We introduced a

new system for large-scale analysis of the autophagy and mitophagy pathways by the combination of stably integrated Rosella constructs in different patients' lines and an image analysis script for classification of the different subcellular structures involved in these pathways activities. This revealed that the basal activity as well as the response against stressors of these pathways are altered in cells derived from patients having different mutations causative of PD. We performed a screen of repurposed drugs as well as of novel compounds to evaluate their impact in this altered developmental transition identifying a potential candidate to be further analysed in an in vivo context.

1. Introduction

1.1 Parkinson's disease

1.1.1 Neurodegeneration and health

Neurodegenerative diseases impose a great health threat for an ageing worldwide population due to increased live expectancies and reduced fertility (World Health Organization, 2011). Even though most countries present this phenomena, it will impact more those in development presenting a lag in the healthcare system progress (Gammon, 2014; World Health Organization, 2017). Ailments that were not common in the last centuries are starting to create problems that can be potentially scalable in the next decades. This can be related to changes in live expectancies as well as modifications in cultural and environmental scenarios. Research advancements in the medical system generated a reduction of infectious and parasitic diseases leading to an epidemiologic transition into an increased level of chronic and degenerative diseases (World Health Organization, 2011, 2015). Neurodegenerative diseases is one of the examples of non-communicable diseases, and Parkinson's disease is amongst them (Checkoway et al., 2011). Reports have stated that the number of patients diagnosed with Parkinson's disease had a percentage increase of 1.24% per decade in the last 30 years with some specific populations having an incidence of 17.9 per 100000 individuals (Caslake et al., 2013; Savica et al., 2016). Even though there were some advances in the detection of prodromal symptoms in PD, they were not significant to explain the recent increase in cases (Checkoway et al., 2011; Mahlknecht et al., 2016; Bellucci et al., 2017). Ageing populations without an intensive care platform surrounding them, represents an economical burden to governments as well as emotional impact on the patient and family members (Findley, 2007; Chiong-Rivero et al., 2011).

Even though Parkinson's is a classic example of neurodegenerative disease its case is particular since its pathogeny is not completely understood and the clinical appearance and features have a diversity that hinders scientific advances (Przedborski, 2017). The overall situation points that further research is needed and encourage in this field with the aim of reducing the impact of PD in the global population.

1.1.2 Clinical manifestation and Age of onset

After two centuries since the description of the disease by James Parkinson, motor symptoms are one of the principal characteristic that PD is associated with but not exclusively. This symptoms include rigidity, bradykinesia, posture instability, and resting tremor, representing the key features of what is denominated as 'parkinsonism', a group of progressive neurodegenerative diseases of which PD is the most prevalent reason (Dauer and Przedborski, 2003; DeMaagd and Philip, 2015). Other motor symptoms have been described such as deficits of gait, speech, and handwriting, leading to a classification in primary and secondary motor symptoms (Moustafa et al., 2016) categorization that help clinicians in making a differential diagnosis (Jankovic, 2008).

Not only motor symptoms have been reported but also symptoms of depression, anhedonia, anxiety and dementia were detected in individuals with PD (Park and Stacy, 2009). Even though they are not clinically pathognomonic of the disease, they have clinical relevance since these symptoms precede the motor ones (Schapira and Tolosa, 2010), and they become the main ailment to treat once the disease is diagnosed (Chaudhuri et al., 2006). The connection between the non-motor symptoms and pathogeny of PD is not completely understood hinting that multifactorial phenomena should be considered (Schapira et al., 2017).

The age of onset of PD leads to an arrangement of the patients into three categories: young (age of onset before 20 years, named juvenile-onset), middle (those individuals with onset between 20 and 50 years, labelled early-onset) and late development (those

presenting the disease after 50 years of age, late-onset)(Pankratz and Foroud, 2007). However, the age boundaries seem to variate across different reports (Mehanna et al., 2014). One thing is clear, ageing is considered as the most important risk factor (Hindle, 2010). This classification is relevant in the context of clinical and pharmacological implications (Arevalo et al., 1997; Pagano et al., 2016), and also in the possible origin of the disease. Causes of PD have been classified in genetic, environmental and idiopathic forms (Schulte and Gasser, 2011). In this context, hereditary forms of PD are prone to trigger the disease earlier than non-mendelian forms, or environmental causes of PD would only be trigger after exposure to certain elements (Brown et al., 2005; Hernandez et al., 2016).

1.1.3 Histopathological Hallmarks of the disease

One of the histopathological hallmarks of Parkinson's diseases is the loss of a specific type of dopaminergic neurons (Antony et al., 2013). These neurons normally reside in the pars compacta of the substantia nigra in the brain, also named A9 region (Dahlstroem and Fuxe, 1964), and make their projections into the striatum (Grealish et al., 2010). Hence they are named midbrain dopaminergic neurons (mbDA). This highly pigmented area (thus the name of substantia nigra) was pointed out as the one containing the neurons implicated with PD when loss of pigmentation in this region was observed in patients with the disease (Trétiakoff, 1919; Marsden, 1983; Gibb and Lees, 1991). However, a more broad affection of the brain was reported, implying that PD might not be an only affected brain region malady (Braak et al., 1995). The main role of these neurons is the production of dopamine that regulates the activity of GABAergics neurons located in the striatum. The dysregulation of the later leads to a higher inhibitory activity that the neurons in the globus pallidus internal segment exert in the thalamus reducing the stimulation of the cortex for generating motor activity and initiation of movement (Smith et al., 2011; de Hemptinne et al., 2015).

Another of the historically described hallmarks of Parkinson's disease is the presence of Lewy aggregates within the neurons. These aggregates, mainly formed by tangles of α-synuclein, are classified as Lewy bodies or Lewy neurites depending on the localization within the neuron (Wakabayashi et al., 2007; Dickson, 2018). However, this does not hold true with all the different forms PD, and Lewy bodies can occur sporadically in the ageing individual (named "incidental Lewy bodies") highlighting the importance of avoiding broad conceptualizations in the context of this disease (Mori et al., 1998; Gaig et al., 2007; Buchman et al., 2012).

1.1.4 Treatment of the disease

Even though around 150 years passed from the first report of PD until the first successful treatment, there is still no current cure for this disease (Fahn, 2015). Treatments for Parkinson's disease involve different strategies of palliative procedures such as the administration of Levodopa or the surgical placement of electrodes for deep brain stimulation (Jankovic and Aguilar, 2008). To date there is no treatment that solves one of the phenomena observed in the pathology that is the loss of cells in the substantia nigra releasing dopamine. The main palliative treatment used today in the clinics is Levodopa. While the therapy reduces the symptoms in some of the patients, it also generates several side effects. Moreover, some specific group of patients, such as those carrying mutations and developing the disease at earlier stages, are refractive to improvements in their condition using levodopa (Lücking et al., 2000; Schrag and Schott, 2006; Jankovic and Aguilar, 2008). Plus, since the vast clinical features of PD cannot be contained by only treating motor symptoms, compounds oriented to sustain the non-motor symptoms have to be included in some patients (Williams-Gray et al., 2006; Chaudhuri and Schapira, 2009; Wu et al., 2017)

The other approach, for managing movement disorders used since the beginning of last century, are surgical interventions (Goetz, 2011). A range of surgical procedures have

been evaluated clinically and experimentally but from all of them Deep Brain Stimulation has been largely promoted over the clinics (Lozano et al., 2018). This procedure requires a surgical intervention of specialized neurologist which select the patients that would benefit from this intervention (Lang and Widner, 2002). Plus, it presents the disadvantage of the risks of any surgical intervention (Voges et al., 2006) and the rehabilitation required after the procedure (Allert et al., 2018).

An alternative to these treatments will largely benefit the patients. A potential systemic treatment is sought by several research groups and several clinical trials have been performed in the last years but without a strong candidate (Dawson, 2005; Athauda and Foltynie, 2016), leaving room for further research in this field.

1.1.5 Pathogenesis of the disease

One of the quick explanations of the unsuccessful drug trails in the last decades is the lack of a complete understanding of PD pathogenesis (Eriksen et al., 2005; Hirsch et al., 2013; Haddad and Nakamura, 2015). The scientific community accepted scenario is an interaction of environmental factors, and a genetic predisposition that triggers the onset of the disease (Shin et al., 2009). Since the hallmark of the disease is the loss of a specific type of dopaminergic neuron, several hypothesis try to explain why these neurons are the first and most affected ones (Forno, 1996). These hypotheses range from an evolutionary concept (the enlarged development of the striatum in humans pushing mbDA to increase their arborisation compared to other species) to the high functionality demands (dopaminergic neurons are one of the most metabolically active cells in the brain, the energy needed to keep up with their firing rate seems to be a limiting step) (Vernier et al., 2004; Bolam and Pissadaki, 2012; Pissadaki and Bolam, 2013; Garcia-Ruiz and Espay, 2017). These induces a higher susceptibility of mbDA to externals stressor as well as those generated within the cell. This was supported by the first two findings that contributed to the understanding of PD pathogenesis (Schapira and Jenner, 2011): the effects of 1-methyl-4-

phenyl-1,2,3,6-tetra-hydropyridine (MPTP) and the formation of protein aggregates due to mutations in α-synuclein (Langston et al., 1984; Polymeropoulos et al., 1997). From this point on, different response mechanism such as microgliosis, reduced vascularization and prion-like spreading could determine the progression of the disease as well as other concomitant symptoms that occur with PD (Globus et al., 1985; McGeer et al., 1988; Braak et al., 2003; Derejko et al., 2006; Tredici and Braak, 2008; Schapira and Jenner, 2011; Heron et al., 2014). However, the concept that the immune response and the spreading from the peripheral nervous system to the brain (defined in the Braak stages) should be considered in the onset of the disease rather than in its later progression, is also supported by the scientific community (Wang et al., 2015a; Le et al., 2016; Rietdijk et al., 2017). Energy demand and protein deposition might be the key features affecting midbrain dopaminergic neurons, with most of the known affected pathways leading to alterations in these two aspects (Hunn et al., 2015). Thus, they will be further discussed in the next sections.

1.1.6 Environmental causes

Knowledge that the environmental exposure to certain elements plays a role in the epidemiology of PD is known since several decades (Langston et al., 1983; Koller et al., 1990). These factors can range from occupational, place of residence, physical activity and diet (Chade et al., 2006; Bellou et al., 2016). The connection between environment and PD is not old but also represents an important factor in the map of PD since only a small fraction of the total cases (10%) has hereditary ties (Sampson et al., 2016). Their mechanism of action in some cases is fully understood and they also had become a tool for generating disease models to study the disease (Sherer et al., 2003; Bové et al., 2005). One aspect of the environmental component of PD that lately gained a lot of attention in the field is the link between the gut and the brain, specifically by influence of the microbiota (Sampson et al., 2016; Li et al., 2017a; Parashar and Udayabanu, 2017; Heintz-Buschart et al., 2018). This

association is also supported by those proposing the spreading mechanism from the periphery to the central nervous system (Braak and Tredici, 2017).

Links between environmental factors and development of neurodegenerative disease have not only been reported in the context of PD but in several other neurodegenerative diseases, concept that might lead to consider evaluating together the genetic aspect and the environmental factors as triggers of neurodegeneration (Brown et al., 2005; Ritz, 2006; Cannon and Greenamyre, 2011; Chin-Chan et al., 2015; Chen et al., 2017; Przedborski, 2017). This enables to think that most of these diseases could have a dual hit concept in which mutations carriers develop the disease after an environmental factor prompts its onset (Sulzer, 2007; Schwamborn, 2018).

1.1.7 Genetic and Idiopathic causes

In the categorization of individuals with PD the first division that is stablished is between those cases with a genetic component (around 10% of the cases) from those which the cause is unknown (hence are named idiopathic), and from the former 90% of the cases is sporadic (due to somatic mutations that occur after fertilization) and the rest is familial (at least a family member has been identified as carrier or presented the disease)(Pankratz and Foroud, 2007; Thomas and Beal, 2007; Klein and Westenberger, 2012; Kim and Jeon, 2014; Perandones et al., 2015). Of all the identified loci associated to the disease, six have been reported as monogenic causes of typical PD with a hereditable link namely SNCA, LRRK2, VPS35, Parkin, PINK1 and DJ-1 of which the three first ones are dominant and the later recessive (Klein and Westenberger, 2012; Bonifati, 2014; Brás et al., 2015). All the those loci that were identify as having a connection with PD were labelled as PARK with numbering according to their time of discovery (hence the locus of the first identified gene, SNCA, is called PARK1) (Thomas and Beal, 2007). This list has been further extended to 34 including risk genes and risk loci linked to different forms of Parkinsonism and in some cases specifically to PD (Brás et al., 2015). Most of this recently found loci are not mapped

to a specific gene and some others are just linked between the detected SNP in the GWAS to the most proximal gene or group of genes, thus they need further confirmation (Brás et al., 2015). We will focus in the analysis of those that are confirmed causes of PD with a more detailed analysis of PINK1. We do so, keeping in mind that the genetic background is a crucial factor accounting for patients' individual variability and that the whole genomic context should be considered. This point will be addressed again in the disease modelling section.

1.1.6.1 SNCA

The first reported gene as causative of PD was α-synuclein (Polymeropoulos et al., 1996). Most of the patients carrying a mutation in SNCA developed early-onset of the disease with the presence of Lewy bodies spread through different regions of the brain, and a fast progression of the disease (Klein and Westenberger, 2012). The function of SNCA is not completely understood but different reports link this protein in a broad interaction with membranes (such as mitochondria and endoplasmic reticulum, ER) but specially to synaptic vesicles for their recycling, as well as neurotransmitters management (Thomas and Beal, 2007; Recasens and Dehay, 2014). It is also the principal aggregated protein in Lewy bodies and it can self-propagate matching some of the hypotheses of the pathogeny of the disease (Spillantini et al., 1997; Kordower et al., 2008; Li et al., 2008; Braak and Tredici, 2017)

1.1.6.2 LRRK2

Patients carrying mutations in LRRK2 gene represent the majority of late-onset and sporadic cases of PD (Kumari and Tan, 2009; Klein and Westenberger, 2012). It encodes a large multidomain protein which, as in the case of SNCA, has an unknown specific function (Wallings et al., 2015). However, the development of PD and the number of reported mutations in LRRK2 differs from the ones of SNCA patients. A mild progression, in most cases without dementia, and around 80 mutations are reported in comparison to

the aggressive diffusion and five mutations in the case of SNCA (Nuytemans et al., 2010; Klein and Westenberger, 2012; Siddiqui et al., 2016). Plus, LRRK2 is involved in both familial and sporadic cases, with a frequency of 2% in the latter (Nuytemans et al., 2010). The two most important domains of this protein are those involve with enzymatic activity: the ROC, the COR and kinase domains, and the main proposed activities range from controlling autophagy pathway and mitochondrial homeostasis to regulating inflammatory response and oxidative stress (Li et al., 2014).

1.1.6.3 DJ-1

Mutations in the PARK7 loci associated with the gene coding for DJ-1 have been connected to early-onset PD with a relative low number of reported mutations compared to the other two genes affected by autosomal recessive mutations, Parkin and PINK1 (Bonifati et al., 2003; Ariga et al., 2013; Brás et al., 2015). Functions of this gene have been better characterized, and they mainly focus in oxidative stress control but also closely involved in gene transcription regulation (Lev et al., 2006; Malgieri and Eliezer, 2008; Biosa et al., 2017)

1.1.6.4 VPS35

One of the recently described genes affected in patients having a classical sporadic PD symptomatology, VPS35, was discovered using whole exome studies rather than linkage analysis, with only one pathogenic mutation confirmed (Vilariño-Güell et al., 2011; Lin and Farrer, 2014; Struhal et al., 2014). Again, the mechanism of contribution in the development of PD is not known (Williams et al., 2017). Nevertheless, some of the known functions of VPS35 overlap with some of the disease mechanism reported in other PD genes, such as organelle's or vesicle's membrane recycling, trafficking and turnover between endosomes and Golgi apparatus as well as of mitochondria (Seaman, 2012; Deng et al., 2013; Wang et al., 2015b).

1.1.6.5 Parkin

The first affected gene described as a cause of autosomal recessive PD was Parkin which is reported to cause juvenile and early-onset of the disease with a slow progression (Dawson and Dawson, 2010; Klein and Westenberger, 2012; Miklya et al., 2014). Due to its ubiquitin ligand nature most of Parkin functions have been associated to the control of altered or misfolded protein inducing their degradation by ubiquitination, with strong ties in the regulation of mitochondrial homeostasis by overseeing its biogenesis, network modulation and degradation (Zhang et al., 2016; Hattori and Mizuno, 2017)

1.1.6.6 PINK1

The PTEN-induced putative kinase 1 (PINK1) gene is linked to PD when mutations are present in one of the more than 80 reported positions of this 8 exons and 581 amino acids protein (Valente et al., 2004; Klein and Westenberger, 2012; Pickrell and Youle, 2015). The symptomatology of the patients is similar to those carrying Parkin mutations, however most of the reported mutations are missense and nonsense mutations compared to the prevalent deletions or duplications observed in Parkin (Kumar et al., 2011). The protein possess a mitochondrial targeting motif and a kinase domain revealing its principal functions (Valente et al., 2004). This kinase domain presents none conserved regions that are exclusive of human PINK1 followed by a C-Terminal extension of not well known and unmatched functions (Kumar et al., 2017). From the moment it was identify as a cause of PD, the main role that was given to PINK1 was the protection of cells from oxidative stress after seeing that overexpression of wild-type PINK1 could protect against external stressors (Valente et al., 2004; Deas et al., 2009). It has been later stablished that controlling the homeostasis of the principal source of ROS, mitochondria, was the way PINK1 is acting (Pickrell and Youle, 2015). Through its mitochondrial targeting motif, PINK1 interacts with the TOM/TIM complex located in the outer and inner membrane of the mitochondria respectively (OMM and IMM) (Ashrafi and Schwarz, 2012). In normal conditions is

internalized through TOM and into TIM complex to be cleaved by proteases, specifically MPP and PARL. However, when the membrane potential of the mitochondria is altered, the internalization to TIM is blocked leading to an accumulation of PINK1 in the outer membrane (Ashrafi and Schwarz, 2012). At this point PINK1 interacts with another protein that is also involved in the pathogeny of PD, Parkin. Through the PINK1 kinase domain, it phosphorylates Parkin and ubiquitin in both of their Ser65 position. Interactions between these last two proteins lead to conformational changes in Parkin that enhances its ubiquitination activity (McWilliams and Muqit, 2017). The amplification signal done by Parkin, of labelling the mitochondria surface with poly-ubiquitin chains of different lengths, leads to the recruitment of the autophagy machinery (Yamano et al., 2016).

At this point is worth mentioning that in the context of the functionality of the genes involved in the genetic form of PD, several pathway intertwine and some key organelles and system are involved in the pathogeny of the disease. This includes mitochondria homeostasis control, protein degradation and oxidative stress protection (Fitzgerald and Plun-Favreau, 2008; Fujita et al., 2014; Merwe et al., 2015; Scott et al., 2017). Hence, main aspects about mitochondria biogenesis, fission/fusion, activity, and degradation as well as general aspects of autophagy will be covered in the next sections.

1.1.7 Mitochondria

Evolution-wise, these organelles were derived from the symbiotic interaction of α-protobacteria and pre eukaryotic cells (Yamano et al., 2016). Even though several different task such as Krebs cycle, β-oxidation and lipids synthesis are carried out within them, their main role is providing a functional structure for oxidative phosphorylation to be carried out (Schapira, 2006). Oxidative phosphorylation, also known as electron transport chain is the main source of ATP in cellular respiration, that although beneficial to the cell it is also the source known as reactive oxygen species (Chaban et al., 2014). These by-products in large quantities can be toxic to the cell by producing damage to proteins, lipids and DNA (Larsen

et al., 2018). The generation of anion superoxide from oxygen is just one of the steps of a vicious cycle that needs to be contained (Beckhauser et al., 2016). Several intracellular mechanisms are active in managing the excess of ROS from its formation (e.g. the enzymatic action of the superoxide dismutase to transform superoxide to hydrogen peroxide and oxygen) to the removal of the damaged structures they generate (Turrens, 2003). Due to the importance of the stability and integrity of the genomic sequence, several mechanism evolved for repairing nuclear DNA sequence alterations (Schärer, 2003; Jena, 2012; Cadet and Wagner, 2013). Mitochondria possess their own genomic sequence that also has specific repair mechanisms for its DNA (Alexeyev et al., 2013). However, when the production of ROS goes out of feasible range of control for this mechanism, other overlapping processes are also taking place for guaranteeing mitochondrial quality (Ashrafi and Schwarz, 2012). The series of checkpoints act from a protein to an organelle level including: an intrinsic proteolytic system within the mitochondria membrane, the cytoplasmic degradation of altered membrane proteins through proteasome, the budding off mitochondria membrane vesicles (mitochondria derived vesicles, MDVs), and the final degradation of an entire organelle (Ni et al., 2015). Except for the first system, the rest requires an interplay with cytosolic proteins to determine the type of cargo and their final destination, and some of these proteins are the ones reported to be affected by mutations in individuals with PD (Antony et al., 2013). Several structural OMM proteins normally undergo ubiquitination, and when these proteins are altered or the membrane potential is imbalanced, PINK1 stabilizes in the OMM to phosphorylate these ubiquitins, and recruits and phosphorylates Parkin as described before (Yamano et al., 2016). The later leads to the extraction of several outer mitochondrial membrane proteins through a process similar to those reported for the ER (named outer mitochondrial membrane associated degradation, OMMAD) by interaction with p97, and to be degraded by the proteasome (Pickrell and Youle, 2015). Some of the proteins regulated this way control mitochondrial network dynamics, mainly those involved in controlling mitochondrial fusion and fission

(Karbowski and Youle, 2011). Fusion of different mitochondria is promoted to dilute the effect of altered proteins in isolated mitochondrion, and involves proteins Mitofusin I and II (Mfn) for fusion of the OMM and OPA1 for the fusion of the IMM (Larsen et al., 2018). When this mechanism is not enough for counterbalancing an altered network, a specific portion of it needs to be isolated (in a process called fission) to be further degraded (Karbowski and Youle, 2011). Fission is controlled by Drp1 which interacts with other OMM proteins as well as with the ER for establishing the point to be split (Friedman et al., 2011; Ni et al., 2015). The dynamic changes that the mitochondrial network goes through are in balance with the mitochondria's anchoring and transporting system to the cellular microtubules formed mainly by the Miro-Milton complex (Schwarz, 2013). Reported interaction between PINK1/Parkin pathway with Miro, Drp1 and Mfn show their close connection for controlling mitochondrial homeostasis (Schwarz, 2013; Buhlman et al., 2014; Pickrell and Youle, 2015). Another mechanism that is active in mitochondrial quality control is the formation of MDVs (Soubannier et al., 2012) . These structures ranging 70 to 150 nm bud off the surface of the mitochondria and transport different types of cargo which would dictate their final destination to the peroxisome or to the late endosome/lysosome, degrading a higher content of altered structures than the previous described mechanism (Sugiura et al., 2014). The ultimate step of the mitochondrial quality control process is its final degradation by the autophagy pathway (Ni et al., 2015).

1.1.8 Autophagy pathway

The process of degrading large intracellular material named autophagy, involves their engulfing by a membrane and the delivery of the content to lysosomes (Youle and Narendra, 2011; Ashrafi and Schwarz, 2012). Three main mechanism are reported in autophagy: chaperon mediated autophagy, microautophagy and macroautophagy (Mizushima and Komatsu, 2011; Ashrafi and Schwarz, 2012; Galluzzi et al., 2017). Of the later process, two types are mainly recognized: the one arising from starvation of cells

known as non-selective macroautophagy, and the targeted degradation of proteins or organelles or pathogens (Youle and Narendra, 2011), of which we are going to focus in the degradation of mitochondria, named mitophagy. Several structures are identified in the autophagy pathway, starting with the formation of an isolation membrane known as phagophore that surrounds the structure to be degraded leaving a double membrane vesicle (named autophagosome) which would then fuse with lysosomes that will release their hydrolytic content, transforming it into an autolysosome (Ashrafi and Schwarz, 2012). In order to target the mitochondria that needs to be degraded, this pathway relies on other system like the PINK1/Parkin pathway described previously that flags the altered mitochondrion by poly-ubiquitination. Three autophagy receptors, p62 (also known as SQSTM1), Optineurin, and NDP52, interact with the ubiquitin chains to make the connection between these marks in the outer membrane of the mitochondria and the autophagy machinery (Ni et al., 2015; Bhujabal et al., 2017). The first structure of the autophagy machinery, the phagophore, is assembled by an interaction of three different complexes: the complex of UNC51-like kinase (ULK, formed by ULK1, ATG13 FIP200 and ATG101), the VPS34 complex (formed by beclin-1, VPS15, VPS34, ATG14 and AMBRA1), and the ATG5/ATG12-ATG16 complex that are responsible of the initiation, nucleation, and conjugation of this isolation membrane respectively (Harper et al., 2018). The conjugation of the phagophore membrane is done with ATG8 homologs, such as LC3 and GABARAPs, that are the ones to interact with the previously named autophagy receptors (Kaur and Debnath, 2015). It has also been reported that other mechanisms independent of the ubiquitination of damaged mitochondria by PINK1/Parkin, trigger mitophagy with a direct interaction with LC3 or GABARAP, namely by BINP3, FUNDC1 and NIX (Bhujabal et al., 2017; Koentjoro et al., 2017). Plus, some other proteins (SMURF1 and MUL1/MULAN) produce mitochondrial ubiquitination that could replace Parkin's activity (Ni et al., 2015). After formation of the autophagosome, it fuses with the lysosome through a process combining the activity of proteins in the HOPS complex (VPS11, VPS16, VPS18, VPS33,

VPS39 AND VSP41), PLEKHM1, the SNARE complex (VAMP7/8, SNAP29 and STX17), and Rab7 (Itakura et al., 2012; McEwan et al., 2015; Wang et al., 2016; Han et al., 2017; Zhi et al., 2018), responsible for tethering, bridging and membrane fusion (Luzio et al., 2007). This fusion induces the release of the lysosomal hydrolases that sequentially interact forming complexes to process their substrate with the help of the acidic environment they possess (Appelqvist et al., 2013; Bonten et al., 2014). The monomers obtained after degradation can be recycled as well as the lysosomal membranes involved in the process (Zhi et al., 2018). To perform the latter, it is reported that the retromer complex (formed by VPS5, VPS17, VPS26, VPS29 and VPS35) plays a main role (Luzio et al., 2007). Not only the PD genes PINK1/Parkin and VPS35 were reported as playing a role in autophagy but also LRRK2 and α-synuclein are involve in its process (Xilouri et al., 2016; Manzoni, 2017).

1.1.9 De novo neuronal formation: Neurodevelopment and neurogenesis

Even though age is a risk factor in the development of PD, there is evidence that the development of the disease is a long process that has in some cases an initiation decades before the appearance of the first motor symptoms (Chaudhuri and Schapira, 2009; Brás et al., 2015). Plus, several genes or risk factors associated with PD determine an early onset or juvenile form of the disease with patients presenting symptoms at the early age of 10 (Fonzo et al., 2008; Myhre et al., 2008; Yalcin-Cakmakli et al., 2014). This would lead to think that there is a connection between neuronal development and the onset of the disease, specifically an alteration on the transition between neuronal precursor cells and differentiated neurons (Schwamborn, 2018). This transition can occur at two different stages in life: during the early stages of development (embryonal, fetal and early childhood), and during adulthood through neurogenesis (Grand et al., 2015). During embryo development, the formation of the neuronal tube after gastrulation of the embryo is one of the structural recognized first steps in the development of the neuronal system (Stiles and Jernigan, 2010). As described previously, the main neurons affected in PD are localized in the

substantia nigra pars compacta of the midbrain, and this specific region in the mesencephalon is early delimited by the expression of two genes OTX2 and GBX2 that mark the caudal limit with the hindbrain in a region named the isthmus organizer (Hegarty et al., 2013). In this position, the expression of the transcription factors PAX2, LMX1B, WNT1 and EN1 regulate the expression of FGF8 to further limit mid and hindbrain, while the interaction between SHH (produced in the floor of the neural plate) and BMPs (produced dorsally) are involved in determining the dorsoventral identity of the progenitors (Oliveira et al., 2017). Moreover, the inhibition of SHH by WNT signalling through β-catenin at the right time, and the activity of LMX1a induced by OTX2 are crucial for dopaminergic specification (Hegarty et al., 2013; Oliveira et al., 2017). Other transcription factors such as FOXA2, NURR1 and PITX3 are needed for the normal maintenance of midbrain dopaminergic neurons (Hegarty et al., 2013; Grand et al., 2015).

Adult neurogenesis is reported to arise from cells known as adult neuronal stem cells that reside in two different places in the brain: the subventricular zone (SVZ), and the subgranullar zone (SGZ) (Marxreiter et al., 2013). A specific type of SVZ stem cells express receptors for dopamine, inferring that the neurotransmitter can control neurogenesis since dopamine depletion is reported to lower the quantity of cells in these two niches (Farzanehfar, 2016). However, there are also conflicting results that did not detect a reduction in the number of cells in those niches in post-mortem brain samples of patients with PD (van den Berge et al., 2011). Further studies are needed to clarify the possible regeneration of functional dopaminergic neurons in the substantia nigra pars compacta coming from these niches (Farzanehfar, 2016)

Several reports have linked genes affected in PD to altered neurogenesis, whether by alterations in the same mechanism as reported in adulthood or by completely independent mechanism (reviewed in Grand et al., 2015). Especially in the case of PINK1, zebrafish models showed that its downregulation leads to reduce levels of midbrain tyrosine

hydroxylase (TH) positive cells, due to an increase in apoptosis during brain development (Anichtchik et al., 2008).

Studying developmental aspects of the central nervous tissue in humans within living embryos is ethically controversial and so far bound to the Warnock rule, hence the need of alternative models to study the pathological implications of PD in neurodevelopment (Hyun et al., 2016).

1.2 Disease Modelling

1.2.1 hiPSC

Since the first publication by Yamanaka and collaborators in 2006 of the so-called human induced pluripotent stem cells (hiPSCs), almost a scientific article a day was published until 2016 about this new cell type (Negoro et al., 2017). This is only one of the measurements that shows the importance that hiPSCs have in the scientific community (Yamanaka, 2012).

Until the discovery of iPSCs, the known ways for obtaining pluripotent cells were derivation of cells from the inner cell mass of an embryo or the somatic cell nuclear transfer (SCNT) of a differentiated cell into an oocyte for further activation and embryo development (Evans and Kaufman, 1981; Wilmut et al., 1997). Both techniques, even though possible, saw their extrapolation in human studies restricted in some countries and in different forms (Curtis, 2003; de Wert and Mummery, 2003; Hurlbut, 2006). The new technique introduced by Yamanaka not only circumvented these ethical issues but also showed to be a simple and repeatable protocol (Shi et al., 2016).

Induced pluripotent stem cells are obtained through a procedure known as cellular reprogramming that implies driving back the differentiation stage of a specific cell into an earlier state in development (Jaenisch and Young, 2008); and it is accomplished by the introduction of the exogenous factors OCT4, SOX2, c-Myc and KLF4 into cells that would induce the reactivation of silenced genes in the cells' own genome in order to maintain their

pluripotency state (implying indefinite self-renewal, differentiation into the three germ layers, teratoma formation in vivo and embryo body formation) (Takahashi and Yamanaka, 2006).

There are different ways and forms of delivery of these factors that range from DNA-based, RNA, and proteins, with the former including integrative (e.g. lentivirus) and non-integrative (e.g. Sendai virus, episomal) approaches (González et al., 2011). Their choice would have an impact in the derivation efficiency as well as in specific properties of the pluripotent cells obtained (Malik and Rao, 2013). Moreover, there are reports of obtaining iPSCs by using small molecules (Hou et al., 2013). Even though it has been stated that some aspects (e.g. epigenetic memory) of the pluripotent cells obtained by induced reprogramming are different from those derived from a fully reprogrammed mechanism (going through an embryo/zygote state) (Kim et al., 2010; Gore et al., 2011; Ma et al., 2014), most of the ESCs properties are properly recapitulated by hiPSC for modelling specific diseases (Halevy and Urbach, 2014). Human iPSCs have also the advantage of requiring a non-invasive sampling of patients to obtain the material for reprogramming and further differentiation into a specific cell type that would instead need in some cases a critical surgical procedure to harvest the same material from an individual (Soldner and Jaenisch, 2012; Hokayem et al., 2016). This opens the door not only for assessing the pathogeny of a disease in the specific cell type (Sánchez-Danés et al., 2012; Rakovic et al., 2015; Wenker et al., 2015; Hillje and Schwamborn, 2016; Ghaffari et al., 2018) but also for screening compounds and elucidating their mechanism of action in the proper target (Kim and Jin, 2012; Sharma et al., 2013; Kim, 2015; Liu and Deng, 2016). Plus, since hiPSCs can be derived from the specific individual that needs to be treated, compound screens can be tailored in a personalized manner (Kim, 2014; Brennand, 2017). The advent of hiPSCs also brought the potential of transplanting specifically differentiated cells as an autologous therapy, circumventing the time required to find an allogeneic match (Ohyama and Okano, 2013; Singh et al., 2015). In case that the patients needing a treatment possess a known disease causing mutation, hiPSCs cells are a suitable starting point for correcting the

alteration by gene editing techniques since their pluripotency characteristics allows selection, purification, and screening of properly modified clones (Hockemeyer and Jaenisch, 2016; Bassett, 2017; Kim et al., 2017). Plus, their proliferation capabilities permits expanding to have enough biological material to transplant back into the patient (Vonk et al., 2015; Shiba et al., 2016; Li et al., 2017b). The importance of gene editing techniques in the context of disease modelling is discussed in the next chapter.

1.2.2 Gene Editing

Most of the late advances in gene editing, the ability of manipulating the genomic sequence, were driven by the development of reliable targeted nucleases (Gaj et al., 2016). The introduction of these nuclease into eukaryotic cells (delivered as DNA, RNA or proteins) have only the function (in the context of gene editing) of generating a double strand break (DSB) in the genome for activating the cell's DNA repair machinery (Kim, 2016). Damages in the DNA can be solved in different ways, but DSBs can be fixed mostly by two competing mechanisms: nonhomologous end-joining (NHEJ), and homologous directed repair (HDR) (Sancar et al., 2004). The former implies the direct binding of the loose ends of the DNA strands using short homologies regions ('microhomology mediated joins') or no homologies at all ('direct joins') (Boboila et al., 2010). In this process, several insertions/deletions can occur in these ends, becoming suitable for generating knock-out models (Sander and Joung, 2014). On the contrary, the mechanism involved in HDR implies that a larger template is used for replacing the damaged section of DNA (Heyer et al., 2010). Normally, the template used for repairing is the homologous chromosome but in the context of gene editing, an exogenously provided template is used for delivering the desired gene modification (Sander and Joung, 2014). Over the last 30 years, different methods have been used for selectively inducing a double strand break in the genome, however the technological leap happened with the advent of programmable nucleases such as zinc finger nucleases (ZFN), transcription activator like effector nucleases (TALEN) and cluster

regularly interspaced short palindromic repeats(CRISPR)/CRISPR associated protein 9 (Cas9) (Kim, 2016). The first two techniques, ZFN and TALEN, rely on a protein based sequence recognition while the later, CRISPR/Cas9, on a nucleotide based approach (Sander and Joung, 2014). The relevance of the CRISPR/Cas9 technique is due to the ease and versatility of the design, and assembly of the guiding sequence into the respective nuclease (Ran et al., 2013b). This technique was developed by modifying the adaptive immune system some bacteria have against virus and plasmids, into a complex formed by the association of a guide RNA (gRNA) and the Cas9 protein (Jinek et al., 2012). The gRNA possesses a sequence for binding to the Cas9 protein and a targeting sequence (comprised of 20 nucleotide base pair) that would serve as a confirmation template for the Cas9 to exert its enzymatic action (Ran et al., 2013b). The Cas9 protein recognizes a specific motif, known as protospacer adjacent motif (PAM, of which 5'-NGG is the most efficient), in a DNA sequence and binds to it, while the targeting sequence of the gRNA confirms the target site following a Watson-Crick base recognition (Barrangou and Doudna, 2016). The enzymatic action of the two nuclease domains in the Cas9 produce a DSB 3-4 nucleotides upstream of the PAM activating the DNA repair machinery of the cell (Ran et al., 2013b). This targeted gene modification represents an important tool for gene function modelling by providing an accessible method for the generation of knockout biological material (Barrangou and Doudna, 2016). Furthermore, it enables the study of diseases triggered by genomic alterations via the correction or insertion of specific mutations (known as isogenic controls) to phenotypically compare to their unaltered counterpart (Kim et al., 2014). Plus, it is possible to evaluate the activation or inhibition of specific genes (by using a mutated version of the Cas9 protein that yields no enzymatic activity), induce epigenetic regulation, generate the direct conversion of nucleotides, and genomic painting for live tracking specific genes in the nucleus (Barrangou and Doudna, 2016; Yang et al., 2016; Badran et al., 2017). Apart from its application in vitro, the in vivo delivery of the parts of the Cas9 complex was shown successful for doing genome editing in target tissue in living animals (Nelson et al., 2016).

Even though other editing techniques have been tested in humans for in vivo gene editing, CRISPR/Cas9 has not yet been taken into clinical studies (Reardon, 2014; Dai et al., 2016; Kaiser, 2017) .

This technique has been proven to be extremely versatile since not only biomedical applications have been shown but also broader uses in livestock, crop and antibiotic/antiviral formulations (Barrangou and Doudna, 2016).

1.2.3 Neuroprecursors and Neuronal differentiation

Different cell types for evaluating in vitro properties of PD patients have been reported (including fibroblast, hiPSCs, immortalized lines and differentiated neurons) all of them with their own limitations to model a multifactorial disease such as PD (Auburger et al., 2012; Rakovic et al., 2015; Hillje and Schwamborn, 2016). Due to their accessibility and the proliferation capacity of fibroblast, samples from PD patients are normally skin biopsies (Mertens et al., 2016). From this starting point, fibroblast can be expanded and directly differentiated into mature neurons following a procedure known as transdifferentiation (Zhao et al., 2015). This requires solely the addition of specific transcription factors in a sequential manner to only de-repress the epigenetic signatures needed to achieve a different differentiated state while keeping their age-related epigenetic marks (Pang et al., 2011; Mertens et al., 2016). This represents a great advantage for a direct analysis of the desired cell type, since different reports showed a decent transdifferentiation efficiency and a short time needed to obtain mature neurons, even specific subtypes of neurons such as dopaminergic neurons (Caiazzo et al., 2011; Pfisterer et al., 2011; Xu et al., 2017) . However, there is still a need for increasing the transdifferentiation efficiency into dopaminergic neurons (Jang and Jung, 2017). Plus, starting from material that is not indefinitely expandable leads to senescent fibroblast at one point, which might hamper the differentiation efficiency (Sun et al., 2014). Moreover, with this process is not possible to model the developmental features of neuronal differentiation (Mertens et al., 2016).

Reprogramming of fibroblast into hiPSC to further direct their differentiation into neurons, circumvent some of the previous limitations (Cobb et al., 2017). Several reports have stated efficient protocols for the direct differentiation of hiPSCs into mature neurons (Chambers et al., 2009; Kriks et al., 2011; Seibler et al., 2011). However, the long time required (3-6 weeks) for obtaining the material needed for each round of experiments might not be suitable for all applications (Mertens et al., 2016). Differentiation into an intermediate state, like a neuronal precursor cells (NPCs) state, maintains similar proliferation capabilities as hiPSCs, and the staging of neuronal development, while adding a shorter handling time of culture maintenance and a shorter differentiation time, reducing the amount of expensive growth factors and media for obtaining mature neurons (Reinhardt et al., 2013; Yan et al., 2013; Noisa et al., 2015). Considering the importance of NPCs for evaluating their transition to differentiated neurons, qualifies them as a suitable model for assessing the developmental aspects of PD in a high-throughput manner (Reinhardt et al., 2013; Grand et al., 2015). Since the ideal cell model should resemble the early stages of neuronal specification, a protocol for obtaining NPCs with properties similar to neuroepithelial stem cells (NESCs) in the neuronal plate is suitable for this endeavour (Reinhardt et al., 2013). These NPCs are obtained by a dual SMAD inhibition of cells in suspension in an embryo body state through the addition of dorsomorphin and SB43152 inhibiting BMP and TGFβ signal respectively (Chambers et al., 2009). Plus, an equilibrium between the WNT and SHH pathways obtained by the supplementation of CHIR99021 and purmorphamine (PMA) maintains the proliferation capacity of these NPCs and the potential formation of cells derived from both neural plate and neural crest (Reinhardt et al., 2013). For further specification into midbrain dopaminergic neurons, removal of the WNT stimuli induces a ventralization of this cell lineage to give rise to ventral midbrain cells after differentiation and maturation (Reinhardt et al., 2013). Obtaining the right cell type is not the only property desired as a first step for modelling neurodegenerative diseases, but a proper architecture as well as cell type composition should be considered for having a better confidence in

extrapolating observations in a dish into an in vivo context. The next chapter will discuss how disease modelling in 3D cultures can recapitulate this transition.

1.2.4 3D cultures and microfluidics

It is relevant for some diseases that animal models are not able to mimic the entire pathogeny of a human disease, hence the need of a more complex cell culture system that bridges the gap between the phenotypes observed in regular 2D culture systems and what it is observed in the clinics (Passier et al., 2016). In the context of human brain development, most of our knowledge comes from the analysis of post-mortem sections or by inference from mouse models or non-human primates (Lullo and Kriegstein, 2017). In vitro culture systems such as 3D cultures and microfluidics can also provide the necessary cellular context to expand this knowledge (Bhatia and Ingber, 2014). The simplest of these approaches relies in pluripotent cells' self-organization capabilities by providing them a suspension state rather than attached in a 2D monolayer (Eiraku et al., 2011; Lancaster et al., 2013). Pluripotent cells in suspension adopt a 3D structure resembling the one observed in embryoid bodies and can further differentiate into what is called organoid, an organ like structure that possess different cell types spatially organized to perform an organ's specific function (Lancaster and Knoblich, 2014). Organoids conserve the required developmental time, and recapitulate most of the diversity of cells in a tissue (Lullo and Kriegstein, 2017). Moreover, they have been proven valid models for human diseases (Lancaster et al., 2013; Clevers, 2016). However, the process of generating a self-organized organoids has a low reproducibility unless it is guided by morphogenic cues (Huch et al., 2017). Several groups have streamlined stringent protocols for generating organoids that represent only a specific region of the organ to reduce the batch to batch variability of the organoid generation procedure (Jo et al., 2016; Qian et al., 2016; Monzel et al., 2017). Even though reproducible, these organoids might lack specific cell types that are originated from other regions (Lullo and Kriegstein, 2017). However, this can be solved by the combination of two or more

specific cell types coming from different lineage in a similar fashion to the desired organ or tissue (Passier et al., 2016). One of the hurdles of introducing this type of culture in the lab is a reduce set of downstream assays that can be readily performed, for instance the difficulties of performing immunofluorescence in a high-throughput manner (Bhatia and Ingber, 2014). Even though, there is still room for improving the flow of similar techniques in organoids, these hurdles can for example be solved by the adaptation of clearing techniques, and the usage of nanobodies (Boutin and Hoffman-Kim, 2014; Herce et al., 2017; Rios and Clevers, 2018). Another system that might avoid the limitations of organoids but still can maintain the tridimensional arrangement, is the use of microfluidic organs-on-chips (Huh et al., 2011). They are micrometre size chambers that apart of containing living cells present a small channel for media supply (Bhatia and Ingber, 2014). One of the advantages of this system is that it uses the minimal functional unit of a tissue or organ for modelling a disease, and that most of the platforms are adapted for a high content screening setup (Huh et al., 2013; Passier et al., 2016). Due to the engineered properties of the microfluidic devices, the diffusion of nutrients is not a drawback as in organoids where the self-arrangement of cells leaves a dense mass of tissue with a nutrient isolated core (Huh et al., 2013; Huch et al., 2017). Plus, the possibility of interconnecting several organs-on-a-chip representing the different organs of the human body is an important asset for evaluating pharmacodynamics and pharmacokinetics during drug screening in vitro, not only for avoiding the use of animal models but also for modelling them in a personalized manner (Sung et al., 2010; Schwamborn, 2018). On the other hand, some limitations of microfluidics arise from the fact that the amount of biological material is reduced, making it difficult for some assays that require it, and for modelling some diseases that require the presence of macro scale structures (Bhatia and Ingber, 2014). It is clear that the list of options for choosing a disease modelling system is vast and that the specific question that needs to be addressed is an important factor in making this decision.

2. Motivation and Aims

2.1 Motivation

Neurodegenerative diseases represent a social and economic burden to modern society since most of the patients rely only in palliative treatments (Hewer, 1997). Parkinson's disease is a considerable example of this current global health situation (Findley, 2007). Even though we have seen recent advancement in our understanding of PD, we still do not fully grasp the entire scenario that might allow us not only to identify the specific mechanism and chain of events involved in the development of the disease, but also to make the necessary links of common neurodegenerative processes between different diseases (Ramanan and Saykin, 2013; Przedborski, 2017). Moreover, opposing situations, such us age being a risk factor and the possible early onset of PD, are still categorized under the same disease which points out the multifactorial aspect of this malady pushing us to comprehend the factors independently as well as integrally (Schrag and Schott, 2006; Reeve et al., 2014). Specific mutations are known causatives of PD, some of them involved in the early onset of the disease (Klein and Westenberger, 2012). This means that when a crucial pathway is altered, the destabilization of the cell's homeostasis is sufficient for triggering the disease without the need of cofounding stimuli that can occur during the life of the individual (Schulte and Gasser, 2011). In some other cases, a point mutation might not be enough for causation but for predisposing the individual to a future alteration, supporting the multiple hit theory that particularly applies to those mutations with a low penetrance (Sulzer, 2007). Based on reports that highlight the role of specific point mutations in the early stages of development (summarized in Grand et al., 2015), we can hypothesize that this predisposed status can be acquired even during developmental stages. Focusing on known mutations that trigger early onset of the disease, such as the ones in PINK1, we would be able to address if altered specific pathways elicit an early

problem in a human in vitro model or if they could potentially predispose to the development of the disease, making our main hypothesis:

“An altered Pink1-Parkin pathway disturbs the dopaminergic differentiation during early stages of development”

2.2 Aims

1. Streamline the gene editing process in the context of biallelic gene correction of patients’ derived cells.
2. Detect, assess, and classify morphological and functional phenotypes in neuroprecursor cells and in their transition into neurons.
3. Analyse and compare specific morphological features of mitochondria and mitophagy events in neuroprecursor cells and neurons.
4. Evaluate the contribution of the point mutations reported in patients to the phenotypes observed.
5. Screen and identify potential compounds rescuing the altered traits in patients’ cells.

3. Results

The three first author articles in the main body of the thesis and the three papers as a contributing author in the appendix, explain in detail the relevant results obtained to fulfil the aims of my PhD. In the first manuscript, a streamlined procedure for gene editing was established using a novel approach (see also Appendices, Patent I) that provides certainty at the moment of screening for positively corrected clones. Plus, it also guarantees a simultaneous biallelic targeting, by the introduction of a composite of different fluorescences and desired modifications that reduces the hands on time of screening. This was a mayor improvement to one of the technologies, we successfully had applied to insert point mutations in healthy controls, covered in the first manuscript of the Appendices (4th manuscript). The second manuscript, was oriented to tackle the lack of a running system for assessing the autophagy and mitophagy flux in cells in an automated and high throughput manner by means of a fluorescent reporter and high-content image analysis. This new system was further studied in the context of PD by introducing the reporter in lines derived from patients carrying different point mutations known to cause PD (namely PINK1, LRRK2 and VPS35) evidencing the altered activity of these pathways in the context of the disease. The third manuscript, evaluates the influence of point mutations present in PD patients' derived cells during the early stages of neurodevelopment. The phenotypes assessed in this article rely on the techniques established in the first two manuscripts as well as in the platform for making and analysing tridimensional cultures developed in the 5th and 6th manuscript. In this study, I highlight the altered features of the mitochondrial network during the transition between neuroprecursors and neurons in patients' derived cells, the difference in the metabolomic status between controls and patients, the activity of the mitophagy pathway in this transition, the influence of the reported point mutation in the phenotype, and the treatment with the repurposed compound 2-hydroxypropyl-β-cyclodextrin.

3.1 Manuscript I

FACS assisted CRISPR-Cas9 genome editing facilitates Parkinson's disease modeling

Jonathan Arias-Fuenzalida [1,2,7], **Javier Jarazo** [1,7], Xiaobing Qing [1], Jonas Walter [1]

Gemma Gomez-Giro [1,4], Sarah Louise Nickels [1,3], Holm Zaehres [4,5], Hans Robert Schöler [4,6], Jens Christian Schwamborn [1]

[1] Luxembourg Centre for Systems Biomedicine (LCSB), Developmental and Cellular Biology, University of Luxembourg, L-4362, 7 avenue des Hauts-Fourneaux, Luxembourg

[2] Graduate School of Biostudies, Kyoto University, Kyoto 606-8502, Japan

[3] Life Science Research Unit (LSRU), Systems Biology, University of Luxembourg, L-4367, 6 avenue du swing, Luxembourg

[4] Max Planck Institute for Molecular Biomedicine, Laboratory of Cell and Developmental Biology, Roentgenstrasse 20, Muenster, Germany

[5] Ruhr-University Bochum, Medical Faculty, Department of Anatomy and Molecular Embryology, 44801 Bochum, Germany

[6] Westphalian Wilhelms University Muenster, Medical Faculty, 48149 Muenster, Germany

[7] These authors equally contributed to the article

Status: The manuscript is published in Stem Cell Reports, 9 (2017) 1423-1431

3.1.1 Preface

Modelling mutation caused diseases in vitro, requires the usage of isogenic controls in order to validate its influence in the phenotype observed. Gene editing techniques were not readily available in all labs until the introduction of the CRISPR technology. Even though promising, we summarize in this article several bottlenecks of the sate-of-the-art of this technique, such as the presence of random integrations of the donor templates, the high levels of NHEJ observed, the impossibility of targeting both alleles at the same time, and the number of colonies to be genotyped until obtaining a positive result. We address these issues with the new procedure known as FACS-Assisted CRISPR/Cas9 genome editing (FACE). We introduced the novel concept of doing biallelic targeting by combining two florescent reporters with homology arms directed to the same genomic region carrying the desired composite of modifications to be introduced (homozygous or heterozygous changes). We then made use of the piggyBac system for removing the inserted cassette by expression of the enzyme transposase. As a proof of concept we selected two known mutations in SCNA causative of PD, A30P and A53T to be introduced in a healthy control line. Furthermore we also included mutations in two more different genes (PINK1 and CLN3) to see if the system was suitable for other genomic regions. We identify that the proportion and type of non-repetitive elements in the homology arms of the donor template is a major factor in the presence of random integration of the construct. We further assessed that the modified lines presented an altered energetic profile, validating the fact that this point mutations are sufficient for producing mitochondrial alterations related to PD.

I contributed in the concept and establishment of this new procedure as well as in the conduction of all the experiments, the conceptualization of all the figures, and in the writing of this manuscript in collaboration with Jonathan Arias-Fuenzalida.

3.1.2 Manuscript

FACS assisted CRISPR-Cas9 genome editing facilitates Parkinson's disease modeling

Jonathan Arias-Fuenzalida [1,2,7], Javier Jarazo [1,7], Xiaobing Qing [1], Jonas Walter [1] Gemma Gomez-Giro [1,4], Sarah Louise Nickels [1,3], Holm Zaehres [4,5], Hans Robert Schöler [4,6], Jens Christian Schwamborn [1]

[1] Luxembourg Centre for Systems Biomedicine (LCSB), Developmental and Cellular Biology, University of Luxembourg, L-4362, 7 avenue des Hauts-Fourneaux, Luxembourg

[2] Graduate School of Biostudies, Kyoto University, Kyoto 606-8502, Japan

[3] Life Science Research Unit (LSRU), Systems Biology, University of Luxembourg, L-4367, 6 avenue du swing, Luxembourg

[4] Max Planck Institute for Molecular Biomedicine, Laboratory of Cell and Developmental Biology, Roentgenstrasse 20, Muenster, Germany

[5] Ruhr-University Bochum, Medical Faculty, Department of Anatomy and Molecular Embryology, 44801 Bochum, Germany

[6] Westphalian Wilhelms University Muenster, Medical Faculty, 48149 Muenster, Germany

[7] These authors equally contributed to the article

Correspondence should be addressed to J.C.S. (jens.schwamborn@uni.lu)

Abstract

Genome editing and human induced pluripotent stem cells hold great promises for the development of isogenic disease models, and the correction of disease-associated mutations for isogenic tissue therapy. CRISPR-Cas9 has emerged as a versatile and simple tool for engineering human cells for such purposes. However, the current protocols to derive genome-edited lines require the screening of a great number of clones to obtain one free of random integration or on-locus NHEJ containing alleles. Here we describe an efficient method to derive biallelic genome-edited populations by the use of fluorescent markers. We call this technique FACS Assisted CRISPR-Cas9 Editing (FACE). FACE allows the derivation of correctly edited polyclones carrying a positive selection fluorescent module, and the exclusion of non-edited, random integrations and on-target allele NHEJ-containing cells. Here we derived a set of isogenic lines containing Parkinson's disease associated mutations in α-Synuclein, and present their comparative phenotypes.

Introduction

Parkinson's disease (PD) is a multifactorial neurodegenerative disorder characterized by motor and non-motor symptoms (Caligiore et al., 2016). A portion of the PD cases results from autosomal dominant mutations in the *SNCA* gene, which encodes α-Synuclein. Physiologically, α-Synuclein is implicated in synaptic transmission and vesicle transport, while pathologically it is part of protein aggregates known as Lewy bodies and Lewy neurites (Goedert et al., 2013). Patients carrying mutations in the *SNCA* gene suffer from early onset of PD. Mutations in *SNCA* include increase in gene dosage (Devine et al., 2011) and heterozygous missense mutations such as p.A30P and p.A53T (Bendor et al., 2013; Soldner et al., 2011). Mutations in *SNCA* can account for up to 15% of the familial early onset PD cases (Bozi et al., 2014).

Importantly, genome editing tools can assist in parsing PD phenotypes. CRISPR-Cas9 reliability as an editing tool has been extensively validated by whole genome sequencing (Veres et al., 2014). Furthermore, Cas9 specificity has been improved with high-fidelity variants (Kleinstiver et al., 2016). However, eliminating uncertainties in genotype outcomes of edited lines has remained challenging. Screening of correctly edited clones is a labor-consuming process that entails the selection of on-target knock-in clones and the exclusion of random integrations, on-target indels, and second-allele indel events. To leverage the power of genome editing tools in the evaluation of polygenic diseases such as PD, it is necessary to overcome such labor and time consuming limitations. Hence, the fast generation of genome-edited populations carrying a known genotype outcome is highly necessary.

Results

Deterministic genotype outcomes for the generation of isogenic lines

The use of donors containing fluorescent protein (FP) reporters associated with defined SNP variants enables editing outcomes of known genotype (Figure 1A and 1E): heterozygous, homozygous healthy and homozygous pathogenic (Figure 1E). One-step biallelic targeting occurs with a mean frequency of 37.5% using dsDNA templates (Table S1). Donor vectors for *SNCA* exon 2 and exon 3 were cloned with an internal positive selection module (PSM) coding EGFP or dTOMATO, and an external negative selection module (NSM) containing tagBFP (Figure 1A). *SNCA* mutations are dominant, and missense *SNCA* PD patients are heterozygote. Hence, donor pairs for the *SNCA* mutations rs104893878 (p.A30P) and rs104893877 (p.A53T) were designed to match heterozygous genotype outcomes (Figure 1E). In the case of *SNCA*e2, an EGFP donor carried the transversion c.88g>c. For *SNCA*e3, an EGFP donor carried the transition c.209g>a. For each locus, a corresponding dTOMATO donor carried the healthy variant, as shown for population type 1A (Figure 1E). Similar expression level of the FP reporters was observed from each allele in *SNCA* chromosome 4, as evidenced by a symmetric FACS analysis (Figure 1D). In order to test whether similar PSM expression levels are observed in other loci, the gene *PINK1* exon 5 of chromosome 1 was targeted. In contrast to *SNCA* mutant PD patients, *PINK1* PD patients are homozygote or compound heterozygote (Ishihara-Paul et al., 2008). Hence, for *PINK1*e5 both donors, EGFP and dTOMATO, carried the pathogenic transversion c.1197t>a, matching population type 1C (Figure 1E). FACS analysis showed that biallelic targeted populations separated clearly from other genotype outcomes, for *PINK1* chromosome 1 (Figure S1C) and *SNCA* chromosome 4 (Figure 1D). These results validate the approach to target both alleles of a gene of interest, independent of the locus.

Repetitive elements reduce on-target genome editing efficiency by increasing random integration

Silent point mutations were introduced in protospacer adjacent motif (PAM) sequences of the donors (Table S2). PAM edited template is resistant to Cas9-induced linearization, avoiding linear DNA induced random integration. Thus, properly targeted alleles are shielded from Cas9 induced secondary incisions, eliminating the risk of on-target indels (Merkle et al., 2015) (Table S2). Two weeks after electroporation, each edited population was expanded up to $15x10^6$ puromycin-resistant and FP positive cells. The inclusion of tagBFP in the NSM allowed quantifying, visualizing, and excluding random integration events (Figure 1A-B and 1F). The tagBFP NSM avoids by-stander toxicity or incomplete negative selection from systems such as thymidine

kinase (Ruby and Zheng, 2009). The percentage of tagBFP^{pos} random integration ranged from 5.8-14.6% for *SNCA*e2, from 42.6-64.2% for *SNCA*e3, and from 27.2-30.4% for *PINK1*e5 (Figure S2A-C). The extent of random integration correlated with the type and proportion of repetitive elements present in the homology arms of the donors. We assessed random integration using donors for six loci with known repetitive element composition, and tested twelve sgRNAs. The loci evaluated include chromosome 1 (*PINK1* exon 5), chromosome 4 (*SNCA* exon 2 and exon 3), and additionally chromosome 16 (ceroid lupofuscinosis 3, *CLN3* exon 5-8, exon 10-13 and exon 14-15) (Figure S2G). For the analysis, we performed a linear optimization model of the form *Ax=b* (Figure S2H). The resulting matrix *A* corresponds to the frequency of repetitive elements in the homology arms (Figure S2G). The vector x corresponds to the type of repetitive elements present in the analyzed dataset (Figure S2G), and a variable of all non-included repetitive elements (upsilon). The vector b corresponds to the experimentally measured random integration level, given by the percentage of tagBFP^{pos} cells (Figure S2A-F). Based on this we derived a model to predict random integration frequency intrinsic to the composition of repetitive elements in the homology arms (Figure S2H-I). The solution allows assigning weight coefficients to each repetitive element. Their value indicates which repetitive element contributes the most to the random integration frequency observed. The solution space is constrained for a maximum of 100% random integration and sequence length boundaries of each repetitive element. The optimization solution indicates that the most relevant repetitive elements correspond to the Short Interspersed Nuclear Elements (SINE) family, specifically Alu and Mir (Figure S2H-I).

FACS purification increases speed and yield of isogenic derivation

For the on-target tagBFP^{neg} cells the ratio of EGFP to dTOMATO was ~50% in all cases analyzed, which is consistent with a comparable efficiency for both donors (Figure 2A and S1C). The initial percentage of double positive EGFP^{pos}/dTOMATO^{pos} cells ranged from a mean 2.15% for *SNCA*e2, 3.4% for *SNCA*e3 to 3.75% for *PINK1*e5 (Figure 2A and S1C). Quantifications were conducted independently using different sgRNAs (Figure 2A and S1C). One sorting step yielded a population of up to 3x10^5 EGFP^{pos}/dTOMATO^{pos} cells (Figure 2C-D). The gating position of the double positive population afforded nearly complete purity with either purity-purity or yield-purity sorting masks (Figure 2B and S1D). Although it is possible to isolate single channel double positive EGFP$^{pos/pos}$ or dTOMATO$^{pos/pos}$ populations (type 2) (Figure 2A) using the FSC-A dimension, there is an extensive overlap with the indel-bearing single positive population (type U) (Figure S1G-J). A high frequency of NHEJ events was detected in the non-targeted allele of the single positive population (type U)

(Figure S1J-K). Hence, purification of the double positive EGFP$^{pos/pos}$ or dTOMATO$^{pos/pos}$ populations presents the risk of co-purifying overlapping indel bearing cells (Figure S1J-K). In this combination of events, only the biallelic EGFP^{pos}/dTOMATO^{pos} group offers a deterministic genotype outcome. Sanger sequencing of biallelic targeted *SNCA* mutations demonstrated the heterozygous integration of the pathogenic SNP rs104893878 (p.A30P) and rs104893877 (p.A53T) in each polyclone (Figure 2E-F), the homozygous integration of the edited PAM, and the transition from genome to PSM (Figure 2E-F). Sequencing isolated single clones from the polyclonal populations permitted composition analysis (Figure 2G, S3F-G and Table S3).

Transposase mediated generation of footprint-free isogenic lines

The PSMs in each double-positive polyclone were excised using a codon-optimized hyperactive and excision-only variant of the piggybac transposase (Li et al., 2013b; Yusa et al., 2011) (Figure 3A-B). Even though the excision-only variant presents an activity of 0.85 times that of wild type (Figure S1M-N), it is preferred as it lacks the reintegration cycle of wild type variants (Li et al., 2013a). The heterozygous *SNCA*e2 and *SNCA*e3 EGFP^{pos}/dTOMATO^{pos} polyclonal populations were transfected with *in vitro* transcribed mRNA encoding excision-only transposase. Subsequently, the excised EGFP^{neg}/dTOMATO^{neg} population was sorted (Figure 3A-B). Using the excision-only variant and two transfection steps, we observed average excision efficiencies of 3.65% for *SNCA*e2, 2.15% for *SNCA*e3, and 6.5% for *PINK1*e5 (Figure 3A and S1E). A second sorting step, to purify cells that underwent selection module removal, yielded up to 2.5x10^6 EGFP^{neg}/dTOMATO^{neg} SNP knocked-in cells. In the FACS analysis, it is possible to observe transition states for single-copy excision and complete removal of both selection modules (Figure 3A-B and S1E). We observed a curved population shifting from the double-positive EGFP^{pos}/dTOMATO^{pos} quadrant to the double-negative EGFP^{neg}/dTOMATO^{neg} quadrant in all cases. Sanger sequencing of the *SNCA* targeted and transposed genomic region demonstrated the heterozygous integration of the pathogenic SNP rs104893878 (p.A30P) and rs104893877 (p.A53T) in each polyclone (Figure 3C-D). Isolation of single cell derived clones from the polyclones, and sequencing permitted quantification of their composition (Figure 3E, S3H-I and Table S3). The polyclone composition analysis demonstrated that PSMs were excised, the edited SNPs and edited PAM sites remained in the non-coding sequence (Figure S3H-I). Karyotype assessment was conducted for each polyclone and parental control (Figure S4A-C). Pluripotency of lines was assessed by immunostaining for OCT4, SOX2, TRA1-81 and SSEA4 (Figure S4D-F).

***SNCA* mutants present early mitochondrial impairment**

In order to validate the edited *SNCA* lines, a phenotypic characterization was conducted (Figure 4). Isogenic iPS cells were differentiated into neuroepithelial stem cells (NESCs) (Reinhardt et al., 2013) (Figure 4A and S4G-H). NESCs typically express the *SNCA* transcript at 0.86 and 0.7 times the level of *GAPDH* and *TUBG1*, respectively (Figure 4B and S4I). Western blot analysis indicated a similar protein level of monomeric α-Synuclein for all genotypes (Figure 4C). Extracellular energy flux analyses were conducted for parental healthy NESCs, and mutant isogenic α-Synuclein p.A30P and p.A53T NESCs (Figure 4D). Cells expressing the α-Synuclein mutation p.A53T showed a significantly reduced maximal respiration capacity compared to the parental isogenic control (Figure 4D-F). Moreover, both the p.A30P and p.A53T α-Synuclein mutant NESCs showed comparatively reduced energy performance, manifested by a lower basal respiration, ATP production, and non-mitochondrial respiration (Figure 4D-F).

Discussion

Overall, FACE constitutes a robust method to achieve deterministic genotype outcomes for the generation of isogenic cell lines. The selection of biallelic editing events ensure a defined genotype. It should be noted that, due to transient disruption of the coding sequence, this approach is restricted to genes with non-essential function in the target cell type. The use of fluorescent NSM excludes random integration events, enabling clearer sorting gates and isolated biallelic populations. This constitutes an advancement over similar approaches (Eggenschwiler et al., 2016). However, potential limitations are that PSMs could be subjected to position-effect variegation or promotor silencing. Nevertheless, usage of the FP markers expedite the selection, reducing the timescale in comparison to potential position-effect variegation (Norrman et al., 2010). It should be noted that editing approaches that use ssDNA or dsDNA could be subjected to cleavage within non-functional or functional sequences. Hence, donor break points within PSM cannot be fully excluded. The advantage of dsDNA approaches, in comparison to ssDNA, are their flexibility to carry larger cargos, in order to deposit designer-insertions, designer-deletions or PSMs. In addition, larger sequences of donors are easier to detect by conventional methods in comparison to short ssDNA. Similarly, potential imperfect integration of dsDNA donor templates can be readily detected by simple methods as PCR, in comparison to ssDNA based methods.

Conventional derivation of single nucleotide mutations, not associated with a direct selection phenotype or selection marker, can require screening an average 911 ± 375 clones and using 8.8 ± 5.9 sgRNAs. Conversely, early elimination of undesirable outcomes obviates the need to perform extensive colony screening and results in a faster, more efficient derivation process. Thus, FACE constitutes an attractive alternative to conventional methods. The efficiency of homology directed repair is influenced by the length of the homology arms used (Hasty et al., 1991). Others and we use homology arms of ~1kbp, which provides a balance between efficiency and specificity (Soldner et al., 2011). The sequence conversion from endogenous sequence to that carried in donor templates extend from ~400bp in dsDNA (Elliott and Jasin, 2001) to ~30bp in ssDNA donors (Paquet et al., 2016). Hence, it is of critical importance to include the edited bases close to the dsDNA break point and close to the PSM unit, independently of the length of homology arms or the type of template used. Post-knock-in and post-transposition clonal composition analysis confirmed that FACE enables the derivation of polyclones, and significantly reduces the screening efforts, if individual clones are needed. On the other hand, the derivation of edited polyclones presents the advantage of avoiding the risk inherent with clone-specific biases. Extensive expansion, required for clonal derivation,

is reported to subject cells to culture aberrations (Martins-Taylor and Xu, 2012). It is widely accepted that single cell passaging for any type of cell culture application, including the here described process of FACS based enrichment, imposes an unavoidable risk of genome instability (Chan et al., 2008). The derivation of polyclones reduces the culture time needed for each step, since sufficient material is available earlier. Karyotype analysis of the edited lines demonstrated that the process did not induce chromosomal abnormalities when compared with the parental line. Previous reports also support the possibility of achieving low incidence of modification with genome editing tools (Tsai and Joung, 2014; Veres et al., 2014).

In order to protect the dsDNA donor template from Cas9 induced linearization and to avoid post-integration cleavage of targeted sequences, we introduced silent mutations in the PAM sequences. This requires special attention to design, in order to introduce the edited-PAM in a non-coding sequence or as a synonymous mutation. Others and we have successfully used this mechanistic insight to protect post-integration targeted sequences from secondary cleavage events (Inui et al., 2014; Paquet et al., 2016). Similarly, design considerations are needed to identify adjacent transposase excision sequences, or to generate a *de novo* TTAA sequence in non-coding regions or by silent editions. Protocol optimization for the use of an excision-only transposase variant (Li et al., 2013b) allowed the derivation of footprint-free isogenic sets for disease modeling. We were able to observe transition states that represent the removal of one or both PSMs. The transition populations presented a curve pattern that accounts for dissimilar stability of the FPs (Snapp, 2009) and transcripts after the CDS module was removed.

The influence of repetitive elements on the efficiency of genome editing has been reported previously (Ishii et al., 2014). Recognizable repetitive elements constitute up to 45% of the human genome (Lander et al., 2001). Repetitive elements in human can be classified in four families: SINE, LINE, LTR retrotransposons and DNA transposons. Each category present multiple sub-families. Using linear optimization modeling, we determined that in our dataset the repetitive elements of SINE family, Alu and Mir, contribute the most to random integration events. These repetitive elements have 1.5 million copies and constitute ~13% of the human genome (Lander et al., 2001). Although this discrete dataset does not include all existing human repetitive elements, it demonstrates their direct contribution to random integration. Other aspects as the composition of repetitive elements, and distance to the dsDNA break point, might modulate the frequency of random integration. Our data confirm previous reports that repetitive elements act as templates for off-target homologous recombination (Ishii et al., 2014). These sequences should be avoided when designing homology arms in order to enhance the on-target recombination and edition.

In summary, we generated an isogenic set of human *SNCA* mutants for PD specific cellular modeling. The set carries disease-associated mutations p.A30P or p.A53T in the *SNCA* gene. We observed energy metabolism phenotypes in human NESCs, early neurodevelopment disease model. Such traits have been previously described in *SNCA* p.A30P mutant differentiated neurons (Ryan et al., 2013). This validates the applicability of the here described approach for the generation of disease relevant models. We envision that FACE could be efficiently implemented for automated high throughput genome editing, enabling fast phenotype assessment in the future.

Experimental procedures

Stem cells A13777 were cultured in Essential 8 medium on Geltrex. Cells were passed with accutase and plated with Y27632 (10μM) for 24h after dissociation. Cells were electroporated using 4D-Nucleofector. Selection was conducted with puromycin (0.5μg/mL). FACS was conducted on ARIA III sorter. Cells were purified with single cell exclusive gating. Post knock-in cells were transfected with *in vitro* transcribed mRNA coding transposase. Human iPS cells were characterized for OCT4, SOX2, TRA1-81 and TRA1-61. Microarray karyotype was conducted using Illumina iScan technology. NESCs were differentiated as represented in Figure 4A. NESCs were characterized for NESTIN and SOX2. Transcription levels for NESCs were evaluated using Affymetrix human gene arrays (GSE101534). Extracellular energy flux analysis was conducted on NESCs using Seahorse XFe96 assay as indicated in Figure 4D. Comprehensive information of the experimental procedures is described in the Supplemental Information.

Figure legends

Figure 1. Biallelic integration of FP-SNP pairs enable deterministic genotype outcomes. (A) Donor vectors contain a PSM expressing EGFP or dTOMATO, and a NSM expressing tagBFP. PSMs contain puromycin resistance gene (Puro). (B) Representative example of *SNCA*e3 polyclone 636. Random integration tagBFP^{pos} cells are excluded from the correctly edited on-target cells tagBFP^{neg}. (C) Theoretical distribution of populations for non-random outcomes. (D) Representative example of *SNCA*e3. On-target cells include homozygous populations, EGFP^{pos}/EGFP^{pos} or dTOMATO^{pos}/dTOMATO^{pos} (type 2), and heterozygous populations of undefined second-allele state EGFP^{pos}/WT-NHEJ or dTOMATO^{pos}/WT-NHEJ (type U). Wild type (WT). (E) Outcomes of the derived population are defined according to donor vector design. (F) The tagBFP NSM allows removal of random integration events, assisting in the derivation of defined outcomes.

Figure 2. FACS purification increases the speed and yield of isogenic derivation (A) Post selection sorting of double-positive biallelic edited cells for *SNCA*e2 and *SNCA*e3 using independent sgRNAs. FACS plots are represented with 2% contour lines. For *SNCA*e3 sgRNA-636, dot plot is included to show the distribution of 1.2%. Diagram of knock-in population types is shown (right). (B) Yield-purity and purity-purity sorting strategies permit the generation of homogenous biallelic knock-in population. Diagram of purification population types is shown (right). (C) Representative post-sorting single cells for *SNCA* polyclone. Single cell gating structures yields high purity biallelic edited cells. Scale bar 50µm. (D) Representative post-sorting culture for biallelic EGFP^{pos}/dTOMATO^{pos} *SNCA* polyclone. Scale bar 200µm. (E) Sanger sequencing chromatogram of *SNCA*e2 p.A30P polyclone 632 knock-in (KI). (F) Sanger sequencing chromatogram of *SNCA*e3 p.A53T polyclone 636 knock-in. (G) Analysis of the polyclone composition as in Figure S3.

Figure 3. Transposase mediated excision of PSMs. (A) FACS analysis for PSM removal. Two transfection steps of excision-only transposase result in removal of the PSMs for *SNCA*e2 and *SNCA*e3. Purification of EGFP^{neg}/dTOMATO^{neg} cells yields footprint-free edited lines. Diagram of removal population types is shown (right). (B) Cultures after transposase transfection for *SNCA*e2 present single and double PSM removal events (in arrows) as shown in A. Scale bar 200µm. (C) Sanger sequencing chromatogram of transposed *SNCA*e2 p.A30P polyclone 632 and parental control. (D) Sanger sequencing chromatogram of transposed

*SNCA*e3 p.A53T polyclone 636 and parental control. (H) Analysis of the respective polyclone composition as in Figure S3.

Figure 4. Edited *SNCA* isogenic lines present PD associated phenotypes. (A) NESCs differentiation protocol. (B) Microarray expression level for *SNCA*, *TUBG1*, and *GAPDH* in healthy control NESCs. Data represent three replicates. (**C**) Western blot subsequent to denaturing SDS-PAGE for α-Synuclein and GAPDH, for NESCs. (**D**) Wave plot of oxygen consumption rates for the α-Synuclein isogenic set. Each wave corresponds to three biological replicates. SD of the sample is included. (E) Maximal respiration, proton leak, basal respiration, ATP production, and non-mitochondrial respiration for the extracellular energy flux analysis in D. (F) Radar plot of fold changes for the parameters in E. Significance levels correspond to the higher p-value assigned to a mutant per category. Significance determined by unpaired Student's t-test. Significance levels are *p<0.05, **p<0.01 and ***p<0.001.

Author contributions

J.AF., J.J., X.Q., G.GG., J.W., and S.N. designed the study and conducted the experiments. J.C.S., H.Z. and H.S. supervised. J.AF., J.J., and J.C.S. wrote the manuscript and organized display items. All the authors read and agreed to the final version of the manuscript.

Competing financial interests. J.C.S. is shareholder of Braingineering Technologies sarl. J.C.S., J.AF., J.J. and X.Q., are inventors on the patent (LU92964).

Acknowledgments

We would like to thank Prof. F. Zhang from the McGovern Institute for Brain Research for providing the Cas9 vector. We acknowledge G. Preciat for valuable feedback on optimization. We acknowledge Prof. J. Hejna, E. Berger and S. Bolognin for their valuable comments on the manuscript. This project was supported by the LCSB pluripotent stem cell core facility. J.J., J.W., and X.Q. were supported by fellowships from the FNR (AFR, Aides à la Formation-Recherche). G.GG. was supported by NCL-Stiftung. J.J. is supported by Pelican award from the Fondation du Pelican de Mie et Pierre Hippert-Faber supported. This is an EU Joint Programme-Neurodegenerative Disease Research (JPND) project (INTER/JPND/14/02; INTER/JPND/15/11092422). Further support comes from the SysMedPD project which has received funding from the European Union's Horizon 2020 research and innovation programme under grant agreement No 668738.

References

Bendor, J.T., Logan, T.P., and Edwards, R.H. (2013). The function of alpha-synuclein. Neuron *79*, 1044-1066.
Bozi, M., Papadimitriou, D., Antonellou, R., Moraitou, M., Maniati, M., Vassilatis, D.K., Papageorgiou, S.G., Leonardos, A., Tagaris, G., Malamis, G., *et al.* (2014). Genetic assessment of familial and early-onset Parkinson's disease in a Greek population. Eur J Neurol *21*, 963-968.
Caligiore, D., Helmich, R.C., Hallett, M., Moustafa, A.A., Timmermann, L., Toni, I., and Baldassarre, G. (2016). Parkinson's disease as a system-level disorder. NPJ Parkinsons Dis *2*, 16025.
Chan, E.M., Yates, F., Boyer, L.F., Schlaeger, T.M., and Daley, G.Q. (2008). Enhanced plating efficiency of trypsin-adapted human embryonic stem cells is reversible and independent of trisomy 12/17. Cloning Stem Cells *10*, 107-118.
Devine, M.J., Ryten, M., Vodicka, P., Thomson, A.J., Burdon, T., Houlden, H., Cavaleri, F., Nagano, M., Drummond, N.J., Taanman, J.W., *et al.* (2011). Parkinson's disease induced pluripotent stem cells with triplication of the alpha-synuclein locus. Nature communications *2*, 440.
Eggenschwiler, R., Moslem, M., Fraguas, M.S., Galla, M., Papp, O., Naujock, M., Fonfara, I., Gensch, I., Wahner, A., Beh-Pajooh, A., *et al.* (2016). Improved bi-allelic modification of a transcriptionally silent locus in patient-derived iPSC by Cas9 nickase. Sci Rep *6*, 38198.
Elliott, B., and Jasin, M. (2001). Repair of double-strand breaks by homologous recombination in mismatch repair-defective mammalian cells. Mol Cell Biol *21*, 2671-2682.
Goedert, M., Spillantini, M.G., Del Tredici, K., and Braak, H. (2013). 100 years of Lewy pathology. Nat Rev Neurol *9*, 13-24.
Hasty, P., Rivera-Perez, J., and Bradley, A. (1991). The length of homology required for gene targeting in embryonic stem cells. Mol Cell Biol *11*, 5586-5591.
Inui, M., Miyado, M., Igarashi, M., Tamano, M., Kubo, A., Yamashita, S., Asahara, H., Fukami, M., and Takada, S. (2014). Rapid generation of mouse models with defined point mutations by the CRISPR/Cas9 system. Sci Rep *4*, 5396.
Ishihara-Paul, L., Hulihan, M.M., Kachergus, J., Upmanyu, R., Warren, L., Amouri, R., Elango, R., Prinjha, R.K., Soto, A., Kefi, M., *et al.* (2008). PINK1 mutations and parkinsonism. Neurology *71*, 896-902.
Ishii, A., Kurosawa, A., Saito, S., and Adachi, N. (2014). Analysis of the role of homology arms in gene-targeting vectors in human cells. PLoS One *9*, e108236.
Kleinstiver, B.P., Pattanayak, V., Prew, M.S., Tsai, S.Q., Nguyen, N.T., Zheng, Z., and Joung, J.K. (2016). High-fidelity CRISPR-Cas9 nucleases with no detectable genome-wide off-target effects. Nature *529*, 490-495.
Lander, E.S., Linton, L.M., Birren, B., Nusbaum, C., Zody, M.C., Baldwin, J., Devon, K., Dewar, K., Doyle, M., FitzHugh, W., *et al.* (2001). Initial sequencing and analysis of the human genome. Nature *409*, 860-921.
Li, M.A., Pettitt, S.J., Eckert, S., Ning, Z., Rice, S., Cadinanos, J., Yusa, K., Conte, N., and Bradley, A. (2013a). The piggyBac transposon displays local and distant reintegration preferences and can cause mutations at noncanonical integration sites. Mol Cell Biol *33*, 1317-1330.
Li, X., Burnight, E.R., Cooney, A.L., Malani, N., Brady, T., Sander, J.D., Staber, J., Wheelan, S.J., Joung, J.K., McCray, P.B., Jr., *et al.* (2013b). piggyBac transposase tools for genome engineering. Proc Natl Acad Sci U S A *110*, E2279-2287.
Martins-Taylor, K., and Xu, R.H. (2012). Concise review: Genomic stability of human induced pluripotent stem cells. Stem Cells *30*, 22-27.
Merkle, F.T., Neuhausser, W.M., Santos, D., Valen, E., Gagnon, J.A., Maas, K., Sandoe, J., Schier, A.F., and Eggan, K. (2015). Efficient CRISPR-Cas9-mediated generation of knockin human pluripotent stem cells lacking undesired mutations at the targeted locus. Cell Rep *11*, 875-883.
Norrman, K., Fischer, Y., Bonnamy, B., Wolfhagen Sand, F., Ravassard, P., and Semb, H. (2010). Quantitative comparison of constitutive promoters in human ES cells. PLoS One *5*, e12413.
Paquet, D., Kwart, D., Chen, A., Sproul, A., Jacob, S., Teo, S., Olsen, K.M., Gregg, A., Noggle, S., and Tessier-Lavigne, M. (2016). Efficient introduction of specific homozygous and heterozygous mutations using CRISPR/Cas9. Nature *533*, 125-129.
Reinhardt, P., Glatza, M., Hemmer, K., Tsytsyura, Y., Thiel, C.S., Hoing, S., Moritz, S., Parga, J.A., Wagner, L., Bruder, J.M., *et al.* (2013). Derivation and expansion using only small molecules of human neural progenitors for neurodegenerative disease modeling. PLoS One *8*, e59252.
Ruby, K.M., and Zheng, B. (2009). Gene targeting in a HUES line of human embryonic stem cells via electroporation. Stem Cells *27*, 1496-1506.
Ryan, S.D., Dolatabadi, N., Chan, S.F., Zhang, X., Akhtar, M.W., Parker, J., Soldner, F., Sunico, C.R., Nagar, S., Talantova, M., *et al.* (2013). Isogenic human iPSC Parkinson's model shows nitrosative stress-induced dysfunction in MEF2-PGC1alpha transcription. Cell *155*, 1351-1364.

Snapp, E.L. (2009). Fluorescent proteins: a cell biologist's user guide. Trends Cell Biol *19*, 649-655.
Soldner, F., Laganiere, J., Cheng, A.W., Hockemeyer, D., Gao, Q., Alagappan, R., Khurana, V., Golbe, L.I., Myers, R.H., Lindquist, S., *et al.* (2011). Generation of isogenic pluripotent stem cells differing exclusively at two early onset Parkinson point mutations. Cell *146*, 318-331.
Tsai, S.Q., and Joung, J.K. (2014). What's changed with genome editing? Cell Stem Cell *15*, 3-4.
Veres, A., Gosis, B.S., Ding, Q., Collins, R., Ragavendran, A., Brand, H., Erdin, S., Cowan, C.A., Talkowski, M.E., and Musunuru, K. (2014). Low incidence of off-target mutations in individual CRISPR-Cas9 and TALEN targeted human stem cell clones detected by whole-genome sequencing. Cell Stem Cell *15*, 27-30.
Yusa, K., Zhou, L., Li, M.A., Bradley, A., and Craig, N.L. (2011). A hyperactive piggyBac transposase for mammalian applications. Proc Natl Acad Sci U S A *108*, 1531-1536.

Experimental procedures

Stem cell culture and electroporation. The following human induced pluripotent stem (iPS) cells reprogrammed with non-integrative episomal methods were used: A13777 (Gibco cat no. A13777) from female cord blood-derived $CD34^{pos}$ cells. Cell lines were cultured in Essential 8 medium (Thermo Fisher cat no. A1517001) on Geltrex (Thermo Fisher cat no. A1413301) or matrigel. Cells were normally dissociated with accutase (Thermo Fisher cat no. A1110501) and plated in media containing ROCK inhibitor Y27632 (Sigma cat no. Y0503) at 10μM for 24h after dissociation. Cells were subjected to positive selection with puromycin (Sigma cat no. P9620) at a concentration of 0.5μg/mL as shown in Figure S9. Cells were electroporated using 4D-Nucleofector System (Lonza) and a 4D kit for human dermal fibroblast (Lonza cat no. V4XP). Parental pre-electroporation line presents micro-duplication 20q11.21.

Construction of sgRNA vectors and donor plasmids. Cas9 target sequences with predicted high catalytic activity were selected (Doench et al., 2014) (**Figure S1**) and cloned into pX330 vector (Addgene 42230) as previously described (Ran et al., 2013). Primers used are indicated in **Supplemental table 3**. The donor vectors were pDONOR-SNCAe2-WT (Addgene 85845), pDONOR-SNCAe2-A30P (Addgene 85846), pDONOR-SNCAe3-WT (Addgene 85847), pDONOR-SNCAe3-A53T (Addgene 85848) and pDONOR-PINK1e5-I368N (Addgene 86154) in EGFP and dTOMATO containing versions. Homology arms were assembled by conventional methods (Gibson, 2011) on donor scaffolds pDONOR-tagBFP-PSM-EGFP (Addgene 100603) and pDONOR-tagBFP-PSM-dTOMATO (Addgene 100604).

In vitro RNA transcription and mRNA transfection. The coding sequence of codon-optimized hyperactive transposase Piggybac from *Trichoplusia ni* (Yusa et al., 2011) and the excision-only mutant (Li et al., 2013b) were amplified to incorporate the T7 promoter. Primers used are indicated in **Supplemental table 3**. The PCR product was used as template for in vitro transcription with an mMESSAGE mMACHINE T7 kit (Thermo Fisher cat no. AM1344) according to the manufacturer's protocol. The transcript was poly-adenylated with a Poly(A) tailing kit (Thermo Fisher cat no. AM1350) and purified with a MEGAclear transcription clean-up kit (Thermo Fisher cat no. AM1908). The transcript quality was evaluated with a Bionalayzer RNA 6000 nano (Aglient cat no. 5067-1511). Transfection was performed with Stemfect RNA transfection kit (Stemgent cat no. 00-0069) according to the manufacturer's protocol.

Fluorescent Activated Cell Sorting. FACS was conducted using sterile line sorting on a baseline and CST calibrated BD FACS ARIA III. Drop delay calibrations were ensured prior to each sample. For all human iPS cells an 85µm nozzle, a yield or purity sorting mask and neutral density filter 2.0 were used. Cells were pre-separated with 35µm and 20µm strainers (Corning cat no. 352235 and Miltenyi cat no. 130-101-812). Sorting was conducted with single cell exclusive gating hierarchies on FSC and SSC wide and high (**Figure S6A**). Use of strainers and single cell gating is highly recommended (**Figure S6B**). For efficiency analysis, live cells were quantified by SYTOX Blue Dead Cell Stain (Thermo Fisher cat no. S34857).

Characterization of polyclones. Composition of polyclones was assessed by sub-cloning. Single cell clones were expanded and genomic DNA extracted using QuickExtract solution (Epicentre cat no. QE09050). Clones were genotyped for the left homology arm junction, right homology arm junction, and wild type junction as indicated in **Figure S3** and **Figure S5**, using primers in **Supplemental table 3**. PCR products of the left homology arm were used for Sanger sequencing of subclones of SNCAe2(A30P) 632 polyclone and SNCAe3(A53T) 636 polyclone as shown in **Figure S3**. The wild type junction was used for Sanger sequencing of subclones of transposed SNCAe2(A30P) 632 polyclone and transposed SNCAe3(A53T) 636 polyclone as shown in **Figure S5**.

Microarray Karyotype. Genomic DNA from the pre-electroporation parental, and isogenic polyclones was purified using GenElute Blood genomic DNA Kit (Sigma cat no. NA2020). Samples were processed at Bonn Univesity Life&Brain genomics facility using Illumina iScan technology (Illumina).

Immunostaining. Cells were fixed on PFA and permeabilized on PBS triton-X 0.2%. For characterizing human iPS cells, primary antibodies used were OCT4 (Santa cruz cat no. sc-5279) dilution 1:100, TRA1-81 (Millipore cat no. MAB4381) dilution 1:50, SOX2 (Abcam cat no. ab97959) dilution 1:100 and SSEA4 (Millipore cat no. MAB4304) dilution 1:50. Secondary antibodies used were donkey anti-mouse alexa fluor 488 (Thermo Fisher cat no. A-21202) and donkey anti-rabbit alexa fluor 488 (Thermo Fisher cat no. A-21206), both at dilution 1:1000. For characterizing NESCs, primary antibodies used were NESTIN (BD cat no. 611659) dilution 1:600 and SOX2 (Abcam cat no. ab97959) dilution 1:200. Secondary antibodies used were donkey anti-mouse 488 (Thermo Fisher cat no. A-21202) and donkey anti-rabbit 647 (Thermo Fisher cat no.

A-31573), both at dilution 1:1000. For nuclear staining, Hoechst-33342 (Thermo Fisher cat no. 62249) was used at dilution 1:1000. Images were acquired in an inverted microscope (Zeiss Axio ObserverZ1).

NESCs differentiation and culture. Induced pluripotent stem cells were clustered on aggrewell plates (Stem cell technologies cat no. 27845) for 12 hours. Embryoid bodies were transferred to ultra-low attachment plates and differentiated with the program in **Figure 4A**. Briefly, cells were cultured on KO-DMEM (Gibco cat no. 10829018) supplemented with 20% knock-out serum replacement (Gibco cat no. A3181501), 2mM glutamax (Gibco cat no. 35050061), 1x non-essential amino acids (Gibco cat no.11140035), 1µM dorsomorphine (Sigma cat no. P5499), 3µM CHIR99021 (Sigma cat no. SML1046) and 0.5µM purmorphamine (Sigma cat no. SML0868). From day three onwards, cells were cultured on DMEM-F12:neurobasal media (1:1) supplemented with N2 (Gibco cat no. 17502048), B27 without vitamin A (Gibco cat no. 12587001) and 2mM glutamax. For day three and four, media was supplemented with 10µM SB431542 (Sigma cat no. S4317). From day five onwards, the culture was maintained with 150µM ascorbic acid (Sigma cat no. A5960), 3µM CHIR99021 and 0.5µM purmorphamine. At day six, embryoid bodies were dissociated with accutase and plated on matrigel coated plates.

Extracellular energy flux analysis. NESCs were plated on Seahorse XFe96 assay plates (Aglient) at a density of 65k cells per well and the oxygen consumption rate was quantified in a Seahorse XFe96 Analyzer. Four baseline measurements were performed before any treatment injection. Three measurements were performed after each injection as shown in **Figure 4**. Final concentrations of compounds were 1µM for oligomycin (Sigma cat no. 75351), FCCP (Sigma cat no. C2920), antimycin A (Sigma cat no. A8674) and rotenone (Sigma cat no. R8875). DNA was quantified using CyQUANT kit (Thermo Fisher cat no. C7026) and normalization based on DNA content as previously described (Silva et al., 2013).

Western Blotting. For western blot analysis of NESCs total protein, an antibody against alpha-Synuclein (C-20)-R (Santa cruz cat no. sc-7011) was used at a dilution of 1:100, and an antibody against GAPDH (abcam cat no. ab9485) was used at a dilution of 1:1000 overnight. Blots were developed using anti-rabbit IgG HRP-linked secondary antibody (GE Healthcare Life Sciences cat no. NA934V) and west-pico chemiluminescent substrate (Thermo Fisher cat no. 34080). Membranes were imaged in a Raytest Stells system with exposure of 30s for both alpha-Synuclein and GAPDH.

Microarray. RNA was extracted from healthy control NESCs using quiazol (Qiagen cat no. 79306) and miRNeasy (Qiagen cat no. 217004). Samples were processed at the EMBL Genomics Core Facility using Affymetrix human Gene 2.0 arrays. Results were processed using GC-RMA analysis. Gene expression omnibus accession code GSE101534.

FACS assisted CRISPR-Cas9 genome editing facilitates Parkinson's disease modeling

- Supplemental Information -

Jonathan Arias-Fuenzalida [1,2,7], Javier Jarazo [1,7], Xiaobing Qing [1], Jonas Walter [1] Gemma Gomez-Giro [1,4], Sarah Louise Nickels [1,3], Holm Zaehres [4,5], Hans Robert Schöler [4,6], Jens Christian Schwamborn [1]

[1] Luxembourg Centre for Systems Biomedicine (LCSB), Developmental and Cellular Biology, University of Luxembourg, L-4362, 7 avenue des Hauts-Fourneaux, Luxembourg

[2] Graduate School of Biostudies, Kyoto University, Kyoto 606-8502, Japan

[3] Life Science Research Unit (LSRU), Systems Biology, University of Luxembourg, L-4367, 6 avenue du swing, Luxembourg

[4] Max Planck Institute for Molecular Biomedicine, Laboratory of Cell and Developmental Biology, Roentgenstrasse 20, Muenster, Germany

[5] Ruhr-University Bochum, Medical Faculty, Department of Anatomy and Molecular Embryology, 44801 Bochum, Germany

[6] Westphalian Wilhelms University Muenster, Medical Faculty, 48149 Muenster, Germany

[7] These authors equally contributed to the article

Correspondence should be addressed to J.S. (jens.schwamborn@uni.lu)

Inventory of Supplemental Information

Figure S8. Microarray karyotype and pluripotency of parental and isogenic lines

Figure S9. Minimal timeframe required for editing.

Supplemental Table 1. Biallelic targeting frequency

Supplemental Table 2. SNCA polyclones summary.

Supplemental Table 3. Oligonucleotides used in this study.

Supplemental Figure legends

Figure S1. **Cleaving region design. Related to Figure 1**. (**A**) Schematic representation of SNCA exon 2 and SNCA exon 3 indicating the binding site of the sgRNAs tested (**Supplemental table 3**), disease-associated SNPs, and PAM edited bases.

Figure S2. Repetitive elements decrease on-target efficiency and increase random integration events. Related to Figure 1. Flow cytometry histogram for tagBFP: (**A**) SNCA exon 2 sgRNA 630 and 632, (**B**) SNCA exon 3 sgRNA 634 and 636, (**C**) PINK1 exon 5 sgRNA 517 and 526, (**D**) CLN3 exon 14-15 sgRNA 788, 789 and 909, (**E**) CLN3 exon 5-8 sgRNA 781 and 783, and (**F**) CLN3 exon 10-13 sgRNA 561 and 563. (**G**) Distribution and type of repetitive elements in the homology arms of the dsDNA donors for SNCAe2, SNCAe3, PINK1e5, CLN3e5-6, CLN3e10-13 and CLN3e14-15. (**H**) Predictive model for random integration. The predictive model *PR* uses the matrix of repetitive element frequency in the homology arms *A*, the repetitive elements vector *x*, and the observed incidence of tagBFP^{pos} random integration *b*. The mathematical model generates coefficients for each repetitive element and the constant of the system for random integration prediction. (**I**) The space of non-zero coefficients derived from **H**: SINE Alu and SINE Mir, allows inferring expected random integration frequencies.

Figure S3. Quantification of polyclone composition and efficiency post-knock-in. Related to Figure 2. (**A**) Schematic representation of the genomic structure after knock-in and genomic structure after transposition. Positive selection module (PSM), left homology arm (LHA) and right homology arm (RHA). The binding sites of the genotyping primers are represented (**Supplemental table 3**), as well as the left homology arm junction, right homology arm junction, and WT junction. (**B**) Genotyping PCR products of 24 clones derived from the polyclone SNCAe2(A30P) 632, and WT control. (**C**) Genotyping PCR products of 24 clones derived from the polyclone SNCAe3(A53T) 636, and WT control. (**D**) Representation of the left homology arm junction of SNCAe2 including the SNP rs104893878 and PSM interface. Sanger sequencing chromatograms of 24 clones derived from the polyclone SNCAe2(A30P) 632 as in **B**. Chromatograms show the transversion

SNCA c.88g>c and the TTAA interface to the PSM. Knock-in (KI). (**E**) Representation of the left homology arm junction of SNCAe3 including the SNP rs104893877 and PSM interface. Sanger sequencing chromatograms of 24 clones derived from the polyclone SNCAe3(A53T) 636 as in **C**. Chromatograms show the transition SNCA c.209g>a and the TTAA interface to the PSM. Knock-in (KI).

Figure S4. Single fluorescent protein homozygous clones present high overlap with heterozygous indel-bearing clones. Related to Figure 2. (**A**) Homozygous and heterozygous dTOMATO^{pos} SNCAe2 clones were analyzed by FACS. The histogram (left) confirms the overlap in the 2D-fluorescent cytometry map (right). (**B**) Schematic representation of overlapping populations as in **Figure 1G**. Knock-in (KI). (**C**) Type U (one copy integration) and type 2 (two copy integration) single cell clones also present high overlap in the FSC-A dimension. Clone type U population overlaps 26.1% with the gate established by the type 2 clone. (**D**) Sequencing of the non-targeted allele amplified from the type U population presents a high frequency of indels as indicated by a set of Sanger sequencing reads (n=20) for SNCAe2 and SNCAe3 type U. (**E**) Representative chromatogram for an indel bearing non-targeted allele of the type U population. Cas9 cleavage site indicated in arrow.

Figure S5. Quantification of polyclone composition and efficiency post-transposition. Related to Figure 3. (**A**) Schematic representation of the genomic structure after knock-in and genomic structure after transposition. Positive selection module (PSM), left homology arm (LHA) and right homology arm (RHA). The binding sites of the genotyping primers are represented (**Supplemental table 3**), as well as the left homology arm junction, right homology arm junction, and WT junction. (**B**) Genotyping PCR products of 24 clones derived from the transposed polyclone SNCAe2(A30P) 632, pre-removal polyclone, and WT control. (**C**) Genotyping PCR products of 24 clones derived from the transposed polyclone SNCAe3(A53T) 636, pre-removal polyclone, and WT control. (**D**) Representation of the WT junction of SNCAe2 including the SNP rs104893878, and the TTAA interface to the genomic region. Sanger sequencing chromatograms of 24 clones derived from the transposed polyclone SNCAe2(A30P) 632. Chromatograms show the transversion SNCA c.88g>c and the TTAA interface to the genomic region. (**E**) Representation of the WT junction of SNCAe3 including the SNP rs104893877, and the TTAA interface to the genomic region. Sanger sequencing chromatograms of 24 clones derived from the transposed polyclone SNCAe3(A53T) 636. Chromatograms show the transition SNCA c.209g>a and the TTAA interface to the genomic region.

Figure S6. Single cell gating structure and biallelic editing of PINK1e5. Related to Figure 2 and Figure 3. (**A**) Hierarchical single cell gating structure of SSC and FSC wide and high for single cell preparations of

PINK1e5(I368N) 517 polyclone. (**B**) Preparation of cells with a cell strainer and single cell gating structure is essential to ensure high quality sorting. Scale bar 25µm. (**C**) Gating structure and population types for knock-in, purification, and excision strategy. (**D**) Post selection sorting of double-positive biallelic edited cells for PINK1e5, using independent sgRNAs (sgRNA 517 and sgRNA 526). FACS plots are represented with 2 percent contour lines. (**E**) Purity-purity sorting allows the generation of a homogenous biallelic knock-in population. (**F**) excision-only transposase expression removes the positive selection module for PINK1e5. (**G**) Parental WT control.

Figure S7. Differentiation, protein, and transcriptional level analysis of NESCs. Related to Figure 4. (**A**) Differentiation of induced pluripotent stem cells to NESCs in 3D culture as shown in **Figure 4A**. (**B**) Immunostaining of NESCs for the neurepithelial stem cell markers NESTIN and SOX2. Scale bar 50µm. (**C**) Relative expression of *SNCA* mRNA with respect to *TUBG1* and *GAPDH* transcripts in microarray expression analysis in **Figure 4B**.

Figure S8. Microarray karyotype and pluripotency of parental and isogenic lines. Related to Figure 2 and Figure 3. (**A**) Microarray karyotype analysis of the parental line before electroporation, (**B**) polyclone 6321421 SNCA p.A30P and (**C**) polyclone 6361868 SNCA p.A53T. (**D**) Immunostaining for the pluripotency markers OCT4, TRA1-81, SOX2 and SSEA4 for parental control, (**E**) polyclone 6321421 SNCA p.A30P and (**F**) polyclone 6361868 SNCA p.A53T. Scale bar 200µm.

Figure S9. Minimal timeframe required for editing. Related to Figure 1, Figure 2 and Figure 3. (**A**) Schematic representation of conventional sgRNA testing experiment. Activity of sgRNA is validated and ranked based on colony counts at day 10. Puromycin (Puro) and ROCK inhibitor Y27632 (Y). (**B**) A minimum of three passages and 25 days are needed for knock-in process. Sorting strategies of yield/purity or purity/purity can be implemented. Puromycin (Puro) and ROCK inhibitor Y27632 (Y). (**C**) A minimum of four passages and 20 days are needed for transposition process. Sorting strategy of yield/purity is recommended. ROCK inhibitor Y27632 (Y).

Supplemental Table 1. Biallelic targeting frequency

Polyclone sample	Frequency composed biallelic[a]	Frequency single channel biallelic[b]	Frequency total biallelic[c]
SNCAe3 636	0.032	0.179	0.390
SNCAe2 630	0.021	0.145	0.311
SNCAe2 632	0.022	0.148	0.319
SNCAe3 634	0.056	0.237	0.529
SNCAe3 636	0.012	0.110	0.231
PINK1e5 517	0.033	0.182	0.396
PINK1e5 526	0.042	0.205	0.452
Mean total			**0.375**

[a]Frequency composed biallelic is defined as the experimentally measured $EGFP^{pos}dTOMATO^{pos}$ population.
[b]Frequency of single channel biallelic represents separately the $EGFP^{pos}EGFP^{pos}$ and $dTOMATO^{pos}dTOMATO^{pos}$ population, calculated as $\sqrt{\text{frequency composed biallelic}}$.
[c]Frequency total biallelic correspond to $\text{frequency composed biallelic} + 2 * \text{frequency of single channel biallelic}$.

Supplemental Table 2. SNCA polyclones summary.

Polyclone	PAM shielded	sgRNA	FACS % non-random	FACS % composed biallelic knock-in	% correct genotype post-knock-in (n correct/total)	FACS % transposition	% correct genotype post-transposition (n correct/total)
SNCAe2(A30P) 632	YES	632	94.1	2.2	100 (24/24)	4.0	100 (24/24)
SNCAe3(A53T) 636	YES	636	56.8	1.2	100 (24/24)	1.1	100 (24/24)
SNCAe2(A30P) 630	NO	630	85.1	2.1	Not determined	3.3	Not determined
SNCAe3(A53T) 634	NO	634	34.2	5.6	Not determined	3.2	Not determined

Supplemental Table 3. Oligonucleotides used in this study.

Primer	Sequence (5' to 3')	Region (Purpose)
SNCAe2_F1 (no1615)	gaggagtcggagttgtggagaag	SNCAe2 (Genotyping)
SNCAe2_R1 (no1616)	ttcccccactgatctatgttgaagag	SNCAe2 (Genotyping)
SNCAe3_F1 (no1617)	actgaaaaatccaacattagagagg	SNCAe3 (Genotyping)
SNCAe3_R1 (no1036)	ccagaacttgccacatgctt	SNCAe3 (Genotyping)
ITR_R1 (no861)	agatgtcctaaatgcacagcg	ITR (Genotyping)
ITR_F1 (no1310)	cgtcaattttacgcatgattatctttaac	ITR (Genotyping)
SNCAe2 (no1065)	tccgtggttaggtggctaga	SNCAe2 (Sequencing)
SNCAe3 (no1034)	gggccccggtgttatctcat	SNCAe3 (Sequencing)
T7-transposase_F (no1673)	gaaattaatacgactcactataggg ccgccaccatgggcagcagcctggac	transposase CDS (T7 fusion IVT)
Transposase_R (no1693)	ggcaaacaacagatggctgg	transposase CDS (IVT)
SNCAe2_628F	caccggtaaaggaattcattagcca	synthetic (sgRNA cloning)
SNCAe2_629F	caccgggactttcaaaggccaagga	synthetic (sgRNA cloning)
SNCAe2_630F	caccggctgctgagaaaaccaaaca	synthetic (sgRNA cloning)
SNCAe2_631F	caccgagggtgttctctatgtaggt	synthetic (sgRNA cloning)
SNCAe2_632F	caccgggtgcttgttcatgagtgat	synthetic (sgRNA cloning)
SNCAe3_633F	caccgtatatcctaaaactagaaga	synthetic (sgRNA cloning)
SNCAe3_634F	caccgtgtaggctccaaaaccaagg	synthetic (sgRNA cloning)
SNCAe3_635F	caccgatctttggatataagcacaa	synthetic (sgRNA cloning)
SNCAe3_636F	caccggatactttaaatatcatctt	synthetic (sgRNA cloning)
SNCAe3_637F	caccgatacttgccaagaataatga	synthetic (sgRNA cloning)
SNCAe2_628R	aaactggctaatgaattcctttacc	synthetic (sgRNA cloning)
SNCAe2_629R	aaactccttggcctttgaaagtccc	synthetic (sgRNA cloning)
SNCAe2_630R	aaactgtttggttttctcagcagcc	synthetic (sgRNA cloning)
SNCAe2_631R	aaacacctacatagagaacaccctc	synthetic (sgRNA cloning)
SNCAe2_632R	aaacatcactcatgaacaagcaccc	synthetic (sgRNA cloning)
SNCAe3_633R	aaactcttctagttttaggatatac	synthetic (sgRNA cloning)
SNCAe3_634R	aaaccttggttttggagcctacac	synthetic (sgRNA cloning)
SNCAe3_635R	aaacttgtgcttatatccaaagatc	synthetic (sgRNA cloning)
SNCAe3_636R	aaacaagatgatatttaaagtatcc	synthetic (sgRNA cloning)
SNCAe3_637R	aaactcattattcttggcaagtatc	synthetic (sgRNA cloning)
U6_F	gagggcctatttcccatgattcc	U6 (sequencing)

3.1.3 Figures

Graphical abstract

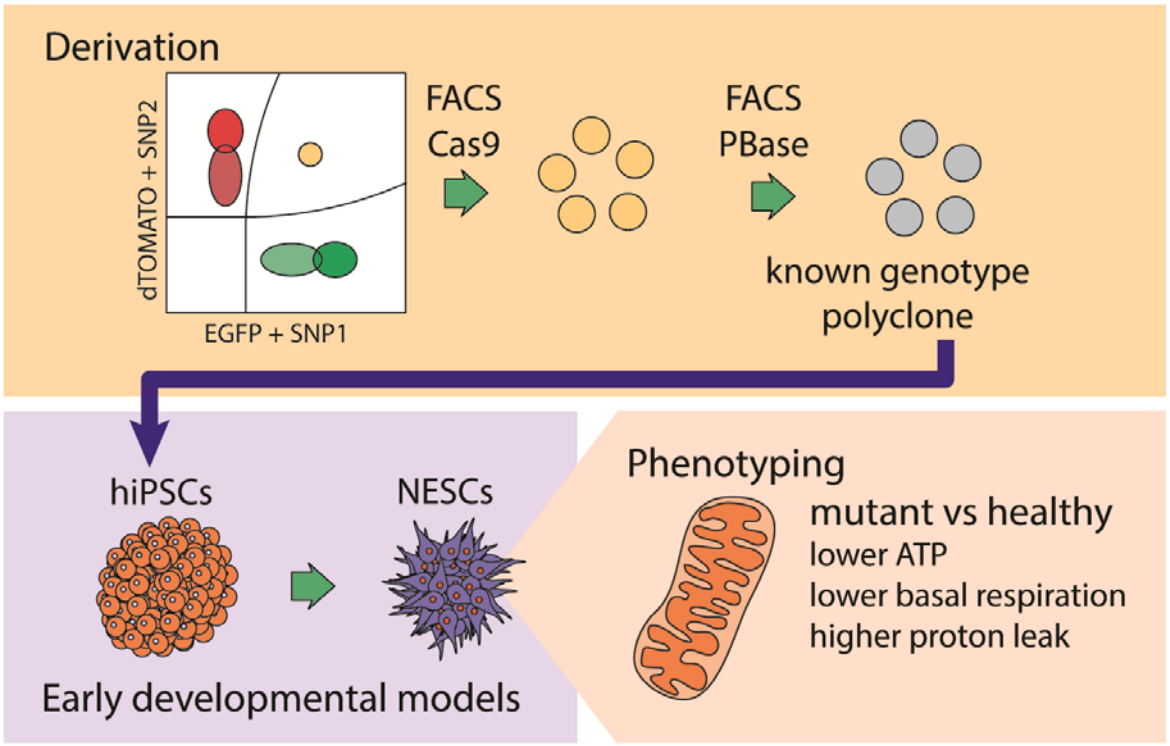

Figure 1

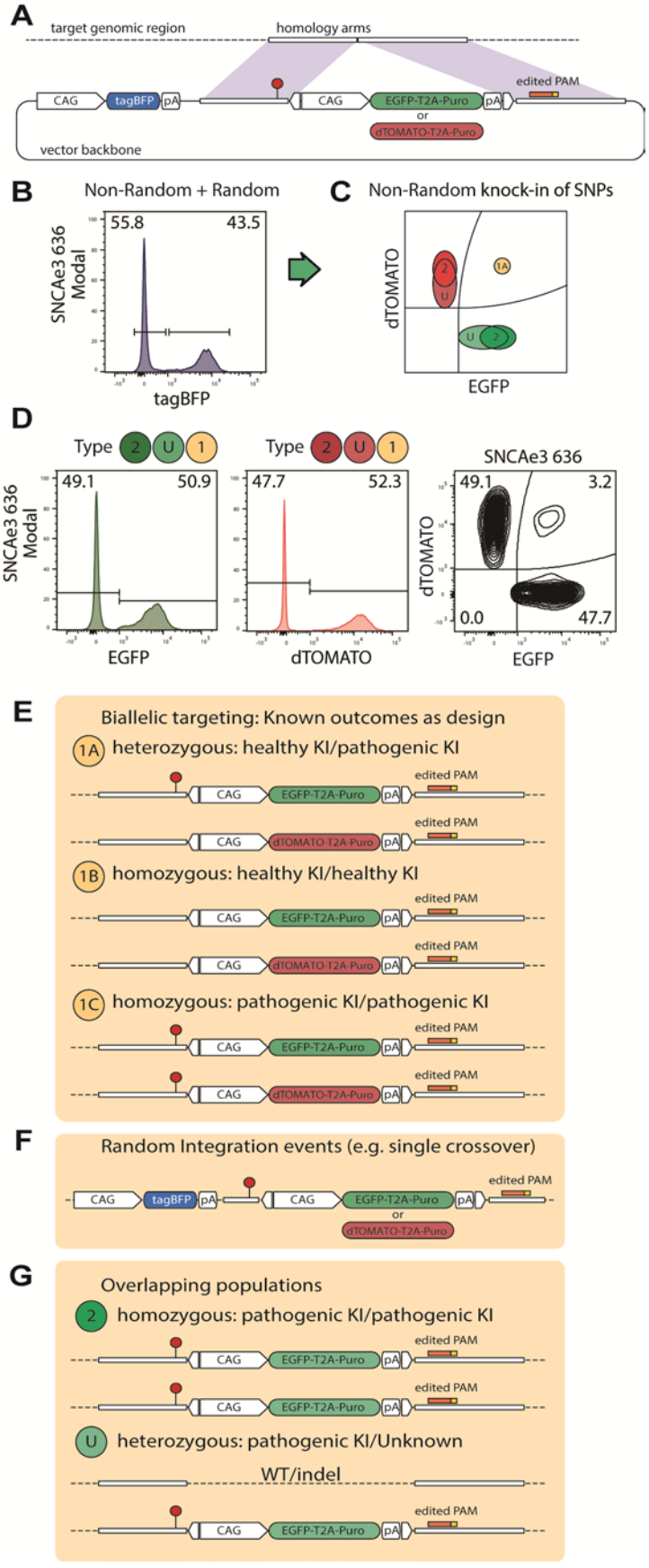
A
target genomic region
homology arms
edited PAM
CAG
tagBFP
pA
CAG
EGFP-T2A-Puro
pA
or
dTOMATO-T2A-Puro
vector backbone
B
Non-Random + Random
55.8
43.5
SNCAe3 636 Modal
tagBFP
C
Non-Random knock-in of SNPs
dTOMATO
EGFP
D
Type 2 U 1
Type 2 U 1
SNCAe3 636
49.1
50.9
47.7
52.3
49.1
3.2
0.0
47.7
SNCAe3 636 Modal
EGFP
dTOMATO
dTOMATO
EGFP
E
Biallelic targeting: Known outcomes as design
1A heterozygous: healthy KI/pathogenic KI
1B homozygous: healthy KI/healthy KI
1C homozygous: pathogenic KI/pathogenic KI
F
Random Integration events (e.g. single crossover)
G
Overlapping populations
2 homozygous: pathogenic KI/pathogenic KI
U heterozygous: pathogenic KI/Unknown
WT/indel

Figure 2

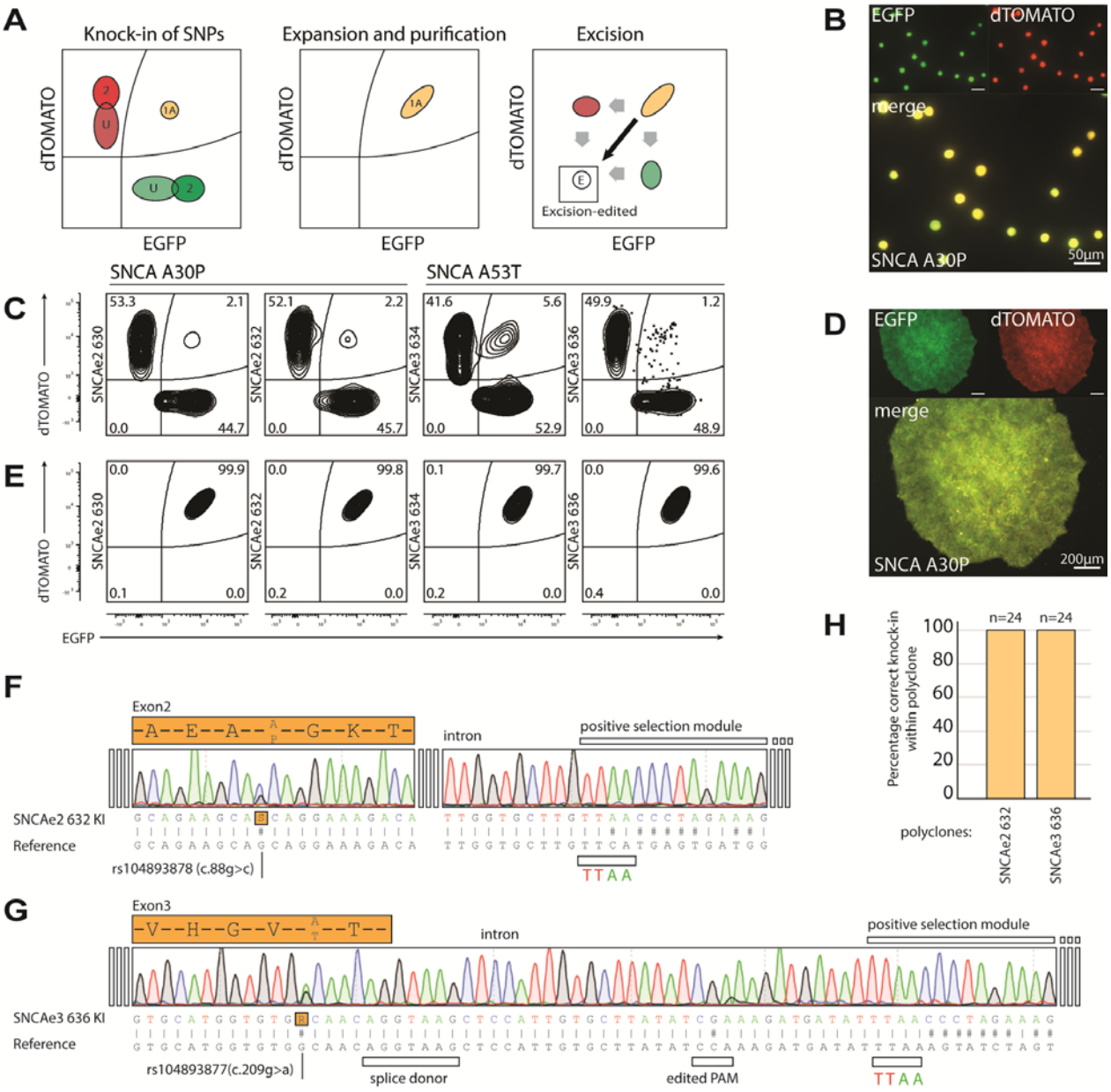
A
Knock-in of SNPs
Expansion and purification
Excision
dTOMATO
EGFP
Excision-edited
B
EGFP
dTOMATO
merge
SNCA A30P
50µm
C
SNCA A30P
SNCA A53T
SNCAe2 630
SNCAe2 632
SNCAe3 634
SNCAe3 636
53.3
2.1
44.7
52.1
2.2
45.7
41.6
5.6
52.9
49.9
1.2
48.9
D
EGFP
dTOMATO
merge
SNCA A30P
200µm
E
99.9
99.8
99.7
99.6
F
Exon2
-A--E--A--A/P--G--K--T-
intron
positive selection module
SNCAe2 632 KI
Reference
rs104893878 (c.88g>c)
TTAA
G
Exon3
-V--H--G--V--A/T--T--
intron
positive selection module
SNCAe3 636 KI
Reference
rs104893877(c.209g>a)
splice donor
edited PAM
TTAA
H
Percentage correct knock-in within polyclone
n=24
n=24
100
80
60
40
20
0
polyclones:
SNCAe2 632
SNCAe3 636

Figure 3

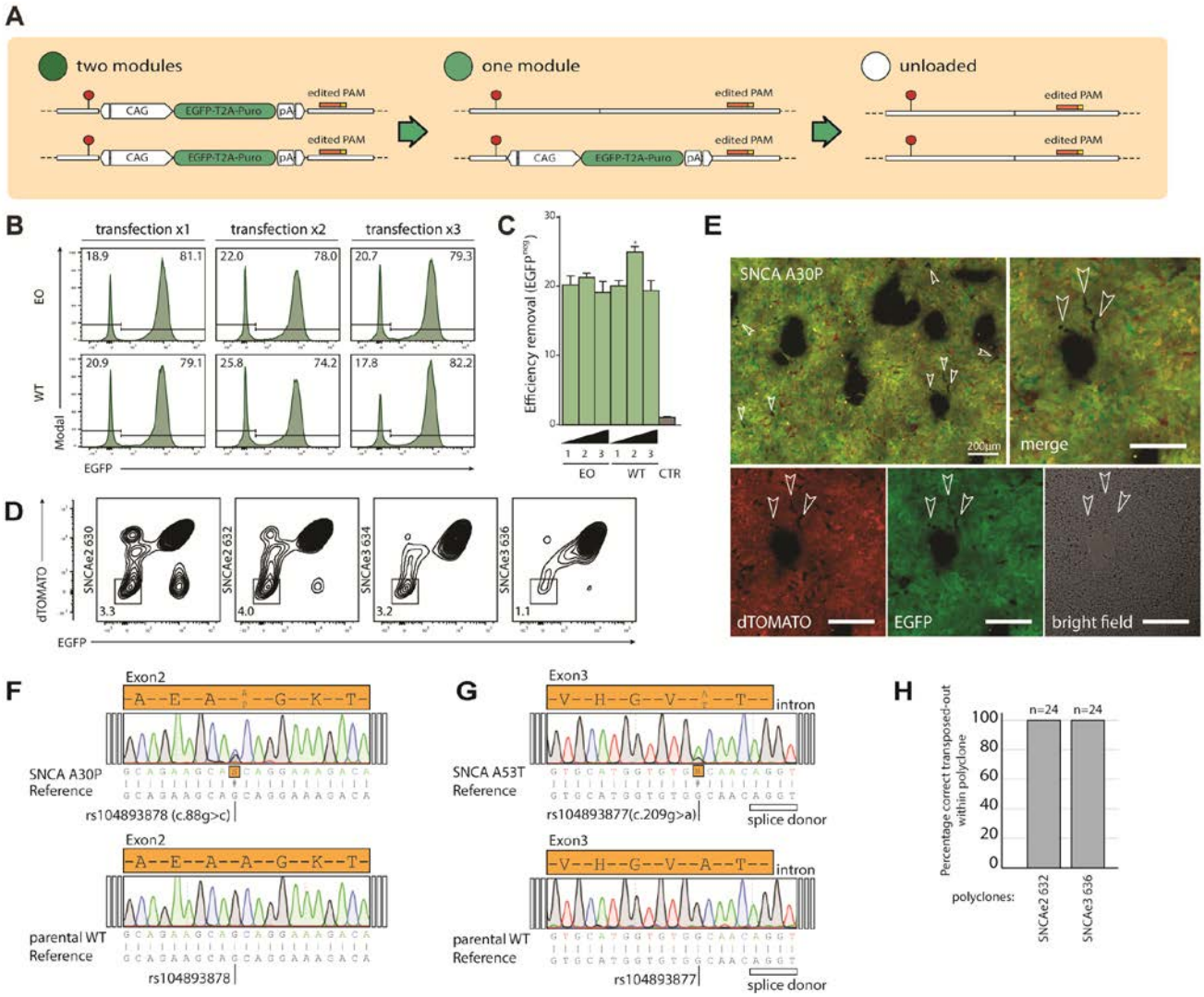
A
two modules
one module
unloaded
CAG
EGFP-T2A-Puro
pA
edited PAM
B
transfection x1
transfection x2
transfection x3
EO
WT
Modal
EGFP
C
Efficiency removal (EGFP neg)
EO
WT
CTR
D
dTOMATO
EGFP
SNCAe2 630
SNCAe2 632
SNCAe3 634
SNCAe3 636
E
SNCA A30P
merge
dTOMATO
EGFP
bright field
F
Exon2
SNCA A30P
Reference
rs104893878 (c.88g>c)
parental WT
rs104893878
G
Exon3
intron
SNCA A53T
rs104893877(c.209g>a)
splice donor
parental WT
rs104893877
H
Percentage correct transposed-out within polyclone
n=24
polyclones:
SNCAe2 632
SNCAe3 636

Figure 4

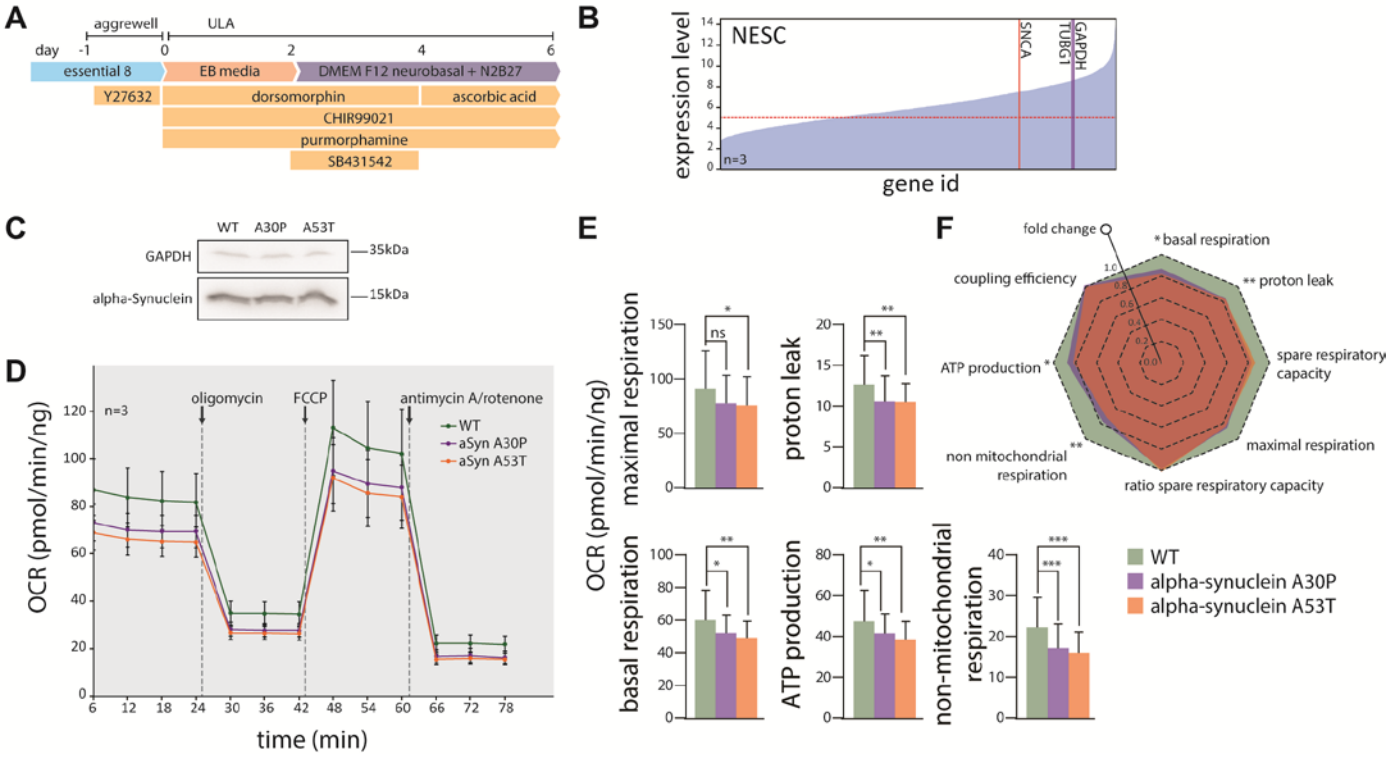
A
aggrewell
ULA
day -1 0 2 4 6
essential 8
EB media
DMEM F12 neurobasal + N2B27
Y27632
dorsomorphin
ascorbic acid
CHIR99021
purmorphamine
SB431542
B
NESC
SNCA
GAPDH
TUBGT
expression level
n=3
gene id
C
WT A30P A53T
GAPDH
alpha-Synuclein
35kDa
15kDa
D
n=3
oligomycin
FCCP
antimycin A/rotenone
WT
aSyn A30P
aSyn A53T
OCR (pmol/min/ng)
time (min)
E
OCR (pmol/min/ng)
maximal respiration
proton leak
basal respiration
ATP production
non-mitochondrial respiration
ns
F
fold change
basal respiration
proton leak
spare respiratory capacity
maximal respiration
ratio spare respiratory capacity
non mitochondrial respiration
ATP production
coupling efficiency
WT
alpha-synuclein A30P
alpha-synuclein A53T

Figure S1

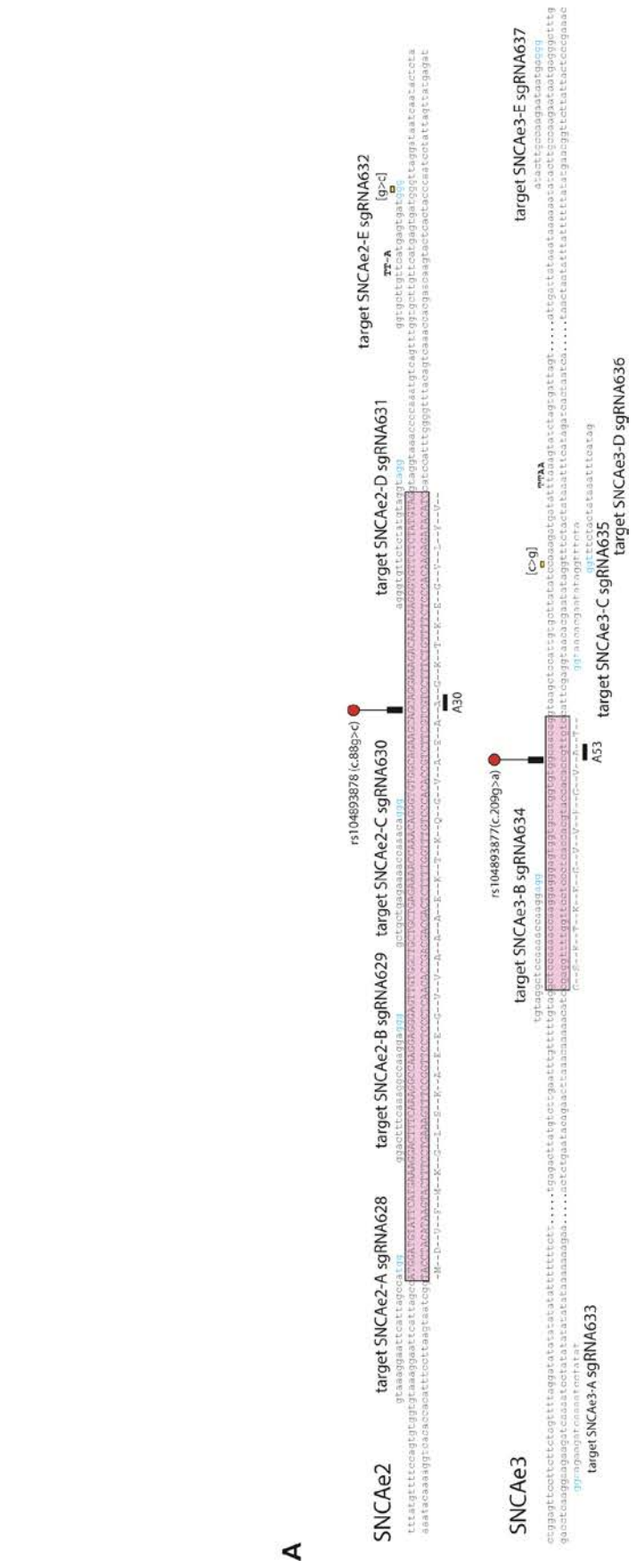
A
SNCAe2
target SNCAe2-A sgRNA628
target SNCAe2-B sgRNA629
target SNCAe2-C sgRNA630
target SNCAe2-D sgRNA631
target SNCAe2-E sgRNA632
rs104893878 (c.88g>c)
A30
SNCAe3
target SNCAe3-A sgRNA633
target SNCAe3-B sgRNA634
target SNCAe3-C sgRNA635
target SNCAe3-D sgRNA636
target SNCAe3-E sgRNA637
rs104893877(c.209g>a)
A53

Figure S2

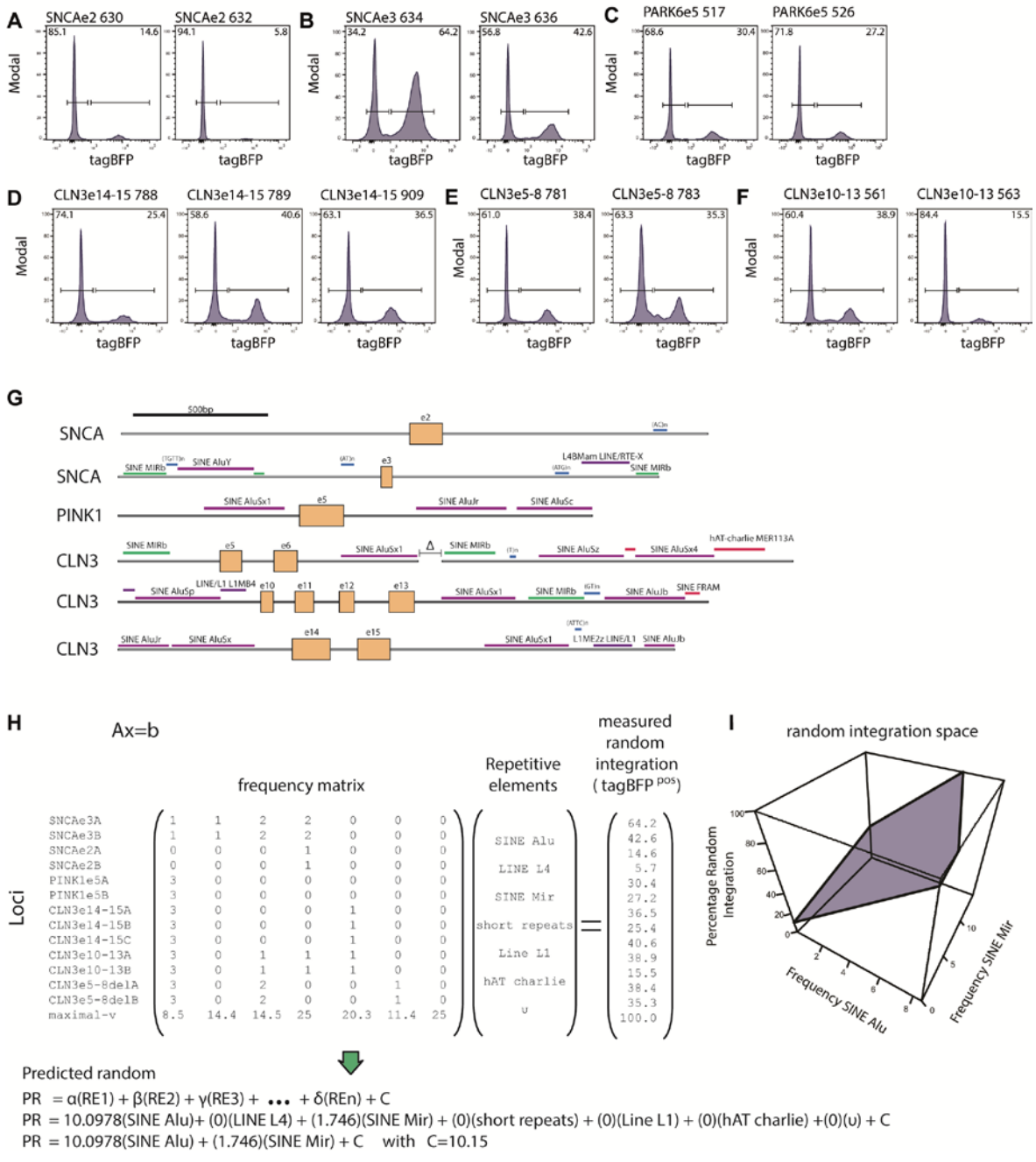

Predicted random

$PR = \alpha(RE1) + \beta(RE2) + \gamma(RE3) + \bullet\bullet\bullet + \delta(REn) + C$

$PR = 10.0978(\text{SINE Alu}) + (0)(\text{LINE L4}) + (1.746)(\text{SINE Mir}) + (0)(\text{short repeats}) + (0)(\text{Line L1}) + (0)(\text{hAT charlie}) + (0)(\upsilon) + C$

$PR = 10.0978(\text{SINE Alu}) + (1.746)(\text{SINE Mir}) + C \quad \text{with} \quad C=10.15$

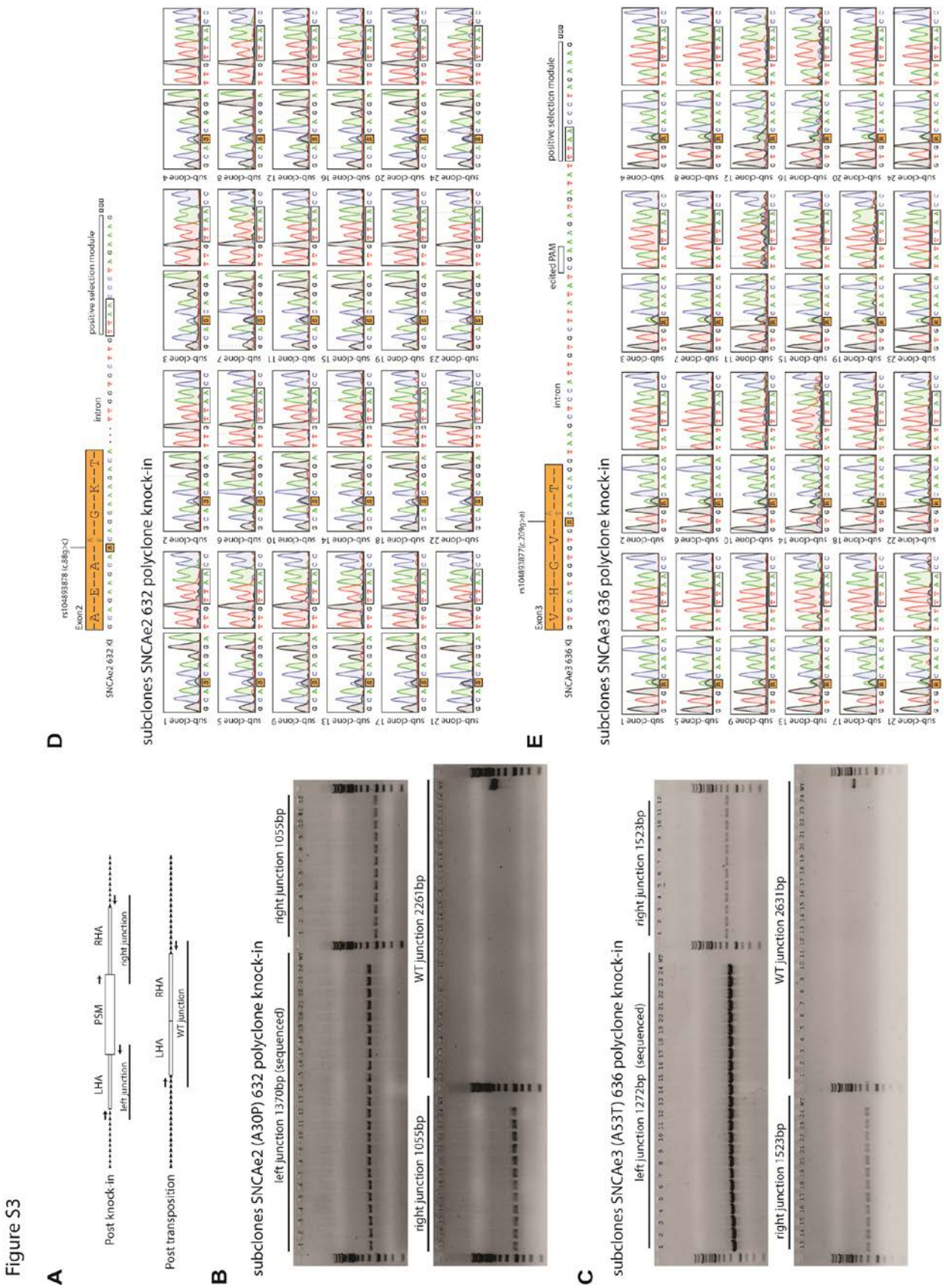
Figure S3
A
Post knock-in
LHA
PSM
RHA
left junction
right junction
Post transposition
LHA
RHA
WT junction
B
subclones SNCAe2 (A30P) 632 polyclone knock-in
left junction 1370bp (sequenced)
right junction 1055bp
right junction 1055bp
WT junction 2261bp
C
subclones SNCAe3 (A53T) 636 polyclone knock-in
left junction 1272bp (sequenced)
right junction 1523bp
right junction 1523bp
WT junction 2631bp
D
subclones SNCAe2 632 polyclone knock-in
rs104893878 (c.88g>c)
Exon2
intron
positive selection module
SNCAe2 632 KI
E
subclones SNCAe3 636 polyclone knock-in
rs104893877(c.209g>a)
Exon3
intron
ecited PAM
positive selection module
SNCAe3 636 KI

Figure S4

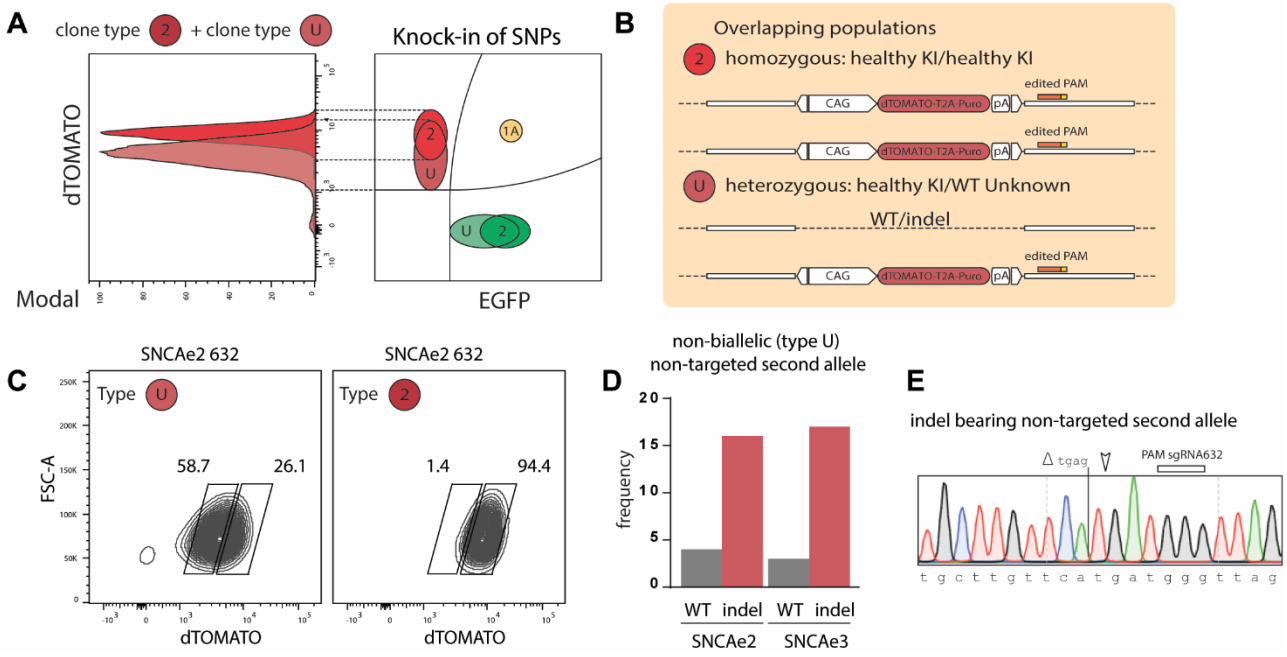
A
clone type 2 + clone type U
Knock-in of SNPs
dTOMATO
Modal
EGFP
2
U
1A
B
Overlapping populations
2 homozygous: healthy KI/healthy KI
edited PAM
CAG
dTOMATO-T2A-Puro
pA
U heterozygous: healthy KI/WT Unknown
WT/indel
C
SNCAe2 632
Type U
58.7
26.1
FSC-A
dTOMATO
SNCAe2 632
Type 2
1.4
94.4
dTOMATO
D
non-biallelic (type U)
non-targeted second allele
frequency
WT indel WT indel
SNCAe2 SNCAe3
E
indel bearing non-targeted second allele
Δ tgag
PAM sgRNA632
t g c t t g t t c a t g a t g g g t t a g

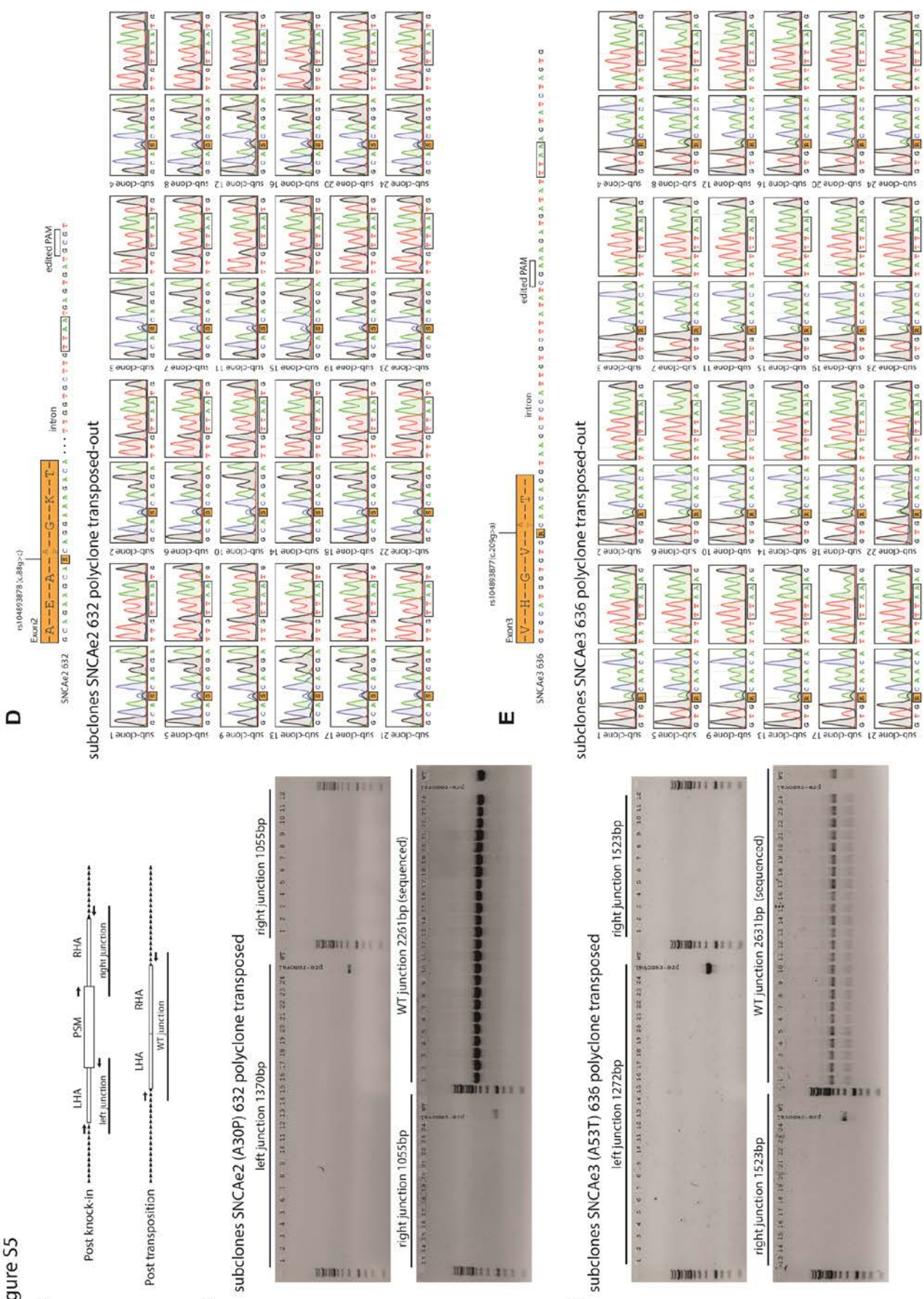
Figure S5
A
Post knock-in
LHA
PSM
RHA
left junction
right junction
Post transposition
LHA
RHA
WT junction
B
subclones SNCAe2 (A30P) 632 polyclone transposed
left junction 1370bp
right junction 1055bp
right junction 1055bp
WT junction 2261bp (sequenced)
C
subclones SNCAe3 (A53T) 636 polyclone transposed
left junction 1272bp
right junction 1523bp
right junction 1523bp
WT junction 2631bp (sequenced)
D
subclones SNCAe2 632 polyclone transposed-out
SNCAe2 632
Exon2
intron
edited PAM
E
subclones SNCAe3 636 polyclone transposed-out
SNCAe3 636
Exon3
intron
edited PAM

Figure S6

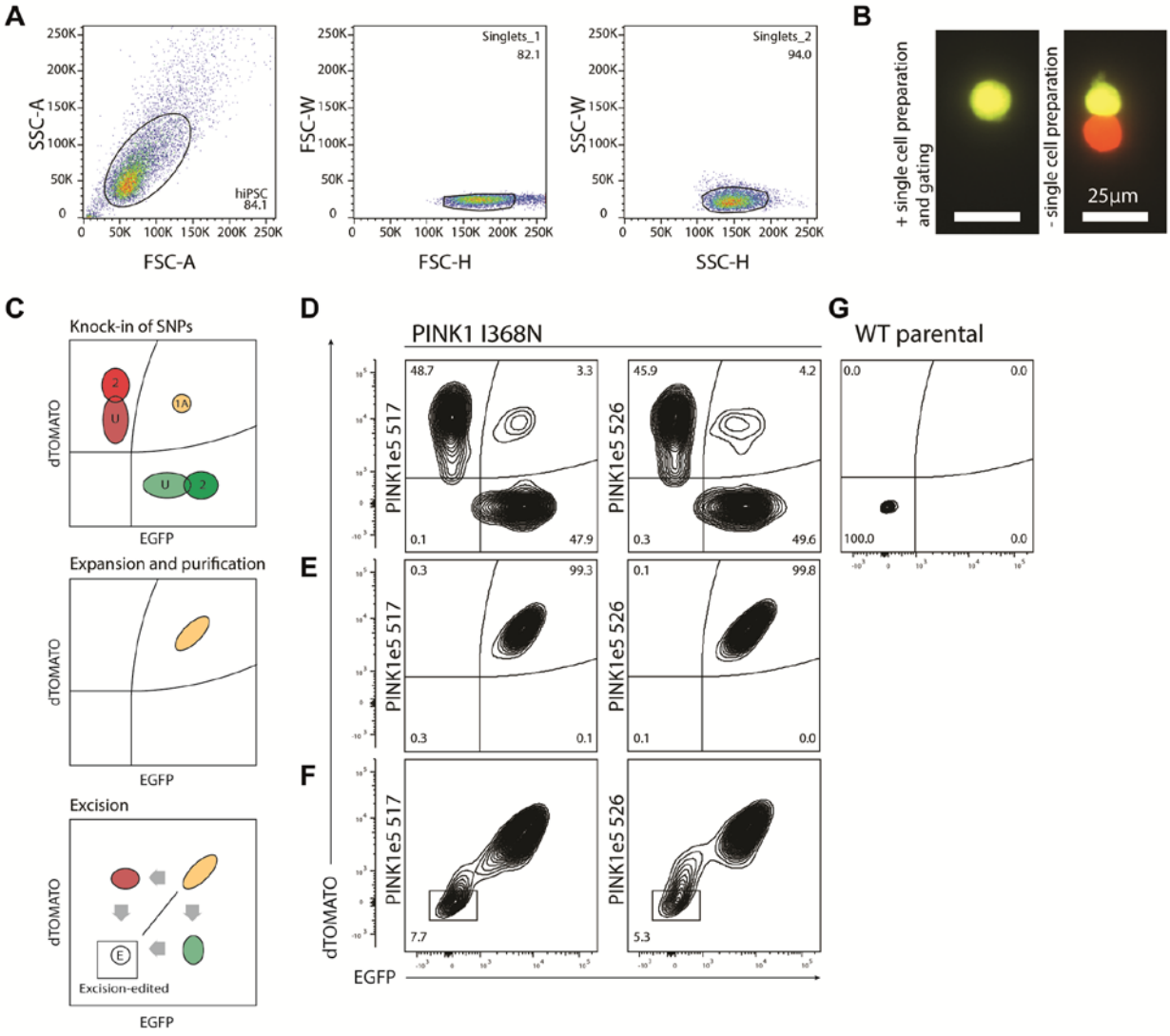
A
SSC-A
FSC-A
hiPSC
84.1
FSC-W
FSC-H
Singlets_1
82.1
SSC-W
SSC-H
Singlets_2
94.0
B
+ single cell preparation and gating
- single cell preparation
25µm
C
Knock-in of SNPs
dTOMATO
EGFP
Expansion and purification
Excision
Excision-edited
D
PINK1 I368N
PINK1e5 517
PINK1e5 526
48.7
3.3
0.1
47.9
45.9
4.2
0.3
49.6
E
0.3
99.3
0.3
0.1
0.1
99.8
0.1
0.0
F
dTOMATO
EGFP
7.7
5.3
G
WT parental
0.0
0.0
100.0
0.0

Figure S7

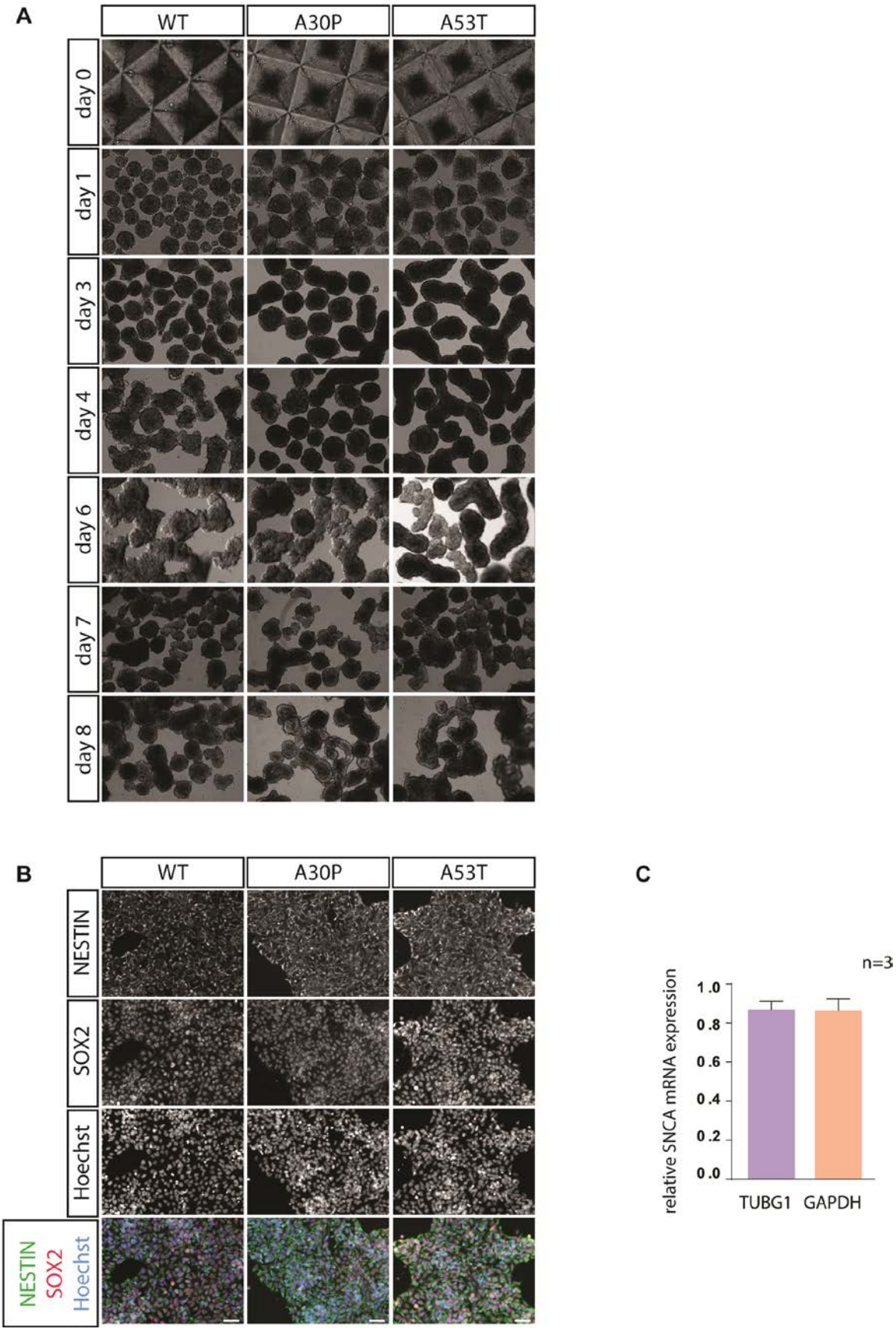
A
WT
A30P
A53T
day 0
day 1
day 3
day 4
day 6
day 7
day 8
B
WT
A30P
A53T
NESTIN
SOX2
Hoechst
NESTIN
SOX2
Hoechst
C
n=3
relative SNCA mRNA expression
1.0
0.8
0.6
0.4
0.2
0.0
TUBG1
GAPDH

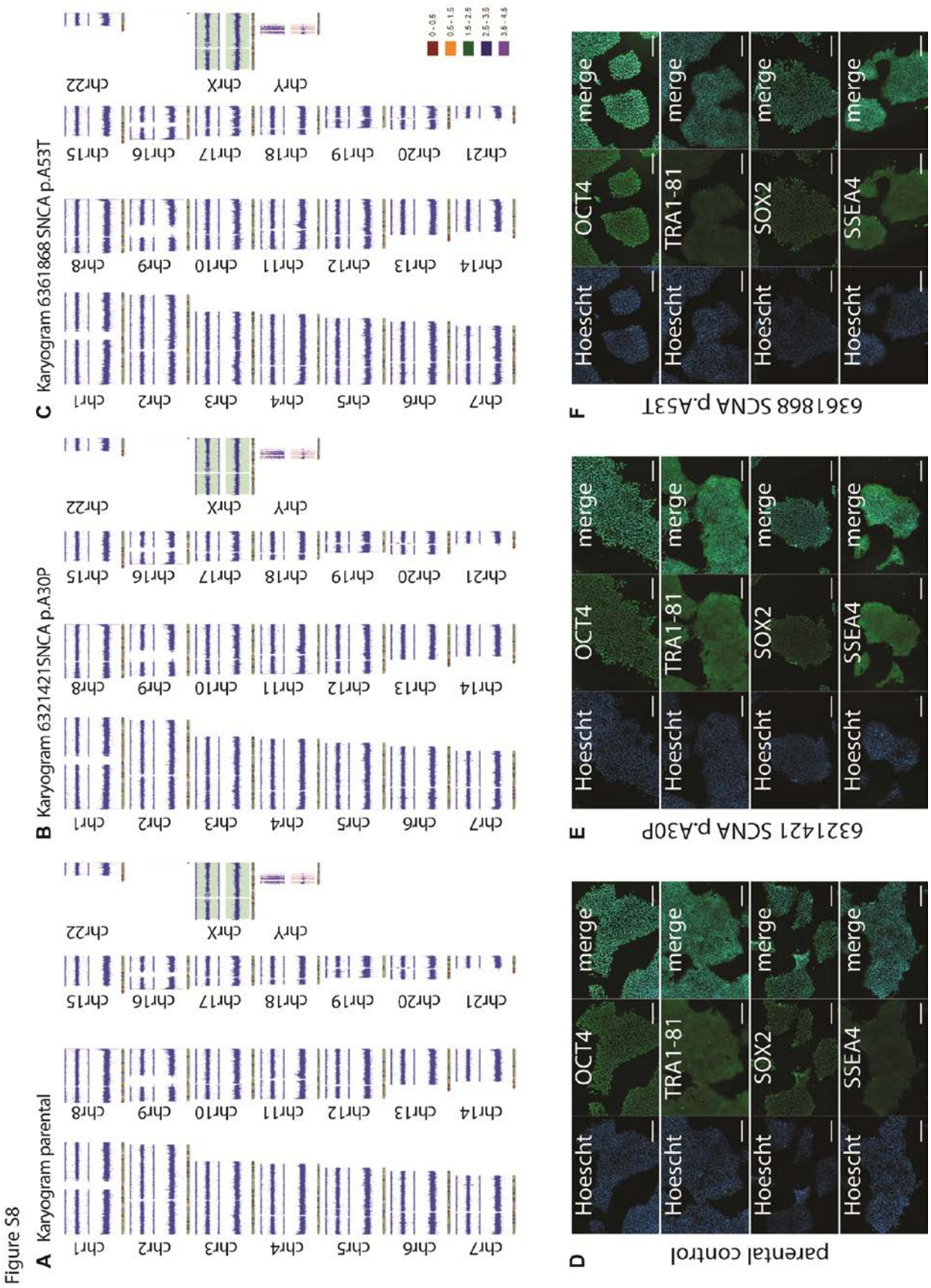
A Karyogram parental
B Karyogram 6321421SNCA p.A30P
C Karyogram 6361868 SNCA p.A53T
chr1 chr2 chr3 chr4 chr5 chr6 chr7 chr8 chr9 chr10 chr11 chr12 chr13 chr14 chr15 chr16 chr17 chr18 chr19 chr20 chr21 chrX chrY chr22
0 - 0.5 0.5 - 1.5 1.5 - 2.5 2.5 - 3.5 3.5 - 4.5
D parental control
E 6321421 SCNA p.A30P
F 6361868 SCNA p.A53T
Hoescht
OCT4
TRA1-81
SOX2
SSEA4
merge

Figure S8

Figure S9

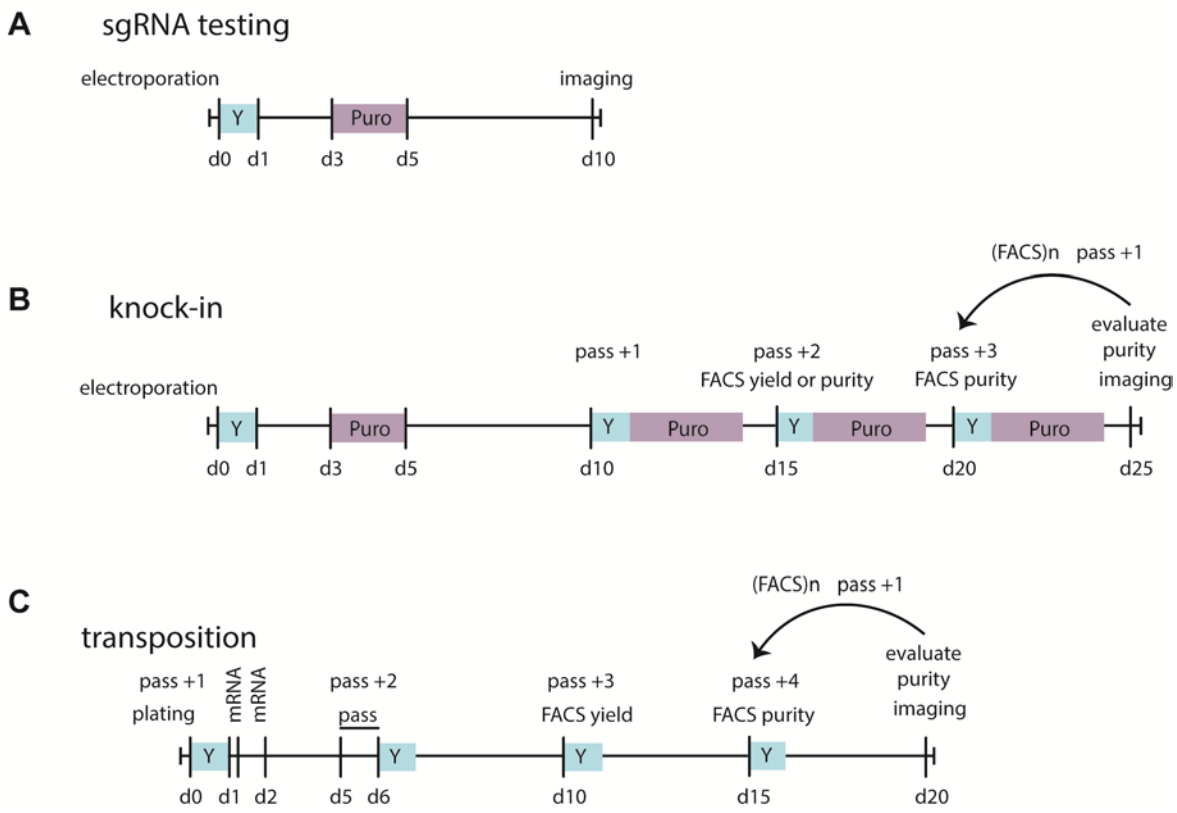
A
sgRNA testing
electroporation
imaging
Y
Puro
d0 d1 d3 d5 d10
B
knock-in
(FACS)n pass +1
evaluate
purity
imaging
pass +1
pass +2
FACS yield or purity
pass +3
FACS purity
electroporation
Y
Puro
d0 d1 d3 d5 d10 d15 d20 d25
C
transposition
(FACS)n pass +1
evaluate
purity
imaging
pass +1
plating
mRNA
mRNA
pass +2
pass
pass +3
FACS yield
pass +4
FACS purity
d0 d1 d2 d5 d6 d10 d15 d20

3.2 Manuscript II

Automated high-throughput high-content autophagy and mitophagy phenotyping in Parkinson's disease

Jonathan Arias-Fuenzalida [1,2,5], **Javier Jarazo** [1,2,5], Jonas Walter [1,2,5], Gemma Gomez-Giro [1,2,4], Julia Forster [1,3], Paul M.A. Antony [1,3,6] & Jens C. Schwamborn [1,2,6]

[1] Luxembourg Centre for Systems Biomedicine (LCSB), University of Luxembourg, Luxembourg, 7 avenue des Hauts-Fourneaux

[2] Laboratory of Developmental and Cellular Biology

[3] Laboratory of Experimental Neurobiology

[4] Max Planck Institute for Molecular Biomedicine, Laboratory of Cell and Developmental Biology, Roentgenstrasse 20, Muenster, Germany

[5] Authors equally contributed to this article

[6] Correspondence should be addressed to P.A. (paul.antony@uni.lu) and J.S. (jens.schwamborn@uni.lu).

Status: The manuscript is submitted to Cell Reports

3.2.1 Preface

In this article we stablished a system for the assessment and classification of subcellular structures in the context of autophagy and mitophagy in an automated manner. For doing so we assessed, in a high-throughput analysis, the status of the autophagy and mitophagy pathways with the combination of a Rosella construct and an algorithm for pattern recognition. The Rosella construct has the property of being a tandem of dsRed and pHluorin fluorescent proteins. This pHluorin is a modified version of GFP that makes it susceptible to low pH. When the tagged structure is within an autolysosome, the pHluorin fluorescence is quenched and only the dsRed remains. Due to this difference in fluorescence and the morphology of the tagged structure, the algorithm we developed is able to recognize the different phases in the process of protein degradation through the interaction with a lysosome. In this case, we generated hiPSCs lines from PD patients (carrying mutations in PINK1, LRRK2 or VPS35) stably expressing either the Rosella construct paired with the protein LC3 or with the protein ATP5C1 (a subunit of the mitochondrial complex 5) which point out the events in the autophagy and mitophagy pathways respectively. We observed that in patient's lines the overall autophagy capacity is reduced compared to control lines. Plus, we modulated the pathway flux by addition of compounds known to target specific stages which allow us to identify potential relevant targets for novel compounds. I contributed with the design of templates and carrying out all the automated image acquisition experiments. I contributed with the logic and writing of the algorithm for classifying that autophagy events together with Paul Antony, and helped in the implementation of the lysosomal and mitophagy pipeline analysis. I performed all the video analysis, 3D reconstructions and interpretations. I performed all the statistical analysis, and figures conceptualization and organization with the collaboration of Jonas Walter and Jonathan Arias-Fuenzalida. Together with Paul Antony, the first co-authors wrote the manuscript. I designed and perform the validation assay of the method so far required by one of the reviewers together with Paul Antony.

3.2.2 Manuscript

Research Paper

Automated high-throughput high-content autophagy and mitophagy phenotyping in Parkinson's disease

Jonathan Arias-Fuenzalida[1,2,5], Javier Jarazo[1,2,5], Jonas Walter[1,2,5], Gemma Gomez-Giro[1,2,4], Julia Forster[1,3], Paul M.A. Antony[1,3,6] & Jens C. Schwamborn[1,2,6]

1 Luxembourg Centre for Systems Biomedicine (LCSB), University of Luxembourg, Luxembourg, 7 avenue des Hauts-Fourneaux

2 Laboratory of Developmental and Cellular Biology

3 Laboratory of Experimental Neurobiology

4 Max Planck Institute for Molecular Biomedicine, Laboratory of Cell and Developmental Biology, Roentgenstrasse 20, Muenster, Germany

5 Authors equally contributed to this article

6 Correspondence should be addressed to P.A. (paul.antony@uni.lu) and J.S. (jens.schwamborn@uni.lu).

Keywords: autophagy, high-content, high-throughput, LRRK2, mitophagy, Parkinson's disease, PINK1, and VPS35

Running title: High-throughput autophagy and mitophagy phenotyping

Abstract

Autophagy and mitophagy play a central role in cellular homeostasis. In pathological conditions, autophagy and mitophagy flow can be affected at multiple and distinctive steps of the pathway. Current state of the art analysis is conducted in low-throughput manner on bulk cell populations, therefore neglecting pathway staging. Defining the autophagy and mitophagy pathway steps with single-cell analysis and in a high-throughput manner is technologically challenging, and has not been addressed so far. Here we developed a novel high-throughput phenotyping platform with automated high-content image analysis to assess autophagy and mitophagy staging. As a proof of concept we outlined the autophagy and mitophagy status in human cells carrying the Parkinson's disease associated mutations LRRK2(p.G2019S), VPS35(p.D620N), and PINK1(p.I368N). Here we validated this platform, and demonstrated that autophagy and mitophagy pathway impairments are a common axis of Parkinson's disease pathology.

Introduction

Autophagy and mitophagy play central roles in normal development and disease[1, 2]. Increasing interest and research in the field point to a need to develop pathway reconstruction tools and reliable quantification methods for autophagy and mitophagy [3, 4]. Analyses of these processes have so far been conducted with low-throughput and semi-quantitative methods such as transmission electron microscopy, transient transfections, and western blotting[5]. Current methodologies to assess autophagy and mitophagy impairments neglect the multiple structural stages of autophagy and mitophagy pathways. The development of technologies for staging autophagy and mitophagy pathway structures is necessary to dissect in which steps the pathways are impaired. Additionally, such technologies would enable to stratify and categorize pathologies that affect these essential homeostasis pathways. Neurodegenerative diseases such as Parkinson's disease (PD) are the product of polygenetic factors that converge in autophagy and mitophagy pathways[6, 7]. The establishment of autophagy and mitophagy categories for polygenetic diseases such as PD could be informative for fundamental research and translational medicine. Furthermore, defining which steps of the pathway are affected can lead to the establishment of new pharmaceutical candidates[8]. The advent of genome editing tools has accelerated the development of genetically encoded reporters in human induced pluripotent stem (iPS) cells[9, 10]. Additionally, the development of pH responsive fluorescent proteins allows evaluating intracellular pH and interrogating specific subcellular compartments[11, 12]. The combined use of genome editing tools and genetically encoded pH sensors now enables the establishment of autophagy and mitophagy stable reporter lines in general, and defining the pathological signatures of PD in particular. Automated high-throughput high-content imaging and analysis approaches have multiple advantages over conventional methods. They allow applying uniformly classification algorithms to specimens in an unbiased manner, and provides high statistical power. Importantly, they enable defining conclusion that would otherwise be missed in population-based analysis. Here we developed and validated automated tools to assess autophagy and mitophagy staging. Furthermore, we use engineered reporter lines and automated approaches to dissect autophagy and mitophagy pathways in the context of PD.

Results

Reconstruction of the complete autophagy and mitophagy pathway

Making use of genetically encoded pH sensors and genome editing tools, we have engineered a set of healthy and patient iPS lines to monitor autophagy and mitophagy. The autophagy sensor Rosella-LC3 allows the identification of pre-autophagosomal structures such as phagophores, and transient structures such as isolation membranes and autophagosomes (Fig. 1A, C and E). Following autophagosome fusion with lysosomes, the internal membrane bound LC3 is degraded, giving rise to early and then late autolysosomes (Fig. 1A, C and E) that converge to lysosomes and re-enter the autophagy cycle [13, 14]. The mitochondrial sensor ATP5C1-Rosella allows the quantification of the rate of mitophagy events (Fig. 1B, D, F) as accounted by acidic $DsRED^{pos}pHluorin^{neg}$ vesicles derived from degraded mitochondria. Using pattern recognition algorithms, we developed a decision tree workflow to automatically identify and categorize the subcellular structures observed during autophagy and mitophagy *in vitro* (Fig. 1A-F, Fig. S2 and Fig. S4). This 3D strategy enables absolute quantification of singular autophagy and mitophagy events in monolayer cultures. In order to validate this approach with traditional immunostaining, we performed high-content quantification of LC3-positive structures. The resolution of conventional LC3-antibody staining lacks the ability to resolve the stage-specific structures in the autophagy pathway. Structures with similar morphologies could not be categorized based on their acidic content, unlike classification using reporter lines. Hence, the LC3 antibody quantification permits only total vesicle count (Fig. S1).

Human iPS show active and dynamic autophagy and mitophagy

We observed a remarkable activity of the autophagy pathway in healthy-control human iPS cells (Video S1-4). Indeed, autophagy has previously been associated with the maintenance of pluripotency and resistance to senescence in stem cells and proved essential for pre-implantation development[15]. Furthermore, we observed mitochondrial network monitoring and abundant mitophagy events (Video S6) in healthy human stem cells (Video S5-7). This is in agreement with reported mechanisms[16, 17] in this cell type[18, 19].

PD mutants present reduced autophagic resources and altered autophagy reaction rate constant

In order to stratify autophagy and mitophagy in PD, we evaluated the differences between healthy human iPS cells and the PD-related mutants LRRK2(p.G2019S), PINK1(p.I368N), and VPS35(p.D620N). LRRK2 is

associated with the endosomal pathway [20] and the transition between the early and late endosome, converging in the lysosomal pathways [21]. VPS35 is required for retromer complex formation, recycling of transmembrane proteins to the ER[22], and modulation of autophagy[23]. PINK1 is needed for monitoring mitochondrial homeostasis and induction of mitophagy. Mutations in PINK1 result in autophagy impairments [24]. The panel of mutations described was assessed for autophagy and mitophagy alterations. We observed that the absolute frequency of phagophores was reduced in PINK1(p.I368N) and VPS35(p.D620N) with respect to the healthy-control line (Fig. 2A). Autophagosome is a transient states with low frequency. We observed reduced level of autophagosomes in LRRK2(p.G2019S) mutant (Fig. 2B). For LRRK2(p.G2019S) early autolysosome levels were similar to healthy-control, while late autolysosomes were significantly reduced (Fig. 2D). Early and late autolysosomes were reduced in PINK1(p.I368N) and VPS35(p.D620N) (Fig. 2C-D). Autophagic-vacuoles comprise all autophagosomes and autolysosomes in a cell [5]. Autophagic vacuoles were reduced in all the mutant lines (Fig. 2E). This indicates that the LRRK2(p.G2019S), PINK1(p.I368N), and VPS35(p.D620N) mutations result in an overall decreased autophagy capacity and progression in basal conditions. The ratio between phagophores and autophagic-vacuoles accounts for the autophagy-rate-constant intrinsic to each mutant. Approximations of this have been previously conducted by western blotting of stage specific protein forms[5]. The autophagy rate for healthy-control and PINK1(p.I368N) cells was close to 0.4 s^{-1} in basal conditions (Fig. 2E). VPS35(p.D620N) and LRRK2(p.G2019S) present higher proportions of phagophores and a decreased ability to progress through autophagy in basal conditions (Fig. 2E).

PD mutants present increase sensitivity and reduced responsiveness to a panel of autophagy and mitophagy modulators

In order to evaluate how responsive each mutant line was to autophagic and mitophagic stress, small molecule perturbations were applied. Upon addition of the proton-ATPase inhibitor bafilomycin, acidification of lysosomes was impaired. In agreement with the expected blockage of trafficking[5], we observed an increased level of phagophores for all mutants (Fig. 3A and Fig. S5), and decreased abundance of autophagic-vacuoles in healthy-control and LRRK2(p.G2019S) cells (Fig. 3B and Fig. S5). Likewise, chloroquine addition increased phagophore abundance in PINK1(p.I368N) and VPS35(p.D620N) cells (Fig. 3A and Fig. S5), but decreased autophagic-vacuoles in healthy-control and LRRK2(p.G2019S) cells (Fig. 3B and Fig. S5). To obtain an independent experimental validation of our method we performed LC3

immunostaining analysis on untreated and chloroquine-induced conditions. Similarly, to the observations of chloroquine induction on the reporter lines, the immunostaining shows the same overall autophagy signature (Fig. S1).

Thapsigargin increases the intracellular concentration of Ca^{+2} and induces the activation of Calcium-Calmodulin-dependent-protein-kinase beta (CaMK-beta)[25] which, through 5'AMP-activated-protein-kinase (AMPK), inhibits mechanistic-target-of-rapamycin (mTOR) and promotes autophagy[26]. Here, thapsigargin was used to quantify the CaMK-beta/AMPK dependent autophagy and mitophagy inputs (Fig. 1A). Thapsigargin increased phagophore levels in VPS35(p.D620N) and PINK1(p.I368N) cells (Fig. 3A and Fig. S5). Furthermore, in VPS35(p.D620N) and PINK1(p.I368N) cells, the CaMK-beta/AMPK input resulted not only in increased phagophore levels but also in increased abundance of autophagic-vacuoles (Fig. 3B and Fig. S5). This highlights a latent demand for phagophores.

It is known that mTOR complex 1 inhibits autophagy by its interaction with ULK1, resulting in the reduced formation of the phagophore complex[26]. Rapamycin, an inhibitor of mTOR, allows quantitation of the direct extent of autophagy controlled by this pathway. Upon addition of rapamycin, we observed increased phagophore levels in VPS35(p.D620N) and PINK1(p.I368N) cells, suggesting that modulation of mTOR could increase the phagophore generation in these mutants (Fig. 3A and Fig. S5). Remarkably, treatment of PINK1(p.I368N) cells with rapamycin restored phagophore levels to healthy-control basal levels (Fig. 3A and Fig. S5). We also observed an increase of phagophore levels for healthy-control cells (Fig. 3A and Fig. S5), confirming conserved mechanisms of mTOR mediated autophagy[26]. We speculated that combined activation of CaMK-beta and repression of mTOR could have synergistic effects, however, with the combined addition of thapsigargin and rapamycin we did not observe further increase in phagophore formation (Fig. 3A and Fig. S5). That is most likely due to the ubiquitous effects of the mTOR pathway[26].

In order to evaluate the contribution of mitophagy to general autophagy, we used a panel of established mitophagy inducers[12]. Oligomycin, valinomycin, and CCCP are modulators of the mitochondrial membrane potential that induce mitochondrial stress and mitophagy. Upon addition of these modulators, we observed increased levels of phagophores and autophagic-vacuoles in VPS35(p.I368N) cells (Fig. 3A-B and Fig. S5). For PINK1(p.I368N) cells, we observed increased levels of phagophores and autophagic-vacuoles, both for PINK1-dependent and PINK1-independent mitochondrial stressors (Fig. 3A-B and Fig. S5). This could be

explained by PINK1-independent mitophagy mechanisms. In LRRK2(p.G2019S) cells, distinct modulators of autophagy consistently decreased the levels of autophagic structures (Fig. 3A-B and Fig. S5).

Next, we performed clustering analysis of all lines and treatments, taking into account the levels of phagophores and autophagic-vacuoles. Heatmap clustering analysis showed two distinct branches, a healthy-control branch and a mutant branch (Fig. 3C). The healthy-control branch includes all its perturbation conditions. The mutant branch include basal conditions of VPS35(p.D620N) and PINK1(p.I368N) (Fig. 3C). Remarkably, mTOR modulation among others rescue the autophagy profile for PINK1(p.I368N) to the healthy-control branch (Fig. 3C). This indicates the existence of characteristic autophagic staging fingerprint alterations in the studied PD mutants.

PD mutants present impaired lysosomal levels and volume

To determine the acidification capacity of autophagic-vacuoles, we combined the autophagy and mitophagy reporters with lysosomal dyes (Fig. 4A), and developed lysosome recognition algorithm (Fig. 4A and Fig. S5). Relative to the healthy- control cells, the lysosome frequency in PINK1(p.I368N) cells was elevated (Fig. 4B). In contrast, VPS35(p.D620N) cells presented decreased lysosome levels (Fig. 4B). LRRK2(p.G2019S) cells showed similar lysosome frequencies to the healthy-control (Fig. 4B). The analysis of lysosomal diameters revealed reduced lysosomal size for all mutants compared to the healthy-control cells (Fig. 4C). Furthermore, the size of autophagic-vacuoles in VPS35(p.I368N) cells was larger than in healthy-control cells (Fig. 4D). This could result in an overall decreased acidification capacity of autolysosomes for VPS35(p.I368N) mutant.

PD mutants present altered mitochondria network volume and mitophagic vesicles volume

Next, we quantified the mitochondria network and mitophagic-vacuoles volume with the aid of pattern recognition algorithms (Fig.5A and Fig. S3). PINK1(p.I368N) mutant cells displayed elongated mitochondria as compared to healthy-control cells (Fig. 5B), in agreement with reports on PINK1 inactivation mutations[27]. In LRRK2(p.G2019S) cells, the mitochondrial volume was decreased (Fig. 5B), in agreement with reports on fragmented mitochondria in this mutant[28]. Accordingly, the autolysosomes that processed mitophagy of mutants followed the same pattern. PINK1(p.I368N) mitophagic vacuoles were larger, and LRRK2(p.G2019S) were smaller (Fig. 5C).

PD mutants present higher mitophagy levels and altered balance between non-mitochondrial autophagy and mitophagy

Next, we dissected the balance between mitophagy and general autophagy. The Rosella-LC3 sensor quantified the combined effect of non-mitochondrial autophagy and mitophagy. To model non-mitochondrial autophagy and to infer how phagocytic resources are distributed upon perturbations, we subtracted the ATP5C1-Rosella data from the Rosella-LC3 data. We observed a significantly increased levels of mitophagic vacuoles for all the mutants in basal conditions (Fig. 6A). Upon addition of mitophagy modulator CCCP, we observed high mitophagy levels in mutants as compared to stressed healthy-control (Fig. 6A). Furthermore, mitophagy levels of CCCP stressed healthy-control are similar or significantly lower than basal condition mutants (Fig. 6A). Then, we assessed the proportion of general autophagy and mitophagy resources in basal and stressed conditions. For LRRK2(p.G2019S) cells, perturbations caused no increased mitophagy, suggesting that mitophagy is already at its maximal capacity (Fig. 6B). Upon stress induction in healthy-control cells, the frequency of autophagic-vacuoles was reduced to 70% and mitophagy increased to 170% (Fig. 6B). In VPS35(p.D620N) cells, the frequency of general autophagy increased to 380%, and the frequency of mitophagy indicates that general autophagy was primarily dedicated to degrading mitochondria (Fig. 6B). Similarly, for PINK1(p.I368N) cells, the mitophagy level increased to 180% and the absolute frequency of general autophagy increased to 140% (Fig. 6B).

Discussion

The autophagy field faces the challenge of identifying the different stages of autophagy and mitophagy in a high-throughput manner[5]. The steps and sub-cellular structures of autophagy and mitophagy are important for the proper interpretation of phenotypic traits. This compartmentalization cannot be accounted when using bulk population analysis such as western blotting. Here, we demonstrate a platform that accounts for vesicular compartmentalization using unbiased automated analysis in combination with automated high-content imaging, providing high statistical power, and assay sensitivity. In the present work, we developed a high-throughput and high-content phenotyping platform for autophagy and mitophagy. Together, our autophagy staging and mitophagy analyses highlight that the mutations LRRK2(p.G2019S), VPS35(p.D620N) and PINK1(p.I368N) not only share autophagy and mitophagy homeostasis impairments as a common trait characteristic of PD but also reveal mutant-specific phenotypic fingerprints. The platform presented was evaluated with an assortment of compounds to test the modulation of autophagy and mitophagy. The patterns observed are in agreement with the expected results of each modulator's mechanism of action. We observed that lysosome fusion blockers bafilomycin and chloroquine increased the proportion of autophagosomes and reduced the proportion of autolysosomes as previously reported[5]. First, we validated our workflow by comparing it to immunostaining analysis of total LC3-positive structures. As mentioned above, the count of LC3-positive structures is lower than the total vesicle count quantified by the reporter. This can be explained by the degradation of LC3 epitope after the acidification of vesicles. On the other hand, in the reporter lines the RFP signal remains visible enabling the quantification of late autophagy pathway structures. We show that the vesicles quantified by immunostaining correspond mainly to pre-acidification structures, principally phagophores (Fig. S1). Comparing the LC3-positive structures from immunostaining and phagophores from autophagy reporter lines validates that both systems present the same autophagy signature upon chloroquine induction (Fig. S1).

Our measurements were conducted on monolayer cultures with optimal seeding and treatment windows that maximized the survival and modulation without evident toxicity induction. In this framework, the mild starvation modulator EBSS did not induce significant alteration of autophagy structure proportion. This demonstrates that the lines are not primed to alterations and that the effects observed with the chemical modulators correspond to bona fide pathway responses. The phagophore upstream pathways modulators

rapamycin and thapsigargin increased the frequency of phagophores in PINK1 and VPS35 mutants. The induced phagophore and autophagic vacuole levels were significantly lower than induced healthy control. This indicates that the CAMKβ-mTOR pathway are still responsive on these mutants. Importantly, our results show that mTOR inhibition can rescue phagophore levels in PINK1(p.I368N) mutant to healthy-control levels. Our approach offers a population-based analysis to determine the probabilistic-flux level from basal conditions to treatment conditions by accounting for the different subcellular structures of the pathway. In order to complement our observations, we combined the use of the reporter lines with lysosome dyes. Our results demonstrated reduced lysosome diameter for all the mutants. Furthermore, VPS35 mutant presented decreased lysosome frequency and increased autophagic vacuole cargo volumes. These observations show a decreased acidification capacity for VPS35 mutant in agreement with previous reports that show retromer function is essential for lysosomal homeostasis in *Drosophila*[29]. Furthermore, the absolute frequency of autophagic structures was decreased in VPS35(D620N) (Fig. 2A) in contrast to healthy control and similarly to previous reports[23]. Previous reports on PINK1 knock down[24, 30] show the existence of PINK1-PARKIN independent mitophagy pathways[31-33], our results demonstrate active mitophagy in PINK1(I368N) mutant supporting these findings. We observed decreased mitochondria volume and mitophagy vacuoles diameter in LRRK2 mutant as previously described[28, 34, 35]. Others attribute mitochondrial loss to increased mitophagy[34], here we observed this same phenomenon (Fig. 5) supporting previous assumptions, despite the fact of decreased general autophagy[36] (Fig. 2 and Fig. 5). It is worth highlighting that autophagy levels are greatly cell-type dependent and conclusions should be carefully extrapolated from one cell type to another. In addition, observations on general autophagy should not be directly correlated to mitophagy levels. Although the phenotypes described are in agreement with the current literature, it should be noted that in our analysis a discrete number of lines was used, including one line per mutant gene and one healthy control line. This prohibit disregarding the inherent patient to patient variation, and its influence on the observed patterns. While we focused our attention on the development of an autophagy staging platform for PD, it should be noted that the methodology can also be leveraged for autophagy research on other pathologies. Due to the substantial level of automation, this platform can be used for genetic and chemical screening and thereby accelerate current endeavors in precision medicine.

Titles and legends to figures

Figure 1. Genetically encoded Rosella-LC3 and ATP5C1-Rosella system allows monitoring of the complete autophagy and mitophagy pathway. **(A)** Structure of the Rosella autophagy reporter system. It is possible to identify phagophores, autophagosomes, and autolysosomes. Small molecule modulators of autophagy can interrogate the autophagy responsiveness and differences between lines. **(B)** Structure of the Rosella mitophagy reporter system. It is possible to determine mitochondrial network structure and mitophagy events. Small molecule mitochondria stressors can test the mitophagy capacity between lines. **(C)** Representative field for Rosella-LC3 healthy-control line. The pHluorin and DsRED channels are shown separately. Scale bar, 10µm. **(D)** Representative field for ATP5C1-Rosella healthy-control line. The pHluorin and DsRED channels are shown separately. Scale bar, 10 µm. **(E)** 3D reconstruction based on the Rosella-LC3 healthy-control line. The insets show $DsRED^{pos}pHluorin^{pos}$ autophagosome structures, $DsRED^{pos}pHluorin^{neg}$ autolysosome structures, and $DsRED^{pos}pHluorin^{pos}$ phagophores. Scale bar 10µm. **(F)** 3D reconstruction based on the ATP5C1-Rosella healthy-control line. An autolysosome structure with an ongoing mitophagy event is shown. The autolysosome appears with an equatorial cross-section and the light DsRED volume is represented in cyan. The residual mitochondria inside the autolysosome are $pHluorin^{neg}$, maintaining the pH-resistant DsRED signal. A phagophore $DsRED^{pos}pHluorin^{pos}$ cluster is located in the upper left-hand corner. In the inset, a single plane overlay is shown. The event was observed upon addition of 5µM valinomycin. Scale bar, 4µm.

Figure 2. Quantification of autophagy structures frequency. Absolute quantification of **(A)** Phagophores, **(B)** autophagosomes, **(C)** early autolysosomes, **(D)** late autolysosomes, and **(E)** autophagic-vacuoles for healthy-control and mutant lines. Kruskal-Wallis and Dunn's multiple comparison tests for all the lines with respect to its reference (ref) and healthy-control counterpart. All structures were measured in basal conditions. **(F)** Autophagy reaction rate constant for healthy-control and mutant lines. Data represent three independent replicates. Significance levels are *p<0.05, ** p<0.01, *** p<0.001, and **** p<0.0001.

Figure 3. Evaluation of responsiveness to autophagy modulation. **(A)** Fold change radar plots comparing healthy-control and mutant lines for phagophores upon stress induction with general autophagy or mitophagy modulators. **(B)** Fold change radar plots comparing healthy-control and mutant lines for autophagic-vacuoles upon stress induction with general autophagy or mitophagy modulators. **(C)** Heatmap clustering for healthy-

control and mutant lines across all mitophagy and autophagy modulating treatments. Scale in absolute event frequency. Data represent three independent replicates.

Figure 4. Evaluation of lysosome properties. **(A)** Representative lysotracker staining for healthy-control and mutant lines. Lysosome mask on red perimeter. Scale bars indicate 20µm. **(B)** Lysosome frequency for each line in basal conditions. One way ANOVA and Dunnett's multiple comparison tests were performed for all the lines with respect to the healthy-control reference (ref). **(C)** Lysosome diameter for healthy-control and mutants. Percentiles 10 to 90 are represented in the boxplot range. Non-parametric Kruskal-Wallis test ($p<0.0001$) and Dunn's multiple comparison test were performed for all the lines with respect to the healthy-control reference (ref). **(D)** Autophagic-vacuole diameter for healthy-control and mutants. Non-parametric Kruskal-Wallis and Dunn's multiple comparison tests were performed for all the lines with respect to the basal healthy-control reference (ref). Data represent three independent replicates. Significance levels are *$p<0.05$, ** $p<0.01$, *** $p<0.001$, and **** $p<0.0001$.

Figure 5. Evaluation of mitochondria network and mitophagic-vacuoles. **(A)** Representative images of ATP5C1-Rosella reporter lines for healthy-control and mutants. Mitochondria network mask on green perimeter and mitophagic-vacuole mask on red perimeter. Scale bars indicate 20µm. **(B)** Mitochondrial volumes for each line in basal conditions. Kruskal-Wallis and Dunn's multiple comparison tests were performed for all the lines with respect to the healthy-control reference (ref). **(C)** Mitophagy volumes for each line in basal conditions. Kruskal-Wallis and Dunn's multiple comparison tests were performed for all the lines with respect to healthy-control reference (ref). Data represent three independent replicates. Significance levels are *$p<0.05$, ** $p<0.01$, *** $p<0.001$, and **** $p<0.0001$.

Figure 6. Evaluation of mitophagy levels and distribution of autophagy resources upon mitochondrial stress. **(A)** Mitophagy frequencies for all lines in basal condition and after mitochondrial stress induction. Kruskal-Wallis and Dunn's multiple comparison tests were performed for all the lines with respect to the basal healthy-control reference (b-ref) and stressed healthy-control reference (s-ref). **(B)** Mitophagy and non-mitochondrial autophagy fractions for each line before and after mitochondria stress induction. Percentages for mitophagy and non-mitochondrial autophagy are indicated. Data represent three independent replicates. Significance levels are *$p<0.05$, ** $p<0.01$, *** $p<0.001$, and **** $p<0.0001$.

Materials and Methods

Human iPS cell culture and electroporation

Human iPS cell line A13777 (Gibco) derived with non-integrative methods was used. Patient lines used are PARK6(PINK1 p.I368N) Coriell ID 40066, LRRK2 (LRRK2 p.G2019S) Coriell ID ND33879, and VPS35 (VPS35 p.D620N) kindly provided by Christine Klein. Cells were maintained in Essential-8 media (Thermo Fisher cat no. A1517001) in feeder free culture condition on laminin 521 (BioLamina) or Matrigel (BD). Cell passage and dissociation were performed with accutase (Thermo Fisher cat no. A11105-01). Cells were electroporated with a Lonza 4D nucleofector system (Lonza V4XP-3024) according to the manufacturer's instructions. After passage or electroporation, cells were cultured with 10μM Y27632 ROCK inhibitor (Sigma cat no. Y0503) for 24h.

Autophagy and mitophagy reporter system.

The pH sensor fluorescent protein pHluorin (F64L, S65T, V193G and H231Q) was fused to DsRED and the mitochondrial or autophagosomal targeting sequence ATP5C1 or LC3II as previously described[12]. The coding sequence was introduced into the AAVS1 safe harbor locus as previously described[10, 37] using the targeting donor (Addgene plasmid # 22075) and TALE nucleases (Addgene plasmid #35432 and #35431).

Pathway contribution dissection

Reporter lines were treated with an assortment of compounds to dissect the stages of mitophagy and autophagy impaired in the patient lines. In order to achieve a homogeneous monolayer of cells in each well, the optimal post-seeding time and cell density were determined for the lines used. The optimal density was identified as 600k/cm2 and the optimal post-seeding time as 8 hours. On 8 hours post-seeded cells, the minimal time required for assessing autophagy and mitophagy modulation were determined between 0.5 to 3h of treatment. The optimal imaging time of all compound was identified as 3h after treatment, and was used for all experiments. Concentration gradients were tested to identify the minimal doses required to observe autophagy and mitophagy modulation without excessive cell toxicity after 3h of treatment, on 8 hours post-seeded cells. Selected concentrations and range evaluated were 8μM (8μM-31.5nM) bafilomycin A1 (Enzo); 8μM (8μM-31.5nM) CCCP (Sigma cat no. C2759); 300μM (300μM-75μM) chloroquine (Sigma cat no. C6628); 160μM (160μM-675nM) DFP (Sigma cat no. D0879); 20μM (20μM-675nM) Oligomycin A (Sigma cat no. 75351); 160μM (160μM-675nM) valinomycin (Sigma cat no. V3639); 40μM (40μM-156nM) thapsigargin (Sigma cat no. T9033); and 160μM (160μM-675nM) Rapamycin (Sigma cat no. R8781). Minimal laser-

exposure time was optimized for the samples in basal conditions. Basal levels of autophagy and mitophagy were established for all the lines.

Lysosome quantification and nuclear contrast

Cells under basal conditions were treated with deep red lysotracker (Thermo cat no. L12492) at a dilution of 1:1000 for 30 minutes. For nuclear staining, cells were treated with 20µM Hoechst 33342 for 10 minutes.

Immunostaining

Cells were fixed on 4% PFA in PBS and permeabilized with PBS triton-X 0.2%. Total human LC3 monoclonal antibody (MBL cat no. M152-3) was incubated at dilution 1:500 overnight. Secondary antibody was goat anti-rabbit alexa fluor 647 (Thermo cat no. A32733) and used at dilution 1:1000.

Time-lapse live cell imaging and three-dimensional pathway reconstruction

Culture dynamics and time-lapse imaging was evaluated in a spinning disk CSU-X1 system (Yokogawa) under controlled atmosphere conditions. Time-lapse imaging was performed for a single confocal plane. For three-dimensional pathway reconstruction, a single time point was evaluated. Reconstruction of 3D structures was performed with an Imaris (Bitplane) image processing 7.0 system.

Microscopy for Rosella-LC3, ATP5C1-Rosella and LC3 antibody staining.

A single time point snapshot of a z-stack was acquired for all reporter lines. Confocal images were acquired on an Opera QEHS spinning disk microscope (Perkin Elmer) using a 60x water immersion objective (NA = 1.2). DsRED and pHluorin images were acquired in parallel using two cameras and binning 2. pHluorin was excited with a 488 nm laser and DsRED with a 561 nm laser. A 568 dichroic mirror was used to deviate the emitted light towards the corresponding cameras. pHluorin was detected on camera 1 behind a 520/35 bandpass filter and DsRED on camera 2 behind a 600/40 bandpass filter. For Rosella-LC3, five planes were set with 400nm z-steps. For ATP5C1-Rosella, eleven planes were set with 400 nm z-steps. Scale of 1 pixel corresponds to 0.2152µm in all the cases described.

Microscopy for the Lysotracker assay.

Images were acquired on an Opera QEHS High content screening microscope using a 60x water immersion objective (NA = 1.2). Lysotracker deep red was excited with a 640 nm laser and detected with a 690/70 bandpass filter using camera binning 2. Z-stacks were defined to contain 11 planes with 400 nm z-steps.

Image analysis for Rosella-LC3 autophagy, ATP5C1-Rosella mitophagy assay, LC3 antibody staining and Lysotracker assay

An automated computational image analysis workflow for the resulting multichannel 3D images was implemented in Matlab (R2017a, Mathworks). Detailed description is provided in Supplementary Information.

Acknowledgements

We thank Prof. J. Hejna and E. Berger for critical comments on the manuscript. We would like to thank Prof. T. Graham and A. Sargsyan from the University of Utah for kindly providing us with pHluorin constructs, Prof. R. Jaenisch from the MIT Whitehead Institute for providing the AAVS1 targeting vector, and Prof. F. Zhang from the McGovern Institute for Brain Research for providing the TALEN vectors. This project was supported by the LCSB pluripotent stem cell core facility. This project was funded by the Fonds National de la Recherche (FNR) Luxembourg (CORE, C13/BM/5791363). This is an EU Joint Program - Neurodegenerative Disease Research (JPND) project (INTER/JPND/14/02; INTER/JPND/15/11092422). J.W., J.J. and J.F. were supported by FNR Aides à la Formation-Recherche (AFR). G.GG. was funded by the NCL-Stiftung (Hamburg, Germany).

Author Contributions

J.AF. and G.GG. performed cloning. J.AF., J.W., and G.GG. performed knock-ins. J.AF., J.W., J.J. and P.A. performed automated image acquisition experiments. J.AF., J.J. and J.W performed compound library experiments. P.A led automated image processing and pattern recognition programming. J.AF., J.J., J.W. and J.F. contributed to automatic image processing coding. P.A., J.AF., J.J. and J.W. performed analysis of results, wrote the manuscript, and organized the figures. J.C.S. supervised. All authors reviewed and agreed to the final version of the manuscript.

Competing Financial Interests

J.C.S. is shareholder of Braingineering Technologies sarl.

References

1. Mizushima, N., Levine, B., Cuervo, A.M. & Klionsky, D.J. Autophagy fights disease through cellular self-digestion. *Nature*. 2008; 451(7182):1069-1075. doi:10.1038/nature06639.
2. Nakatogawa, H., Suzuki, K., Kamada, Y. & Ohsumi, Y. Dynamics and diversity in autophagy mechanisms: lessons from yeast. *Nat Rev Mol Cell Biol*. 2009; 10(7):458-467. doi:10.1038/nrm2708.
3. Marx, V. Autophagy: eat thyself, sustain thyself. *Nature*. 2015(451):1069-1075. doi:10.1038/nmeth.3661
4. Ohsumi, Y. Historical landmarks of autophagy research. *Cell Res*. 2014; 24(1):9-23. doi:10.1038/cr.2013.169.
5. Klionsky, D.J., Abdelmohsen, K., Abe, A., Abedin, M.J., Abeliovich, H., Acevedo Arozena, A., Adachi, H., Adams, C.M., Adams, P.D., Adeli, K. et al. Guidelines for the use and interpretation of assays for monitoring autophagy (3rd edition). *Autophagy*. 2016; 12(1):1-222. doi:10.1080/15548627.2015.1100356.
6. Lynch-Day, M.A., Mao, K., Wang, K., Zhao, M. & Klionsky, D.J. The role of autophagy in Parkinson's disease. *Cold Spring Harb Perspect Med*. 2012; 2(4):a009357. doi:10.1101/cshperspect.a009357.
7. Ryan, B.J., Hoek, S., Fon, E.A. & Wade-Martins, R. Mitochondrial dysfunction and mitophagy in Parkinson's: from familial to sporadic disease. *Trends Biochem Sci*. 2015; 40(4):200-210. doi:10.1016/j.tibs.2015.02.003.
8. Galluzzi, L., Bravo-San Pedro, J.M., Levine, B., Green, D.R. & Kroemer, G. Pharmacological modulation of autophagy: therapeutic potential and persisting obstacles. *Nat Rev Drug Discov*. 2017; 16(7):487-511. doi:10.1038/nrd.2017.22.
9. Mali, P., Yang, L., Esvelt, K.M., Aach, J., Guell, M., DiCarlo, J.E., Norville, J.E. & Church, G.M. RNA-guided human genome engineering via Cas9. *Science*. 2013; 339(6121):823-826. doi:10.1126/science.1232033.
10. Hockemeyer, D., Soldner, F., Beard, C., Gao, Q., Mitalipova, M., DeKelver, R.C., Katibah, G.E., Amora, R., Boydston, E.A., Zeitler, B. et al. Efficient targeting of expressed and silent genes in human ESCs and iPSCs using zinc-finger nucleases. *Nat Biotechnol*. 2009; 27(9):851-857. doi:10.1038/nbt.1562.
11. Sankaranarayanan, S., De Angelis, D., Rothman, J.E. & Ryan, T.A. The use of pHluorins for optical measurements of presynaptic activity. *Biophys J*. 2000; 79(4):2199-2208. doi:10.1016/S0006-3495(00)76468-X.
12. Sargsyan, A., Cai, J., Fandino, L.B., Labasky, M.E., Forostyan, T., Colosimo, L.K., Thompson, S.J. & Graham, T.E. Rapid parallel measurements of macroautophagy and mitophagy in mammalian cells using a single fluorescent biosensor. *Sci Rep*. 2015; 5:12397. doi:10.1038/srep12397.
13. Platt, F.M., Boland, B. & van der Spoel, A.C. The cell biology of disease: lysosomal storage disorders: the cellular impact of lysosomal dysfunction. *J Cell Biol*. 2012; 199(5):723-734. doi:10.1083/jcb.201208152.
14. Luzio, J.P., Pryor, P.R. & Bright, N.A. Lysosomes: fusion and function. *Nat Rev Mol Cell Biol*. 2007; 8(8):622-632. doi:10.1038/nrm2217.
15. Tsukamoto, S., Kuma, A., Murakami, M., Kishi, C., Yamamoto, A. & Mizushima, N. Autophagy is essential for preimplantation development of mouse embryos. *Science*. 2008; 321(5885):117-120. doi:10.1126/science.1154822.
16. Jahreiss, L., Menzies, F.M. & Rubinsztein, D.C. The itinerary of autophagosomes: from peripheral formation to kiss-and-run fusion with lysosomes. *Traffic*. 2008; 9(4):574-587. doi:10.1111/j.1600-0854.2008.00701.x.
17. Wang, H., Sun, H.Q., Zhu, X., Zhang, L., Albanesi, J., Levine, B. & Yin, H. GABARAPs regulate PI4P-dependent autophagosome:lysosome fusion. *Proc Natl Acad Sci U S A*. 2015; 112(22):7015-7020. doi:10.1073/pnas.1507263112.
18. Lorenz, C., Lesimple, P., Bukowiecki, R., Zink, A., Inak, G., Mlody, B., Singh, M., Semtner, M., Mah, N., Aure, K. et al. Human iPSC-Derived Neural Progenitors Are an Effective Drug Discovery Model for Neurological mtDNA Disorders. *Cell Stem Cell*. 2017. doi:10.1016/j.stem.2016.12.013.
19. Ma, H., Folmes, C.D., Wu, J., Morey, R., Mora-Castilla, S., Ocampo, A., Ma, L., Poulton, J., Wang, X., Ahmed, R. et al. Metabolic rescue in pluripotent cells from patients with mtDNA disease. *Nature*. 2015; 524(7564):234-238. doi:10.1038/nature14546.

20. Steger, M., Tonelli, F., Ito, G., Davies, P., Trost, M., Vetter, M., Wachter, S., Lorentzen, E., Duddy, G., Wilson, S. et al. Phosphoproteomics reveals that Parkinson's disease kinase LRRK2 regulates a subset of Rab GTPases. *Elife*. 2016; 5. doi:10.7554/eLife.12813.
21. Roosen, D.A. & Cookson, M.R. LRRK2 at the interface of autophagosomes, endosomes and lysosomes. *Mol Neurodegener*. 2016; 11(1):73. doi:10.1186/s13024-016-0140-1.
22. Tang, F.L., Liu, W., Hu, J.X., Erion, J.R., Ye, J., Mei, L. & Xiong, W.C. VPS35 Deficiency or Mutation Causes Dopaminergic Neuronal Loss by Impairing Mitochondrial Fusion and Function. *Cell Rep*. 2015; 12(10):1631-1643. doi:10.1016/j.celrep.2015.08.001.
23. Zavodszky, E., Seaman, M.N., Moreau, K., Jimenez-Sanchez, M., Breusegem, S.Y., Harbour, M.E. & Rubinsztein, D.C. Mutation in VPS35 associated with Parkinson's disease impairs WASH complex association and inhibits autophagy. *Nat Commun*. 2014; 5:3828. doi:10.1038/ncomms4828.
24. Allen, G.F., Toth, R., James, J. & Ganley, I.G. Loss of iron triggers PINK1/Parkin-independent mitophagy. *EMBO Rep*. 2013; 14(12):1127-1135. doi:10.1038/embor.2013.168.
25. Hoyer-Hansen, M., Bastholm, L., Szyniarowski, P., Campanella, M., Szabadkai, G., Farkas, T., Bianchi, K., Fehrenbacher, N., Elling, F., Rizzuto, R. et al. Control of macroautophagy by calcium, calmodulin-dependent kinase kinase-beta, and Bcl-2. *Mol Cell*. 2007; 25(2):193-205. doi:10.1016/j.molcel.2006.12.009.
26. Kim, J., Kundu, M., Viollet, B. & Guan, K.L. AMPK and mTOR regulate autophagy through direct phosphorylation of Ulk1. *Nat Cell Biol*. 2011; 13(2):132-141. doi:10.1038/ncb2152.
27. Yu, W., Sun, Y., Guo, S. & Lu, B. The PINK1/Parkin pathway regulates mitochondrial dynamics and function in mammalian hippocampal and dopaminergic neurons. *Hum Mol Genet*. 2011; 20(16):3227-3240. doi:10.1093/hmg/ddr235.
28. Su, Y.C. & Qi, X. Inhibition of excessive mitochondrial fission reduced aberrant autophagy and neuronal damage caused by LRRK2 G2019S mutation. *Hum Mol Genet*. 2013; 22(22):4545-4561. doi:10.1093/hmg/ddt301.
29. Maruzs, T., Lorincz, P., Szatmari, Z., Szeplaki, S., Sandor, Z., Lakatos, Z., Puska, G., Juhasz, G. & Sass, M. Retromer Ensures the Degradation of Autophagic Cargo by Maintaining Lysosome Function in Drosophila. *Traffic*. 2015; 16(10):1088-1107. doi:10.1111/tra.12309.
30. Dagda, R.K., Cherra, S.J., 3rd, Kulich, S.M., Tandon, A., Park, D. & Chu, C.T. Loss of PINK1 function promotes mitophagy through effects on oxidative stress and mitochondrial fission. *J Biol Chem*. 2009; 284(20):13843-13855. doi:10.1074/jbc.M808515200.
31. Kageyama, Y., Hoshijima, M., Seo, K., Bedja, D., Sysa-Shah, P., Andrabi, S.A., Chen, W., Hoke, A., Dawson, V.L., Dawson, T.M. et al. Parkin-independent mitophagy requires Drp1 and maintains the integrity of mammalian heart and brain. *EMBO J*. 2014; 33(23):2798-2813. doi:10.15252/embj.201488658.
32. Bhujabal, Z., Birgisdottir, A.B., Sjottem, E., Brenne, H.B., Overvatn, A., Habisov, S., Kirkin, V., Lamark, T. & Johansen, T. FKBP8 recruits LC3A to mediate Parkin-independent mitophagy. *EMBO Rep*. 2017; 18(6):947-961. doi:10.15252/embr.201643147.
33. Chu, C.T., Ji, J., Dagda, R.K., Jiang, J.F., Tyurina, Y.Y., Kapralov, A.A., Tyurin, V.A., Yanamala, N., Shrivastava, I.H., Mohammadyani, D. et al. Cardiolipin externalization to the outer mitochondrial membrane acts as an elimination signal for mitophagy in neuronal cells. *Nat Cell Biol*. 2013; 15(10):1197-1205. doi:10.1038/ncb2837.
34. Zhu, Y., Wang, C., Yu, M., Cui, J., Liu, L. & Xu, Z. ULK1 and JNK are involved in mitophagy incurred by LRRK2 G2019S expression. *Protein Cell*. 2013; 4(9):711-721. doi:10.1007/s13238-013-3910-3.
35. Cherra, S.J., 3rd, Steer, E., Gusdon, A.M., Kiselyov, K. & Chu, C.T. Mutant LRRK2 elicits calcium imbalance and depletion of dendritic mitochondria in neurons. *Am J Pathol*. 2013; 182(2):474-484. doi:10.1016/j.ajpath.2012.10.027.
36. Sanchez-Danes, A., Richaud-Patin, Y., Carballo-Carbajal, I., Jimenez-Delgado, S., Caig, C., Mora, S., Di Guglielmo, C., Ezquerra, M., Patel, B., Giralt, A. et al. Disease-specific phenotypes in dopamine neurons from human iPS-based models of genetic and sporadic Parkinson's disease. *EMBO Mol Med*. 2012; 4(5):380-395. doi:10.1002/emmm.201200215.
37. Hockemeyer, D., Wang, H., Kiani, S., Lai, C.S., Gao, Q., Cassady, J.P., Cost, G.J., Zhang, L., Santiago, Y., Miller, J.C. et al. Genetic engineering of human pluripotent cells using TALE nucleases. *Nat Biotechnol*. 2011; 29(8):731-734. doi:10.1038/nbt.1927.

Supplementary Information Research Paper

Automated high-throughput high-content autophagy and mitophagy phenotyping in Parkinson's disease

Jonathan Arias-Fuenzalida[1,2,5], Javier Jarazo[1,2,5], Jonas Walter[1,2,5], Gemma Gomez-Giro[1,2,4], Julia Forster[1,3], Paul M.A. Antony[1,3,6] & Jens C. Schwamborn[1,2,6]

1 Luxembourg Centre for Systems Biomedicine (LCSB), University of Luxembourg, Luxembourg, 7 avenue des Hauts-Fourneaux

2 Laboratory of Developmental and Cellular Biology

3 Laboratory of Experimental Neurobiology

4 Max Planck Institute for Molecular Biomedicine, Laboratory of Cell and Developmental Biology, Roentgenstrasse 20, Muenster, Germany

5 Authors equally contributed to this article

6 Correspondence should be addressed to P.A. (paul.antony@uni.lu) and J.S. (jens.schwamborn@uni.lu).

Supplementary Materials and Methods

Image analysis for Rosella-LC3.

As shown in (Fig. S1), an automated computational image analysis workflow for the resulting multichannel 3D images was implemented in Matlab (R2017a, Mathworks). First, the raw images (Fig. S1A-C, pHluorinImRaw and dsRedImRaw) were flatfield corrected on the basis of reference images from an adjustment plate (Perkin Elmer HH10000650). The flatfield corrected images were deconvolved using the deconvblind function (Fig. S1D-E, pHluorinDeconvolved and dsRedDeconvolved). The number of iterations was set to 10 and the initial estimate of the point spread function was generated with the PSFGenerator tool [1]. In the PSFGenerator, the Richards & Wolf 3D optical model was used. The detailed parameter settings are summarized in (Table S1).

After deconvolution of the DsRed channel, differences of Gaussians were computed in order to highlight DsRed positive vesicles via spatial bandpass filtering. For the detection of small DsRed vesicles, a foreground image was computed via convolution with a Gaussian filter of size and standard deviation (GF-S-SD) 20 pixel and 1 pixel, respectively. The subtracted background image was returned from convolution with GF-S-SD 20

pixel and 7 pixel (Fig. S1F, dsRedDoG). The mask of small DsRed vesicles was defined via thresholding (>400) (Fig. S2G, dsRedDoGmask). To further improve the sensitivity of detection for dsRed positive vesicles, this approach was complemented with a top-hat filtering approach. Top-hat filtering of dsRedDeconvolved was done using the imtophat function and a disk shaped structuring element of radius 25 pixel (Fig. S2H, dsRedTopHat). Thresholding (>1200) returned the corresponding mask (Fig. S2I, dsRedTopHatMask). To refine dsRedTopHatMask, connected components with more than 500 pixels, overlapping with more than 10% of its pixels with the dsRedDoGmask, were substituted with the corresponding pixels in dsRedDoGmask (Fig. S2J, dsRedTopHatMaskSplit).

Both, dsRedDoGmask and dsRedTopHatMaskSplit were combined using Boolean OR logic (Fig. S2K, dsRedMask1). To confirm the detection of DsRed vesicles, a second difference of Gaussians was computed. Here the foreground image was convolved with a GF-S-SD of 11 pixel and 1 pixel while the background image was convolved with a GF-S-SD of 25 pixel and 6 pixel. The image resulting from subtraction of the background image from the foreground image (Fig. S2L, dsRedDoG2) was thresholded with gray tone value 1000 and objects high-pass filter 200 pixel and low-pass filter 2000 pixel (Fig. S2M, dsRedDoG2Mask). To split the vesicles, dsRedMask1 was used as a seed for an Euclidean distance transform and then the watershed function was applied. The resulting watershed mask (Fig. S2N, dsRedStencil1) was elementwise multiplied with the confirmative dsRedDoG2Mask (Fig. S2O, dsRedStencil2). The Final DsRed mask (Fig. S2P, dsRedMask) was computed via Boolean operation by pooling all pixels which were either present in dsRedMask1 or in dsRedStencil2.

To add more sensitivity for the detection of non-acidic vesicles, segmentation steps based on the deconvolved pHluorin channel were added. First, a difference of Gaussians was computed to segment larger vesicles. The GF-S-SD used to compute the foreground image was 100 pixel and 1 pixel, and the subtracted background image was convolved with a GF-S-SD of 100 pixel and 5 pixel (Fig. S2Q, GreenDoG). The mask of big green fluorescent vesicles was returned from intensity thresholding (>1000) (Fig. S2R, GreenDoGMask). To detect edges in the deconvolved pHluorin channel, a Laplacian of Gaussian filter with size 20 pixel and standard deviation 1 pixel was applied (Fig. S2S, GreenLoG), and pixels with values <-2000 were returned into the mask of edges (Fig. S2T, GreenLoGmask). The mask combining all vesicles detected in the pHluorin channel was computed via Boolean OR operation where the mask of big green fluorescent vesicles and the mask of edges were merged and connected components with less than 10 pixels were removed (Fig. S2U, pHluorinMask).

Ratio images (Fig. S2V, RatioIm) were computed by applying convolution GF-S-SD of 5 pixel and 2 pixel to the raw pHluorin and the raw DsRed channel. The ratio image was computed by elementwise division between the blurred pHluorin image and the blurred DsRed image.

To detect potentially missed autolysosomes, RatioIm was complemented using the imcomplement function (Fig. S2W, RatioImComp), and top-hat filtered using a disk-shaped structuring element of radius 15 pixel. Connected components above threshold 1.5 (Fig. S2X, AutoLysoMaskCandidates) were further validated as autolysomes by comparing their green fluorescence with the green fluorescence in the neighborhood defined by dilatation with a disk shaped structuring element of radius 7 pixel. Only when the neighborhood was at least 50% brighter than the vesicle and the vesicle volume was larger than 100 pixel, it was retained as an autolysosome candidate (Fig. S2Y, AutoLysoMask).

To detect autophagosomes based on their hollow vesicle property, an algorithm combining Fourier transform and Euler filtering was implemented. First, the GreenDoG image was plane by plane filtered with a Butterworth high pass filter in the Fourier transform domain. The cutoff frequency of the Butterworth filter was set to 10 and the order of the filter was set to 5. The resulting image (Fig. S2Z, GreenDoGFTB) was binarized via thresholding (>150) (Fig. S1AA, GreenDoG150). The resulting mask was maximum projected along the z axis. Objects with less than 20 pixel were removed, and median filtering using a 3x3 structuring element was applied. To prepare for the downstream analysis of connected components, the mask was further opened with a disk shaped structuring element of radius 1 pixel (Fig. S1AB, GreenDoG150b). Euler numbers were used to detect connected components containing holes. Indeed, an Euler number of 0 indicates that a connected component contains exactly one hole. Only connected components with Euler number 0 were retained (Fig. S2AC, EulerZero). For further filter refinement, the proportions between object size and hole size were evaluated. For that purpose the imfill function was used in order to create a filled mask (Fig. S2AD, EulerZeroFilled). In the proportion filter, only objects with a ratio between area and filled area larger than 1.01, and a difference between filled area and area larger than 20 were retained (Fig. S2AE, EulerSelect). To segment the holes, the mask was inverted and the background was removed by applying a size threshold (10000 pixels) (Fig. S2AF, EulerZeroHoles). Next, the imreconstruct function was used, with the hole mask described above as the seed mask, and the FilledMask as the limiting mask. Finally, the shapes of autophagosome candidate vesicles were restored via morphological operations by applying image opening with a disk shaped structuring element of radius 5 pixel. For 3D reconstruction, only those planes which were already positive in GreenDoG150 were retained (Fig. S2AG, EulerMask).

To detect remaining autophagosomes, Hough transforms for circle detection were applied to the raw pHluorin channel. To minimize false positive detections, the already identified vesicle pixels were substituted by low pass filtered pixels. To highlight the not yet detected circular vesicles, graytone erosion with a disk shaped structuring element of radius 2 pixel was applied (Fig. S2AH, HoughInput). For the detection of circles, the function imfindcircles was used, where the radius was set to a range between 3-30 pixel. To remove false positives from the Hough transform algorithm, each candidate circle was further analyzed with respect to its value in the raw green and red channels. Only candidate circles with a large median absolute deviation among raw pHluorin pixels (>20), and a low 0.9th quantile of raw DsRed pixels (<300) were retained (Fig. S2AI, HoughOutput).

The mask of all autophagosome candidates was computed by combining autopagosome candidates detected via the Fourrier-Euler algorithm or the Hough algorithm. To minimize the number of false positive autophagosomes, filters based on size, shape, and the ratio between vesicle border and vesicle center intensities were applied. The allowed sizes were set to the range between 50-10,000 pixel (Fig. S2AJ, AutophagosomeCandidates). For shape evaluation, the vesicle surface was defined by erosion with a sphere shaped structuring element of radius 1 pixel. Two sphericity indices were computed as bellow.

(i) $$SphericityIdx1 = \frac{\pi\text{^}(1/3)*6A\text{^}(2/3)}{S}$$

(ii) $$SphericityIdx2 = \frac{A}{S}\ ; A = area\ and\ S = surface$$

Only vesicles with SphericityIdx1> 1 and SphericityIdx2> 1.5 were retained. For classification, all vesicles detected via the different approaches shown above were combined via Boolean operations. In order to maintain vesicle splitting, the perimeter of the autophagosome mask was excluded from the pooled vesicle mask. To exclude DsRed negative vesicles from the downstream analysis, the mean intensity in the raw DsRed channel was measured for all connected components. Only vesicles with a mean intensity above 300 and not touching the border of the image were considered for the classification (Fig. S2AK, VesiclesAll). For the remaining vesicles, the eccentricity was computed and all connected components with eccentricity >0.9 were collected in the mask named NonCircularVesicleMask (Fig. S2AL).

The classification of the segmented vesicles was designed to classify four vesicle types, namely phagophores, autophagosomes, early autolysosomes, and late autolysosomes. For this purpose, a progressive exclusion algorithm was implemented. First, vesicles overlapping with the autophagosome mask and not overlapping with the NonCircularVesicleMask were classified as autophagosomes. Three condition-sets were defined to classify the remaining vesicles as phagophores. Case1: vesicles with at least 25%

overlap with both the pHluorinMask and the DsRedMask, a median ratio above 2 and without overlap with the AutoLysoMask. Case2: the 3rd quantile of the green channel was above 7500 and the 3rd quantile of the red channel above 4000. Case3: the green fluorescence in the center of the vesicle was at least 25% brighter than at the vesicle's surface. For the remaining vesicles that were not classified as autophagosomes or phagophores, two conditions were defined for the vesicle labeling as late autolysosome. Case1: vesicles with at least 25% overlap with the DsRedMask and less than 10% overlap with the pHluorinMask or, alternatively, a median ratio below or equal to 2. Case2: the green fluorescence was lower in the vesicle center than at the surface. Remaining vesicles, not classified as autophagosomes, phagophores, or late autolysosomes were defined as early autolysosomes if they had at least 25% overlap with the DsRedMask and less or equal to 25% overlap with the pHluorinMask, or if they overlapped with the AutoLysoMask (Fig. S2AM-AN). Diameters shown in the results section correspond to the major axis length of the respective vesicles.

Image analysis for the ATP5C1-Rosella mitophagy assay.

As shown in (Fig. S2), an automated computational image analysis workflow for the resulting multichannel 3D images was implemented in Matlab (R2017a, Mathworks). For the segmentation of mitochondria, the DsRed channel (Fig. S2C) foreground signal was computed via convolution GF-S-SD of 50 pixel and 1 pixel. The subtracted background signal was computed via convolution with a GF-S-SD of 50 pixel and 2 pixel. Pixels with graytone values above 12 in this difference of Gaussians image (Fig. S2D, MitoDoG) were defined as mitochondrial pixels (Fig. S2E, MitoMask).

MitophagyEvents were defined via a combination of green to red fluorescence ratio analysis and morphological filtering based on difference of Gaussians thresholding. First, 26 connected components within MitoMask were defined as mitophagy event markers (Fig. S2F, MitophagySeedMask) if the mean ratio value within the connected components was below 0.6. To refine the shape of the detected mitophagy events, the imreconstruct function was used with the parameters MitophagySeedMask and MitoPhagyLimitingMask Fig. S2G). The MitoPhagyLimitingMask was defined by pixel values above 50 in a difference of Gaussians of the DsRed channel (Fig. S2H, MitophagyDoG). MitophagyDoG was defined by GF-S-SD of 50 pixel and 1pixel for the foreground and GF-S-SD of 50 pixel and 5 pixel for the background. Resulting segmented mitochondria and autophagic vacuoles are shown for DsRed and pHluorin (Fig. S2I-J).

Image analysis for the Lysotracker assay.

Deconvolution of raw images (Fig. S4A, LysoTDR) was done as described above according to the settings shown in table 1 (Fig. S4B, LysoTDR_deconvolved). For the segmented lysotracker positive vesicles, an algorithm with different morphological filters was implemented. First, a difference of Gaussians was computed using a GF-S-SD of 100 pixel and 1 pixel for convolving the foreground image and a GF-S-SD of 100 pixel and 5 pixel for convolving the substracted background image (Fig. S4C, LysoTDR_DoG). A first mask with Lysotracker pixels was returned by thresholding (>2000) LysoTDR_DoG (Fig. S4E, LysoTracker_DoG_Mask). An addition detection option was implemented using convolution of LysoTDR_deconvolved with a Laplacian of Gaussian of GF-S-SD 20 pixel and 1 pixel (Fig. S4D, LysoTDR_LoG). The second mask of lysotracker pixels was returned by retaining pixels with graytone values <-2000 in LysoTDR_LoG (Fig. S4F, LysoTDR_LoG_Mask). The final mask of lysotracker stained vesicles was computed via Boolean OR combination of both masks and size exclusion of connected components with less than 10 pixels (Fig. S4G, LysoTDR_Mask). To compute the major axis length of each vesicle, LysoTDR_Mask was maximum projected and subsequently the function regionprops was used to extract the major axis length of each connected component in the projected mask.

Titles and legends to Supplementary Figures

Figure S1. (**A**) Heatmap of scaled (0.0-2.0) category-mean normalized absolute frequency per well for autophagic structures for live Rosella and fixed LC3 antibody Rosella-LC3 lines. Significance matrix of Kruskal-Wallis and Dunn's multiple comparison test is shown below. (**B**) Representative fields of live Rosella-LC3 and (**C**) fixed LC3 antibody in healthy control line. Scale bar 20µm.

Figure S2. Image analysis workflow for autophagy Rosella-LC3 reporter lines. The names of the images match those of Supplementary Materials and Methods. (**A**) Overlay of raw dsRed and pHluoring channels. (**B**) Raw image for dsRed, dsRedImRaw. (**C**) Raw image for pHluorin, pHluorinImRaw channel. (**D**) dsRedDeconvolved. (**E**) pHluorinDeconvolved. (**F**) dsRedDoG. (**G**) dsRedDoGmask. (**H**) dsRedTopHat. (**I**) dsRedTopHatMask. (**J**) dsRedTopHatMaskSplit. (**K**) dsRedMask1. (**L**) dsRedDoG2. (**M**) dsRedDoG2Mask. (**N**) dsRedStencil1. (**O**) dsRedStencil2. (**P**) dsRedMask. (**Q**) GreenDoG. (**R**) GreenDoGMask. (**S**) GreenLoG. (**T**) GreenLoGmask. (**U**) pHluorinMask. (**V**) RatioIm. (**W**) RatioImComp. (**X**) AutoLysoMaskCandidates. (**Y**) AutoLysoMask. (**Z**) GreenDoGFTB. (**AA**) GreenDoG150. (**AB**) GreenDoG150b. (**AC**) EulerZero. (**AD**) EulerZeroFilled. (**AE**) EulerSelect. (**AF**) EulerZeroHoles. (**AG**) EulerMask. (**AH**) HoughInput. (**AI**)

HoughOutput. (**AJ**) AutophagosomeCandidates. (**AK**) VesiclesAll. (**AL**) NonCircularVesicleMask. (**AM**) All vesicles mapped on dsRed channel. (**AN**) All vesicles mapped in pHluorin channel. Diameters shown in the results section correspond to the major axis length of the respective vesicles. Scale bars indicate 20µm and 3x zoomed insets are highlighted with yellow boxes.

Figure S3. Image analysis workflow for mitophagy with ATP5C1-Rosella reporter lines. The names of the images match those of online methods. (**A**) Overlay of raw dsRed and pHluoring channels. (**B**) Raw image for pHluorin. (**C**) Raw image for DsRed channel. (**D**) MitoDoG. (**E**) MitoMask. (**F**) MitophagySeedMask. (**G**) MitoPhagyLimitingMask. (**H**) MitophagyDoG. (**I**) All vesicles mapped in pHluorin channel. (**J**) All vesicles mapped on dsRed channel. Diameters shown in the results section correspond to the major axis length of the respective vesicles. Scale bars indicate 20µm and 3x zoomed insets are highlighted with yellow boxes.

Figure S4. Quantification of autophagy structures before and after addition of mitophagy or autophagy modulators. Phagophores, autophagosomes, early autolysosomes, late autolysosomes and autophagy vacuoles are quantified for (**A**) healthy-control, (**B**) PINK1(p.I368N), (**C**) VPS35(p.D620N) and (**D**) LRRK2(p.G2019S). Autophagic-vacuoles are quantified as the sum of autophagosomes, early autolysosomes, and late autolysosomes. Dunnett's multiple comparison of means was performed for all lines and all conditions with respect to their respective basal reference (ref). The ordinate frequency axis is presented with a maximum of 1000 for phagophores, 8 for autophagosomes, 60 for early autolysosomes, 800 for late autolysosomes, and 800 for autophagic vacuoles. Standard deviations are shown. Data represent three independent replicates. Significance levels are *p<0.05, **p<0.01, ***p<0.001 and ****p<0.0001.

Figure S5. Image analysis workflow for the Lysotracker assay in reporter lines. The names of the images match those in the online methods. (**A**) Raw images for lysotracker, LysoTDR. (**B**) LysoTDR_deconvolved. (**C**) LysoTDR_DoG. (**D**) LysoTDR_LoG. (**E**) LysoTracker_DoG_Mask. (**F**) LysoTDR_LoG_Mask. (**G**) LysoTDR_Mask. Projected major axis length of each connected component is represented. Scale bars indicate 20 µm and 3x zoomed insets are highlighted with yellow boxes.

Video S1. Autophagy dynamics in iPS cells. The Rosella-LC3 healthy-control line was imaged for 1 hour 15min. Arrows depict examples of phagophores and autophagic vacuoles. Squares represent the close-up area of VideoS2 and Video S3. Phagophores mobilized throughout the cell. Autophagic vacuoles appear and interact with other vesicles. Speed 25fps. Scale bar 20µm.

Video S2. Autophagy dynamics in iPS cells. The Rosella-LC3 healthy-control line was imaged for 1 hour 15min. Close-up of video S1 shows the emergence of autophagosomes of dsRED^{pos}pHluorin^{pos} and of autolysosomes of dsRED^{pos}pHluorin^{neg} lumen. Speed 25fps. Scale bar 5 µm.

Video S3. Autophagy dynamics in iPS cells. The Rosella-LC3 healthy-control line was imaged for 1 hour 15min. Close-up of video S1 shows the partitioning of autophagic vacuoles previous to telophase. Speed 25fps. Scale bar 5 µm.

Video S4. Autophagy dynamics in iPS cells. Navigation through a 3D reconstruction of the Rosella-LC3 healthy-control culture. Phagophores, autophagosomes, and late autolysosomes are indicated. The fluorescence intensity of the pH sensor highlights the transitions in the autophagy cycle. Dynamic scale bar.

Video S5. Mitophagy dynamics in iPS cells. The ATP5C1-Rosella healthy-control line was imaged for 1 hour 15min. Mitochondrial networks dynamically reorganize and split. Autolysosomes that are responsible for mitophagy are visible. Speed 25fps. Scale bar 20 µm.

Video S6. Mitophagy dynamics in iPS cells. The ATP5C1-Rosella healthy-control line was imaged for 1 hour 15min. Close-up of video S5. Autolysosomes associate with the mitochondrial network and present a “kiss and run” monitoring behavior. Mitochondrial networks dynamically reorganize and split. Speed 25fps. Scale bar 20 µm.

Video S7. Mitophagy dynamics in iPS cells. The ATP5C1-Rosella healthy-control line was imaged for 1 hour 15min. Close-up of video S5. Autolysosomes associate with the mitochondrial network and present a “kiss and run” monitoring behavior. Speed 25fps. Scale bar 20 µm.

Table S1. PSF generator settings

Channel	pHluorin	DsRed	LysoTDR
Refractive index immersion	1.3	1.3	1.3
Accuracy computation	Best	Best	Best
Wavelength	520 nm	600 nm	690
NA	1.2	1.2	1.2
Pixel size	215.2 nm	215.2 nm	215.2 nm
Z-step	400 nm	400 nm	400 nm
Size XYZ	256, 256, 5	256, 256, 5	256, 256, 11

Supplementary references

1. Kirshner, H., Aguet, F., Sage, D. & Unser, M. 3-D PSF fitting for fluorescence microscopy: implementation and localization application. *J Microsc*. 2013; 249(1):13-25. doi:10.1111/j.1365-2818.2012.03675.x.

3.2.3 Figures

Figure 1

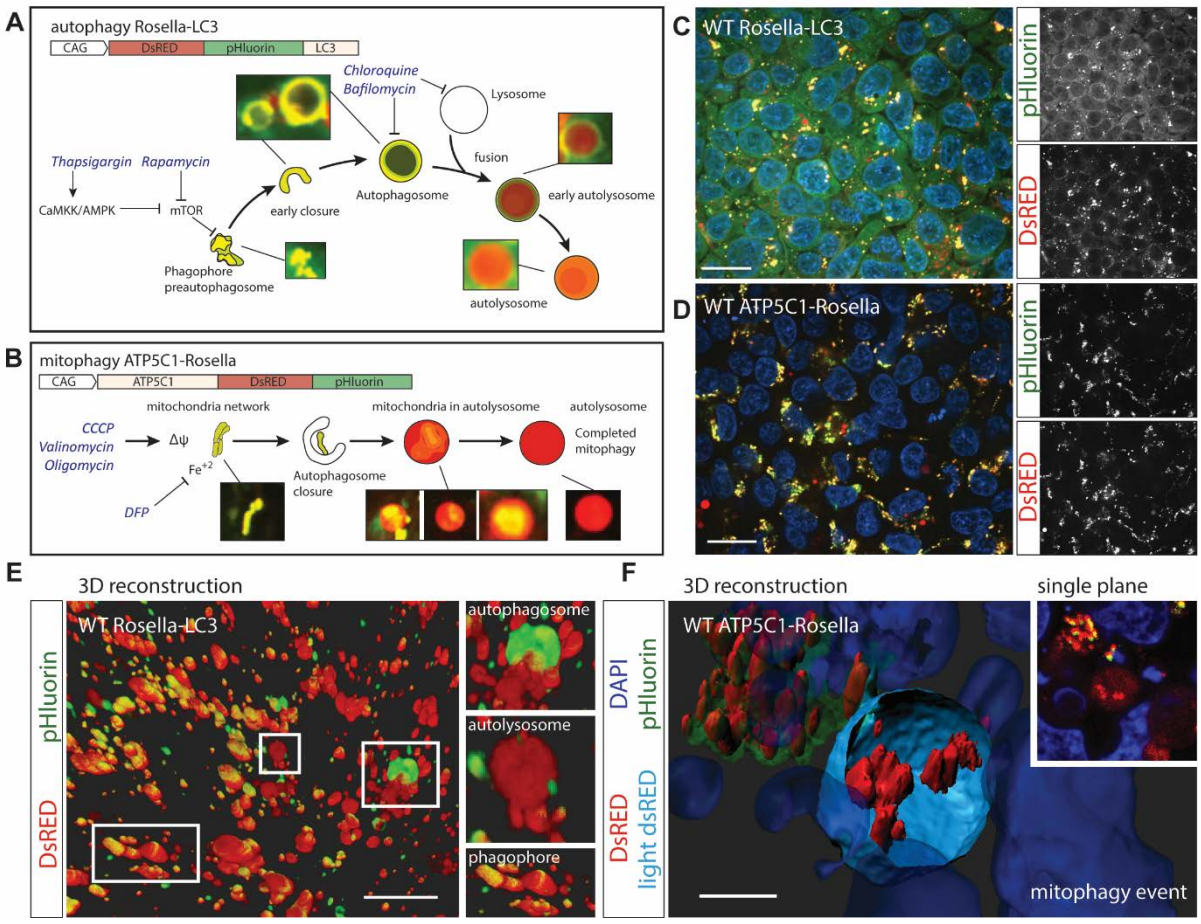

Figure 2

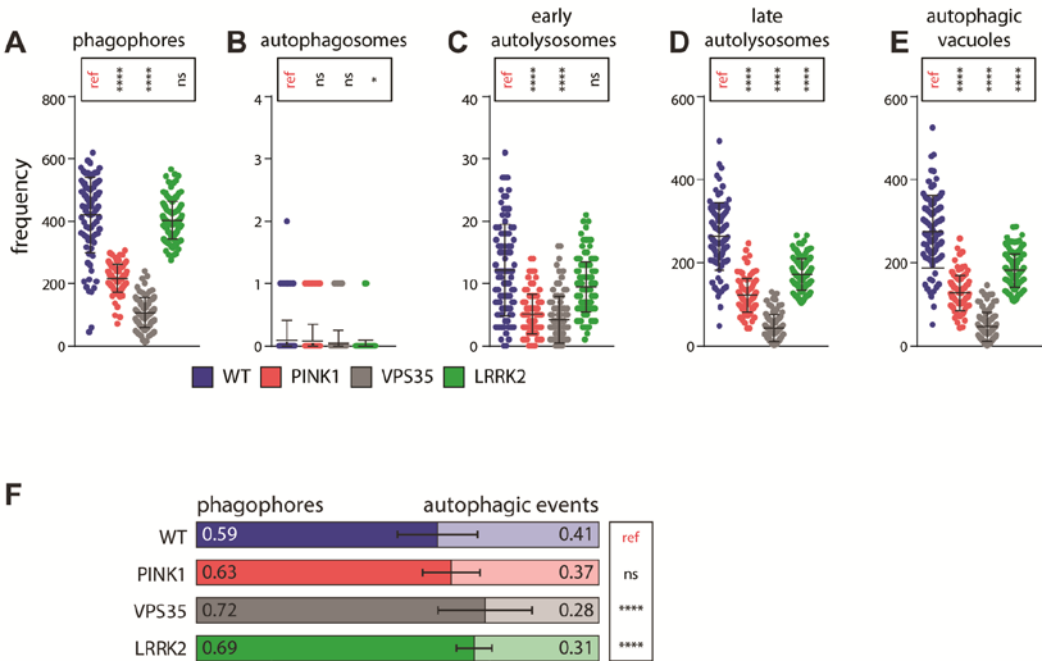

Figure 3

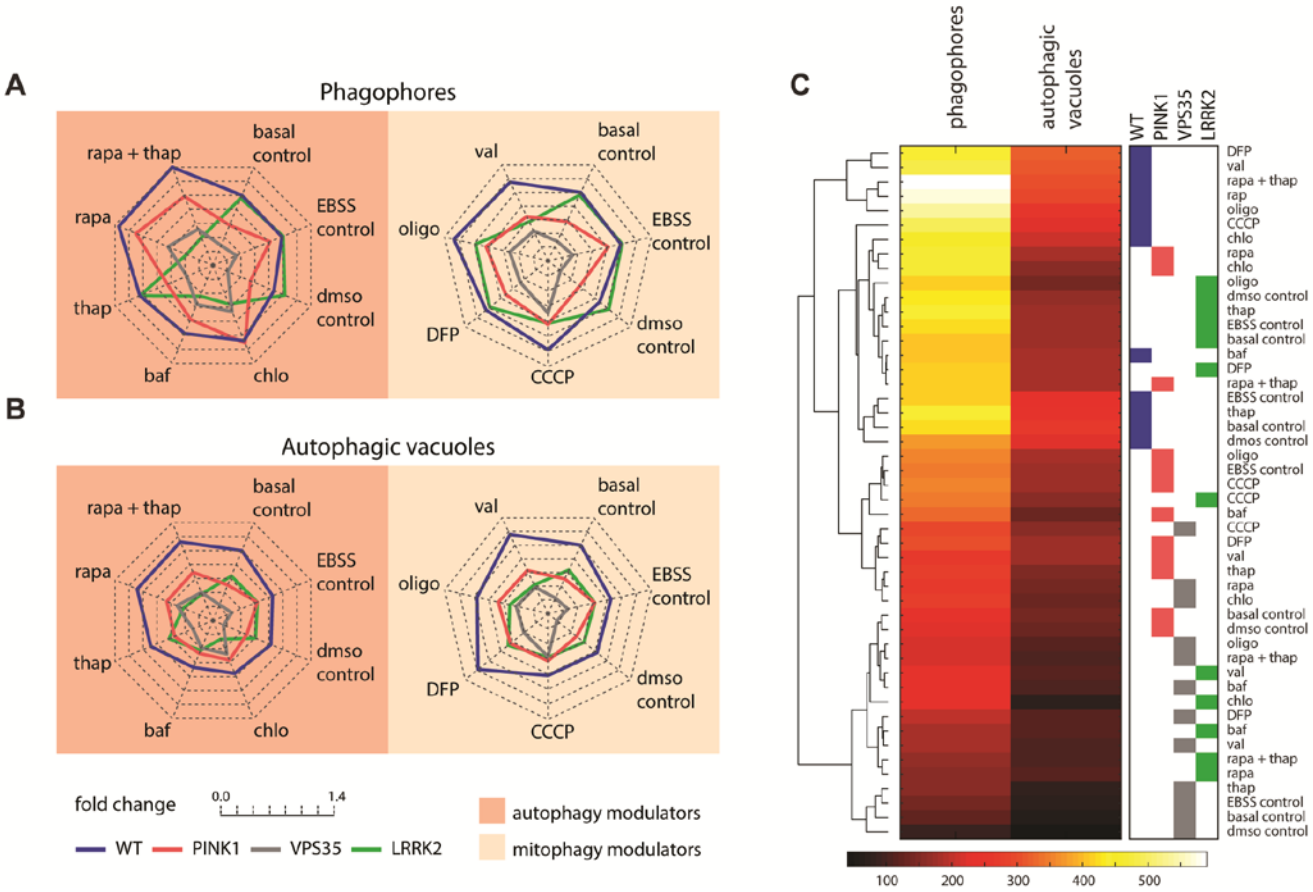

Figure 4

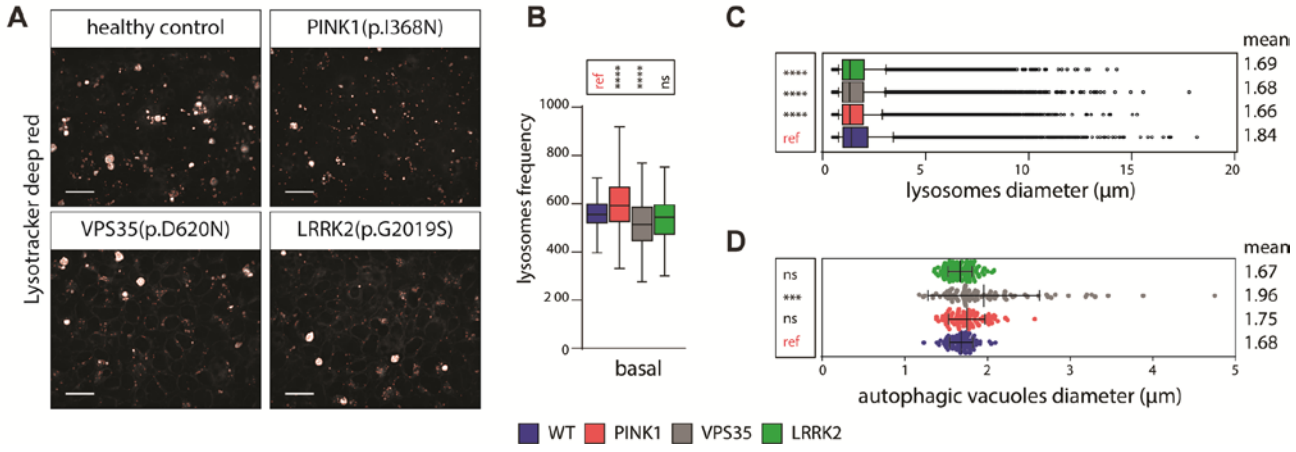

Figure 5

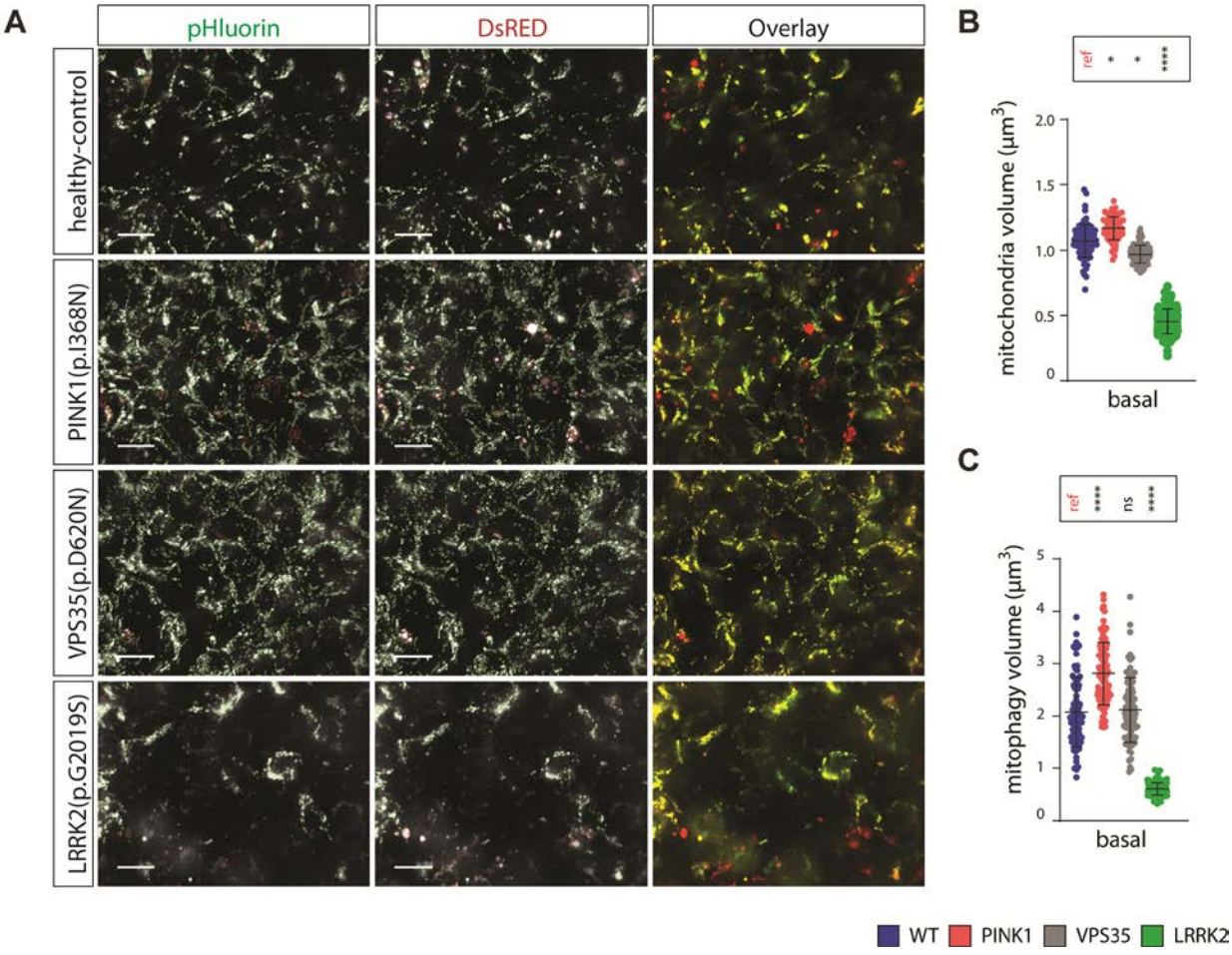

Figure 6

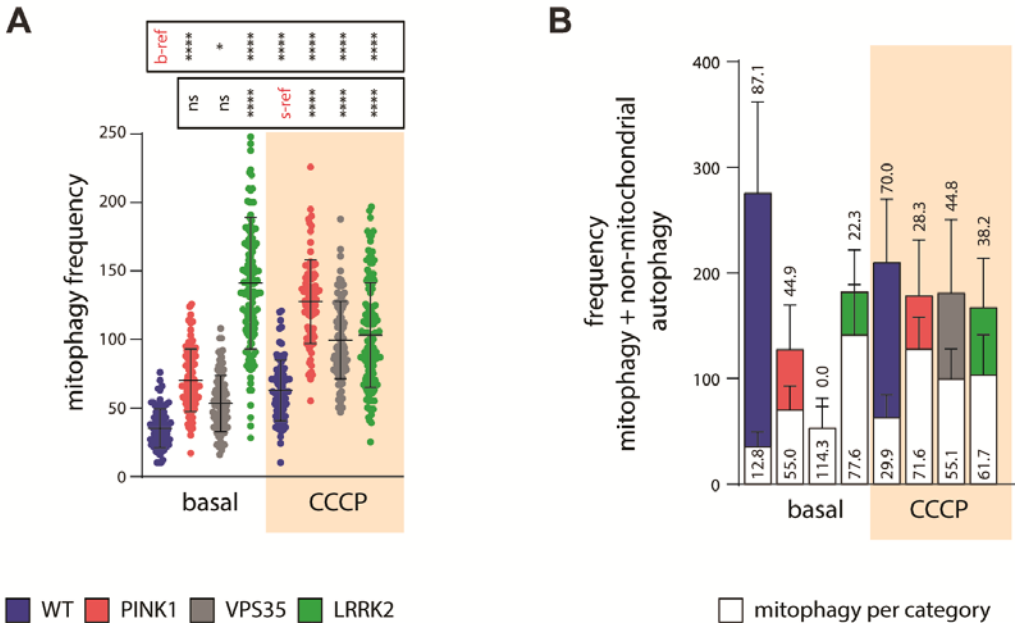

Figure S1

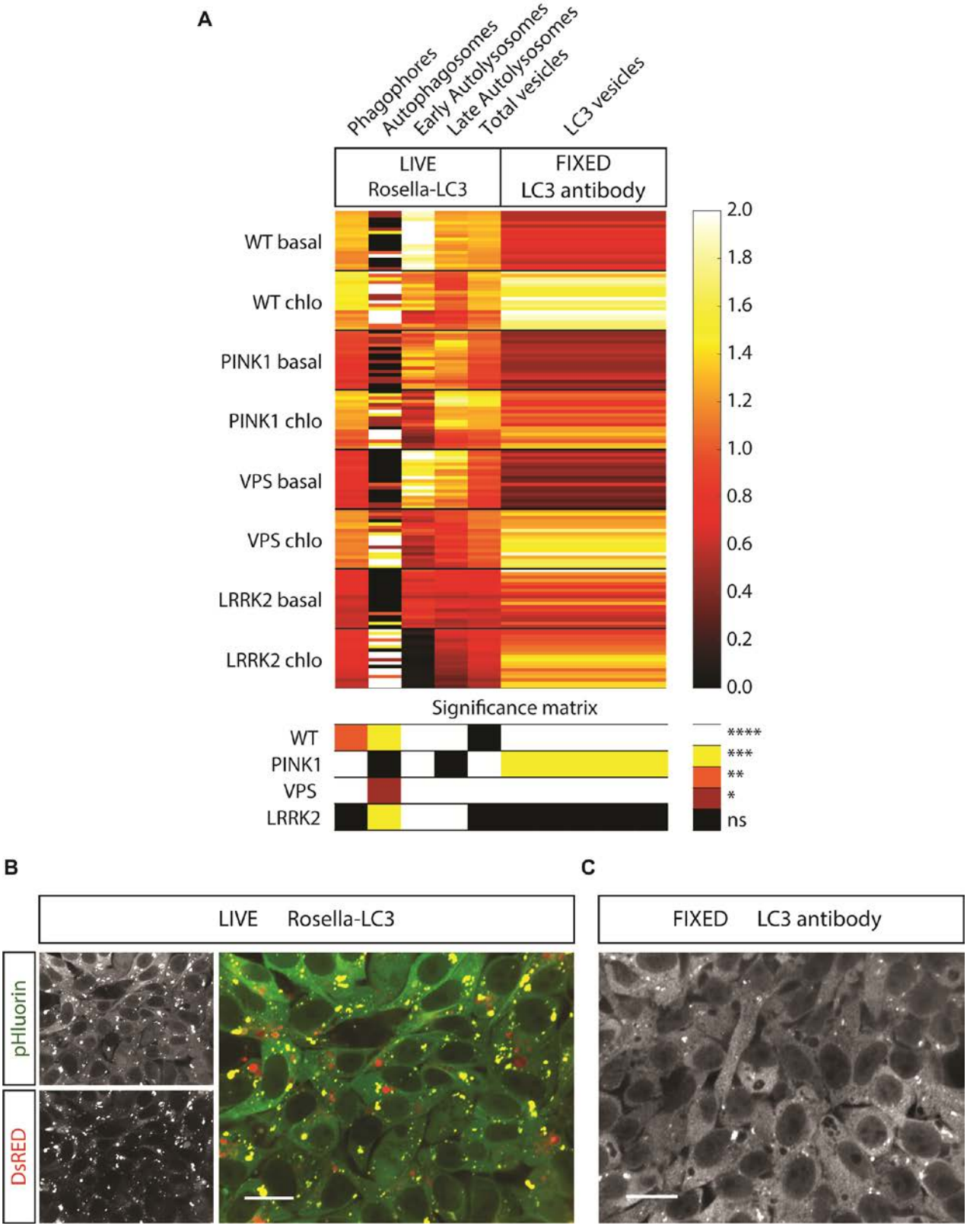
A
Phagophores
Autophagosomes
Early Autolysosomes
Late Autolysosomes
Total vesicles
LC3 vesicles
LIVE
Rosella-LC3
FIXED
LC3 antibody
WT basal
WT chlo
PINK1 basal
PINK1 chlo
VPS basal
VPS chlo
LRRK2 basal
LRRK2 chlo
2.0
1.8
1.6
1.4
1.2
1.0
0.8
0.6
0.4
0.2
0.0
Significance matrix
WT
PINK1
VPS
LRRK2
****
***
**
*
ns
B
C
LIVE Rosella-LC3
FIXED LC3 antibody
pHluorin
DsRED

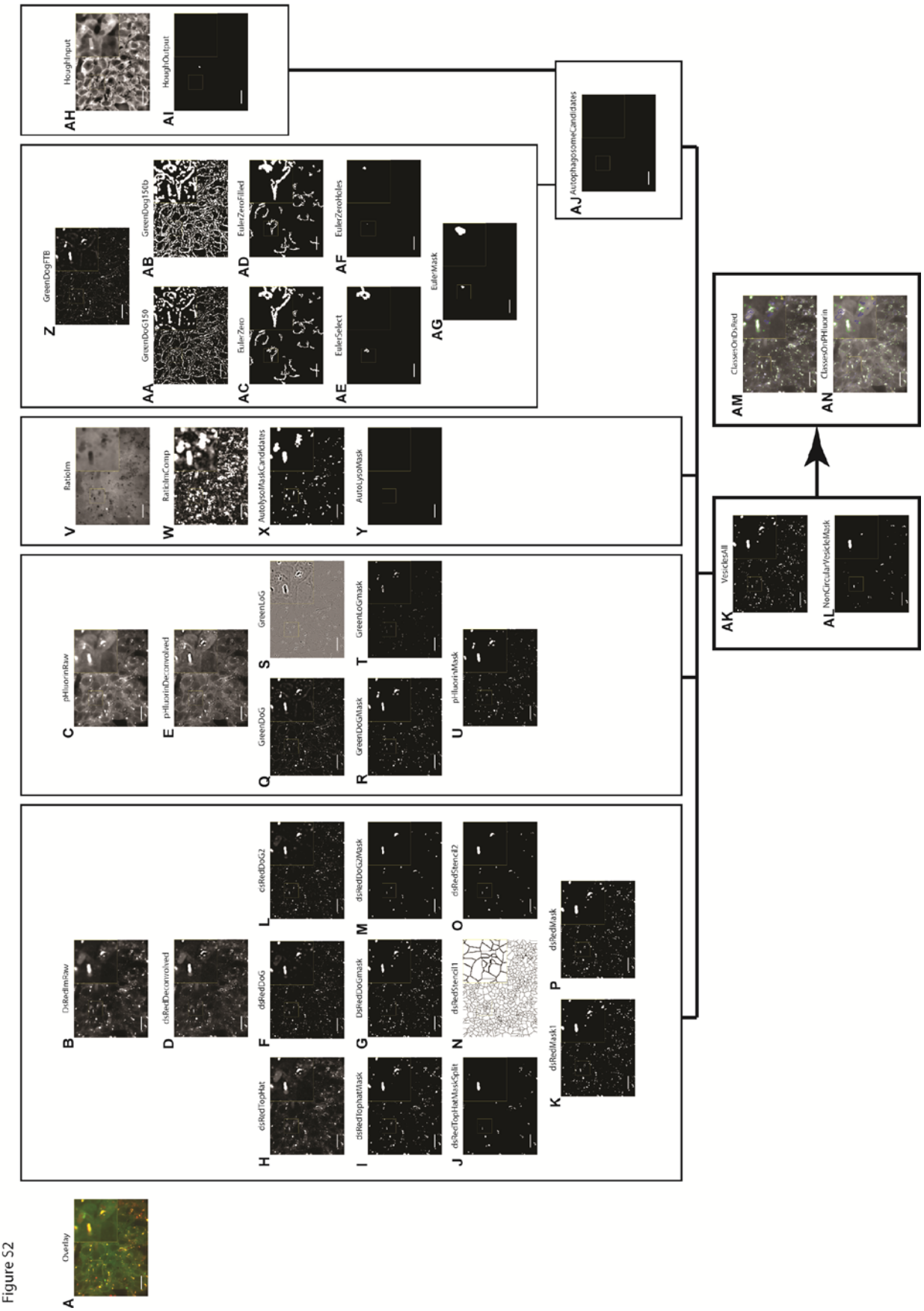
A Overlay
B DsRedImRaw
C pHluorinRaw
D dsRedDeconvolved
E pHluorinDeconvolved
F dsRedDoG
G DsRedDoGmask
H dsRedTopHat
I dsRedTophatMask
J dsRedTopHatMaskSplit
K dsRedMask1
L dsRedDoG2
M dsRedDoG2Mask
N dsRedStencil1
O dsRedStencil2
P dsRedMask
Q GreenDoG
R GreenDoGMask
S GreenLoG
T GreenLoGmask
U pHluorinMask
V RatioIm
W RatioImComp
X AutolysoMaskCandidates
Y AutoLysoMask
Z GreenDogFTB
AA GreenDoG150
AB GreenDog150b
AC EulerZero
AD EulerZeroFilled
AE EulerSelect
AF EulerZeroHoles
AG EulerMask
AH HoughInput
AI HoughOutput
AJ AutophagosomeCandidates
AK VesiclesAll
AL NonCircularVesicleMask
AM ClassesOnDsRed
AN ClassesOnPHluorin

Figure S2

Figure S3

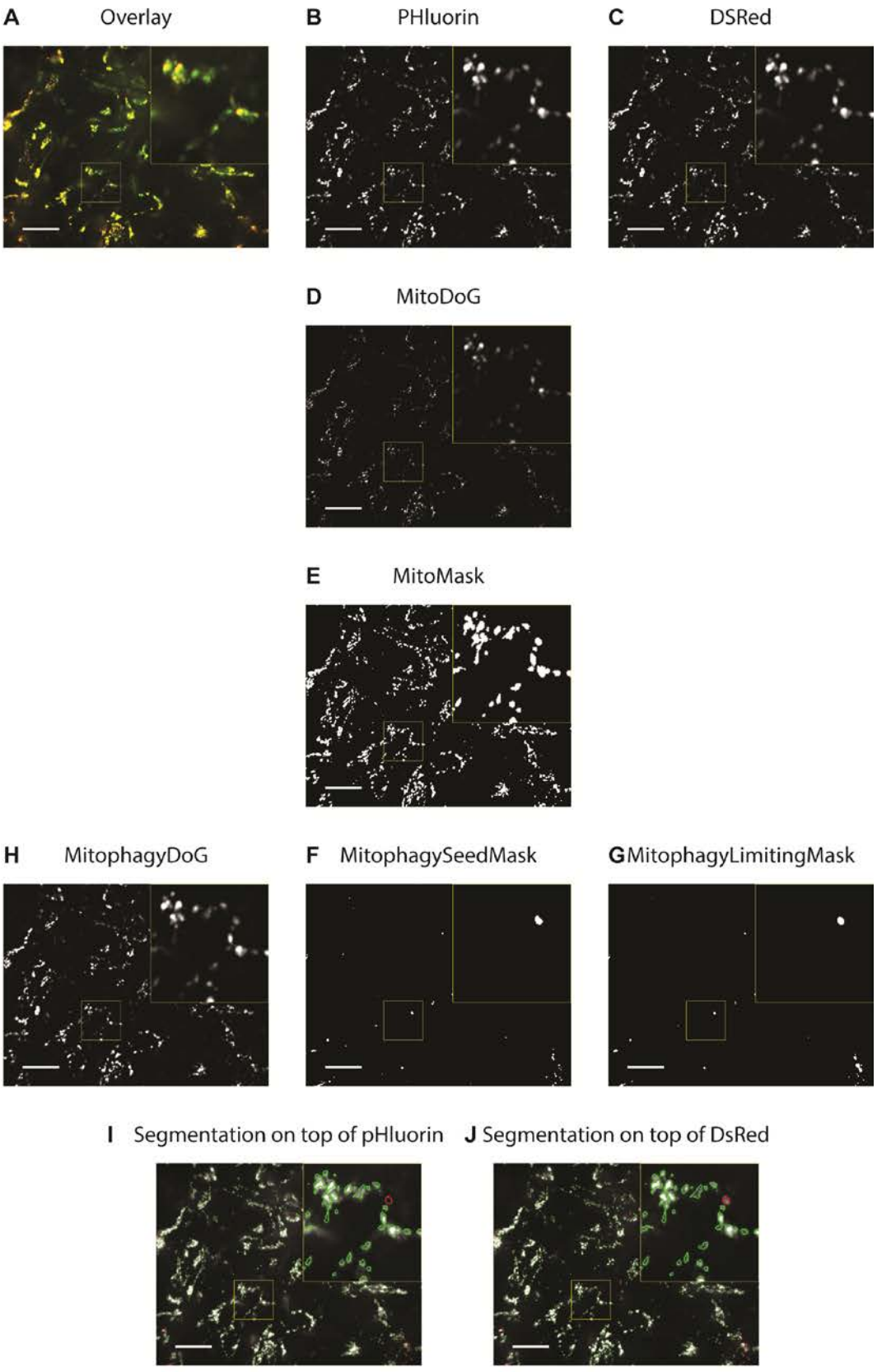
A Overlay
B PHluorin
C DSRed
D MitoDoG
E MitoMask
H MitophagyDoG
F MitophagySeedMask
G MitophagyLimitingMask
I Segmentation on top of pHluorin
J Segmentation on top of DsRed

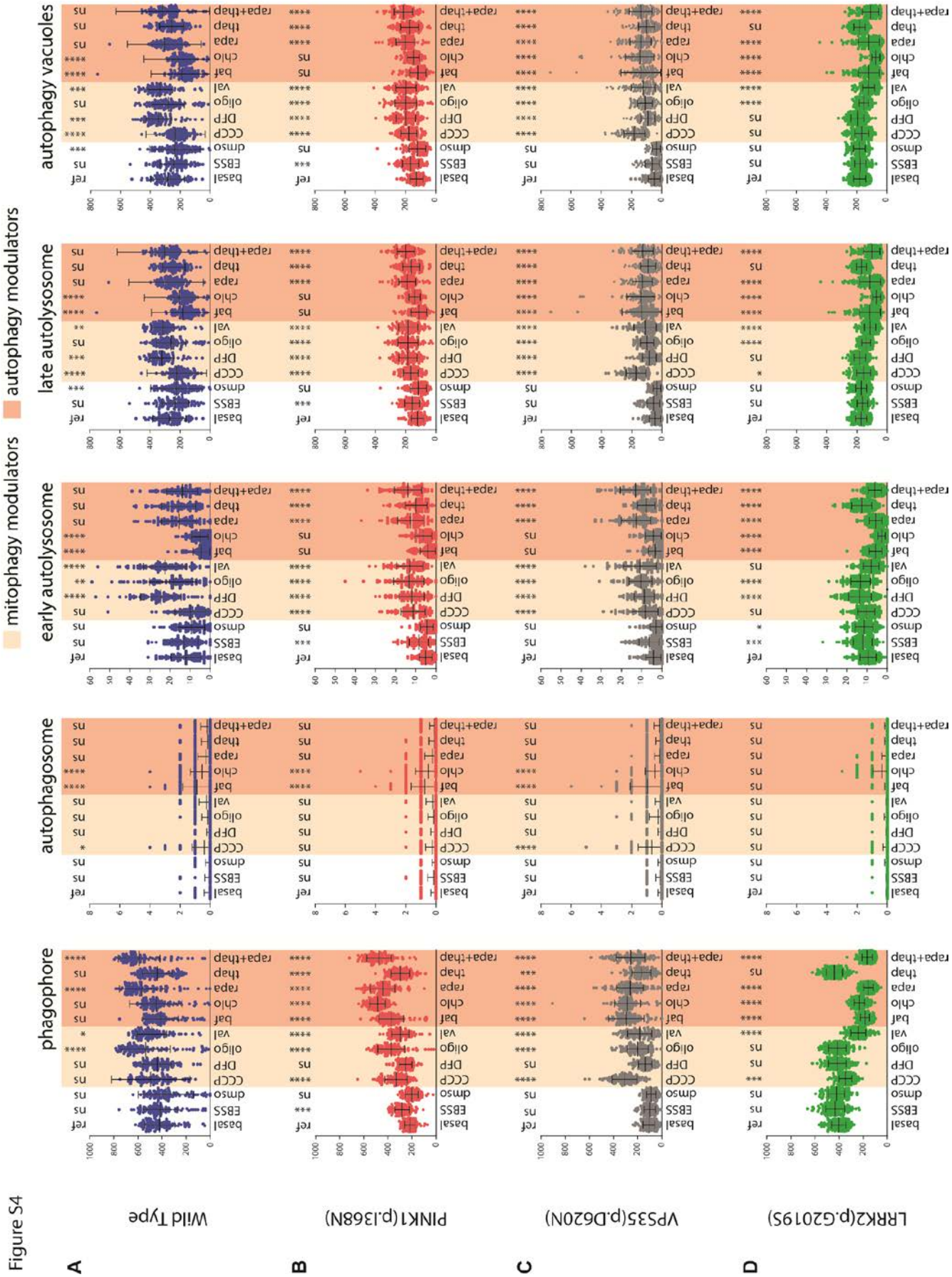
mitophagy modulators
autophagy modulators
A
B
C
D
Wild Type
PINK1(p.I368N)
VPS35(p.D620N)
LRRK2(p.G2019S)
phagophore
autophagosome
early autolysosome
late autolysosome
autophagy vacuoles

Figure S4

Figure S5

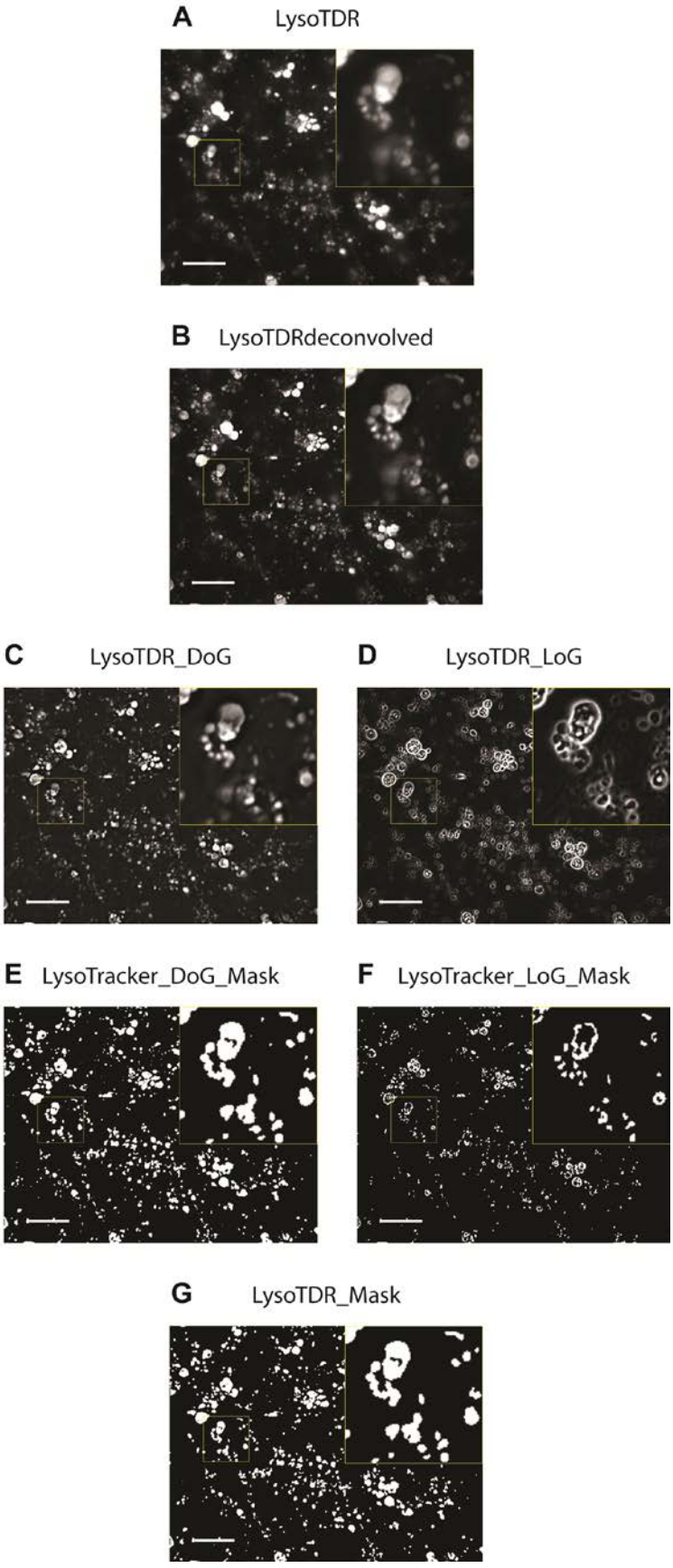
A
LysoTDR
B
LysoTDRdeconvolved
C
LysoTDR_DoG
D
LysoTDR_LoG
E
LysoTracker_DoG_Mask
F
LysoTracker_LoG_Mask
G
LysoTDR_Mask

3.3 Manuscript III

Impaired dopaminergic differentiation of Parkinson's disease derived neuroprecursor cells improved by 2-hydroxypropyl-β-cyclodextrin treatment

Javier Jarazo [1], Lisa Smits [1], Eligio Ianetti [4,5], Jonathan Arias-Fuenzalida [1], Jonas Walter [1], Gemma Gomez-Giro [1,6], Xiaobing Qing [1], Christian Jäger [3], Zdenka Hodak [3], Philip Seibler [7], Aleksandar Rakovic [7], Emmanuel Berger [1], Silvia Bolognin [1], Julien Beyrath [5], Paul Antony [2], Christine Klein [7], Jens C. Schwamborn [1,8]

[1] Developmental and Cellular Biology, Luxembourg Centre for Systems Biomedicine, University of Luxembourg, 6 Avenue du Swing, 4367, Belvaux, Luxembourg

[2] Experimental Neurobiology, Luxembourg Centre for Systems Biomedicine, University of Luxembourg, 6 Avenue du Swing, 4367, Belvaux, Luxembourg

[3] Enzymology and Metabolism, Luxembourg Centre for Systems Biomedicine, University of Luxembourg, 6 Avenue du Swing, 4367, Belvaux, Luxembourg

[4] Department of Biochemistry, Radboud Institute for Molecular Life Sciences, Nijmegen, the Netherlands

[5] Khondrion BV, Nijmegen, the Netherlands

[6] Max Planck Institute for Molecular Biomedicine, Laboratory of Cell and Developmental Biology, Roentgenstrasse 20, Münster, Germany

[7] Institute of Neurogenetics, University of Lübeck, D-23538, Lübeck, Germany

[8] Corresponding author: jens.schwamborn@uni.lu

Status: This manuscript is about to be sent to Nature Medicine

3.3.1 Preface

This manuscript uses all the techniques developed during my PhD (described in the previous articles) to evaluate the effect of known point mutations causative of PD during neurodevelopment. We identified an altered differentiation efficiency that can be linked to the different energetic capabilities, mitochondrial network properties, and mitochondrial degradation between control and patient lines. The usage of isogenic controls allowed us to dissect the influence of a point mutation in PINK1 in the phenotype observed. Plus, we identified a compound able to resolve the differentiation deficit.

For this manuscript, I did the reprogramming to hiPSCs and further differentiation to the intermediate state of NECSs of some of the fibroblast samples of controls and patient lines. I designed and performed all the cell culture work related to the phenotyping of the hiPSCs, NESCs and neurons in 2D and in microfluidics. I developed the scripts for all the properties analysed during the differentiation stages under the supervision of Paul Antony. I performed all the cloning of constructs and gene editing with the collaboration of Gemma Gomez-Giro and Jonathan Arias-Fuenzalida. I performed the design and analysis of the mitochondrial morphology analysis in fibroblast with the collaboration of Eligio Ianetti. I performed the mitochondrial morphology analysis in NESCs and neurons with the collaboration of Paul Antony. I performed the multielectrode array measurements and analysis with the collaboration of Lisa Smits. I performed the generation of the reporter lines with the help of Jonas Walter, Gemma Gomez-Giro and Jonathan-Arias. I generated the NESCs reporter lines, their further differentiation into neurons, designed and performed all the experiments. I performed the design, implementation, experiments and image analysis of the screening of compounds. I performed the image analysis of the microfluidic cultures under the supervision of Silvia Bolognin and Paul Antony. I did the statistical analysis, conceptualization and organization of all the elements in all the figures of the manuscript.

3.3.2 Manuscript

Impaired dopaminergic differentiation of Parkinson's disease derived neuroprecursor cells improved by 2-hydroxypropyl-β-cyclodextrin treatment

Javier Jarazo [1], Lisa Smits [1], Eligio Ianetti [4,5], Jonathan Arias-Fuenzalida [1], Jonas Walter [1], Gemma Gomez-Giro [1,6], Xiaobing Qing [1], Christian Jäger [3], Zdenka Hodak [3], Philip Seibler [7], Aleksandar Rakovic [7], Emmanuel Berger [1], Silvia Bolognin [1], Julien Beyrath [5], Paul Antony [2], Christine Klein [7], Jens C. Schwamborn [1,8]

[1] Developmental and Cellular Biology, Luxembourg Centre for Systems Biomedicine, University of Luxembourg, 6 Avenue du Swing, 4367, Belvaux, Luxembourg

[2] Experimental Neurobiology, Luxembourg Centre for Systems Biomedicine, University of Luxembourg, 6 Avenue du Swing, 4367, Belvaux, Luxembourg

[3] Enzymology and Metabolism, Luxembourg Centre for Systems Biomedicine, University of Luxembourg, 6 Avenue du Swing, 4367, Belvaux, Luxembourg

[4] Department of Biochemistry, Radboud Institute for Molecular Life Sciences, Nijmegen, the Netherlands

[5] Khondrion BV, Nijmegen, the Netherlands

[6] Max Planck Institute for Molecular Biomedicine, Laboratory of Cell and Developmental Biology, Roentgenstrasse 20, Münster, Germany

[7] Institute of Neurogenetics, University of Lübeck, D-23538, Lübeck, Germany

[8] Corresponding author: jens.schwamborn@uni.lu

Introductory paragraph

Parkinson's disease (PD) has an etiology not completely understood even though environmental causes, risk factors and specific point mutations have been identified as contributors to the onset of the disease[1-3]. Homozygous point mutations of PTEN-induced putative kinase 1 (PINK1), involved in mitochondrial homeostasis, vesicle trafficking and autophagy, are sufficient for triggering the disease at an early age[4-7]. Here we show that patient derived neuroprecursors cells have a different energetic profile and a modified mitochondrial network morphology concomitant with an imbalanced proliferation, apoptosis and differentiation efficiency in their transition to dopaminergic neurons. Mitophagy abnormalities during differentiation were detected in patient derived neurons related to the count and size of these events. Correcting the point mutation by gene editing was able to ameliorate the metabolic properties and neuronal firing rates but not completely the differentiation phenotype. 2-Hydroxypropyl-β-Cyclodextrin (HP-β-CD) is reported to modulate autophagy by increasing transcription factor EB (TFEB) expression[8,9]. Impaired dopaminergic differentiation of patient neurons was improved by treatment with HP-β-CD. Our findings suggest that TFEB modulation can reduce neuronal loss in the context of PD.

Main text

Neurodegenerative diseases pose a great threat to ageing populations, especially for those patients suffering PD that rely only in palliative treatments or surgical treatments [10,11]. Affected loci, reported as risk or causative factors of PD, are involved in controlling major cellular processes such as cell proliferation, membrane trafficking, mitochondria homeostasis and autophagy[12]. Individuals that present homozygous point mutations in PINK1 develop the disease at an early age denoting that an altered mitochondrial function, morphology and degradation are important processes in the pathogeny of PD[13-15].

One of the hallmarks of PD is the loss of dopaminergic neurons in the substantia nigra pars compacta, even though other regions have also been reported to be altered [16,17]. To evaluate if these impaired functions could altered the differentiation potential of dopaminergic neurons, hiPSCs derived from 3 patients carrying a mutation in PINK1 (2 carrying Q456X and 1 carrying I368N) and 3 control (age and gender matched) (Supplementary Fig.1a) were further differentiated into a neuroprecursor state (neuroepithelial stem cells, NESCs) as a starting point in their transition into dopaminergic neurons (Supplementary Fig.1b). An early time point of differentiation (14 days after initiation of differentiation) was selected for evaluating if patient cells present an impaired differentiation by using the dopaminergic marker tyrosine hydroxylase (TH) in

respect to a general neuronal marker (neuron-specific class III β-tubulin, Tuj1) (Fig. 1a). An automated image analysis algorithm (Supplementary Fig.2) was developed for segmenting and quantifying the proportion of voxels (tridimensional pixels) having a colocalization of TH and Tuj1, as well as for quantifying the nuclear volume. While having the same differentiation into neurons, patient derived NESCs have a reduced tendency of developing TH+ neurons (Fig. 1a). Since a higher nuclear volume measurement in patient's cells was also observed, serial time points (7, 14 and 21 days of differentiation) were used to complement this observation by adding the proliferation marker Ki67 and the apoptotic marker poly(ADP-ribose) polymerase (PARP) (Fig. 1c-g) (Supplementary Fig.3). Patient derived cells maintain their proliferative capacity after induction of differentiation through a longer period than control cells (Fig. 1e), this can be related to an impaired exit of the stem cell status while maintaining their proliferative capacity. In addition, an increase in PARP signal was observed in patient cells in the context of a TH+ neuron (Fig. 1g) pointing out that the reduce level of differentiation observed can be a combination of both factors, stem cells having a lower differentiation capacity into dopaminergic neurons and an increased apoptosis of them. To validate the impaired differentiation in a more similar to in vivo environment, we differentiated NESCs in a 3D context by using a microfluidic (Fig. 1h, i) observing the same pattern.

We next evaluated the mitochondrial network status due to the close relation between PINK1 function and mitochondrial homeostasis[5]. Morphological assessment of mitochondria was carried in different cell types (fibroblast, NESCs and neurons) (Fig.2 and Supplementary Fig. 4) and features denoting their volume, shape and degree of ramification were extracted with an automated algorithm for pattern recognition (Supplementary Fig. 5), allowing the evaluation of the fission/fusion status of the network. When evaluating fibroblast, the total mitochondrial volume as well as mitochondrion count per nuclei unit are significantly increased in case of the patients (Supplementary Fig. 4b). In the case of NESCs, the same thing is observed (Fig. 2b). More interestingly, the median size of the mitochondrion is higher in individuals carrying PINK1 mutations (Fig. 2b, top panel). Regarding the shape of the mitochondrial network, the reduced number of bottlenecks (evaluated by the number of mitochondrial bodies) in the case of the patients NESCs indicates the reduced tendency of the network to produce fission, in accordance with previous reports[18,19] (Fig. 2b, mid panel). On the contrary, control cells seem to have a more spherical than elongated network structure, while patient NESCs possess a reduced number of shorter ramifications (Fig. 2b, bottom panel). Upon differentiation into dopaminergic neurons, an automated pre-scan/re-scan strategy was developed for recognizing the areas with higher amount of TH+ cells for increased sampling during higher magnification

acquisitions for mitochondria morphology reconstruction (Supplementary Fig. 4c). Indistinctively of the TH+ region analyzed (perinuclear and neurites), the difference in median size switched (being control mitochondrion bigger) but patient mitochondrial network seems to be more fragmented due to an increased mitochondrion count and equal total mitochondria volume (Fig. 2c). Focusing only on the mitochondria located in the perinuclear area, we observed that in TH+ cells the median size of the mitochondrion was equal while the control cells have a higher count and total mitochondria area than patients (Fig. 2d) (Supplementary Fig. 4d). This differences are not observed in TH- cells (Fig. 2e). In both perinuclear areas control cells have a network more prone to fission (Fig. 2d, e). The mitochondrial network was also metabolically analyzed by extracellular flux analysis (Seahorse) (Fig. 2f and Supplementary Fig. 6a,b) indicating that the control lines have a higher basal respiration and ATP production from the electron transport chain (ETC) leading to significantly increased coupling efficiency (Fig. 2f), while patients' NESCs have a significantly higher glycolytic activity (Fig. 2g). These observations go in hand with the increased proliferation and the difficulty of patients derived NESCs of entering into a differentiation phase that requires a higher activity of the ETC rather than glycolysis for ATP production.

To further understand the mitochondrial dynamics in these cells we generated a stable patient (PINK1, I368N) and control lines expressing the Rosella construct bound to ATP synthase F1 subunit gamma (ATP5C1) to evaluate mitochondrial degradation by mitophagy[20] (Fig. 3). These cells were generated at the hiPSCs levels and further differentiated into NESCs and subsequently to neurons. Through serial measurements the dynamic changes of the mitophagy activity during the differentiation process were automatically analyzed (Supplementary Fig. 7) observing that the amount of mitophagy events in patients' neurons was significantly reduced but the mean area of the mitophagy event was bigger (Fig. 3b). This can be explained by a lag in fission in the transition between NESCs and neurons in the early stages. Events of mitophagy observed in patient's cells can be explained by reported PINK1/Parkin independent mitophagy pathways[21-23]. However, PINK1 mutation influence in the mitophagy capacity here described, highlights the importance of an active PINK1 mitochondrial quality control, especially during the functional and morphological changes occurring during neuronal development.

Given the altered mitochondria morphology and activity, and the impaired mitophagy capacity in patient cells, we decided to evaluate the influence of gene correcting the PINK1 mutation as well as the treatment with compounds known to modify the expression of TFEB in the phenotypes observed. Using FACS assisted CRIPSR/Cas9 editing (FACE)[24] (Supplementary Fig. 8), homozygous correction of the PINK1

mutation was able to improve the metabolic shift and the impaired mitochondrial activity observed in patient cells (Fig. 4a, b). Microelectrode array (MEA) measurements showed that the reduced firing activity and the network burst firing observed in patients is increased by the gene correction (Fig. 4c,d and Supplementary Fig. 6c). These two features show that correction of the PINK1 mutation, induced positive metabolic changes for meeting the ATP demand necessary to switch from stem cells (complemented with the observation of a reduced proliferation upon differentiation, assessed by a reduction in the nuclear area) to differentiated cells[25,26]. Restoration of the mitochondrial activity increased the overall neuronal differentiation and dopaminergic differentiation per nuclear voxel but it was not sufficient for significantly changing the levels of dopaminergic neurons in the entire neuronal population (TH+ per Tuj1 voxel not significant) (Fig. 4e). Treatment with HP-β-CD known to increase TFEB expression was able to increase the proportion of TH+ voxel over the total neuronal volume (Fig. 4g). This increased was observed with a rise in the number of mitophagy events as well as with an increase in the total volume of mitophagy (Fig. 4f). To assess the effectiveness of HP-β-CD in the context of another PD causing mutation, hiPSCs reprogrammed fibroblast from patient carrying an homozygous Parkin mutation (R275W) were further differentiated into NESCs and neurons, observing also a significant increase in dopaminergic neurons (Fig. 4h). We further determine the specific finger print of the HP-β-CD mixture used (Supplementary Fig. 9), highlighting the importance of characterizing the complex composition of cyclodextrins for guaranteeing its efficacy in future clinical trials and for comparing treatment results between different neurodegenerative diseases[27].

These data suggest that a loss of function mutation in PINK1[28,29], normally involved in regulating mitochondria function and morphology by quarantining damaged mitochondria before their degradation as well as triggering the process of mitophagy, is relevant in the metabolic switch needed for the transition between a neuroprecursor state and a differentiated neuron. An altered mitochondria turnover, due to an imbalanced fission/fusion status of the network unable to separate the altered part of the mitochondria that needs to be degraded, and due to a reduced mitophagy activity during differentiation, was also observed in patient cells matching what was proposed by previous reports[19,30-32]. A pre-mitophagy process recently described involves the formation of a structure called mitochondria derived vesicles (MDVs)[33,34]. These structures have an average size that ranges from 70-150nm and they transport small portions of altered mitochondria membrane directly to the lysosome or peroxisome depending on their content and they rely on the activity of PINK1[35]. One can presume that since this mechanism might not be functioning properly in patient lines, circumscribed regions of an altered mitochondrion are not cleared in time reaching a point when

a larger portion of the mitochondrial network needs to be degraded, explaining the increased size of the mitophagy events in the case of the patients (Fig. 3b).

These phenomena occurred simultaneously with an altered dopaminergic differentiation efficiency in patient cells. Gene correction of the point mutation allowed neuroprecursor cells to change their metabolic profile switching from glycolysis to oxidative phosphorylation, and the neuronal firing activity, yet the efficiency of dopaminergic differentiation did not change, implying that the patients' genetic background[36,37] or acquired mtDNA mutations[38] might also play a role. Treatments using repurposed drugs known to increase TFEB expression, are currently on clinical trials for treating neurodegenerative diseases like Niemman Pick disease (NPD, with HP-β-CD, NCT02534844) and PD (with Ambroxol, NCT02941822). This work provides an example of a TFEB activator rescuing the dopaminergic neuronal loss phenotype observed in the context of PD causative mutations, reinforcing the importance of modulating the autophagy/lysosomal pathway for potentially treating neurodegenerative diseases. Additionally, it emphasizes the need for identifying common altered pathways since different starting points (e.g. the inability of produce subunit C for cholesterol processing in NPD type C or the increase overflow of damaged mitochondria due to an altered surveillance by PINK/Parkin in PD) might face the same roadblock in the end, facilitating the transference of working compounds between neurodegenerative diseases.

Acknowledgements

We thank Prof. Dr. Hans R. Schöler of the Max Planck Institute, Dr. Jared Sterneckert of the CRTD, Prof. Dr. Thomas Gasser of the Hertie Institute in Tübingen, William Skarnes of the Jackson Laboratory and the Coriell Institute for providing cell lines. We would like to thank Prof. T. Graham and A. Sargsyan from the University of Utah for kindly providing us with the Rosella construct. Acquisition of flow cytometry data was supported by the flow cytometry core of the LCSB bio-imaging platform. This project was funded by the Fonds National de la Recherche (FNR) Luxembourg (CORE, C13/BM/5791363). This is an EU Joint Program - Neurodegenerative Disease Research (JPND) project (INTER/JPND/14/02; INTER/JPND/15/11092422). This project is also supported by the European Union's Horizon 2020 research and innovation programme under grant agreement No 668738, SysMedPD. J.J. is supported by a Pelican award from the Fondation du Pelican de Mie et Pierre Hippert-Faber. J.J., L.S., J.W. and X.Q. were supported by FNR Aides à la

Formation-Recherche (AFR). G.GG. was funded by the NCL-Stiftung (Hamburg, Germany). Finally, we also thank the private donors who support our work at the Luxembourg Centre for Systems Biomedicine.

Author contributions

J.J. and J.C.S. designed the study. J.J., L.S., E.I., J.A.F., J.W., G.G.G., X.Q., C.J., Z.H., P.S., A.R., E.B., S.B. and P.A. established methodology. J.J., L.S., E.I., J.A.F., J.W., G.G.G., X.Q., C.J., Z.H., P.S., A.R., S.B. and P.A. performed experiments. J.B. and C.K. supervised J.J. made the final figures and wrote the manuscript. J.C.S. conceived and supervised the study.

Figure legends

Figure 1

Differentiation impairment in PD patient derived dopaminergic neurons. (**a**) Median representative images of a 14 day differentiation neuronal culture of controls and patients groups. In the upper panel of each group, raw images of the markers TH, Tuj1 and Hoechst are presented and in the lower panel the raw channel with its respective perimeter mask (scale bar = 100µm). (**b**) Quantification of the markers TH, Tuj1 and Hoechst in a 14 day differentiation neuronal culture with their respective ratios. Each dot represents one field analysed over three replicates (n=3).1300 fields of controls (fc) and 1304 (fp) of patients were analysed. (**c**) Quantification of TH, Tuj1 and Hoechst at time points 7 (fc=219; fp=215), 14 (fc=209; fp=219) and 21 (fc=207; fp=220) after the induction of differentiation. Pixel quantification (lower panel) with their respective ratios (upper panel). (**d**) Median representative images of proliferation marker Ki67 and Hoechst of control and patient derived cells at day 7 of differentiation (scale bar = 50µm). (**e**) Quantification of Ki67 at time points 7 (fc=425; fp=421), 14 (fc=411; fp=424) and 21 (fc=416; fp=432) after the induction of differentiation, normalized to the nuclear area. (**f**) Representative images of apoptotic marker PARP, dopaminergic marker TH and Hoechst at day 14 of differentiation (scale bar = 50µm). (**g**) Quantification of PARP within TH area at time points 7 (fc=219; fp=215), 14 (fc=209; fp=219) and 21 (fc=207; fp=220) after the induction of differentiation, normalized to TH area. (**h**) Representative images of a 14 day differentiation neuronal culture in chip of an OrganoPlate stained for TH, Tuj1 and a nuclear marker (scale bar = 100µm). (**i**) Quantification of TH normalized to neuronal area. Each dot represents a chip in an OrganoPlate over three replicates. Statistical analysis was performed using a two sample Kolmogorov-Smirnov test. *P<0.05, **P <0.01, ***P <0.001; ns, not significant.

Figure 2

Mitochondrial morphometric and cellular metabolism are altered in patient derived cells. (**a**) Representative images of NESCs stained for Tom20 and Nuclei marker. In the upper two panels raw images are depicted, while in the lower panel the raw channel with its respective perimeter mask (scale bar = 20µm). (**b**) Quantification of the morphometric 3D analysis of NESCs mitochondria depicting properties of their volume, shape and degree of ramification. (fc=868; fp=738) (**c**) Quantification of the morphometric 3D analysis of mitochondria within TH+ neurons depicting properties of their volume and shape. (**d**) Quantification of the morphometric 3D analysis of mitochondria within the perinuclear area TH+ neurons depicting properties of their volume and shape. (**e**) Quantification of the morphometric 3D analysis of mitochondria within the perinuclear area TH- cells depicting properties of their volume and shape (for figures c-e, fc=675; fp=663). (**f**) Extracellular flux analysis (Seahorse) in NESCs for evaluating mitochondrial respiratory capacity and efficiency between control and patient derived cells. (**g**) Extracellular flux analysis (Seahorse) in NESCs for evaluating glycolytic activity. Statistical analysis was performed using a two sample Kolmogorov-Smirnov test. **P*<0.05, ***P* <0.01, ****P* <0.001; ns, not significant.

Figure 3

Mitophagy capacity in patient neurons is reduced. (**a**) Median representative images of neurons tagged with the Rosella construct for depicting mitophagy events at day 8 of differentiation showing the dsRed and pHluorin raw signal (with their corresponding masks) in the left and centre panel respectively, of both control and patient derived cells. A merged image of both channels is shown in the right panel (scale bar = 20µm). (**b**) Time series quantification of the mitophagy capacity during neuronal differentiation for 14 days. Different properties of mitochondria and mitophagy events were assessed. Measurements were performed once a day during the entire differentiation protocol. Each dot represents one field analysed over three replicates (n=3, fc=97-217 and fp=126-224 range measured per day for 14 days). Statistical analysis was performed using a non-parametric test for repeated measures in factorial design (nparLD). **P*<0.05, ***P* <0.01, ****P* <0.001, *****P* <0.0001; ns, not significant.

Figure 4

Gene correction and effects of HP-β-CD treatment on NESCs and differentiating neurons. (**a**) Extracellular flux analysis (Seahorse) in NESCs for evaluating mitochondrial respiratory capacity and efficiency between patient and gene corrected cells. (**b**) Extracellular flux analysis (Seahorse) in NESCs for evaluating glycolytic

activity between patient and gene corrected cells. (**c**) Evaluation of spontaneous neuronal firing by microelectrode measurements (MEA) represented by the mean firing rate, the number of spikes and burst of the neuronal network between patient and gene corrected cells during differentiation. (**d**) Representative raw data trace before and after addition of the voltage-dependent sodium channel blocker tetrodotoxin (TTX) showing that the traces observed were produced by firing neurons. (**e**) Quantification of the markers TH, Tuj1 and Hoechst in a 14 day differentiation neuronal culture with their respective ratios and comparison between patient, gene corrected and control derived neurons (fc=1868, field gene corrected =1169, fp=785). (**f**) Time series quantification and comparison of the mitophagy capacity during neuronal differentiation for 14 days between untreated and HP-β-CD treated patients' derived neurons. Different properties of mitochondria and mitophagy events were assessed. Measurements were performed once a day during the entire differentiation protocol. Each dot represents one field analysed over three replicates (n=3, fc=157-225 and fp=215-225 range measured per day for 14 days). Statistical analysis was performed using a non-parametric test for repeated measures in factorial design (nparLD). (**g** and **h**) Quantification of the markers TH, Tuj1 and Hoechst in a 14 day differentiation neuronal culture with their respective ratios and comparison between untreated and HP-β-CD treated PINK1 patients' derived neurons (g) (fp=1774; fp treated=895), and between untreated and HP-β-CD treated Parkin patients' derived neurons (fp=218; fp treated=215) (h). Except for (f), statistical analysis was performed using a two sample Kolmogorov-Smirnov test. **P*<0.05, ***P* <0.01, ****P* <0.001, *****P* <0.0001; ns, not significant.

References

1 Przedborski, S. The two-century journey of Parkinson disease research. *Nature Reviews Neuroscience* **18**, doi:10.1038/nrn.2017.25 (2017).
2 Farrer, M. Genetics of Parkinson disease: paradigm shifts and future prospects. *Nature Reviews Genetics* **7**, doi:10.1038/nrg1831 (2006).
3 Schapira, A. H. V. & Tolosa, E. Molecular and clinical prodrome of Parkinson disease: implications for treatment. *Nature Reviews Neurology* **6**, 309-317, doi:10.1038/nrneurol.2010.52 (2010).
4 Klein, C. & Westenberger, A. Genetics of Parkinson's Disease. *Cold Spring Harbor Perspectives in Medicine* **2**, doi:10.1101/cshperspect.a008888 (2012).
5 Pickrell, A. M. & Youle, R. J. The roles of PINK1, parkin, and mitochondrial fidelity in Parkinson's disease. *Neuron* **85**, 257-273, doi:10.1016/j.neuron.2014.12.007 (2015).
6 Yamano, K., Matsuda, N. & Tanaka, K. The ubiquitin signal and autophagy: an orchestrated dance leading to mitochondrial degradation. *EMBO reports* **17**, 300-316, doi:10.15252/embr.201541486 (2016).
7 Youle, R. J. & Narendra, D. P. Mechanisms of mitophagy. *Nature reviews. Molecular cell biology* **12**, 9-14, doi:10.1038/nrm3028 (2011).
8 Kilpatrick, K., Zeng, Y., Hancock, T. & Segatori, L. Genetic and Chemical Activation of TFEB Mediates Clearance of Aggregated α-Synuclein. *PLOS ONE* **10**, doi:10.1371/journal.pone.0120819 (2015).
9 Song, W., Wang, F., Lotfi, P., Sardiello, M. & Segatori, L. 2-Hydroxypropyl-β-cyclodextrin Promotes Transcription Factor EB-mediated Activation of Autophagy. *Journal of Biological Chemistry* **289**, 10211-10222, doi:10.1074/jbc.m113.506246 (2014).
10 Fahn, S. The medical treatment of Parkinson disease from James Parkinson to George Cotzias. *Movement Disorders* **30**, 4-18, doi:10.1002/mds.26102 (2015).

11 Lozano, C. S., Tam, J. & Lozano, A. M. The changing landscape of surgery for Parkinson's Disease. *Movement Disorders* **33**, 36-47, doi:10.1002/mds.27228 (2018).
12 Brás, J., Guerreiro, R. & Hardy, J. SnapShot: Genetics of Parkinson's Disease. *Cell* **160**, 570-5700, doi:10.1016/j.cell.2015.01.019 (2015).
13 Abou-Sleiman, P. M., Muqit, M. M. K. & Wood, N. W. Expanding insights of mitochondrial dysfunction in Parkinson's disease. *Nature Reviews Neuroscience* **7**, doi:10.1038/nrn1868 (2006).
14 Larsen, S. B., Hanss, Z. & Krüger, R. The genetic architecture of mitochondrial dysfunction in Parkinson's disease. *Cell and Tissue Research*, 1-17, doi:10.1007/s00441-017-2768-8 (2018).
15 Schapira, A. H. V. Mitochondrial dysfunction in Parkinson's disease. *Cell Death and Differentiation* **14**, 4402160, doi:10.1038/sj.cdd.4402160 (2007).
16 Goedert, M., Spillantini, M., Tredici, K. & Braak, H. 100 years of Lewy pathology. *Nature Reviews Neurology* **9**, 13-24, doi:10.1038/nrneurol.2012.242 (2012).
17 Poewe, W. *et al.* Parkinson disease. *Nature Reviews Disease Primers* **3**, doi:10.1038/nrdp.2017.13 (2017).
18 Deng, H., Dodson, M. W., Huang, H. & Guo, M. The Parkinson's disease genes pink1 and parkin promote mitochondrial fission and/or inhibit fusion in Drosophila. *Proceedings of the National Academy of Sciences* **105**, 14503-14508, doi:10.1073/pnas.0803998105 (2008).
19 Liu, W. *et al.* Pink1 regulates the oxidative phosphorylation machinery via mitochondrial fission. *Proceedings of the National Academy of Sciences* **108**, 12920-12924, doi:10.1073/pnas.1107332108 (2011).
20 Sargsyan, A. *et al.* Rapid parallel measurements of macroautophagy and mitophagy in mammalian cells using a single fluorescent biosensor. *Scientific Reports* **5**, 12397, doi:10.1038/srep12397 (2015).
21 Bhujabal, Z. *et al.* FKBP8 recruits LC3A to mediate Parkin-independent mitophagy. *EMBO reports* **18**, 947-961, doi:10.15252/embr.201643147 (2017).
22 Koentjoro, B., Park, J.-S. & Sue, C. M. Nix restores mitophagy and mitochondrial function to protect against PINK1/Parkin-related Parkinson's disease. *Scientific Reports* **7**, doi:10.1038/srep44373 (2017).
23 McWilliams, T. G. *et al.* Basal Mitophagy Occurs Independently of PINK1 in Mouse Tissues of High Metabolic Demand. *Cell Metabolism* **27**, 439-44900000, doi:10.1016/j.cmet.2017.12.008 (2018).
24 Arias-Fuenzalida, J. *et al.* FACS-Assisted CRISPR-Cas9 Genome Editing Facilitates Parkinson's Disease Modeling. *Stem Cell Reports* **9**, 1423-1431, doi:10.1016/j.stemcr.2017.08.026 (2017).
25 Ito, K. & Suda, T. Metabolic requirements for the maintenance of self-renewing stem cells. *Nature Reviews Molecular Cell Biology* **15**, doi:10.1038/nrm3772 (2014).
26 Zhang, J., Nuebel, E., Daley, G. Q., Koehler, C. M. & Teitell, M. A. Metabolic Regulation in Pluripotent Stem Cells during Reprogramming and Self-Renewal. *Cell Stem Cell* **11**, 589-595, doi:10.1016/j.stem.2012.10.005 (2012).
27 Yergey, A. L. *et al.* Characterization of hydroxypropyl-beta-cyclodextrins used in the treatment of Niemann-Pick Disease type C1. *PLOS ONE* **12**, doi:10.1371/journal.pone.0175478 (2017).
28 Grünewald, A. *et al.* Biological effects of the PINK1 c.1366C>T mutation: implications in Parkinson disease pathogenesis. *Neurogenetics* **8**, 103-109, doi:10.1007/s10048-006-0072-y (2007).
29 Seibler, P. *et al.* Mitochondrial Parkin recruitment is impaired in neurons derived from mutant PINK1 induced pluripotent stem cells. *The Journal of neuroscience : the official journal of the Society for Neuroscience* **31**, 5970-5976, doi:10.1523/JNEUROSCI.4441-10.2011 (2011).
30 Geisler, S. *et al.* The PINK1/Parkin-mediated mitophagy is compromised by PD-associated mutations. *Autophagy* **6**, 871-878, doi:10.4161/auto.6.7.13286 (2010).
31 Vincow, E. S. *et al.* The PINK1-Parkin pathway promotes both mitophagy and selective respiratory chain turnover in vivo. *Proceedings of the National Academy of Sciences of the United States of America* **110**, 6400-6405, doi:10.1073/pnas.1221132110 (2013).
32 Yang, Y. *et al.* Pink1 regulates mitochondrial dynamics through interaction with the fission/fusion machinery. *Proceedings of the National Academy of Sciences* **105**, 7070-7075, doi:10.1073/pnas.0711845105 (2008).
33 McLelland, G.-L., Lee, S. A., McBride, H. M. & Fon, E. A. Syntaxin-17 delivers PINK1/parkin-dependent mitochondrial vesicles to the endolysosomal system. *The Journal of Cell Biology* **214**, 275-291, doi:10.1083/jcb.201603105 (2016).
34 Soubannier, V. *et al.* A Vesicular Transport Pathway Shuttles Cargo from Mitochondria to Lysosomes. *Current Biology* **22**, 135-141, doi:10.1016/j.cub.2011.11.057 (2012).
35 Sugiura, A., McLelland, G.-L. L., Fon, E. A. & McBride, H. M. A new pathway for mitochondrial quality control: mitochondrial-derived vesicles. *The EMBO journal* **33**, 2142-2156, doi:10.15252/embj.201488104 (2014).

36 Momcilovic, O. *et al.* Derivation, Characterization, and Neural Differentiation of Integration-Free Induced Pluripotent Stem Cell Lines from Parkinson's Disease Patients Carrying SNCA, LRRK2, PARK2, and GBA Mutations. *PLOS ONE* **11**, doi:10.1371/journal.pone.0154890 (2016).
37 Soldner, F. *et al.* Generation of Isogenic Pluripotent Stem Cells Differing Exclusively at Two Early Onset Parkinson Point Mutations. *Cell* **146**, 318-331, doi:10.1016/j.cell.2011.06.019 (2011).
38 Dölle, C. *et al.* Defective mitochondrial DNA homeostasis in the substantia nigra in Parkinson disease. *Nature Communications* **7**, 13548, doi:10.1038/ncomms13548 (2016).

Supplementary methods

hiPSCs culture, NESCs derivation, neurons differentiation

Fibroblast derived from 3 control individuals and 4 PD patients were reprogrammed to hiPSCs as described in [1]. Human iPSCs were cultured in Matrigel (Corning, 354277) coated plates using Essential 8 (E8) medium (ThermoFisher, A1517001) under 5%CO2 in air mixture. Passages were performed using Accutase (Sigma, A6964) depending on confluency and plated in the same conditions supplemented overnight with 10μM ROCK inhibitor Y-27632 (MerckMilipore, 688000). Human NESCs were generated as described elsewhere [2]. Briefly, low density iPSCs colonies were treated with dispase (MerckMilipore, SCM133) for isolation and placed in a low addition plate. Cells were cultured in different media for 6 days as described in Supplementary Figure 1. Maintenance culture was performed with N2B27 media supplemented with 3μM CHIR-99021 (Axon Medchem, CT 99021), 0.75μM purmorphamine (PMA, Enzo Life Science, ALX-420-045-M005) and 150μM ascorbic acid (Sigma, A4544) as described in [3]. Neuronal differentiation was induced by culturing NESCs in N2B27 supplemented with 10 ng/ml hBDNF (Peprotech, 450-02), 10 ng/ml hGDNF (Peprotech, 450-10), 500 μM dbcAMP (Sigma, D0627), 200 μM ascorbic acid, 1 ng/ml TGF-β3 (Peprotech, 100-36E), and 1 μM PMA for 6 days. Afterwards, the same media without PMA was used for the duration of the correspondent experiment. Media changes during differentiation were done every third day. For imaging experiments, cells were seeded in a Cell Carrier Ultra (PerkinElmer, 6055300) 96 well plate. Depending on the assay performed, cell density used was 60000cells/well (Differentiation 14 days) or 30000cells/well (Differentiation staging, proliferation, apoptosis and mitochondria morphology). Experiments were carried out in three replicates (*n*=3). Human iPSCs with a passage number between 15 and 20 after colony picking from the reprogramming plate were used for generating hNESCs. Human NESCs with no more than 10 passages after characterization (at passage 5) were assayed or induced to further differentiate.

Immunocytochemistry

Fixation was done using 4% PFA in 1xPBS, pH 7.4, for 15min at RT. After 3x 1xPBS washing steps, cells were permeabilized using 0.5% Triton-X100 in 1xPBS for 15 min at RT. Blocking was performed by incubating cells in 5% Normal Goat Serum (ThermoFisher, 10000C), and 0.1% Tween20 in 1xPBS (blocking buffer) for 1 hour at RT. Incubation with the first antibodies was done overnight at 4°C in blocking buffer. Incubation with the secondary antibodies was done after 3x 1xPBS washing steps, for 2h at RT in blocking buffer with 1:1000 Hoechst33342. Cells were washed 3x with 1xPBS, covered with 1xPBS and imaged directly after.

Microfluidics culture

Neuroepithelial stem cells were seeded in an OrganoPlate (Mimetas, 9603-400-B) as explained elsewhere [4]. Briefly, a cell suspension in liquid Matrigel was prepared at a concentration of 20000 cells/μl of Matrigel. Cells were seeded with a repeating pipette with 1 μl of the solution per chip. The media perfusion was achieved by gravity, with an average fluid flow of 1.5μl/h [5]. For immunocytochemistry, cells were fixed with 4% PFA in 1xPBS, pH 7.4 overnight at 4°C and both antibodies incubation were kept overnight at 4°C .All the other steps were as described in the previous section.

Extracellular flux analysis (SeaHorse measurements)

Human NESCs were seeded in a Matrigel coated XF 96-well plate (Agilent, 102416-100) at a density of 65000 cells per well. Cells were incubated in a normal incubator for 6h for attachment. Media was removed and washed 2x using Assay medium consisting of 1mM Pyruvate (ThermoFisher, 11360-039), 21.25 mM D+glucose (Sigma, G8270), 2mM glutamax (ThermoFisher, 35050061) in DMEM (Sigma, D5030), at 37°C, pH 7.4. For equilibrating the plate, cells were left in assay medium at 37°C in air for 1 hour before running the assay in a Seahorse XFe96 Analyser according to manufacturer instructions. Concentrations of compounds after the injection were 1µM oligomycin (Sigma, 75351), 1µM FCCP (Sigma, C2920), 1µM antimycin A (Sigma, A8674) and 1µM rotenone (Sigma, R8875). Three baseline measures and three measurements after each compound injection were performed. For normalization, DNA was quantified using CyQUANT kit (ThermoFisher, C7026) and absorbance was measured in a Cytation 5 plate reader (BioTek) at 480/52.

MEA measurements

The Maestro microelectrode array (MEA, Axion BioSystems) system was used to measure spontaneous activity of dopaminergic neurons. 96-well MEA plates were pre-coated with 0.1 mg/ml poly-D-lysine hydrobromide (Sigma, P7886) in 0.1 M borate buffer (Sigma, T9525) for 1h at RT. 1*10^5 hNESCs were placed onto each array in a Matrigel droplet and incubated for 1 h at 37 °C before adding culturing media. Cells were recorded during the course of dopaminergic differentiation at a sampling rate of 12.5 kHz for 10 min at 37 °C. Axion Integrated Studio (AxIS 2.1) was used to process the raw data as previously described [3]. Using Axion Integrated Studio (AxIS 2.1), a Butterworth band pass filter with 200-3000 Hz cut-off frequency and a threshold of 6 x SD were set to minimize both false-positives and missed detections. The Neural Metric Tool (Axion BioSystems) was used to analyse the spike raster plots. Electrodes with an average of ≥5 spikes/min were defined as active. The spike count files generated from the recordings were used to calculate the number of spikes/active electrode/measurement. For the pharmacological treatment (n=3) neurons were treated with Tetrodotoxin (TTX, Cayman Chemical, 14964, 1 µM) for blocking and hence verifying the neuronal activity. The spike count files generated from the recordings were used to calculate the number of spikes/active electrode.

Rosella mitophagy reporter

The pH sensor fluorescent protein pHluorin was fused to DsRed and the entire open reading frame of the mitochondrial sequence of ATP5C1 as described in [6]. The entire cassette was introduced into the AAVS1 safe-harbour locus as previously described using the targeting donor (Addgene 22075) and TALE nucleases (Addgene 35431 and 35432) as described in [7]. Human iPSCs were electroporated with a Lonza 4D nucleofector system subunit X (Lonza, AAF-1002X) according to manufacturer instructions, using a P3 primary cells kit (Lonza, V4XP-3024) and pulse CB-150.

Gene editing

Gene correction of patient's point mutation was performed as previously described [8]. Briefly, for designing the gRNAs targeting sequence for PINK1e7 456 candidates were selected in silico (https://portals.broadinstitute.org/gpp/public/analysis-tools/sgrna-design) and inserted into pX330 vector (Addgene 42230) as described in [9]. Donor constructs were assembled by introducing the correspondent

homology arms into donor scaffold containing a positive selection module (PSM) and either EGFP or dTomato (PSM-EGFP and PSM-dTomato) and a blue florescence in the backbone of the plasmid for detecting random integrations (tagBFP), using Gibson assembly. After sorting of yellow colonies in BD FACS ARIA III, removal of the positive selection module (PSM) was performed by transfecting transposase piggyBac excision only mRNA with Stemfect RNA transfection kit (Stemgent, 00-0069) following manufacturer's protocol. Cell sorting was performed again for isolating cells with a proper removal of the PSM.

Compound treatment

Evaluation of the compound treatment was performed using Cell Carrier Ultra plates seeding NESCs at a density of 30000 cells/well. 2-Hydroxypropyl-β-Cyclodextrin (HP-β-CD, Sigma, H-107) was added and on every media change at a concentration of 100nM and kept in culture throughout the entire differentiation process.

Image acquisition

Cell carrier Ultra plates were imaged in an automated manner using an OPERA QEHS spinning disk microscope (PerkinElmer). Depending on the experiment images were acquired with a 10x air objective (for pre-scan and Differentiation efficiency) or 20x water immersion objective (for apoptosis, proliferation and microfluidics) or a 63x water immersion objective (mitochondria morphology and mitophagy). Imaging of live cells (mitophagy assessment) was performed under normal incubation conditions (37°C, 80% humidity and 5% CO2 in air). Both fluorescence (pHluorin and DsRed) were acquired at the same time using two cameras using bandpass filters (520/35 and 600/40 respectively). For 3D evaluation Z stacks were performed with an interval of 3.2 µm (acquisition of the entire height of the microfluidic chip) or 400nm for the images acquired with the 63x objective.

Image analysis

The flow of the algorithm designed, threshold values used and representative images of the image processing (MatLab, The MatWorks Inc.) are described in Supplementary Figures 6 to 9. Mitochondria morphology analysis was performed as described in [10] using the skeletonization tool and graphical representation from [11].

Mass Spectrometry

Ion mobility - MS experiments were performed using an Agilent 6560 Ion Mobility – QTOF MS equipped with an Dual Agilent Jet Stream ESI source (Agilent Technologies). First, three stock solutions of 2-Hydroxpropyl-ß-cyclodextrin (c = 1 mg/mL, Sigma, H107) were prepared in 1M ammonium hydroxide solution. Then, samples were diluted in 50:50 (v/v) ACN:H2O+0.1% formic acid to a final concentration of 10 µg/mL. Samples were directly infused into the ion source for 2 min using a flow rate of 200 µL/min. Nitrogen was used as drying gas at a temperature of 300 °C, a drying gas flow of 5 L/min, a sheath gas temperature of 350 °C, and a sheath gas flow rate of 11 L/min. The nebulizer gas pressure was set to 35 psig, the MS capillary voltage was 3.5 kV, the nozzle voltage was 1 kV, and the fragmentor was set to 400 V. Data was acquired in a mass range from m/z 100 to 3200. The Instrument was operated in IM-QTOF mode and tuned in high resolution mode (slicer position: 5) and Extended Dynamic Range (2GHz). Ions were trapped for 20,000 µs and

released every 60 ms with a trap release time of 150 µs. The drift tube was operated with an absolute entrance voltage of 1700 V and an exit voltage of 250 V with a drift tube pressure of 3.94 Torr and a temperature of 31 °C using nitrogen as the collision gas. The acquisition settings were adjusted to yield 32 ion mobility transients/frame corresponding to 0.5 frames/sec. External mass calibration as well as SingleFieldCalibration was performed before measurement of each set of samples and according to the manufacture instructions. All data were acquired with Agilent Mass Hunter LC/MS Data Acquisition (ver B.08.00) and analysed with Agilent Mass Hunter IM-MS Browser (ver B.08.00), where all acquisition frames were extracted from a total time frame of approx. 1.8 min.

Statistical Analysis and graphical representation

Statistical analysis performed on each assay is mentioned on each figure legend. All the statistical analysis were performed in R. When residuals of the data were not normally distributed after QQplot evaluation, non-parametric analysis were performed using Kruskal-Wallis (KW) test. If the assumption of identical distributions (same shape) of non-normally distributed was not fulfilled for performing a KW test, a two-sample Kolmogorov-Smirnov (KS) test was used to evaluate if the samples were drawn from significantly different distributed populations between control and patient lines. For the repeated measures studies done with the lines tagged with the Rosella construct, a non-parametric test for repeated measures in factorial design was performed using the R package nparLD with an F1.LD.F1 design [12]. Adjustment of the p-value for multiple tests was performed using Benjamini-Hochberg. Horizontal lines in dot plots, violin plots and box plots represent the median. Vertical lines in dot plots, violin plots and line plot, and hinges of the box plots represent the first and third quantile (the 25th and 75th percentiles). Whiskers of the box plots extend to 1.5*Inter-quantile range from the hinges. A dot in a dot plot represents a field of a well, except for the microfluidic experiment where each dot represents an entire chip. Significance asterisks represent: $P<0.05$ *, $P<0.01$ **, $P<0.001$ ***; ns stands for not significant.

Supplementary figures legends

Supplementary Figure 1

(A) Table summarizing the lines used in the article. (B) Time line and procedure for the generation of the lines and quality controls performed in the lines used. hiPSCs characterization scale bar = 100µm. hNESCs characterization scale bar = 500µm. Differentiation evaluation scale bar = 100µm.

Supplementary Figure 2

(A) Flowchart depicting the algorithm developed for image analysis of the differentiation cultures, with the different steps as well as threshold used. (B) Representative images of the stepwise segmentation and the final masks.

Supplementary Figure 3

(A) Flowchart depicting the algorithm developed for image analysis of the proliferation and apoptosis experiments, with the different steps as well as threshold used. (B) Representative images of the stepwise segmentation and the final masks.

Supplementary Figure 4

(A) Representative raw images of fibroblast stained for the mitochondrial marker Tom20 and a Nuclei marker with their respective masks. (B) Quantification of the morphometric 2D analysis of fibroblast mitochondria depicting properties of their volume and shape. (C) Pre-scan image performed at 10x with a bounding box representing the automatically selected area with a high level of TH+ somas at day 14 of differentiation. Zoom of the selected bounding box. Automatic re-scan performed at 60x in the preselected area. (D) Pre-scan/Re-scan selected area of 14 day differentiated neuronal culture. Raw images and correspondent perimeter masks are shown. Statistical analysis was performed using a two sample Kolmogorov-Smirnov test. **P*<0.05, ***P* <0.01, ****P* <0.001; ns, not significant.

Supplementary Figure 5

(A) Flowchart depicting the algorithm developed for image analysis of the 3D mitochondria morphology reconstruction, with the different steps as well as threshold used. (B) Representative images of the stepwise segmentation and the final masks.

Supplementary Figure 6

(A) Representative scheme of the mitochondrial stress test profile for mitochondrial respiration and the areas used for the calculations obtained from the extracellular flux analysis. (B) Representative oxygen consumption rates during the mitochondrial stress test. (C) Spike raster plots for single electrodes before and after treatment with the voltage-dependent sodium channel blocker tetrodotoxin (TTX).

Supplementary Figure 7

(A) Flowchart depicting the algorithm developed for image analysis of the mitophagy assay, with the different steps as well as threshold used. (B) Representative images of the stepwise segmentation and the final masks.

Supplementary Figure 8

(A) Representative images of hiPSCs colonies expressing the different possible outcomes of gene modification as described in [8]. Scale bar = 500 µm. (B) A one-well plate screened for detecting correct biallelic targeting (dTomato+/EGFP+/BFP-). Bounding box shows selected isolated region. Scale bar = 2cm. (C) Graph representing a proper biallelic modification with the positive selection cassette within the targeted genomic region. (D) Single cell isolation gating strategy performed, plus exclusion of BFP+ cells from an expanded culture derived from the selected region in (B). (E) First (upper panel) and second (lower panel) purity sort for purifying dTomato+/EGFP+/BFP- cells. (F) Removal of the positive selection module after treatment with transposase. (G) First sort after transposase induction (top left panel). Last purity sort before sequencing (n=3) (top right panel and bottom panels). (H) Sequencing results of the gene correction of the patient line.

Supplementary Figure 9

(A) Ion mobility heatmap of HP-β-CD (B) Mass spectra of the HP-β-CD mixture showing the different degrees of substitution. (C) Relative intensity showing the different proportions of the degrees of substitution in the HP-β-CD mixture.

References

1 Warlich, E. *et al.* Lentiviral vector design and imaging approaches to visualize the early stages of cellular reprogramming. *Molecular therapy : the journal of the American Society of Gene Therapy* **19**, 782-789, doi:10.1038/mt.2010.314 (2011).

2 Reinhardt, P. *et al.* Derivation and Expansion Using Only Small Molecules of Human Neural Progenitors for Neurodegenerative Disease Modeling. *PLoS ONE* **8**, doi:10.1371/journal.pone.0059252 (2013).

3 Monzel, A. S. *et al.* Derivation of Human Midbrain-Specific Organoids from Neuroepithelial Stem Cells. *Stem Cell Reports* **8**, 1144-1154, doi:10.1016/j.stemcr.2017.03.010 (2017).

4 Moreno, E. *et al.* Differentiation of neuroepithelial stem cells into functional dopaminergic neurons in 3D microfluidic cell culture. *Lab on a Chip* **15**, 2419-2428, doi:10.1039/C5LC00180C (2015).

5 Trietsch, S. J., Israëls, G. D., Joore, J., Hankemeier, T. & Vulto, P. Microfluidic titer plate for stratified 3D cell culture. *Lab on a Chip* **13**, 3548-3554, doi:10.1039/C3LC50210D (2013).

6 Sargsyan, A. *et al.* Rapid parallel measurements of macroautophagy and mitophagy in mammalian cells using a single fluorescent biosensor. *Scientific Reports* **5**, 12397, doi:10.1038/srep12397 (2015).

7 Hockemeyer, D. *et al.* Efficient targeting of expressed and silent genes in human ESCs and iPSCs using zinc-finger nucleases. *Nature biotechnology* **27**, 851 (2009).

8 Arias-Fuenzalida, J. *et al.* FACS-Assisted CRISPR-Cas9 Genome Editing Facilitates Parkinson's Disease Modeling. *Stem Cell Reports* **9**, 1423-1431, doi:10.1016/j.stemcr.2017.08.026 (2017).

9 Ran, A. F. *et al.* Genome engineering using the CRISPR-Cas9 system. *Nature Protocols* **8**, 2281-2308, doi:10.1038/nprot.2013.143 (2013).

10 Baumuratov, A. S. *et al.* Enteric neurons from Parkinson's disease patients display ex vivo aberrations in mitochondrial structure. *Scientific Reports* **6**, 33117, doi:10.1038/srep33117 (2016).

11 Kerschnitzki, M. *et al.* Architecture of the osteocyte network correlates with bone material quality. *Journal of Bone and Mineral Research* **28**, 1837-1845, doi:10.1002/jbmr.1927 (2013).

12 Noguchi, K., Gel, Y. R., Brunner, E. & Konietschke, F. nparLD: AnRSoftware Package for the Nonparametric Analysis of Longitudinal Data in Factorial Experiments. *Journal of Statistical Software* **50**, doi:10.18637/jss.v050.i12 (2012).

3.3.3 Figures

Figure 1

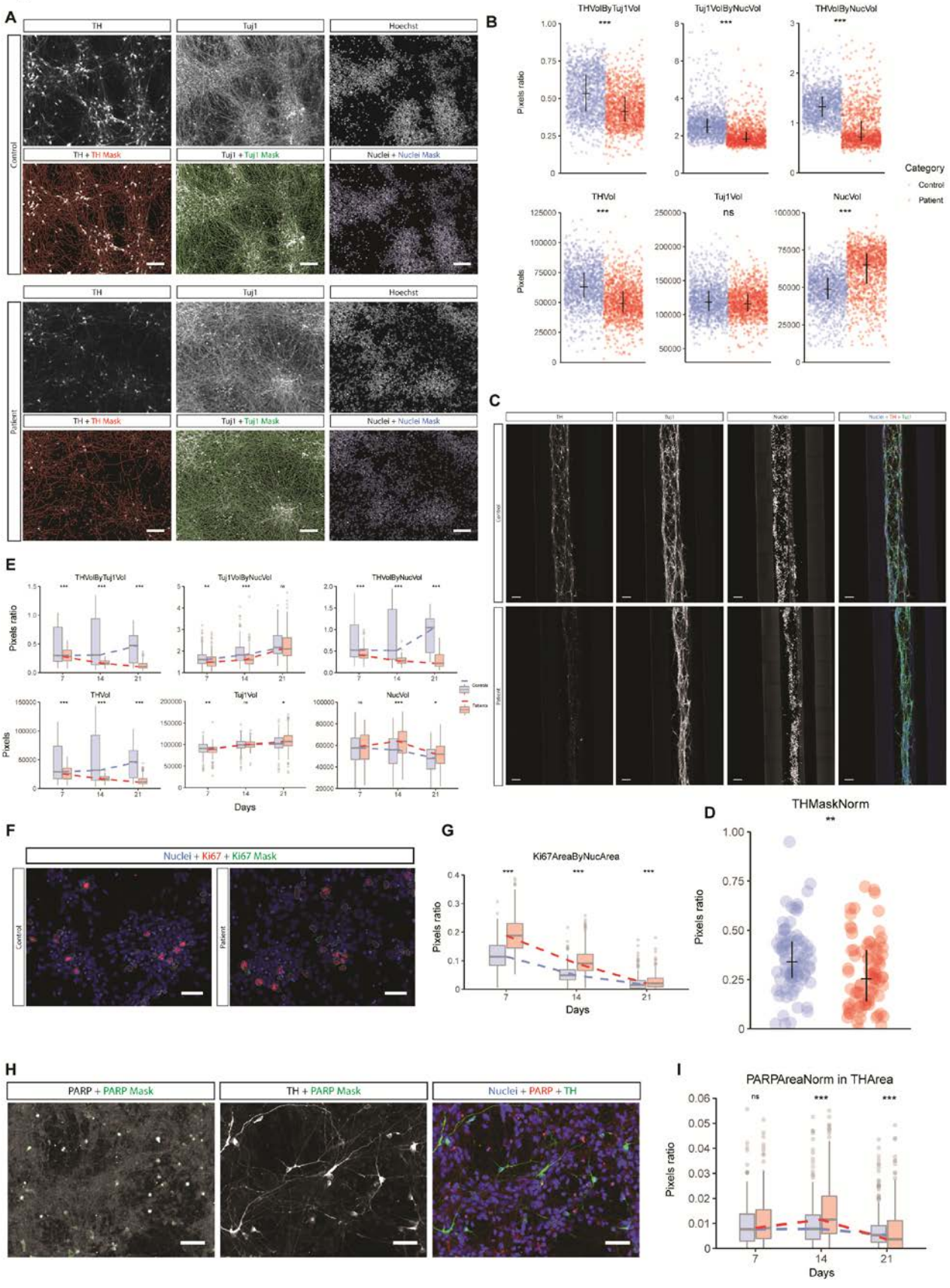

Figure 2

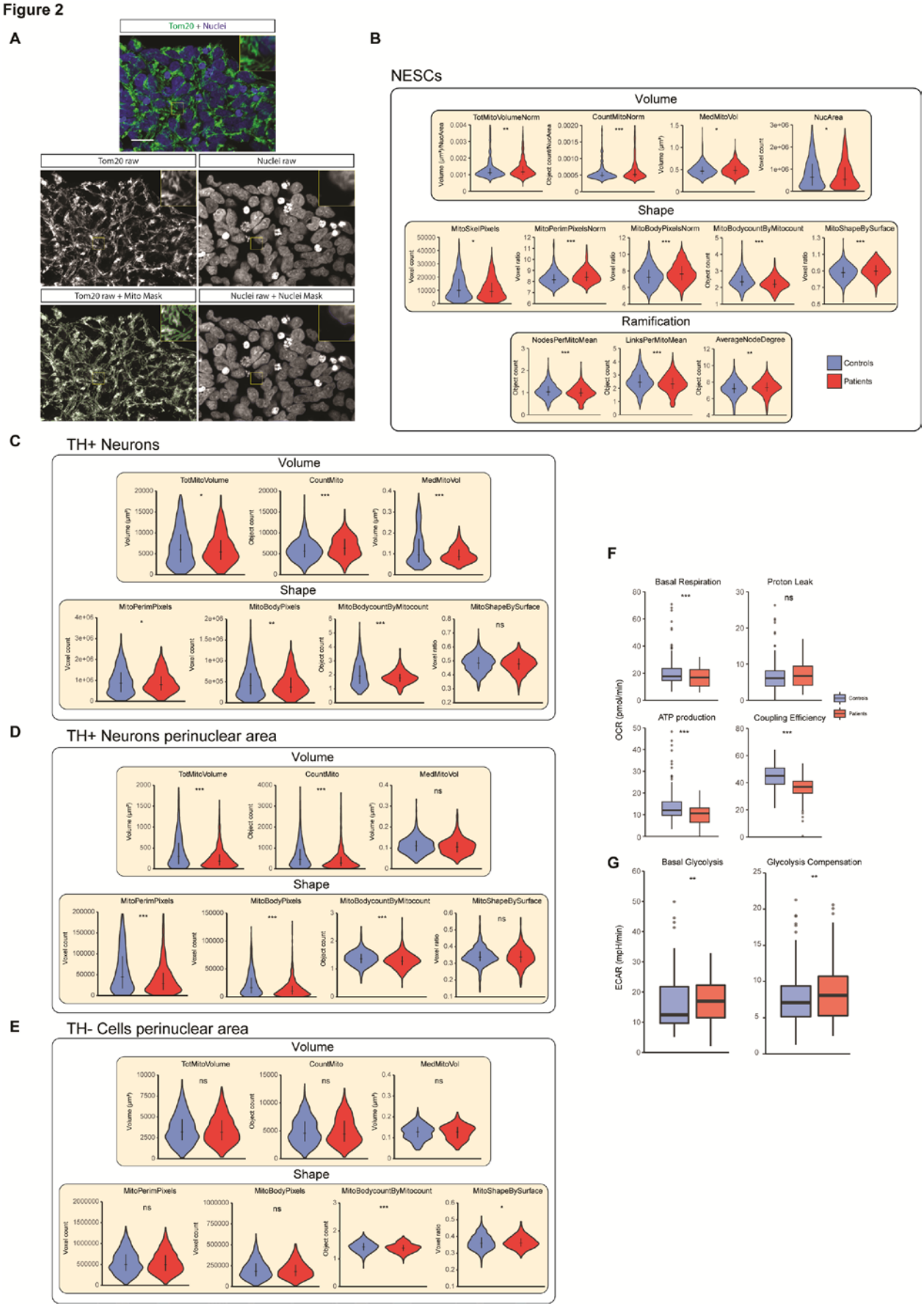
A
Tom20 + Nuclei
Tom20 raw
Nuclei raw
Tom20 raw + Mito Mask
Nuclei raw + Nuclei Mask
B
NESCs
Volume
TotMitoVolumeNorm
CountMitoNorm
MedMitoVol
NucArea
Shape
MitoSkelPixels
MitoPerimPixelsNorm
MitoBodyPixelsNorm
MitoBodycountByMitocount
MitoShapeBySurface
Ramification
NodesPerMitoMean
LinksPerMitoMean
AverageNodeDegree
Controls
Patients
C
TH+ Neurons
Volume
TotMitoVolume
CountMito
MedMitoVol
Shape
MitoPerimPixels
MitoBodyPixels
MitoBodycountByMitocount
MitoShapeBySurface
D
TH+ Neurons perinuclear area
E
TH- Cells perinuclear area
F
Basal Respiration
Proton Leak
ATP production
Coupling Efficiency
OCR (pmol/min)
G
Basal Glycolysis
Glycolysis Compensation
ECAR (mpH/min)

Figure 3

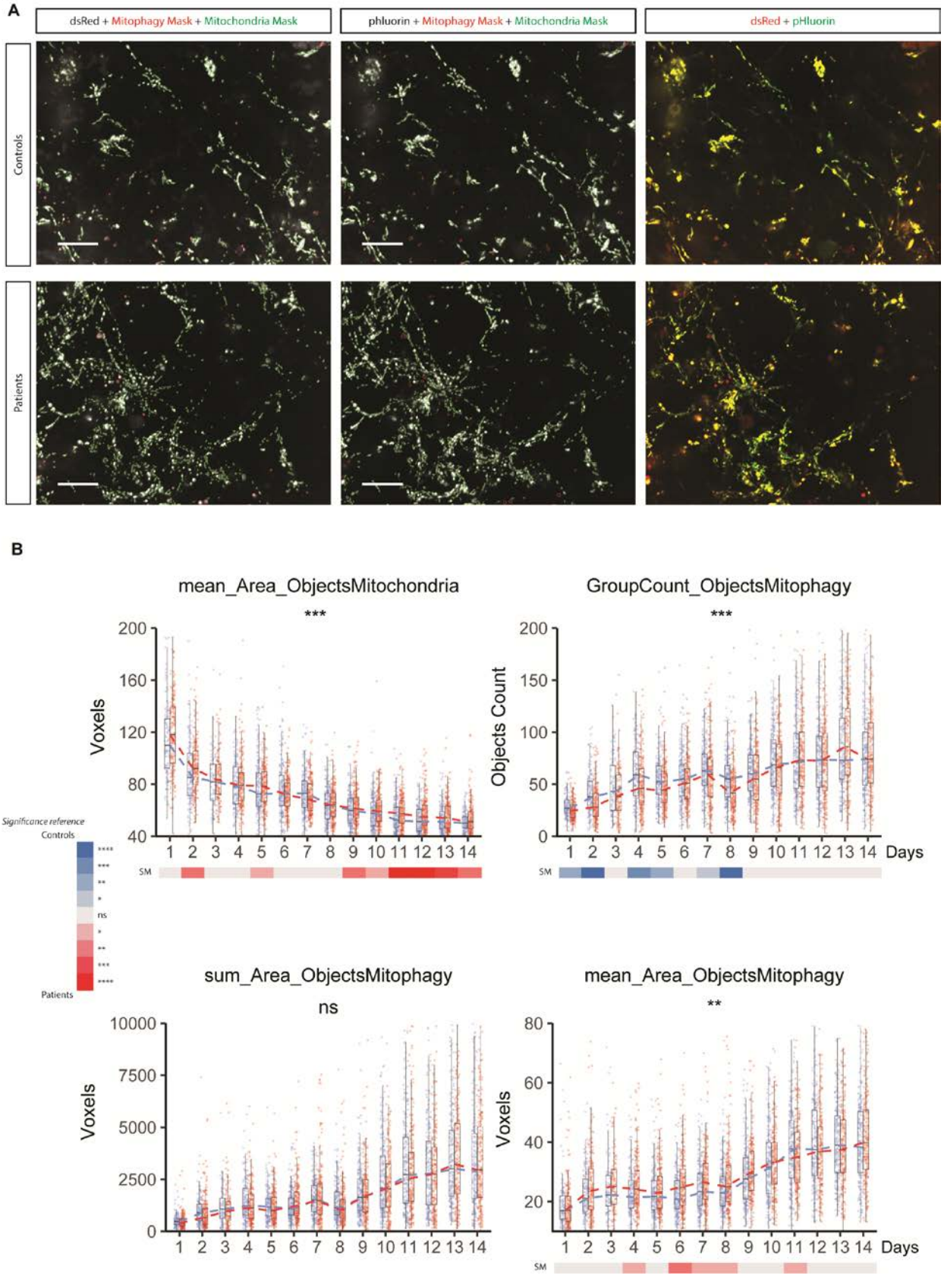
A
dsRed + Mitophagy Mask + Mitochondria Mask
phluorin + Mitophagy Mask + Mitochondria Mask
dsRed + pHluorin
Controls
Patients
B
mean_Area_ObjectsMitochondria
***
Voxels
GroupCount_ObjectsMitophagy
***
Objects Count
Days
Significance reference
Controls
Patients
sum_Area_ObjectsMitophagy
ns
Voxels
mean_Area_ObjectsMitophagy
**
Voxels
Days
SM

Figure 4

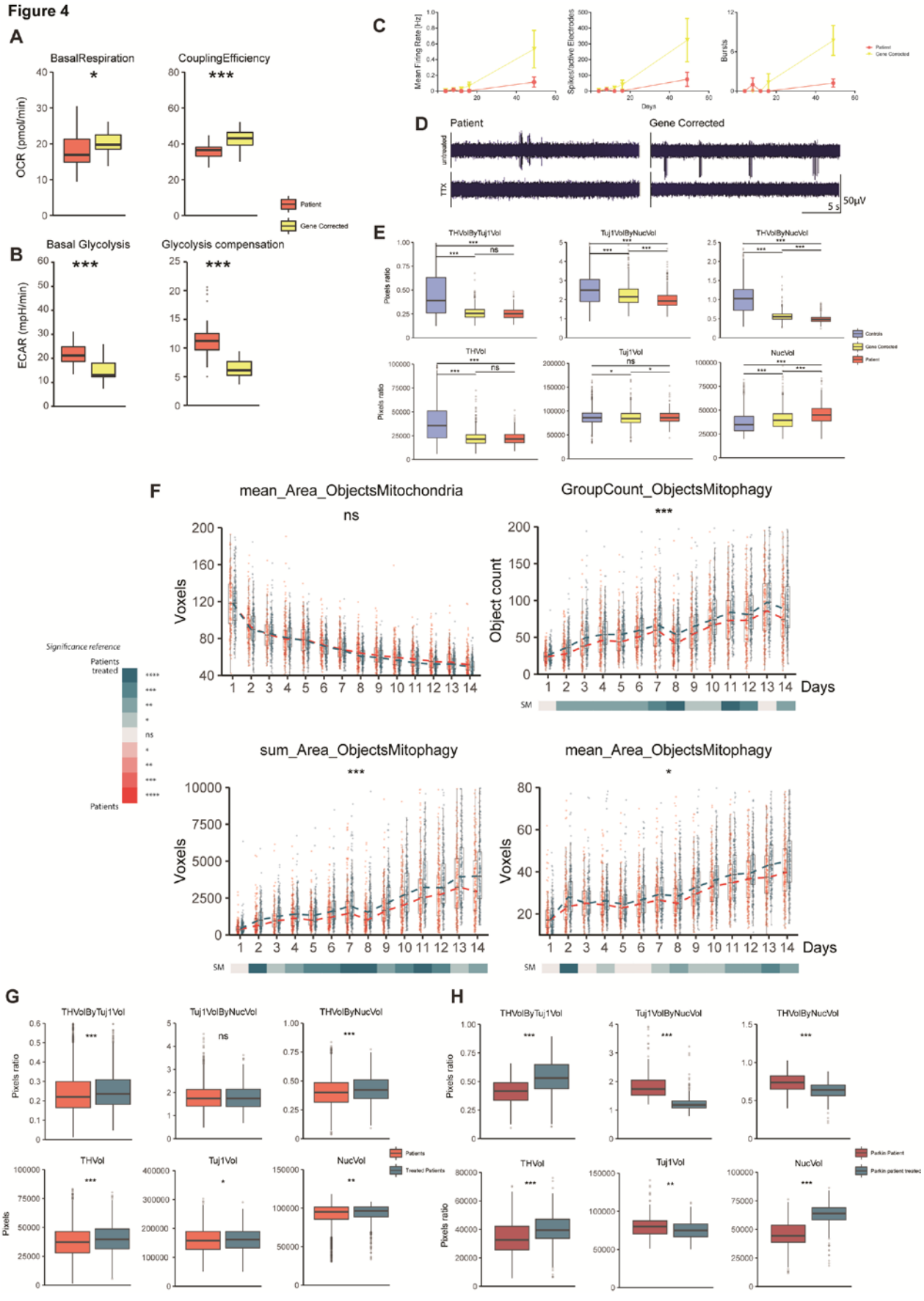
A
BasalRespiration
CouplingEfficiency
OCR (pmol/min)
Patient
Gene Corrected
B
Basal Glycolysis
Glycolysis compensation
ECAR (mpH/min)
C
Mean Firing Rate [Hz]
Spikes/active Electrodes
Bursts
Days
D
Patient
Gene Corrected
untreated
TTX
50µV
5 s
E
THVolByTuj1Vol
Tuj1VolByNucVol
THVolByNucVol
Pixels ratio
THVol
Tuj1Vol
NucVol
Controls
Gene Corrected
Patient
F
mean_Area_ObjectsMitochondria
GroupCount_ObjectsMitophagy
sum_Area_ObjectsMitophagy
mean_Area_ObjectsMitophagy
Voxels
Object count
Days
SM
Significance reference
Patients treated
Patients
G
H
Pixels ratio
Pixels
Patients
Treated Patients
Parkin Patient
Parkin patient treated

Supplementary Fig. 1

A

	Mutation	Gender	Age onset	Age sampling	Source
Healthy control 1	-	♀	-	81	Reinhardt et al., 2013
Healthy control 2	-	♀	-	53	Reinhardt et al., 2013
Healthy control 3	-	♂	-	59	W. Skarnes
Patient PINK1 1	Q456X	♀	61	69	C. Klein
Patient PINK1 2	Q456X	♀	53	61	C. Klein
Patient PINK1 3	I368N	♂	33	64	Coriell
Patient Parkin	R275W	♀	43	61	Coriell

B

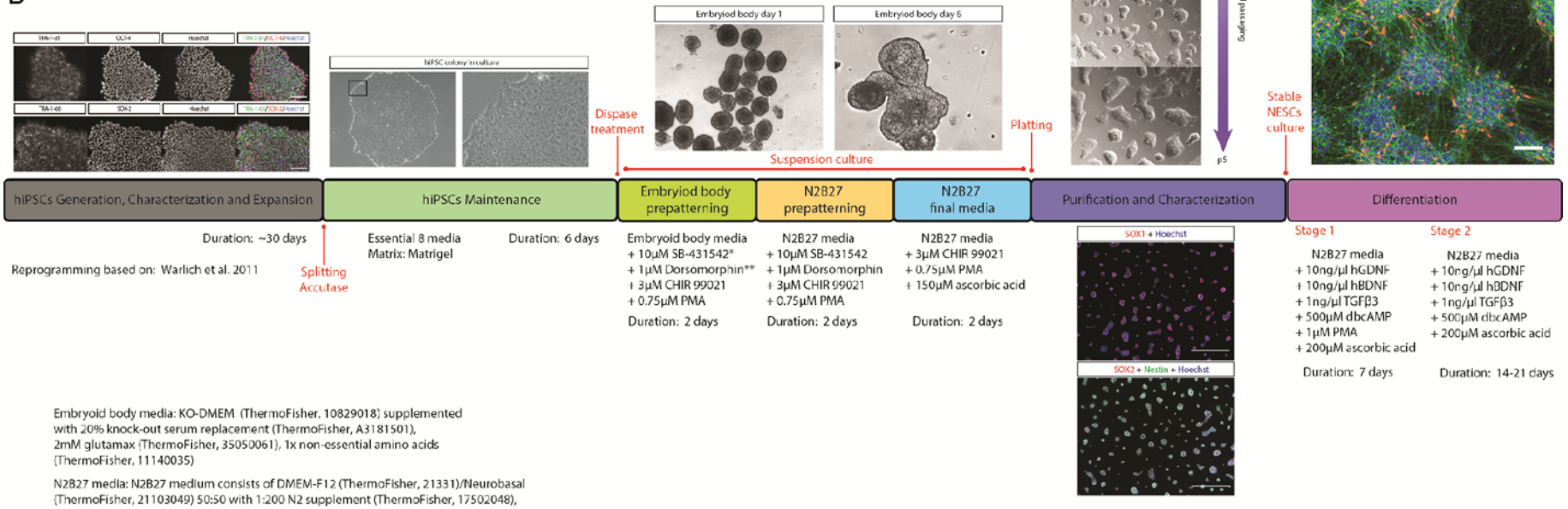

Embryoid body media: KO-DMEM (ThermoFisher, 10829018) supplemented with 20% knock-out serum replacement (ThermoFisher, A3181501), 2mM glutamax (ThermoFisher, 35050061), 1x non-essential amino acids (ThermoFisher, 11140035)

N2B27 media: N2B27 medium consists of DMEM-F12 (ThermoFisher, 21331)/Neurobasal (ThermoFisher, 21103049) 50:50 with 1:200 N2 supplement (ThermoFisher, 17502048), 1:100 B27 supplement without Vitamin A (ThermoFisher, 12587010), 2mM glutamax (ThermoFisher, 35050061) and 1% penicillin/streptomycin (ThermoFisher, 15140122).

*SB-431542 (abcam, ab120163)

**Dorsomorphin (Tocris, 3093)

Supplementary Fig. 2

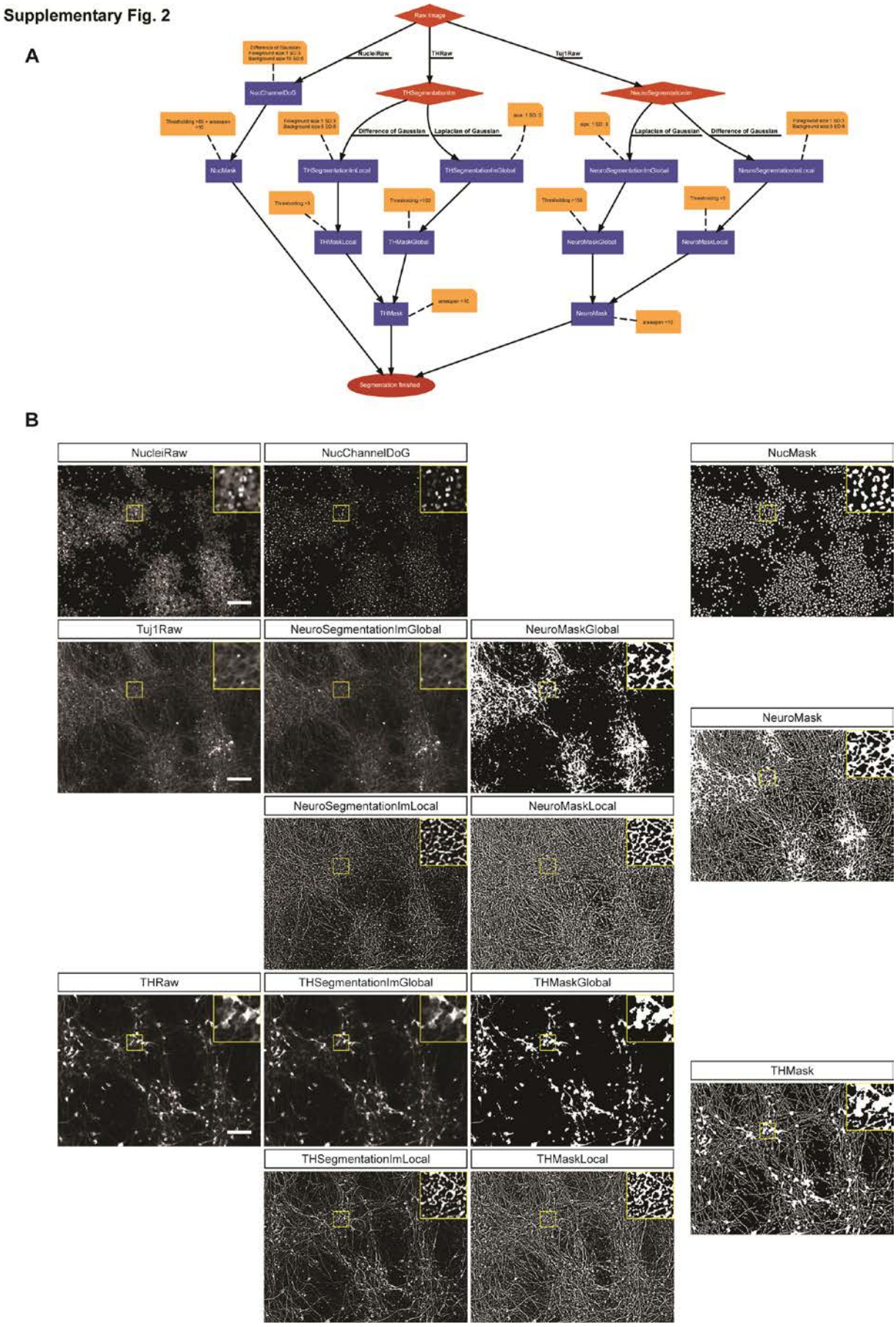

Supplementary Fig. 3

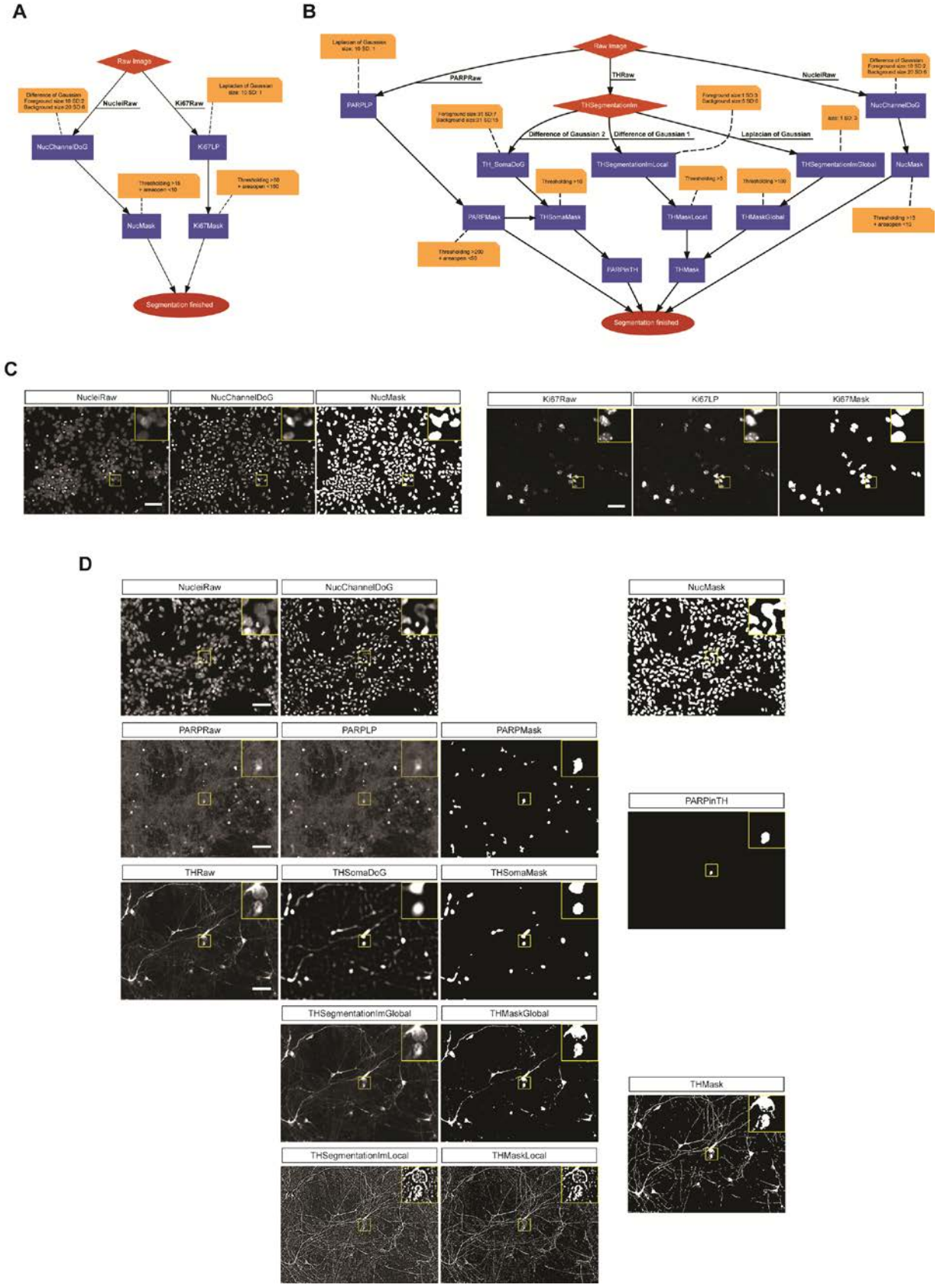

Supplementary Fig. 4

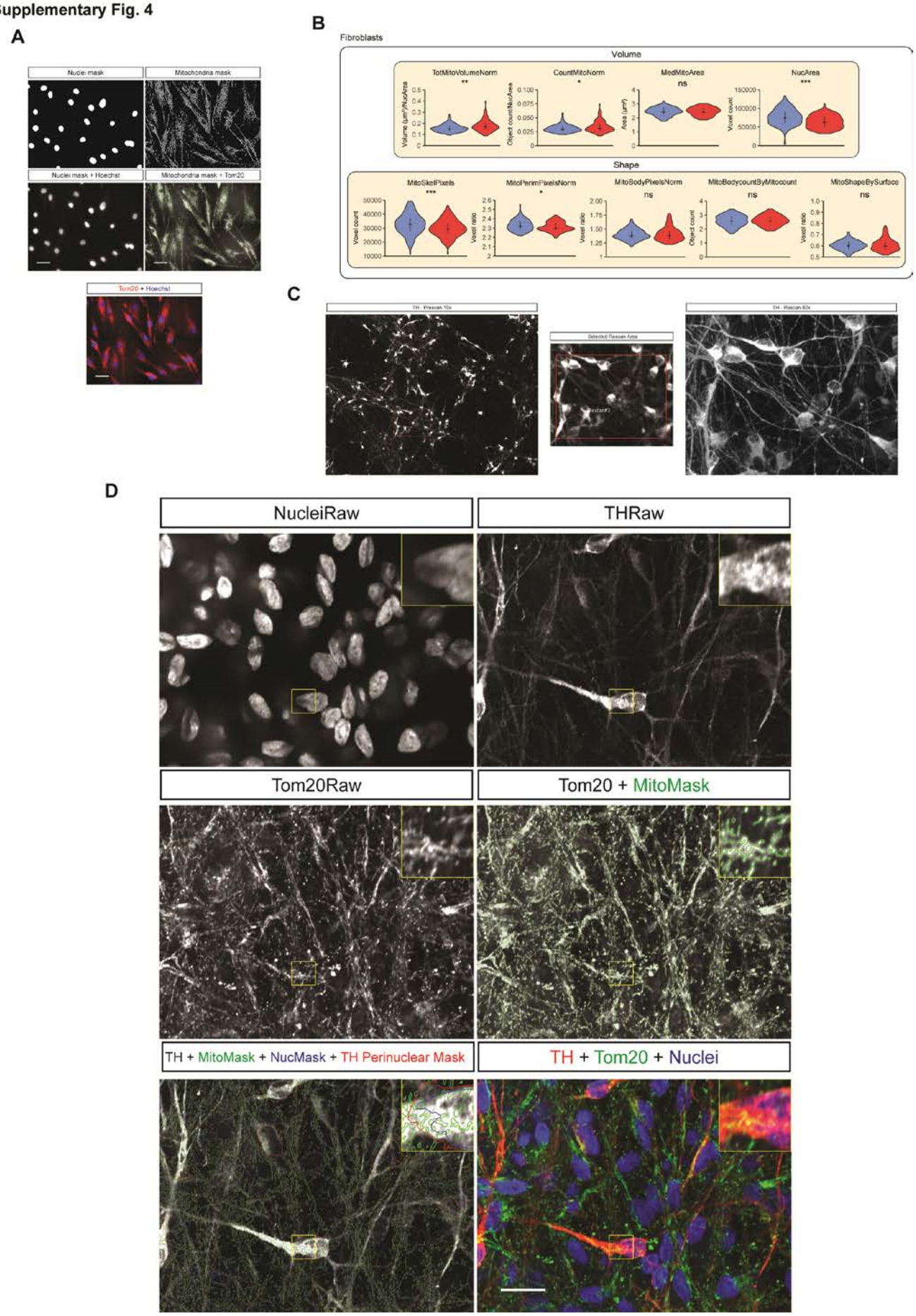

Supplementary Fig. 5

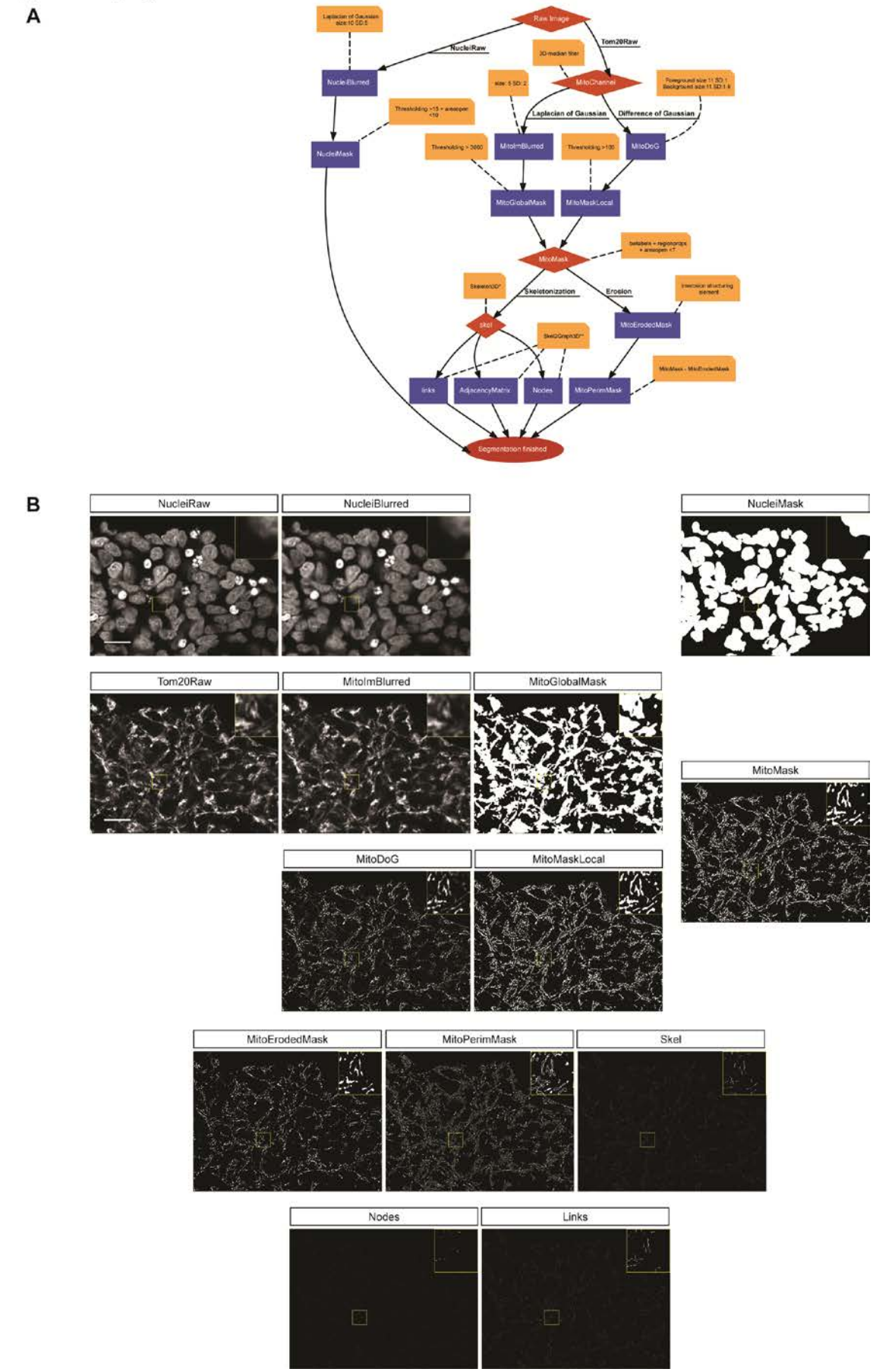

Supplementary Fig. 6

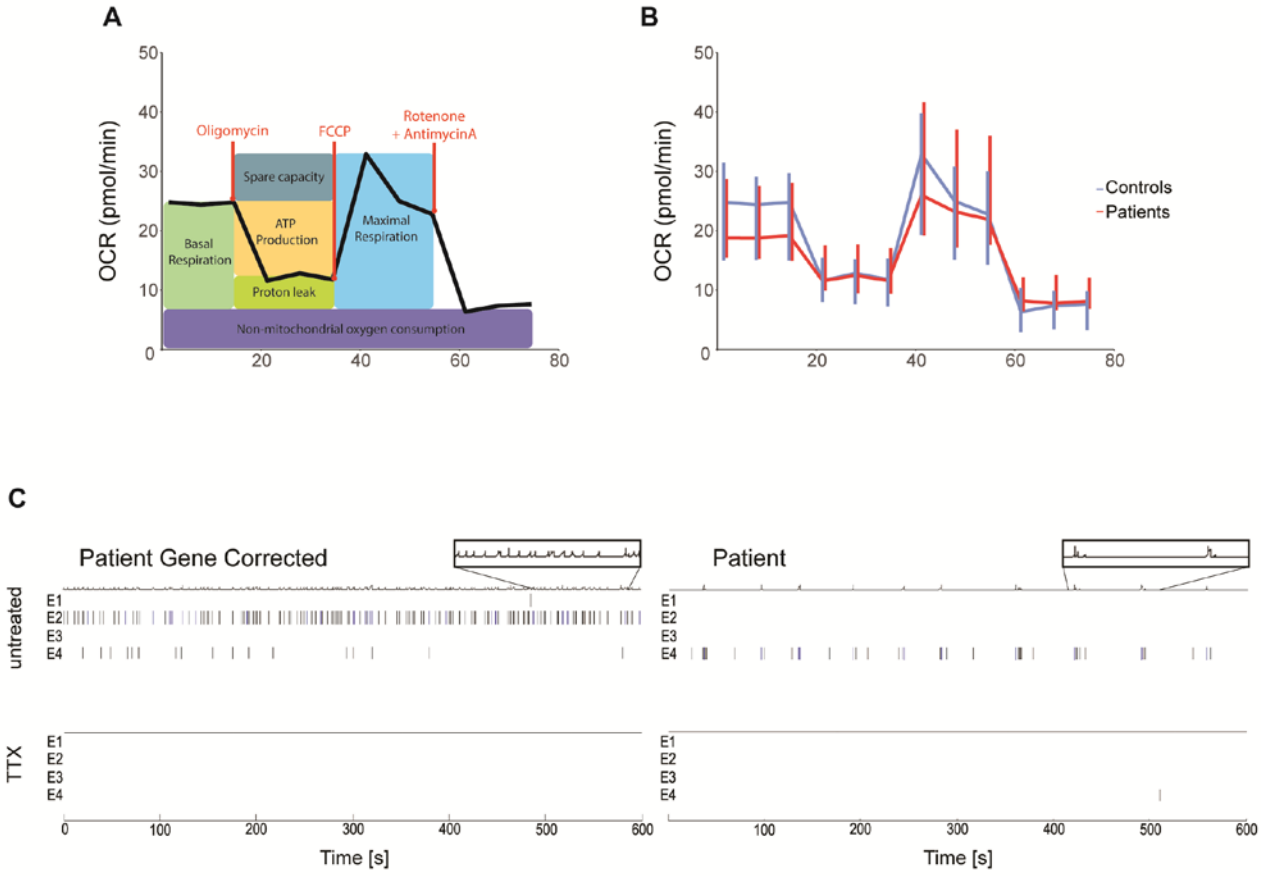

Supplementary Fig. 7

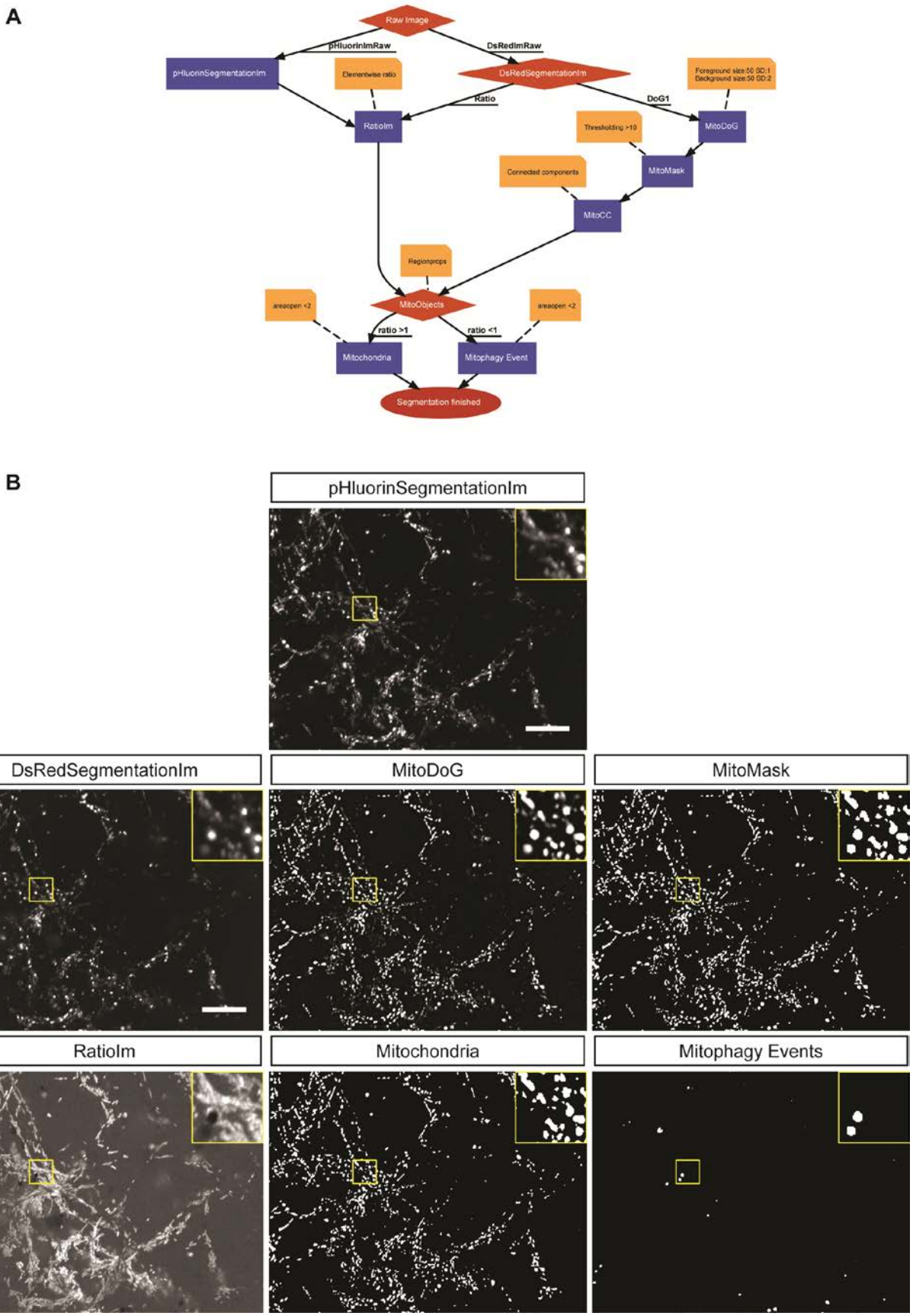

Supplementary Fig. 8

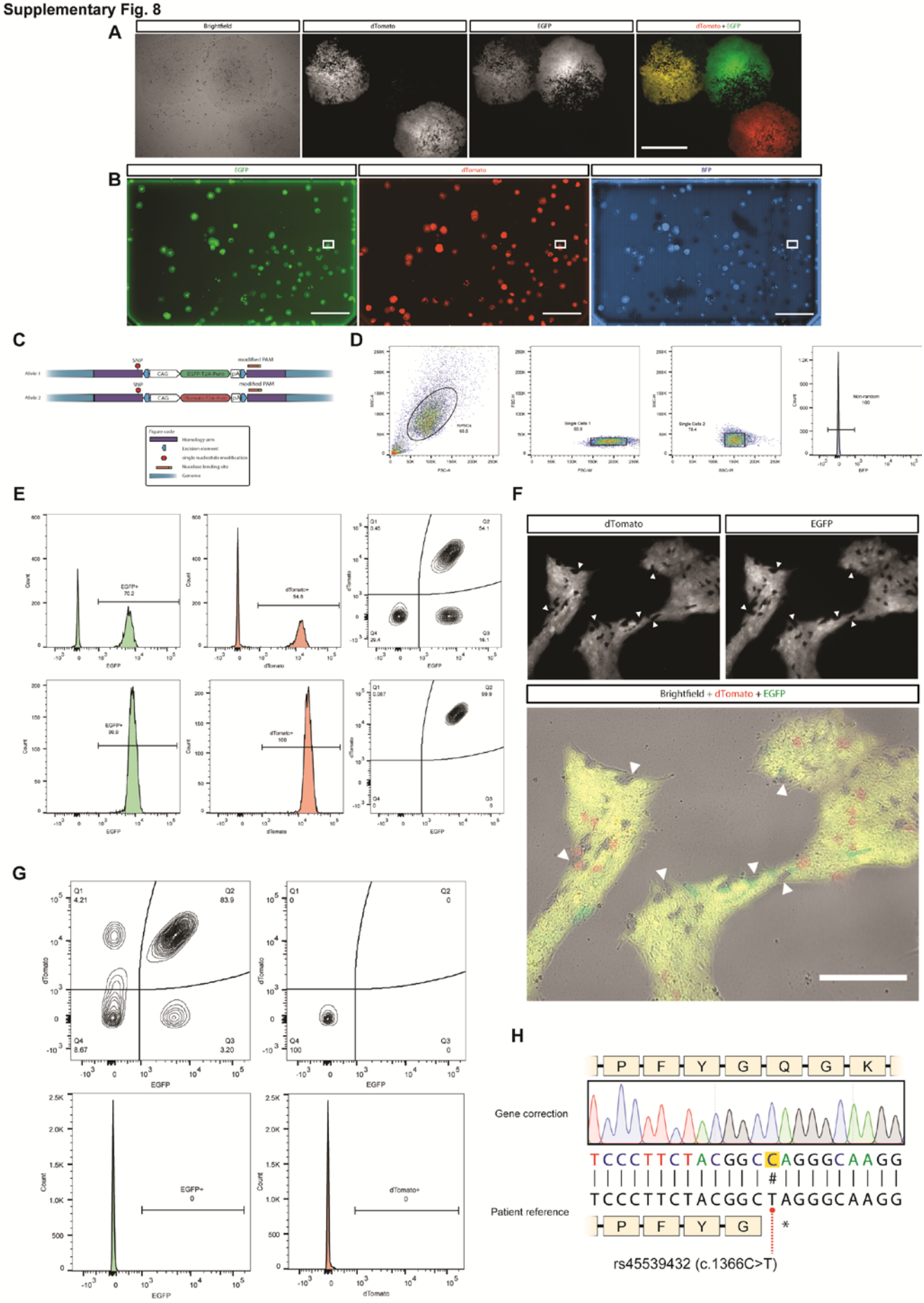

Supplementary Fig. 9

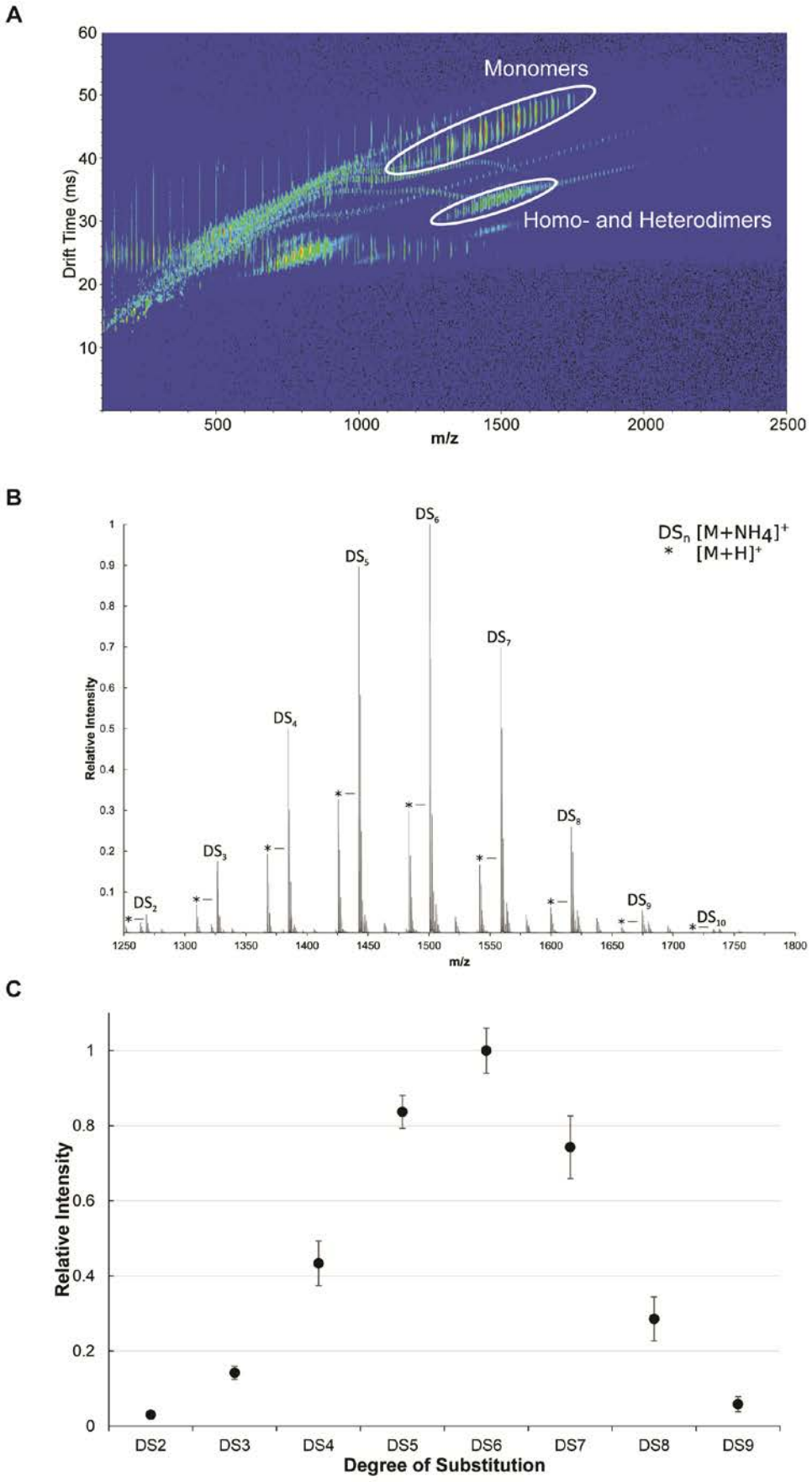

4. Discussion and Perspectives

Throughout this thesis, several aspects of the uncertain PD pathogeny such as mitochondrial and autophagy homeostasis have been described and analysed (Manuscript II and III). Moreover, new methodologies as well as disease modelling platforms have been evaluated in the context of PD (Manuscript I and II). This allowed us to assess the main hypothesis proposed in this project: an altered functionality of the PINK1/Parkin pathway can be the trigger of an impaired dopaminergic differentiation.

Derivation of hiPSCs from patient fibroblast was our starting point for studying this disease in vitro. Several studies remark the importance of their pluripotent state for developing tissue from different regions of the body in order to assess in vitro the affected cell type of a disease (Wenker et al., 2015). It is also known that their use might also lead to some opposing disadvantages, such as having epigenetic memory of the tissue of origin or the loss of specific signatures accumulated over time that might contribute to the onset of the disease (Kim et al., 2010; Mertens et al., 2016). Nevertheless, in order to have a similar epigenetic landscape of the cells affected by a specific disease, one would have to sample the actual altered organ where they reside which can be unfeasible and extremely invasive for certain diseases. Since obtaining samples of this gold standard is out of reach, the cell models we are working with have an assumed limitation that we must acknowledge when reaching our conclusions. In our case, the study of a well stablished gene alteration in PINK1 known for causing early onset of the disease with an understood mechanism allowed us to disregard the involvement of age as a contributor of the phenotypes we observed in culture (Grünewald et al., 2007; Seibler et al., 2011; Klein and Westenberger, 2012). Moreover, the known starting point of the disease mechanism in the context of PINK1 patients allows setting up a baseline from where we can build enough body of knowledge

to model and more easily extrapolate our observations into those cases where the causes of the disease are not yet known (sysmedpd.eu, Ronan Fleming, Horizon 2020, No. 668738).

The intermediate state of neuroprecursor cells chosen as a more differentiated starting point allows a quick transition between an expandable state and differentiated neurons resulting advantageous not only for its reduce hands-on-work culture but also for assessing in a timely manner the response capacity that cells have facing a differentiation stimuli. Moreover this cell type has been validated as a relevant disease model especially for those involving mitochondrial abnormalities (Lorenz et al., 2017; Walter et al., 2017).

One of the first alterations we focused on was the evaluation of a specific hallmark of the disease that is the loss of dopaminergic neurons. We did first an assessment of an early point of differentiation to see if in the context of an altered PINK1 activity the cells presented an impaired differentiation capability. Using an automated algorithm for unbiasedly quantifying the proportion of dopaminergic neurons, we observed a reduced differentiation into TH+ cells of patient lines versus control (Manuscript III, Figure 1A and B). We also evaluated several time points for controlling the dynamics of this differentiation process (Manuscript III, Figure 1C). Other groups have reported time point related differentiation impairments in PD lines with mutations in SNCA, LRRK2 and GBA. (Woodard et al., 2014; Borgs et al., 2016; Adil et al., 2017). Likewise, cells carrying PINK1 mutations present a reduced dopaminergic proportion of neurons during different points of the differentiation process.

Knowing the processes where PINK1 is involved also helped us to focus in specific cellular pathways for detecting differences between control and patient derived cells. Due to its normal function in mitochondrial quality control, mitochondrial phenotypes were observed in different cell types (Manuscript II, Figure 5 and Manuscript III Figure 2 and Supplementary 4). Not only morphological but also metabolic alterations were observed in patient cells, posing a scenario where the morphological dynamism of the network is not

correctly responding to the energy demands leading to an altered cellular metabolism. Impaired basal respiration here reported (Manuscript III, Figure 2F) can be linked to known alterations in the respiratory chain of cells derived from patients having PINK1 mutations, specifically in complex I and complex IV (Liu et al., 2011).

This is also elucidated by the higher dependency on glycolysis for obtaining their energetic demands (Manuscript III, Figure 2G) and the maintained higher proliferation rates of patient cells even after the induction of the neuronal differentiation process (Manuscript III, Figure 1E). This presents similarities to what have been already reported in the context of loss of PINK1 activity which triggers an increase in glycolysis through a ROS mediated stabilization of hypoxia-inducible factor-1α (HIF1α), which is also linked to cancer due to its close relation to the Warburg effect (Requejo-Aguilar et al., 2014; Agnihotri et al., 2016). This adds to the previous chain of reasoning that the failure in matching the energetic requirements due to an unbalanced mitochondrial morphology network for making the shift from a proliferation status to a fully functional neuronal profile leads to a reduction in dopaminergic differentiation.

Furthermore, those that were able to reach this differentiated status were also more prone to present apoptotic markers in the case of the patient lines, showing that not only the differentiation is reduced but the final number is also diminished by an increased cell death in those carrying PD related mutations (Manuscript III, Figure 1G). Expression of apoptotic and necroptotic markers in other PD mutations have also been reported as increased in patient cells, depicting a common end point for dopaminergic neurons in the context of PD (Michel et al., 2016; Zhang et al., 2017; Iannielli et al., 2018). Moreover, in the those carrying PINK1 mutations, this predisposition can be traced back to an improper metabolic status in mature neurons, since oxidative stress mediated neurodegeneration can arise from two sources: altered mitochondria and a compensatory decreased of the pentose-phosphate pathway (leading to a reduced NADPH content and hence a reduced

regeneration of GSH) to increase the glycolytic rate (Herrero-Mendez et al., 2009; Dias et al., 2013).

Evaluation of the differentiation capabilities of these cells in the context of a more physiological environment was assessed by the use of a microfluidic chamber that allows a tridimensional organization of the cells (Manuscript III, Figure 1H). This type of culture permits not only the evaluation of the cells disposition but also the influence of the media flow in their status (Moreno et al., 2015). It also allows the modelling of an aspect that cannot be achieved in 2D that is the impact of cells in degeneration process in the entire culture viability. Normally in a regular cell culture system, dying cells are washed away in the process of media change and apoptotic/necrotic factors are diluted in the media. In a 3D setting, these factors need to diffuse through an extracellular matrix that can also retain them forming areas were healthy cells are affected by the degeneration process of those surrounding them. Protein accumulation is also another important factor in the process of neurodegenerative diseases that was reported in 3D cultures with a dense extracellular matrix (Choi et al., 2014; Kim et al., 2015). In this project, we were able to recapitulate the differentiation phenotype observed in 2D in the context of a microfluidic culture.

In order to evaluate the effect of the point mutation in the phenotypes observed, we used the CRISPR/Cas9 system for correcting it. As previously mentioned, one of the advantages of this system compared to other technologies for gene editing is that the design and construction of the necessary elements is broadly accessible. Several inconveniences have been reported regarding the state-of-the-art of this technique for successfully knocking-in gene editing, such as the high number of clones needed to screen to obtain a possible result or the uncontrolled modification of only one of the two alleles (Soldner et al., 2011; Ran et al., 2013a; Paquet et al., 2016).

As described in the first manuscript of the thesis, we developed a novel system for doing simultaneous biallelic targeting with an easier to screen result. The composite of

donors carrying two different fluorescence in their selection cassette allows the visualization of a biallelic correctly modified colony that can be selected by cell sorting or fluorescent guided picking (Manuscript I, Figure 1E). These selection cassettes were surrounded by inverted terminal repeat (ITR) that together with the flanking sequence TTAA, form the piggyBac transposon system (Ding et al., 2005). The latter, is recognized by the transposase enzyme that circularizes and removes the entire construct restoring the TTAA sequence without leaving residual bases in the genome (Yusa, 2013; Xie et al., 2014). We designed our system in a way that after selection and purification of the cells with both modified alleles, mRNA expression of the excision-only variant of the transposase enzyme removed the selection cassette to further purify the cells with the desired modification (Li et al., 2013). We also introduced another fluorescence that allowed us to recognize the events of random integration that can arise during the procedure which are tightly linked to the number of non-repetitive elements present in the homology sequences used for triggering the homologous recombination (Manuscript I, Figure S2).

Even though we were able to induce reported phenotypes by the introduction of specific point mutations in the SNCA gene (Manuscript I, Figure 4F), the gene correction of patient cells with mutations in PINK1 was able to ameliorate some but not all of the phenotypes observed (Manuscript III, Figure 4). In the case of these cells, the metabolic alterations observed were reverted by correcting the point mutation, and NESCs presented an improved efficiency in ATP production relying more in the mitochondrial electron transport chain than in glycolysis (Manuscript III, Figure 4 A and B). Plus, the reduced firing activity of patient neurons was increased after the gene correction, showing that an improved mitochondrial functionality is a key element in the neuronal network activity (Manuscript III, Figure 4 C and D). However, the gene correction was not sufficient for restoring the differentiation impairment observed, by not significantly increasing the total area of Tuj1 positive neurons that are also TH+ (Manuscript III, Figure 4 E). A reduced nuclear volume in the imaged field was detected after the gene correction, pointing out that

the induced energetic shift facilitated the reduction of the proliferation after the induction of differentiation. These observations point out that the patients' genetic background has an important role in the establishment of the phenotype. Similarly, it has been reported that genetically identical individuals, have different susceptibility for developing PD (Woodard et al., 2014). The role of epigenetics in monozygotic twins modifying the onset of an illness has been highlighted in other diseases (Castillo-Fernandez et al., 2014; Malki et al., 2016; Young et al., 2017).

The assessment of risk factors as well as epigenetic modifications that might be present in the context of the disease is relevant at the moment of modelling and defining potential treatments. Further studies are planned for evaluating the transcriptomic, proteomic and metabolomic profile of 3 different patients carrying the same point mutation causative of PD with their respective isogenic controls in order to fully assess the disease profile against healthy individuals.

One of the cellular processes that seems to be impaired in PD patients carrying mutations in different genes as well as for other neurodegenerative diseases, is the autophagy pathway (Nixon, 2013; Menzies et al., 2015; Guo et al., 2018). In the context of this PhD project, the altered gene evaluated is involved in one aspect of macroautophagy that is the degradation of mitochondria, process known as mitophagy. Even though it has been reported the status of these pathways in PD derived cells, to date no system allowed the simultaneous analysis of the different structures involved in autophagy in an unbiased high-throughput manner (Klionsky et al., 2016; Manzoni, 2017). In order to address this point, we generated stable lines of hiPSCs derived from different patients carrying PD causative mutations in the genes LRRK2, VPS35 and PINK1 with a fluorescent construct known as Rosella (Manuscript II, Figure 1). It consists of two fluorescent proteins in tandem of which one (pHluorin) is quenched when subjected to low pH that inside a cell can only be reached within a lysosome (Miesenböck et al., 1998). For evaluating the overall

autophagy and specifically the mitophagy pathway we tagged with this construct the proteins LC3 and ATP5C1 (Sargsyan et al., 2015). We developed an automated algorithm for image analysis that recognizes the different categories of structures in these pathways (Manuscript II, Figure S2 and S3). We identified that patients' cells present a reduced level of all the structures involved in autophagy in basal conditions compared to control cells, with a greater tendency of presenting an increased proportion of early stages structures in relation to the overall autophagic pathway (Manuscript II, Figure 2).

Even though PINK1 is altered in patient lines we were able to identify events of mitophagy in the different cell types we have used (Manuscript II, Figure 5 and Manuscript III, Figure 3). This can be explained by reported mitophagy pathways that are independent of PINK1-Parkin (Ni et al., 2015; Bhujabal et al., 2017; Koentjoro et al., 2017; McWilliams et al., 2018). However, one of the feature that presents differences between patient and control lines is the size of the mitophagy events, which are bigger in the patient lines (Manuscript II, Figure 5C and Manuscript III, Figure 3B). A pre-mitophagy process recently described, involves the formation of a structure called mitochondria derived vesicles (MDVs) (Soubannier et al., 2012). These structures have an average size that ranges from 70-150nm and they induce the degradation of small portions of altered mitochondria and their formation depends on the activity of PINK1 (Sugiura et al., 2014). As mentioned in Manuscript III, an altered MDVs formation can cause the accumulation of bigger mitochondrial structures that need to be degraded, requiring bigger events of mitophagy, matching what was observed in patient derived cells. Further studies are planned for assessing the content of MDVs in patient and control cells.

Stably tagged hiPSCs with the Rosella construct derived from PINK1 patients were further differentiated into NESCs and neurons, assessing in a time lapse manner the behaviour of the mitophagy pathway during the early stages of neuronal differentiation compared to cells derived from healthy individuals (Manuscript III, Figure 3B). We were able

to observe that in the early stages of differentiation control cells presented a higher count of mitophagy events, while the events of mitophagy in case of the patient were bigger in size, strengthening the proposed scenario.

By using known modulators of these pathways, we modified the autophagy pathway activity in patients' cells so they can resemble the pattern observed in control lines (Manuscript II, Figure 3). Looking specifically at PINK1, treatment with rapamycin, a known inhibitor of mTOR, made that the patient cells clustered together with those derived from healthy individuals showing us a potential candidate pathway to be targeted for compound screening (Manuscript II, Figure 3C).

Impairments in the autophagy pathway can be broaden into a larger spectrum of mechanisms known together as coordinated lysosomal expression and regulation (CLEAR) pathway which includes all lysosomal depending processes such endocytosis, autophagy and lysosomal exocytosis (Settembre et al., 2013; Sardiello, 2018). These pathways are commonly regulated under the activity of the transcription factor EB (TFEB) which promotes lysosomal biogenesis as well as increases their enzymatic content, plus it binds to several promoter regions of genes involved in autophagy inducing their expression (Napolitano and Ballabio, 2016; Sardiello, 2018). Moreover it has been linked to several neurodegenerative diseases, where its expression increases the degradation of protein aggregates in the context of Alzheimer's, Niemman Pick and Gaucher diseases (Awad et al., 2015; Zhang and Zhao, 2015; Willett et al., 2017).

Interestingly, TFEB is regulated by mTOR phosphorylation in the surface of the lysosome, reducing the translocation of TFEB to the nucleus for inducing transcription of genes involved in the autophagy machinery (Martini-Stoica et al., 2016).

The close connection between TFEB and mTOR and the results we observed with the modulation of the autophagy pathway using rapamycin in cells derived from patients carrying PINK1 mutations, lead us to look into ways of modulating TFEB activity with

repurposed compounds. Several compounds were reported to increase its activity, with one of them (Ambroxol) already reported to reduce phenotypes observed in the context of patient derived cells carrying mutations in the gene GBA which is linked to 2 different neurodegenerative diseases Gaucher's and Parkinson's disease (Yang et al., 2017). However, the exact mechanism of increased levels of TFEB by using Ambroxol is not fully understood, and controversial since recent results reported an overall reduction of autophagy concomitant with a small increase in nuclear translocation of TFEB, which can be explained as a normal physiological response after the autophagy inhibition caused by Ambroxol rather than its direct effect over the transcription factor (Magalhaes et al., 2018). Among other known TFEB activators, 2-hydroxypropyl-β-cyclodextrin (HP-β-CD) has been thoroughly characterized, increasing TFEB translocation to the nucleus while inducing activation of autophagy (Song et al., 2014). Moreover, it has been shown to reduce neuronal loss, and even to revert some of the general phenotypes observed in a mouse model of Niemman Pick Type C disease (NPD) (Aqul et al., 2011). This lysosomal storage disorder causes neurodegeneration in different brain regions in a progressive and widespread manner with a multisystemic affected context since most of the organs are altered (Ong et al., 2001; McGovern et al., 2013). Clinical trials using HP-β-CD in patient with Niemman Pick disease showed promising results in the phase 1/2a with an ongoing phase 2b/3. (NCT01747135 and NCT02534844).

The effect of cyclodextrin in dopaminergic neurons derived from PD patients was not determined to date, becoming a suitable candidate for our screen. We first started evaluating the use of HP-β-CD during differentiation with a low dose sustained throughout the entire differentiation protocol. Compared to the results observed after the gene correction of PINK1 line, treatment with HP-β-CD was able to significantly increase the proportion of dopaminergic neurons derived from PINK1 patients at day 14 of differentiation (Manuscript III, Figure 4G). Moreover, we tested the effect of this compound in PD patient derived cells carrying a mutation in the Parkin gene during the process of differentiation,

and we were also able to observe a significant increase in the proportion of dopaminergic neurons (Manuscript III, Figure 4H). In order to assess whether the treatment had a direct impact in autophagy as it was proposed, we treated with HP-β-CD patient derived NESCs tagged with the mitophagy reporter during differentiation and imaged each day of the protocol for 14 days to evaluate the mitochondrial degradation profile (Manuscript III, Figure 4F). We observed that the overall mitophagy was significantly increased upon treatment showing a higher number of mitophagy events as well as an increased total area of mitophagy. This change occurred without modifying the mean size of the mitochondrion, implying that it is an increase in the rate of degradation rather than a modification of the fission/fusion balance that could isolate parts of the network for removal (Manuscript III, Figure 4F). These last observations confirm that the treatment with HP-β-CD is suitable for improving the mitophagy status of a neuronal culture while increasing the proportion of dopaminergic neurons in patient derived cells.

It is important to highlight, based on the phenotypes observed in this project and the positive response observed after treatment with a compound used in a different malady, that there is a strong correlation between neurodegenerative diseases and it should not be disregarded. The identification of common altered pathways and treatments for them, would help us tackle complex diseases that are normally grouped under narrow classifications. Steps are being taken in order to stratify and define subgroups of PD patients presenting distinct biomarkers in order to find personalized treatments (sysmedpd.eu, Christine Klein, Horizon 2020, No. 668738). This approach could lead to a new reclassification of the disease based on state-of-the-art techniques similar to what has been reported in the cancer or diabetes field (cancergenome.nih.gov, Cancer Genome Atlas Research Network et al., 2017; Ahlqvist et al., 2018).

Even though there are still questions that remained unanswered, we consider that the goals set up at the beginning of the project were covered with interesting and novel results that have been, and will be, shared with the entire scientific community.

Outlook

Of those questions remaining unanswered, the first one we are currently addressing is the lack of rescuing effect after the gene correction of the patient derived line. Studies performed with identical twins stablished that even though individuals were originated from the same genetic pool, only one of them developed PD (Woodard et al., 2014). This and other features like the reduce penetrance of some specific mutations or the low rate of familial cases, point out the strong influence of the epigenetic profile. As mentioned before, we will perform a transcriptomic, proteomic and metabolomic analysis of 3 patient lines with their respective isogenic controls and compared them with age and gender matched healthy individuals. This will allow us to study the influence of the genetic and epigenetic background of the cells and validate which proportion of the phenotypes observed depend on the point mutations presented by the patients.

Another topic that drove our attention during this research project is the formation of mitochondria derived vesicles (MDVs) as a mitochondrial quality control mechanism. The formation of these structures relies on the activity of PINK1 and their content depends on the type of stimuli that triggers its formation (Sugiura et al., 2014; Matheoud et al., 2016; McLelland et al., 2016). We are planning to assess by electron or super resolution microscopy if the occurrence of these events is reduced in patient derived cells. We hypothesize that one of the reasons we are seeing bigger mitochondrial network and mitophagy events in the case of patient derived cells is due to an insufficient formation of MDVs as one of the first steps for controlling altered proteins in the mitochondrial membrane.

We would like to further characterize and isolate the different components of the mixture of HP-β-CD to determine if it is the actual mixture of substitutions or one of the substitution in particular that is effective in producing the effects we observed. Obtaining a more controllable compound preparation would allow us to search for specific modifications that could increase its properties, to be ideally validated in a tridimensional cell culture system before its further application to in vivo models and potential clinical trials.

5. References

Adil, M.M., Rodrigues, G.M.C., Kulkarni, R.U., Rao, A.T., Chernavsky, N.E., Miller, E.W., and Schaffer, D.V. (2017). Efficient generation of hPSC-derived midbrain dopaminergic neurons in a fully defined, scalable, 3D biomaterial platform. Scientific Reports *7*, 40573.

Agnihotri, S., Golbourn, B., Huang, X., Remke, M., Younger, S., Cairns, R.A., Chalil, A., Smith, C.A., Krumholtz, S.-L., Mackenzie, D.*, et al.* (2016). PINK1 Is a Negative Regulator of Growth and the Warburg Effect in Glioblastoma. Cancer Research *76*, 4708-4719.

Ahlqvist, E., Storm, P., Käräjämäki, A., Martinell, M., Dorkhan, M., Carlsson, A., Vikman, P., Prasad, R.B., Aly, D., Almgren, P.*, et al.* (2018). Novel subgroups of adult-onset diabetes and their association with outcomes: a data-driven cluster analysis of six variables. The Lancet Diabetes & Endocrinology.

Alexeyev, M., Shokolenko, I., Wilson, G., and LeDoux, S. (2013). The Maintenance of Mitochondrial DNA Integrity—Critical Analysis and Update. Cold Spring Harbor Perspectives in Biology *5*.

Allert, N., Cheeran, B., Deuschl, G., Barbe, M.T., Csoti, I., Ebke, M., Glaser, M., Kang, J.-S., Kelm, S., Krack, P.*, et al.* (2018). Postoperative rehabilitation after deep brain stimulation surgery for movement disorders. Clinical neurophysiology : official journal of the International Federation of Clinical Neurophysiology *129*, 592-601.

Anichtchik, O., Diekmann, H., Fleming, A., Roach, A., Goldsmith, P., and Rubinsztein, D.C. (2008). Loss of PINK1 Function Affects Development and Results in Neurodegeneration in Zebrafish. The Journal of Neuroscience *28*, 8199-8207.

Antony, P.M.A., Diederich, N.J., Krüger, R., and Balling, R. (2013). The hallmarks of Parkinson's disease. FEBS Journal *280*, 5981-5993.

Appelqvist, H., Wäster, P., Kågedal, K., and Öllinger, K. (2013). The lysosome: from waste bag to potential therapeutic target. Journal of Molecular Cell Biology *5*, 214-226.

Aqul, A., Liu, B., Ramirez, C.M., Pieper, A.A., Estill, S., Burns, D.K., Liu, B., Repa, J.J., Turley, S.D., and Dietschy, J.M. (2011). Unesterified Cholesterol Accumulation in Late Endosomes/Lysosomes Causes Neurodegeneration and Is Prevented by Driving Cholesterol Export from This Compartment. The Journal of Neuroscience *31*, 9404-9413.

Arevalo, G.G., Jorge, R., Garcia, S., Scipioni, O., and Gershanik, O. (1997). Clinical and pharmacological differences in early- versus late-onset Parkinson's disease. Movement Disorders *12*, 277-284.

Ariga, H., Takahashi-Niki, K., Kato, I., Maita, H., Niki, T., and Iguchi-Ariga, S.M.M. (2013). Neuroprotective Function of DJ-1 in Parkinson's Disease. Oxidative Medicine and Cellular Longevity *2013*, 683920.

Ashrafi, G., and Schwarz, T.L. (2012). The pathways of mitophagy for quality control and clearance of mitochondria. Cell Death & Differentiation *20*, 31-42.

Athauda, D., and Foltynie, T. (2016). Challenges in detecting disease modification in Parkinson's disease clinical trials. Parkinsonism & Related Disorders *32*, 1-11.

Auburger, G., Klinkenberg, M., Drost, J., Marcus, K., Morales-Gordo, B., Kunz, W.S., Brandt, U., Broccoli, V., Reichmann, H., Gispert, S.*, et al.* (2012). Primary Skin Fibroblasts as a Model of Parkinson's Disease. Molecular Neurobiology *46*, 20-27.

Awad, O., Sarkar, C., Panicker, L.M., Miller, D., Zeng, X., Sgambato, J.A., Lipinski, M.M., and Feldman, R.A. (2015). Altered TFEB-mediated lysosomal biogenesis in Gaucher disease iPSC-derived neuronal cells. Human Molecular Genetics *24*, 5775-5788.

Badran, A.H., Komor, A.C., Bryson, D.I., Liu, D.R., Rees, H.A., Packer, M.S., and Gaudelli, N.M. (2017). Programmable base editing of A•T to G•C in genomic DNA without DNA cleavage. Nature *551*, 464.

Barrangou, R., and Doudna, J.A. (2016). Applications of CRISPR technologies in research and beyond. Nature Biotechnology *34*, 933.

Bassett, A.R. (2017). Editing the genome of hiPSC with CRISPR/Cas9: disease models. Mammalian Genome *28*, 348-364.

Beckhauser, T., Francis-Oliveira, J., and Pasquale, R. (2016). Reactive Oxygen Species: Physiological and Physiopathological Effects on Synaptic Plasticity. Journal of Experimental Neuroscience *10*, 23-48.

Bellou, V., Belbasis, L., Tzoulaki, I., Evangelou, E., and Ioannidis, J. (2016). Environmental risk factors and Parkinson's disease: An umbrella review of meta-analyses. Parkinsonism & Related Disorders *23*, 1-9.

Bellucci, A., Antonini, A., Pizzi, M., and Spano, P. (2017). The End Is the Beginning: Parkinson's Disease in the Light of Brain Imaging. Frontiers in Aging Neuroscience *9*, 330.

Bhatia, S.N., and Ingber, D.E. (2014). Microfluidic organs-on-chips. Nature Biotechnology *32*.

Bhujabal, Z., Birgisdottir, Å.B., Sjøttem, E., Brenne, H.B., Øvervatn, A., Habisov, S., Kirkin, V., Lamark, T., and Johansen, T. (2017). FKBP8 recruits LC3A to mediate Parkin-independent mitophagy. EMBO reports *18*, 947-961.

Biosa, A., Sandrelli, F., Beltramini, M., Greggio, E., Bubacco, L., and Bisaglia, M. (2017). Recent findings on the physiological function of DJ-1: Beyond Parkinson's disease. Neurobiology of Disease *108*, 65-72.

Boboila, C., Yan, C., Wesemann, D.R., Jankovic, M., Wang, J.H., Manis, J., Nussenzweig, A., Nussenzweig, M., and Alt, F.W. (2010). Alternative end-joining catalyzes class switch recombination in the absence of both Ku70 and DNA ligase 4. The Journal of Experimental Medicine *207*, 417-427.

Bolam, P.J., and Pissadaki, E.K. (2012). Living on the edge with too many mouths to feed: Why dopamine neurons die. Movement Disorders *27*, 1478-1483.

Bonifati, V. (2014). Genetics of Parkinson's disease – state of the art, 2013. Parkinsonism & Related Disorders *20*.

Bonifati, V., Rizzu, P., van Baren, M.J., Schaap, O., Breedveld, G.J., Krieger, E., Dekker, M.C.J., Squitieri, F., Ibanez, P., Joosse, M.*, et al.* (2003). Mutations in the DJ-1 Gene Associated with Autosomal Recessive Early-Onset Parkinsonism. Science *299*, 256-259.

Bonten, E.J., Annunziata, I., and d'Azzo, A. (2014). Lysosomal multienzyme complex: pros and cons of working together. Cellular and Molecular Life Sciences *71*, 2017-2032.

Borgs, L., Peyre, E., Alix, P., Hanon, K., Grobarczyk, B., Godin, J.D., Purnelle, A., Krusy, N., Maquet, P., Lefebvre, P.*, et al.* (2016). Dopaminergic neurons differentiating from LRRK2 G2019S induced pluripotent stem cells show early neuritic branching defects. Scientific Reports *6*, 33377.

Boutin, M.E., and Hoffman-Kim, D. (2014). Application and assessment of optical clearing methods for imaging of tissue-engineered neural stem cell spheres. Tissue engineering Part C, Methods *21*, 292-302.

Bové, J., Prou, D., Perier, C., and Przedborski, S. (2005). Toxin-induced models of Parkinson's disease. NeuroRX *2*, 484-494.

Braak, H., Braak, E., Yilmazer, D., Schultz, C., de Vos, R.A., and Jansen, E.N. (1995). Nigral and extranigral pathology in Parkinson's disease. Journal of neural transmission Supplementum *46*, 15-31.

Braak, H., Rüb, U., Gai, W.P., and Tredici, D.K. (2003). Idiopathic Parkinson's disease: possible routes by which vulnerable neuronal types may be subject to neuroinvasion by an unknown pathogen. Journal of Neural Transmission *110*, 517-536.

Braak, H., and Tredici, K. (2017). Neuropathological Staging of Brain Pathology in Sporadic Parkinson's disease: Separating the Wheat from the Chaff. Journal of Parkinson's Disease *7*.

Brás, J., Guerreiro, R., and Hardy, J. (2015). SnapShot: Genetics of Parkinson's Disease. Cell *160*, 570-5700.

Brennand, K.J. (2017). Personalized medicine in a dish: the growing possibility of neuropsychiatric disease drug discovery tailored to patient genetic variants using stem cells. Stem Cell Investigation *4*, 91-91.

Brown, R.C., Lockwood, A.H., and Sonawane, B.R. (2005). Neurodegenerative Diseases: An Overview of Environmental Risk Factors. Environmental Health Perspectives *113*, 1250-1256.

Buchman, A.S., Shulman, J.M., Nag, S., Leurgans, S.E., Arnold, S.E., Morris, M.C., Schneider, J.A., and Bennett, D.A. (2012). Nigral pathology and parkinsonian signs in elders without Parkinson disease. Annals of Neurology *71*, 258-266.

Buhlman, L., Damiano, M., Bertolin, G., Ferrando-Miguel, R., Lombès, A., Brice, A., and Corti, O. (2014). Functional interplay between Parkin and Drp1 in mitochondrial fission and clearance. Biochimica et Biophysica Acta (BBA) - Molecular Cell Research *1843*, 2012-2026.

Cadet, J., and Wagner, R.J. (2013). DNA Base Damage by Reactive Oxygen Species, Oxidizing Agents, and UV Radiation. Cold Spring Harbor Perspectives in Biology *5*.

Caiazzo, M., Dell'Anno, M., Dvoretskova, E., Lazarevic, D., Taverna, S., Leo, D., Sotnikova, T.D., Menegon, A., Roncaglia, P., Colciago, G.*, et al.* (2011). Direct generation of functional dopaminergic neurons from mouse and human fibroblasts. Nature *476*.

Cancer Genome Atlas Research Network, Abeshouse, A., Adebamowo, C., Adebamowo, S.N., Akbani, R., Akeredolu, T., Ally, A., Anderson, M.L., Anur, P., Appelbaum, E.L.*, et al.* (2017). Comprehensive and Integrated Genomic Characterization of Adult Soft Tissue Sarcomas. Cell *171*.

Cannon, J.R., and Greenamyre, T.J. (2011). The Role of Environmental Exposures in Neurodegeneration and Neurodegenerative Diseases. Toxicological Sciences *124*, 225-250.

Caslake, R., Taylor, K., Scott, N., Gordon, J., Harris, C., Wilde, K., Murray, A., and Counsell, C. (2013). Age-, gender-, and socioeconomic status-specific incidence of Parkinson's disease and parkinsonism in North East Scotland: The PINE study. Parkinsonism & Related Disorders *19*, 515-521.

Castillo-Fernandez, J.E., Spector, T.D., and Bell, J.T. (2014). Epigenetics of discordant monozygotic twins: implications for disease. Genome Medicine *6*, 1-16.

Chaban, Y., Boekema, E.J., and Dudkina, N.V. (2014). Structures of mitochondrial oxidative phosphorylation supercomplexes and mechanisms for their stabilisation. Biochimica et Biophysica Acta (BBA) - Bioenergetics *1837*, 418-426.

Chade, A.R., Kasten, M., and Tanner, C.M. (2006). Parkinson's Disease and Related Disorders. springer *70*, 147-151.

Chambers, S.M., Fasano, C.A., Papapetrou, E.P., Tomishima, M., Sadelain, M., and Studer, L. (2009). Highly efficient neural conversion of human ES and iPS cells by dual inhibition of SMAD signaling. Nature Biotechnology *27*, 275-280.

Chaudhuri, R.K., Healy, D.G., Schapira, A.H.V., and for Excellence, N. (2006). Non-motor symptoms of Parkinson's disease: diagnosis and management. The Lancet Neurology *5*, 235-245.

Chaudhuri, R.K., and Schapira, A.H.V. (2009). Non-motor symptoms of Parkinson's disease: dopaminergic pathophysiology and treatment. The Lancet Neurology *8*, 464-474.

Checkoway, H., Lundin, J.I., and Kelada, S.N. (2011). Neurodegenerative diseases. IARC scientific publications, 407-419.

Chen, H., Kwong, J.C., Copes, R., Tu, K., Villeneuve, P.J., van Donkelaar, A., Hystad, P., Martin, R.V., Murray, B.J., Jessiman, B.*, et al.* (2017). Living near major roads and the incidence of dementia, Parkinson's disease, and multiple sclerosis: a population-based cohort study. The Lancet *389*, 718-726.

Chin-Chan, M., Navarro-Yepes, J., and Quintanilla-Vega, B. (2015). Environmental pollutants as risk factors for neurodegenerative disorders: Alzheimer and Parkinson diseases. Frontiers in Cellular Neuroscience *9*, 124.

Chiong-Rivero, H., Ryan, G.W., Flippen, C., Bordelon, Y., Szumski, N.R., Zesiewicz, T.A., Vassar, S., Weidmer, B., García, R., Bradley, M*., et al.* (2011). Patients' and caregivers' experiences of the impact of Parkinson's disease on health status. Patient Related Outcome Measures *2*, 57-70.

Choi, S., Kim, Y., Hebisch, M., Sliwinski, C., Lee, S., D'Avanzo, C., Chen, H., Hooli, B., Asselin, C., Muffat, J*., et al.* (2014). A three-dimensional human neural cell culture model of Alzheimer/'s disease. Nature *515*, 274-278.

Clevers, H. (2016). Modeling Development and Disease with Organoids. Cell *165*, 1586-1597.

Cobb, M.M., Ravisankar, A., Skibinski, G., and Finkbeiner, S. (2017). iPS cells in the study of PD molecular pathogenesis. Cell and Tissue Research, 1-17.

Curtis, M.G. (2003). Cloning and stem cells: processes, politics, and policy. Current women's health reports *3*, 492-500.

Dahlstroem, A., and Fuxe, K. (1964). Evidence for the existence of monoamine-containing neurons in the central nervous system. I. Demonstration of monoamines in the cell bodies of brain stem neurons. Acta physiologica Scandinavica Supplementum, 55.

Dai, W.-J., Zhu, L.-Y., Yan, Z.-Y., Xu, Y., Wang, Q.-L., and Lu, X.-J. (2016). CRISPR-Cas9 for in vivo Gene Therapy: Promise and Hurdles. Molecular Therapy - Nucleic Acids *5*.

Dauer, W., and Przedborski, S. (2003). Parkinson's Disease Mechanisms and Models. Neuron *39*, 889-909.

Dawson, T.M. (2005). Failures and Successes of Clinical Trials for Parkinson Disease Treatments. RETINA *25*.

Dawson, T.M., and Dawson, V.L. (2010). The role of parkin in familial and sporadic Parkinson's disease. Movement Disorders *25*.

de Hemptinne, C., Swann, N.C., Ostrem, J.L., Ryapolova-Webb, E.S., Luciano, M., Galifianakis, N.B., and Starr, P.A. (2015). Therapeutic deep brain stimulation reduces cortical phase-amplitude coupling in Parkinson's disease. Nature Neuroscience *18*.

de Wert, G., and Mummery, C. (2003). Human embryonic stem cells: research, ethics and policy. Human Reproduction *18*, 672-682.

Deas, E., Plun-Favreau, H., and Wood, N.W. (2009). PINK1 function in health and disease. EMBO Molecular Medicine *1*, 152-165.

DeMaagd, G., and Philip, A. (2015). Parkinson's Disease and Its Management: Part 1: Disease Entity, Risk Factors, Pathophysiology, Clinical Presentation, and Diagnosis. P & T : a peer-reviewed journal for formulary management *40*, 504-532.

Deng, H., Gao, K., and Jankovic, J. (2013). The VPS35 gene and Parkinson's disease. Movement Disorders *28*, 569-575.

Derejko, M., Slawek, J., Wieczorek, D., Brockhuis, B., Dubaniewicz, M., and Lass, P. (2006). Regional cerebral blood flow in Parkinson's disease as an indicator of cognitive impairment. Nuclear Medicine Communications *27*, 945.

Dias, V., Junn, E., and Mouradian, M.M. (2013). The role of oxidative stress in Parkinson's disease. Journal of Parkinson's disease *3*, 461-491.

Dickson, D.W. (2018). Neuropathology of Parkinson disease. Parkinsonism & Related Disorders *46*.

Ding, S., Wu, X., Li, G., Han, M., Zhuang, Y., and Xu, T. (2005). Efficient Transposition of the piggyBac (PB) Transposon in Mammalian Cells and Mice. Cell *122*, 473-483.

Eiraku, M., Takata, N., Ishibashi, H., Kawada, M., Sakakura, E., Okuda, S., Sekiguchi, K., Adachi, T., and Sasai, Y. (2011). Self-organizing optic-cup morphogenesis in three-dimensional culture. Nature *472*, 51-56.

Eriksen, J.L., Wszolek, Z., and Petrucelli, L. (2005). Molecular Pathogenesis of Parkinson Disease. Archives of Neurology *62*, 353-357.

Evans, M.J., and Kaufman, M.H. (1981). Establishment in culture of pluripotential cells from mouse embryos. Nature *292*.

Fahn, S. (2015). The medical treatment of Parkinson disease from James Parkinson to George Cotzias. Movement Disorders *30*, 4-18.

Farzanehfar, P. (2016). Towards a Better Treatment Option for Parkinson's Disease: A Review of Adult Neurogenesis. Neurochemical Research *41*, 3161-3170.

Findley, L.J. (2007). The economic impact of Parkinson's disease. Parkinsonism & Related Disorders *13*.

Fitzgerald, J.C., and Plun-Favreau, H. (2008). Emerging pathways in genetic Parkinson's disease: Autosomal-recessive genes in Parkinson's disease – a common pathway? FEBS Journal *275*, 5758-5766.

Fonzo, D.A., Dekker, M.C.J., Montagna, P., Baruzzi, A., Yonova, E.H., Guedes, C.L., Szczerbinska, A., Zhao, T., Dubbel-Hulsman, L.O.M., Wouters, C.H.*, et al.* (2008). FBXO7 mutations cause autosomal recessive, early-onset parkinsonian-pyramidal syndrome. Neurology *72*, 240-245.

Forno, L.S. (1996). Neuropathology of Parkinson's Disease. Journal of Neuropathology & Experimental Neurology *55*, 259-272.

Friedman, J.R., Lackner, L.L., West, M., DiBenedetto, J.R., Nunnari, J., and Voeltz, G.K. (2011). ER tubules mark sites of mitochondrial division. Science (New York, NY) *334*, 358-362.

Fujita, K.A., Ostaszewski, M., Matsuoka, Y., Ghosh, S., Glaab, E., Trefois, C., Crespo, I., Perumal, T.M., Jurkowski, W., Antony, P.M.A.*, et al.* (2014). Integrating Pathways of Parkinson's Disease in a Molecular Interaction Map. Molecular Neurobiology *49*, 88-102.

Gaig, C., Martí, M., Ezquerra, M., Rey, M., Cardozo, A., and Tolosa, E. (2007). G2019S LRRK2 mutation causing Parkinson's disease without Lewy bodies. Journal of Neurology, Neurosurgery & Psychiatry *78*, 626-628.

Gaj, T., Sirk, S.J., Shui, S.-l., and Liu, J. (2016). Genome-Editing Technologies: Principles and Applications. Cold Spring Harbor Perspectives in Biology *8*.

Galluzzi, L., Baehrecke, E.H., Ballabio, A., Boya, P., Pedro, J., Cecconi, F., Choi, A.M., Chu, C.T., Codogno, P., Colombo, M.*, et al.* (2017). Molecular definitions of autophagy and related processes. The EMBO Journal *36*, 1811-1836.

Gammon, K. (2014). Neurodegenerative disease: Brain windfall. Nature *515*, 299-300.

Garcia-Ruiz, P.J., and Espay, A.J. (2017). Parkinson Disease: An Evolutionary Perspective. Frontiers in Neurology *8*, 157.

Ghaffari, L.T., Starr, A., Nelson, A.T., and Sattler, R. (2018). Representing Diversity in the Dish: Using Patient-Derived in Vitro Models to Recreate the Heterogeneity of Neurological Disease. Frontiers in Neuroscience *12*, 56.

Gibb, W.R., and Lees, A.J. (1991). Anatomy, pigmentation, ventral and dorsal subpopulations of the substantia nigra, and differential cell death in Parkinson's disease. Journal of Neurology, Neurosurgery & Psychiatry *54*, 388-396.

Globus, M., Mildworf, B., and Melamed, E. (1985). Cerebral blood flow and cognitive impairment in Parkinson's disease. Neurology *35*, 1135-1139.

Goetz, C.G. (2011). The History of Parkinson's Disease: Early Clinical Descriptions and Neurological Therapies. Cold Spring Harbor Perspectives in Medicine *1*.

González, F., Boué, S., and Belmonte, J. (2011). Methods for making induced pluripotent stem cells: reprogramming à la carte. Nature Reviews Genetics *12*, 231-242.

Gore, A., Li, Z., Fung, H.-L., Young, J.E., Agarwal, S., Antosiewicz-Bourget, J., Canto, I., Giorgetti, A., Israel, M.A., Kiskinis, E.*, et al.* (2011). Somatic coding mutations in human induced pluripotent stem cells. Nature *471*.

Grand, L.J.N., Gonzalez-Cano, L., and Pavlou, M.A. (2015). Neural stem cells in Parkinson's disease: a role for neurogenesis defects in onset and progression. Cellular and Molecular Life Sciences *72*, 773-797.

Grealish, S., Jönsson, M.E., Li, M., Kirik, D., Björklund, A., and Thompson, L.H. (2010). The A9 dopamine neuron component in grafts of ventral mesencephalon is an important determinant for recovery of motor function in a rat model of Parkinson's disease. Brain *133*, 482-495.

Grünewald, A., Breedveld, G.J., Lohmann-Hedrich, K., Rohé, C.F., König, I.R., Hagenah, J., Vanacore, N., Meco, G., Antonini, A., Goldwurm, S.*, et al.* (2007). Biological effects of the PINK1 c.1366C>T mutation: implications in Parkinson disease pathogenesis. Neurogenetics *8*, 103-109.

Guo, F., Liu, X., Cai, H., and Le, W. (2018). Autophagy in neurodegenerative diseases: pathogenesis and therapy. Brain Pathology *28*, 3-13.

Haddad, D., and Nakamura, K. (2015). Understanding the susceptibility of dopamine neurons to mitochondrial stressors in Parkinson's disease. FEBS Letters *589*, 3702-3713.

Halevy, T., and Urbach, A. (2014). Comparing ESC and iPSC—Based Models for Human Genetic Disorders. Journal of Clinical Medicine *3*, 1146-1162.

Han, J., Pluhackova, K., and Böckmann, R.A. (2017). The Multifaceted Role of SNARE Proteins in Membrane Fusion. Frontiers in Physiology *8*, 5.

Harper, W.J., Ordureau, A., and Heo, J.-M. (2018). Building and decoding ubiquitin chains for mitophagy. Nature Reviews Molecular Cell Biology *19*, 93.

Hattori, N., and Mizuno, Y. (2017). Twenty years since the discovery of the parkin gene. Journal of Neural Transmission *124*, 1037-1054.

Hegarty, S.V., Sullivan, A.M., and O'Keeffe, G.W. (2013). Midbrain dopaminergic neurons: A review of the molecular circuitry that regulates their development. Developmental Biology *379*, 123-138.

Heintz-Buschart, A., Pandey, U., Wicke, T., Sixel-Döring, F., Janzen, A., Sittig-Wiegand, E., Trenkwalder, C., Oertel, W.H., Mollenhauer, B., and Wilmes, P. (2018). The nasal and gut microbiome in Parkinson's disease and idiopathic rapid eye movement sleep behavior disorder. Movement Disorders *33*, 88-98.

Herce, H.D., Schumacher, D., Schneider, A.F.L., Ludwig, A.K., Mann, F.A., Fillies, M., Kasper, M.-A., Reinke, S., Krause, E., Leonhardt, H.*, et al.* (2017). Cell-permeable nanobodies for targeted immunolabelling and antigen manipulation in living cells. Nature Chemistry *9*.

Hernandez, D.G., Reed, X., and Singleton, A.B. (2016). Genetics in Parkinson disease: Mendelian versus non-Mendelian inheritance. Journal of Neurochemistry *139*, 59-74.

Heron, C.J., Wright, S.L., Melzer, T.R., Myall, D.J., MacAskill, M.R., Livingston, L., Keenan, R.J., Watts, R., Dalrymple-Alford, J.C., and Anderson, T.J. (2014). Comparing Cerebral Perfusion in Alzheimer's Disease and Parkinson's Disease Dementia: An ASL-MRI Study. Journal of Cerebral Blood Flow & Metabolism *34*, 964-970.

Herrero-Mendez, A., Almeida, A., Fernández, E., Maestre, C., Moncada, S., and Bolaños, J.P. (2009). The bioenergetic and antioxidant status of neurons is controlled by continuous degradation of a key glycolytic enzyme by APC/C–Cdh1. Nature Cell Biology *11*.

Hewer, R.L. (1997). The economic impact of neurological illness on the health and wealth of the nation and of individuals. Journal of neurology, neurosurgery, and psychiatry *63 Suppl 1*, 23.

Heyer, W.-D., Ehmsen, K.T., and Liu, J. (2010). Regulation of Homologous Recombination in Eukaryotes. Annual review of genetics *44*, 113-139.

Hillje, A.-L., and Schwamborn, J.C. (2016). Utilization of stem cells to model Parkinson's disease – current state and future challenges. Future Neurology *11*, 171-186.

Hindle, J.V. (2010). Ageing, neurodegeneration and Parkinson's disease. Age and Ageing *39*, 156-161.

Hirsch, E.C., Jenner, P., and Przedborski, S. (2013). Pathogenesis of Parkinson's disease. Movement Disorders *28*, 24-30.

Hockemeyer, D., and Jaenisch, R. (2016). Induced Pluripotent Stem Cells Meet Genome Editing. Cell Stem Cell *18*, 573-586.

Hokayem, J., Cukier, H.N., and Dykxhoorn, D.M. (2016). Blood Derived Induced Pluripotent Stem Cells (iPSCs): Benefits, Challenges and the Road Ahead. Journal of Alzheimers Disease & Parkinsonism *6*, 1-3.

Hou, P., Li, Y., Zhang, X., Liu, C., Guan, J., Li, H., Zhao, T., Ye, J., Yang, W., Liu, K.*, et al.* (2013). Pluripotent Stem Cells Induced from Mouse Somatic Cells by Small-Molecule Compounds. Science *341*, 651-654.

Huch, M., Knoblich, J.A., Lutolf, M.P., and Martinez-Arias, A. (2017). The hope and the hype of organoid research. Development *144*, 938-941.

Huh, D., Hamilton, G.A., and Ingber, D.E. (2011). From 3D cell culture to organs-on-chips. Trends in Cell Biology *21*, 745-754.

Huh, D., Kim, H., Fraser, J.P., Shea, D.E., Khan, M., Bahinski, A., Hamilton, G.A., and Ingber, D.E. (2013). Microfabrication of human organs-on-chips. Nature Protocols *8*.

Hunn, B., Cragg, S.J., Bolam, P.J., Spillantini, M.-G., and Wade-Martins, R. (2015). Impaired intracellular trafficking defines early Parkinson's disease. Trends in Neurosciences *38*, 178-188.

Hurlbut, W.B. (2006). Framing the Future: Embryonic Stem Cells, Ethics and the Emerging Era of Developmental Biology. Pediatric Research *59*.

Hyun, I., Wilkerson, A., and Johnston, J. (2016). Embryology policy: Revisit the 14-day rule. Nature News *533*, 169.

Iannielli, A., Bido, S., Folladori, L., Segnali, A., Cancellieri, C., Maresca, A., Massimino, L., Rubio, A., Morabito, G., Caporali, L.*, et al.* (2018). Pharmacological Inhibition of Necroptosis Protects from Dopaminergic Neuronal Cell Death in Parkinson's Disease Models. Cell Reports *22*, 2066-2079.

Itakura, E., Kishi-Itakura, C., and Mizushima, N. (2012). The Hairpin-type Tail-Anchored SNARE Syntaxin 17 Targets to Autophagosomes for Fusion with Endosomes/Lysosomes. Cell *151*, 1256-1269.

Jaenisch, R., and Young, R. (2008). Stem Cells, the Molecular Circuitry of Pluripotency and Nuclear Reprogramming. Cell *132*, 567-582.

Jang, Y., and Jung, J. (2017). Direct conversion from skin fibroblasts to functional dopaminergic neurons for biomedical application. Biomedical Dermatology *1*, 4.

Jankovic, J. (2008). Parkinson's disease: clinical features and diagnosis. Journal of Neurology, Neurosurgery & Psychiatry *79*, 368-376.

Jankovic, J., and Aguilar, G.L. (2008). Current approaches to the treatment of Parkinson's disease. Neuropsychiatric Disease and Treatment *Volume 4*, 743-757.

Jena, N.R. (2012). DNA damage by reactive species: Mechanisms, mutation and repair. Journal of Biosciences *37*, 503-517.

Jinek, M., Chylinski, K., Fonfara, I., Hauer, M., Doudna, J.A., and Charpentier, E. (2012). A programmable dual-RNA–guided DNA endonuclease in adaptive bacterial immunity. Science *337*, 816-821.

Jo, J., Xiao, Y., Sun, A., Cukuroglu, E., Tran, H.-D., Göke, J., Tan, Z., Saw, T., Tan, C.-P., Lokman, H.*, et al.* (2016). Midbrain-like Organoids from Human Pluripotent Stem Cells Contain Functional Dopaminergic and Neuromelanin-Producing Neurons. Cell Stem Cell *19*, 248-257.

Kaiser, J. (2017). A human has been injected with gene editing tools to cure his disabling disease. Here's what you need to know. Science.

Karbowski, M., and Youle, R.J. (2011). Regulating mitochondrial outer membrane proteins by ubiquitination and proteasomal degradation. Current Opinion in Cell Biology *23*, 476-482.

Kaur, J., and Debnath, J. (2015). Autophagy at the crossroads of catabolism and anabolism. Nature Reviews Molecular Cell Biology *16*.

Kim, C. (2014). Disease modeling and cell based therapy with iPSC: future therapeutic option with fast and safe application. Blood Research *49*, 7-14.

Kim, C. (2015). iPSC technology-Powerful hand for disease modeling and therapeutic screen. BMB Reports *48*, 256-265.

Kim, E., Kang, K., and Ju, J. (2017). CRISPR-Cas9: a promising tool for gene editing on induced pluripotent stem cells. The Korean Journal of Internal Medicine *32*, 42-61.

Kim, H.-J., and Jeon, B.S. (2014). Hypothesis: Somatic Mosaicism and Parkinson Disease. Experimental Neurobiology *23*, 271-276.

Kim, H.-J., and Jin, C. (2012). Stem Cells in Drug Screening for Neurodegenerative Disease. The Korean Journal of Physiology & Pharmacology *16*, 1-9.

Kim, H., Bernitz, J.M., Lee, D.-F., and Lemischka, I.R. (2014). Genomic editing tools to model human diseases with isogenic pluripotent stem cells. Stem cells and development *23*, 2673-2686.

Kim, J.-S. (2016). Genome editing comes of age. Nature Protocols *11*, 1573-1578.

Kim, K., Doi, A., Wen, B., Ng, K., Zhao, R., Cahan, P., Kim, J., Aryee, M.J., Ji, H., Ehrlich, L.I.R.*, et al.* (2010). Epigenetic memory in induced pluripotent stem cells. Nature *467*, 285-290.

Kim, Y., Choi, S., D'Avanzo, C., Hebisch, M., Sliwinski, C., Bylykbashi, E., Washicosky, K.J., Klee, J.B., Brüstle, O., Tanzi, R.E.*, et al.* (2015). A 3D human neural cell culture system for modeling Alzheimer's disease. Nature Protocols *10*, 985-1006.

Klein, C., and Westenberger, A. (2012). Genetics of Parkinson's Disease. Cold Spring Harbor Perspectives in Medicine *2*.

Klionsky, D.J., Abdelmohsen, K., Abe, A., Abedin, M., Abeliovich, H., Arozena, A., Adachi, H., Adams, C.M., Adams, P.D., Adeli, K.*, et al.* (2016). Guidelines for the use and interpretation of assays for monitoring autophagy (3rd edition). Autophagy *12*, 1-222.

Koentjoro, B., Park, J.-S., and Sue, C.M. (2017). Nix restores mitophagy and mitochondrial function to protect against PINK1/Parkin-related Parkinson's disease. Scientific Reports *7*.

Koller, W., Vetere-Overfield, B., Gray, C., Alexander, C., Chin, T., Dolezal, J., Hassanein, R., and Tanner, C. (1990). Environmental risk factors in Parkinson's disease. Neurology *40*, 1218-1218.

Kordower, J.H., Chu, Y., Hauser, R.A., Freeman, T.B., and Olanow, W.C. (2008). Lewy body–like pathology in long-term embryonic nigral transplants in Parkinson's disease. Nature Medicine *14*, 504-506.

Kriks, S., Shim, J.-W., Piao, J., Ganat, Y.M., Wakeman, D.R., Xie, Z., Carrillo-Reid, L., Auyeung, G., Antonacci, C., Buch, A.*, et al.* (2011). Dopamine neurons derived from human ES cells efficiently engraft in animal models of Parkinson/'s disease. Nature *480*, 547-551.

Kumar, A., Tamjar, J., Waddell, A.D., Woodroof, H.I., Raimi, O.G., Shaw, A.M., Peggie, M., Muqit, M.M.K., and van Aalten, D.M.F. (2017). Structure of PINK1 and mechanisms of Parkinson's disease associated mutations. eLife *6*.

Kumar, K., Djarmati-Westenberger, A., and Grünewald, A. (2011). Genetics of Parkinson's Disease. Seminars in Neurology *31*, 433-440.

Kumari, U., and Tan, E.K. (2009). LRRK2 in Parkinson's disease: genetic and clinical studies from patients. FEBS Journal *276*, 6455-6463.

Lancaster, M.A., and Knoblich, J.A. (2014). Organogenesis in a dish: Modeling development and disease using organoid technologies. Science.

Lancaster, M.A., Renner, M., Martin, C.-A., Wenzel, D., Bicknell, L.S., Hurles, M.E., Homfray, T., Penninger, J.M., Jackson, A.P., and Knoblich, J.A. (2013). Cerebral organoids model human brain development and microcephaly. Nature *501*, 373-379.

Lang, A.E., and Widner, H. (2002). Deep brain stimulation for Parkinson's disease: Patient selection and evaluation. Movement Disorders *17*.

Langston, J.W., Ballard, P., Tetrud, J.W., and Irwin, I. (1983). Chronic Parkinsonism in humans due to a product of meperidine-analog synthesis. Science *219*, 979-980.

Langston, J.W., Langston, E.B., and Irwin, I. (1984). MPTP-induced parkinsonism in human and non-human primates--clinical and experimental aspects. Acta neurologica Scandinavica Supplementum *100*, 49-54.

Larsen, S.B., Hanss, Z., and Krüger, R. (2018). The genetic architecture of mitochondrial dysfunction in Parkinson's disease. Cell and Tissue Research, 1-17.

Le, W., Wu, J., and Tang, Y. (2016). Protective Microglia and Their Regulation in Parkinson's Disease. Frontiers in Molecular Neuroscience *9*, 89.

Lev, N., Roncevic, D., Roncevich, D., Ickowicz, D., Melamed, E., and Offen, D. (2006). Role of DJ-1 in Parkinson's disease. Journal of Molecular Neuroscience *29*, 215-225.

Li, J.-Q., Tan, L., and Yu, J.-T. (2014). The role of the LRRK2 gene in Parkinsonism. Molecular Neurodegeneration *9*, 1-17.

Li, J.-Y., Englund, E., Holton, J.L., Soulet, D., Hagell, P., Lees, A.J., Lashley, T., Quinn, N.P., Rehncrona, S., Björklund, A*., et al.* (2008). Lewy bodies in grafted neurons in subjects with Parkinson's disease suggest host-to-graft disease propagation. Nature Medicine *14*, 501-503.

Li, W., Wu, X., Hu, X., Wang, T., Liang, S., Duan, Y., Jin, F., and Qin, B. (2017a). Structural changes of gut microbiota in Parkinson's disease and its correlation with clinical features. Science China Life Sciences *60*, 1223-1233.

Li, X., Burnight, E.R., Cooney, A.L., Malani, N., Brady, T., Sander, J.D., Staber, J., Wheelan, S.J., Joung, K.J., McCray, P.B*., et al.* (2013). piggyBac transposase tools for genome engineering. Proceedings of the National Academy of Sciences *110*.

Li, Y.-C., Zhu, K., and Young, T.-H. (2017b). Induced pluripotent stem cells, form in vitro tissue engineering to in vivo allogeneic transplantation. Journal of thoracic disease *9*, 455-459.

Lin, M.K., and Farrer, M.J. (2014). Genetics and genomics of Parkinson's disease. Genome Medicine *6*, 1-16.

Liu, W., Acín-Peréz, R., Geghman, K.D., Manfredi, G., Lu, B., and Li, C. (2011). Pink1 regulates the oxidative phosphorylation machinery via mitochondrial fission. Proceedings of the National Academy of Sciences *108*, 12920-12924.

Liu, Y., and Deng, W. (2016). Reverse engineering human neurodegenerative disease using pluripotent stem cell technology. Brain Research *1638*, 30-41.

Lorenz, C., Lesimple, P., Bukowiecki, R., Zink, A., Inak, G., Mlody, B., Singh, M., Semtner, M., Mah, N., Auré, K*., et al.* (2017). Human iPSC-Derived Neural Progenitors Are an Effective Drug Discovery Model for Neurological mtDNA Disorders. Cell Stem Cell.

Lozano, C.S., Tam, J., and Lozano, A.M. (2018). The changing landscape of surgery for Parkinson's Disease. Movement Disorders *33*, 36-47.

Lücking, C.B., Dürr, A., Bonifati, V., Vaughan, J., Michele, G., Gasser, T., Harhangi, B.S., Meco, G., Denèfle, P., Wood, N.W*., et al.* (2000). Association between Early-Onset Parkinson's Disease and Mutations in the Parkin Gene. The New England Journal of Medicine *342*, 1560-1567.

Lullo, E., and Kriegstein, A.R. (2017). The use of brain organoids to investigate neural development and disease. Nature Reviews Neuroscience *18*.

Luzio, P.J., Pryor, P.R., and Bright, N.A. (2007). Lysosomes: fusion and function. Nature Reviews Molecular Cell Biology *8*, 622-632.

Ma, H., Morey, R., O'Neil, R.C., He, Y., Daughtry, B., Schultz, M.D., Hariharan, M., Nery, J.R., Castanon, R., Sabatini, K.*, et al.* (2014). Abnormalities in human pluripotent cells due to reprogramming mechanisms. Nature *511*, 177-183.

Magalhaes, J., Gegg, M.E., Migdalska-Richards, A., and Schapira, A.H. (2018). Effects of ambroxol on the autophagy-lysosome pathway and mitochondria in primary cortical neurons. Scientific Reports *8*, 1385.

Mahlknecht, P., Gasperi, A., Willeit, P., Kiechl, S., Stockner, H., Willeit, J., Rungger, G., Sawires, M., Nocker, M., Rastner, V.*, et al.* (2016). Prodromal Parkinson's disease as defined per MDS research criteria in the general elderly community. Movement Disorders *31*, 1405-1408.

Malgieri, G., and Eliezer, D. (2008). Structural effects of Parkinson's disease linked DJ-1 mutations. Protein Science *17*, 855-868.

Malik, N., and Rao, M.S. (2013). Methods in Molecular Biology. Methods in molecular biology (Clifton, NJ) *997*, 23-33.

Malki, K., Koritskaya, E., Harris, F., Bryson, K., Herbster, M., and Tosto, M.G. (2016). Epigenetic differences in monozygotic twins discordant for major depressive disorder. Translational Psychiatry *6*.

Manzoni, C. (2017). The LRRK2–macroautophagy axis and its relevance to Parkinson's disease. Biochemical Society Transactions *45*, 155-162.

Marsden, C.D. (1983). Neuromelanin and Parkinson's disease. Journal of neural transmission Supplementum *19*, 121-141.

Martini-Stoica, H., Xu, Y., Ballabio, A., and Zheng, H. (2016). The Autophagy–Lysosomal Pathway in Neurodegeneration: A TFEB Perspective. Trends in Neurosciences *39*, 221-234.

Marxreiter, F., Regensburger, M., and Winkler, J. (2013). Adult neurogenesis in Parkinson's disease. Cellular and Molecular Life Sciences *70*.

Matheoud, D., Sugiura, A., Bellemare-Pelletier, A., Laplante, A., Rondeau, C., Chemali, M., Fazel, A., Bergeron, J.J., Trudeau, L.-E.E., Burelle, Y.*, et al.* (2016). Parkinson's Disease-Related Proteins PINK1 and Parkin Repress Mitochondrial Antigen Presentation. Cell.

McEwan, D.G., Popovic, D., Gubas, A., Terawaki, S., Suzuki, H., Stadel, D., Coxon, F.P., Miranda de Stegmann, D., Bhogaraju, S., Maddi, K.*, et al.* (2015). PLEKHM1 Regulates Autophagosome-Lysosome Fusion through HOPS Complex and LC3/GABARAP Proteins. Molecular Cell *57*, 39-54.

McGeer, P.L., Itagaki, S., Boyes, B.E., and McGeer, E.G. (1988). Reactive microglia are positive for HLA-DR in the substantia nigra of Parkinson's and Alzheimer's disease brains. Neurology *38*, 1285-1291.

McGovern, M.M., Lippa, N., Bagiella, E., Schuchman, E.H., Desnick, R.J., and Wasserstein, M.P. (2013). Morbidity and mortality in type B Niemann–Pick disease. Genetics in Medicine *15*.

McLelland, G.-L., Lee, S.A., McBride, H.M., and Fon, E.A. (2016). Syntaxin-17 delivers PINK1/parkin-dependent mitochondrial vesicles to the endolysosomal system. The Journal of Cell Biology *214*, 275-291.

McWilliams, T.G., and Muqit, M.M.K. (2017). PINK1 and Parkin: emerging themes in mitochondrial homeostasis. Current Opinion in Cell Biology *45*, 83-91.

McWilliams, T.G., Prescott, A.R., Montava-Garriga, L., Ball, G., Singh, F., Barini, E., Muqit, M., Brooks, S.P., and Ganley, I.G. (2018). Basal Mitophagy Occurs Independently of PINK1 in Mouse Tissues of High Metabolic Demand. Cell Metabolism *27*, 439-449.

Mehanna, R., Moore, S., Hou, G.J., Sarwar, A.I., and Lai, E.C. (2014). Comparing clinical features of young onset, middle onset and late onset Parkinson's disease. Parkinsonism & Related Disorders *20*, 530-534.

Menzies, F.M., Fleming, A., and Rubinsztein, D.C. (2015). Compromised autophagy and neurodegenerative diseases. Nature Reviews Neuroscience *16*, 345-357.

Mertens, J., Marchetto, M.C., Bardy, C., and Gage, F.H. (2016). Evaluating cell reprogramming, differentiation and conversion technologies in neuroscience. Nature Reviews Neuroscience *17*.

Merwe, C., Dashti, Z., Christoffels, A., Loos, B., and Bardien, S. (2015). Evidence for a common biological pathway linking three Parkinson's disease-causing genes: parkin, PINK1 and DJ-1. European Journal of Neuroscience *41*, 1113-1125.

Michel, P.P., Hirsch, E.C., and Hunot, S. (2016). Understanding Dopaminergic Cell Death Pathways in Parkinson Disease. Neuron *90*, 675-691.

Miesenböck, G., Angelis, D.A., and Rothman, J.E. (1998). Visualizing secretion and synaptic transmission with pH-sensitive green fluorescent proteins. Nature *394*, 192-195.

Miklya, I., Göltl, P., Hafenscher, F., and Pencz, N. (2014). The role of parkin in Parkinson's disease. Neuropsychopharmacologia Hungarica *16*, 67-76.

Mizushima, N., and Komatsu, M. (2011). Autophagy: Renovation of Cells and Tissues. Cell *147*, 728-741.

Monzel, A.S., Smits, L.M., Hemmer, K., Hachi, S., Moreno, E., van Wuellen, T., Jarazo, J., Walter, J., Brüggemann, I., Boussaad, I.*, et al.* (2017). Derivation of Human Midbrain-Specific Organoids from Neuroepithelial Stem Cells. Stem Cell Reports *8*, 1144-1154.

Moreno, E., Hachi, S., Hemmer, K., Trietsch, S.J., Baumuratov, A.S., Hankemeier, T., Vulto, P., Schwamborn, J.C., and Fleming, R.M.T. (2015). Differentiation of neuroepithelial stem cells into functional dopaminergic neurons in 3D microfluidic cell culture. Lab on a Chip *15*, 2419-2428.

Mori, H., Kondo, T., Yokochi, M., Matsumine, H., Nakagawa-Hattori, Y., Miyake, T., Suda, K., and Mizuno, Y. (1998). Pathologic and biochemical studies of juvenile parkinsonism linked to chromosome 6q. Neurology *51*, 890-892.

Moustafa, A.A., Chakravarthy, S., Phillips, J.R., Gupta, A., Keri, S., Polner, B., Frank, M.J., and Jahanshahi, M. (2016). Motor symptoms in Parkinson's disease: A unified framework. Neuroscience & Biobehavioral Reviews *68*, 727-740.

Myhre, R., Steinkjer, S., Stormyr, A., Nilsen, G.L., Zayyad, H., Horany, K., Nusier, M.K., and Klungland, H. (2008). Significance of the parkin and PINK1gene in Jordanian families with incidences of young-onset and juvenile parkinsonism. BMC Neurology *8*, 1-11.

Napolitano, G., and Ballabio, A. (2016). TFEB at a glance. J Cell Sci *129*, 2475-2481.

Negoro, T., Okura, H., and Matsuyama, A. (2017). Induced Pluripotent Stem Cells: Global Research Trends. BioResearch Open Access *6*, 63-73.

Nelson, C.E., Hakim, C.H., Ousterout, D.G., Thakore, P.I., Moreb, E.A., Rivera, R.M., Madhavan, S., Pan, X., Ran, A.F., Yan, W.X.*, et al.* (2016). In vivo genome editing improves muscle function in a mouse model of Duchenne muscular dystrophy. Science *351*, 403-407.

Ni, H.-M., Williams, J.A., and Ding, W.-X. (2015). Mitochondrial dynamics and mitochondrial quality control. Redox Biology *4*, 6-13.

Nixon, R.A. (2013). The role of autophagy in neurodegenerative disease. Nature Medicine *19*, 983-997.

Noisa, P., Raivio, T., and Cui, W. (2015). Neural Progenitor Cells Derived from Human Embryonic Stem Cells as an Origin of Dopaminergic Neurons. Stem Cells International *2015*, 647437.

Nuytemans, K., Theuns, J., Cruts, M., and Broeckhoven, C. (2010). Genetic etiology of Parkinson disease associated with mutations in the SNCA, PARK2, PINK1, PARK7, and LRRK2 genes: a mutation update. Human Mutation *31*, 763-780.

Ohyama, M., and Okano, H. (2013). Promise of Human Induced Pluripotent Stem Cells in Skin Regeneration and Investigation. Journal of Investigative Dermatology *134*, 605-609.

Oliveira, M.A.P., Balling, R., Smidt, M.P., and Fleming, R.M.T. (2017). Embryonic development of selectively vulnerable neurons in Parkinson's disease. npj Parkinson's Disease *3*, 21.

Ong, W.-Y., Kumar, U., Switzer, R., Sidhu, A., Suresh, G., Hu, C.-Y., and Patel, S. (2001). Neurodegeneration in Niemann-Pick type C disease mice. Experimental Brain Research *141*, 218-231.

Pagano, G., Ferrara, N., Brooks, D.J., and Pavese, N. (2016). Age at onset and Parkinson disease phenotype. Neurology *86*, 1400-1407.

Pang, Z.P., Yang, N., Vierbuchen, T., Ostermeier, A., Fuentes, D.R., Yang, T.Q., Citri, A., Sebastiano, V., Marro, S., Südhof, T.C*., et al.* (2011). Induction of human neuronal cells by defined transcription factors. Nature *476*.

Pankratz, N., and Foroud, T. (2007). Genetics of Parkinson disease. Genetics in Medicine *9*.

Paquet, D., Kwart, D., Chen, A., Sproul, A., Jacob, S., Teo, S., Olsen, K., Gregg, A., Noggle, S., and Tessier-Lavigne, M. (2016). Efficient introduction of specific homozygous and heterozygous mutations using CRISPR/Cas9. Nature *533*, 125-129.

Parashar, A., and Udayabanu, M. (2017). Gut microbiota: Implications in Parkinson's disease. Parkinsonism & Related Disorders *38*, 1-7.

Park, A., and Stacy, M. (2009). Non-motor symptoms in Parkinson's disease. Journal of Neurology *256*, 293-298.

Passier, R., Orlova, V., and Mummery, C. (2016). Complex Tissue and Disease Modeling using hiPSCs. Cell Stem Cell *18*, 309-321.

Perandones, C., Pellene, L.A., Giugni, J.C., Calvo, D.S., Raina, G.B., Cuevas, Mata, I.F., Zabetian, C.P., Caputo, M., Corach, D*., et al.* (2015). Letter to the Editor: Hypothesis: Somatic Mosaicism and Parkinson Disease. Experimental Neurobiology *24*, 173-175.

Pfisterer, U., Kirkeby, A., Torper, O., Wood, J., Nelander, J., Dufour, A., Björklund, A., Lindvall, O., Jakobsson, J., and Parmar, M. (2011). Direct conversion of human fibroblasts to dopaminergic neurons. Proceedings of the National Academy of Sciences *108*, 10343-10348.

Pickrell, A.M., and Youle, R.J. (2015). The roles of PINK1, parkin, and mitochondrial fidelity in Parkinson's disease. Neuron *85*, 257-273.

Pissadaki, E.K., and Bolam, P.J. (2013). The energy cost of action potential propagation in dopamine neurons: clues to susceptibility in Parkinson's disease. Frontiers in Computational Neuroscience *7*, 13.

Polymeropoulos, M.H., Higgins, J.J., Golbe, L.I., Johnson, W.G., Ide, S.E., Iorio, G., Sanges, G., Stenroos, E.S., Pho, L.T., Schaffer, A.A*., et al.* (1996). Mapping of a Gene for Parkinson's Disease to Chromosome 4q21-q23. Science *274*, 1197-1199.

Polymeropoulos, M.H., Lavedan, C., Leroy, E., Ide, S.E., Dehejia, A., Dutra, A., Pike, B., Root, H., Rubenstein, J., Boyer, R*., et al.* (1997). Mutation in the α-Synuclein Gene Identified in Families with Parkinson9s Disease. Science *276*, 2045-2047.

Przedborski, S. (2017). The two-century journey of Parkinson disease research. Nature Reviews Neuroscience *18*.

Qian, X., Nguyen, H., Song, M.M., Hadiono, C., Ogden, S.C., Hammack, C., Yao, B., Hamersky, G.R., Jacob, F., Zhong, C*., et al.* (2016). Brain-Region-Specific Organoids Using Mini-bioreactors for Modeling ZIKV Exposure. Cell *165*, 1238-1254.

Rakovic, A., Seibler, P., and Klein, C. (2015). iPS models of Parkin and PINK1. Biochemical Society Transactions *43*, 302-307.

Ramanan, V.K., and Saykin, A.J. (2013). Pathways to neurodegeneration: mechanistic insights from GWAS in Alzheimer's disease, Parkinson's disease, and related disorders. American journal of neurodegenerative disease *2*, 145-175.

Ran, A.F., Hsu, P.D., Lin, C.-Y., Gootenberg, J.S., Konermann, S., Trevino, A.E., Scott, D.A., Inoue, A., Matoba, S., Zhang, Y*., et al.* (2013a). Double Nicking by RNA-Guided CRISPR Cas9 for Enhanced Genome Editing Specificity. Cell *154*.

Ran, A.F., Hsu, P.D., Wright, J., Agarwala, V., Scott, D.A., and Zhang, F. (2013b). Genome engineering using the CRISPR-Cas9 system. Nature Protocols *8*, 2281-2308.

Reardon, S. (2014). Gene-editing method tackles HIV in first clinical test. Nature.

Recasens, A., and Dehay, B. (2014). Alpha-synuclein spreading in Parkinson's disease. Frontiers in Neuroanatomy *8*, 159.

Reeve, A., Simcox, E., and Turnbull, D. (2014). Ageing and Parkinson's disease: Why is advancing age the biggest risk factor? Ageing Research Reviews *14*, 19-30.

Reinhardt, P., Glatza, M., Hemmer, K., Tsytsyura, Y., Thiel, C.S., Höing, S., Moritz, S., Parga, J.A., Wagner, L., Bruder, J.M.*, et al.* (2013). Derivation and Expansion Using Only Small Molecules of Human Neural Progenitors for Neurodegenerative Disease Modeling. PLoS ONE *8*.

Requejo-Aguilar, R., Lopez-Fabuel, I., Fernandez, E., Martins, L.M., Almeida, A., and Bolaños, J.P. (2014). PINK1 deficiency sustains cell proliferation by reprogramming glucose metabolism through HIF1. Nature Communications *5*.

Rietdijk, C.D., Perez-Pardo, P., Garssen, J., van Wezel, R.J.A., and Kraneveld, A.D. (2017). Exploring Braak's Hypothesis of Parkinson's Disease. Frontiers in Neurology *8*, 37.

Rios, A.C., and Clevers, H. (2018). Imaging organoids: a bright future ahead. Nature Methods *15*, 24.

Ritz, B. (2006). Environmental Toxins and Neurodegenerative Diseases: A Challenge for Epidemiologists. Epidemiology *17*, 2.

Sampson, T.R., Debelius, J.W., Thron, T., Janssen, S., Shastri, G.G., Ilhan, Z., Challis, C., Schretter, C.E., Rocha, S., Gradinaru, V.*, et al.* (2016). Gut Microbiota Regulate Motor Deficits and Neuroinflammation in a Model of Parkinson's Disease. Cell *167*, 1469-1514438656.

Sancar, A., Lindsey-Boltz, L.A., Ünsal-Kaçmaz, K., and Linn, S. (2004). MOLECULAR MECHANISMS OF MAMMALIAN DNA REPAIR AND THE DNA DAMAGE CHECKPOINTS. Annual review of biochemistry *73*, 39-85.

Sánchez-Danés, A., Richaud-Patin, Y., Carballo-Carbajal, I., Jiménez-Delgado, S., Caig, C., Mora, S., Guglielmo, C., Ezquerra, M., Patel, B., Giralt, A.*, et al.* (2012). Disease-specific phenotypes in dopamine neurons from human iPS-based models of genetic and sporadic Parkinson's disease. EMBO Molecular Medicine *4*, 380-395.

Sander, J.D., and Joung, K.J. (2014). CRISPR-Cas systems for editing, regulating and targeting genomes. Nature Biotechnology *32*, 347-355.

Sardiello, M. (2018). Transcription factor EB: from master coordinator of lysosomal pathways to candidate therapeutic target in degenerative storage diseases. Annals of the New York Academy of Sciences *1371*, 3-14.

Sargsyan, A., Cai, J., Fandino, L.B., Labasky, M.E., Forostyan, T., Colosimo, L.K., Thompson, S.J., and Graham, T.E. (2015). Rapid parallel measurements of macroautophagy and mitophagy in mammalian cells using a single fluorescent biosensor. Scientific Reports *5*, 12397.

Savica, R., Grossardt, B.R., Bower, J.H., Ahlskog, E.J., and Rocca, W.A. (2016). Time Trends in the Incidence of Parkinson Disease. JAMA Neurology *73*, 981.

Schapira, A., Chaudhuri, R.K., and Jenner, P. (2017). Non-motor features of Parkinson disease. Nature Reviews Neuroscience *18*, 435-450.

Schapira, A.H., and Jenner, P. (2011). Etiology and pathogenesis of Parkinson's disease. Movement Disorders *26*, 1049-1055.

Schapira, A.H.V. (2006). Mitochondrial disease. The Lancet *60*, 288-291.

Schapira, A.H.V., and Tolosa, E. (2010). Molecular and clinical prodrome of Parkinson disease: implications for treatment. Nature Reviews Neurology *6*, 309-317.

Schärer, O.D. (2003). Chemistry and Biology of DNA Repair. Angewandte Chemie International Edition *42*, 2946-2974.

Schrag, A., and Schott, J.M. (2006). Epidemiological, clinical, and genetic characteristics of early-onset parkinsonism. The Lancet Neurology *5*, 355-363.

Schulte, C., and Gasser, T. (2011). Genetic basis of Parkinson's disease: inheritance, penetrance, and expression. The Application of Clinical Genetics *Volume 4*, 67-80.

Schwamborn, J. (2018). Is Parkinson's disease a neurodevelopmental disorder and will brain organoids help us to understand it? Stem cells and development.

Schwarz, T.L. (2013). Mitochondrial Trafficking in Neurons. Cold Spring Harbor Perspectives in Biology *5*.

Scott, L., Dawson, V.L., and Dawson, T.M. (2017). Trumping neurodegeneration: Targeting common pathways regulated by autosomal recessive Parkinson's disease genes. Experimental Neurology *298*, 191-201.

Seaman, M.N.J. (2012). The retromer complex – endosomal protein recycling and beyond. J Cell Sci *125*, 4693-4702.

Seibler, P., Graziotto, J., Jeong, H., Simunovic, F., Klein, C., and Krainc, D. (2011). Mitochondrial Parkin recruitment is impaired in neurons derived from mutant PINK1 induced pluripotent stem cells. The Journal of neuroscience : the official journal of the Society for Neuroscience *31*, 5970-5976.

Settembre, C., Fraldi, A., Medina, D.L., and Ballabio, A. (2013). Signals from the lysosome: a control centre for cellular clearance and energy metabolism. Nature Reviews Molecular Cell Biology *14*, 283-296.

Sharma, A., Wu, J.C., and Wu, S.M. (2013). Induced pluripotent stem cell-derived cardiomyocytes for cardiovascular disease modeling and drug screening. Stem Cell Research & Therapy *4*, 150.

Sherer, T.B., Betarbet, R., Testa, C.M., Seo, B., Richardson, J.R., Kim, J., Miller, G.W., Yagi, T., Matsuno-Yagi, A., and Greenamyre, T.J. (2003). Mechanism of toxicity in rotenone models of Parkinson's disease. The Journal of neuroscience : the official journal of the Society for Neuroscience *23*, 10756-10764.

Shi, Y., Inoue, H., Wu, J.C., and Yamanaka, S. (2016). Induced pluripotent stem cell technology: a decade of progress. Nature Reviews Drug Discovery *16*, 115-130.

Shiba, Y., Gomibuchi, T., Seto, T., Wada, Y., Ichimura, H., Tanaka, Y., Ogasawara, T., Okada, K., Shiba, N., Sakamoto, K.*, et al.* (2016). Allogeneic transplantation of iPS cell-derived cardiomyocytes regenerates primate hearts. Nature *538*.

Shin, J.-H., Dawson, V.L., and Dawson, T.M. (2009). SnapShot: Pathogenesis of Parkinson's Disease. Cell *139*, 4400-44000.

Siddiqui, I., Pervaiz, N., and Abbasi, A. (2016). The Parkinson Disease gene SNCA: Evolutionary and structural insights with pathological implication. Scientific Reports *6*.

Singh, V.K., Kalsan, M., Kumar, N., Saini, A., and Chandra, R. (2015). Induced pluripotent stem cells: applications in regenerative medicine, disease modeling, and drug discovery. Frontiers in Cell and Developmental Biology *3*, 2.

Smith, Y., Wichmann, T., Factor, S.A., and DeLong, M.R. (2011). Parkinson's Disease Therapeutics: New Developments and Challenges Since the Introduction of Levodopa. Neuropsychopharmacology *37*.

Soldner, F., and Jaenisch, R. (2012). iPSC Disease Modeling. Science *338*, 1155-1156.

Soldner, F., Laganière, J., Cheng, A.W., Hockemeyer, D., Gao, Q., Alagappan, R., Khurana, V., Golbe, L.I., Myers, R.H., Lindquist, S.*, et al.* (2011). Generation of Isogenic Pluripotent Stem Cells Differing Exclusively at Two Early Onset Parkinson Point Mutations. Cell *146*, 318-331.

Song, W., Wang, F., Lotfi, P., Sardiello, M., and Segatori, L. (2014). 2-Hydroxypropyl-β-cyclodextrin Promotes Transcription Factor EB-mediated Activation of Autophagy IMPLICATIONS FOR THERAPY. Journal of Biological Chemistry *289*, 10211-10222.

Soubannier, V., McLelland, G.-L., Zunino, R., Braschi, E., Rippstein, P., Fon, E.A., and McBride, H.M. (2012). A Vesicular Transport Pathway Shuttles Cargo from Mitochondria to Lysosomes. Current Biology *22*, 135-141.

Spillantini, M., Schmidt, M., Lee, V., Trojanowski, J.Q., Jakes, R., and Goedert, M. (1997). α-Synuclein in Lewy bodies. Nature *388*, 839-840.

Stiles, J., and Jernigan, T.L. (2010). The Basics of Brain Development. Neuropsychology Review *20*, 327-348.

Struhal, W., Presslauer, S., Spielberger, S., Zimprich, A., Auff, E., Bruecke, T., Poewe, W., and Ransmayr, G. (2014). VPS35 Parkinson's disease phenotype resembles the sporadic disease. Journal of Neural Transmission *121*, 755-759.

Sugiura, A., McLelland, G.-L.L., Fon, E.A., and McBride, H.M. (2014). A new pathway for mitochondrial quality control: mitochondrial-derived vesicles. The EMBO journal *33*, 2142-2156.

Sulzer, D. (2007). Multiple hit hypotheses for dopamine neuron loss in Parkinson's disease. Trends in Neurosciences *30*, 244-250.

Sun, C.-k., Zhou, D., Zhang, Z., He, L., Zhang, F., Wang, X., Yuan, J., Chen, Q., Wu, L.-G., and Yang, Q. (2014). Senescence impairs direct conversion of human somatic cells to neurons. Nature Communications *5*, 4112.

Sung, J., Kam, C., and Shuler, M.L. (2010). A microfluidic device for a pharmacokinetic–pharmacodynamic (PK – PD) model on a chip. Lab on a Chip *10*, 446-455.

Takahashi, K., and Yamanaka, S. (2006). Induction of Pluripotent Stem Cells from Mouse Embryonic and Adult Fibroblast Cultures by Defined Factors. Cell *126*, 663-676.

Thomas, B., and Beal, F.M. (2007). Parkinson's disease. Human Molecular Genetics *16*.

Tredici, K., and Braak, H. (2008). A not entirely benign procedure: progression of Parkinson's disease. Acta Neuropathologica *115*, 379-384.

Trétiakoff, C. (1919). … à l'étude de l'anatomie pathologique du locus niger de Soemmering avec quelques déductions relatives à la pathogénie des troubles du tonus musculaire …. … à l'étude de l'anatomie pathologique du locus niger de Soemmering avec quelques déductions relatives à la pathogénie des troubles du tonus musculaire ….

Turrens, J.F. (2003). Mitochondrial formation of reactive oxygen species. The Journal of Physiology *552*, 335-344.

Valente, E., Abou-Sleiman, P.M., Caputo, V., Muqit, M.M.K., Harvey, K., Gispert, S., Ali, Z., Turco, D., Bentivoglio, A., Healy, D.G.*, et al.* (2004). Hereditary Early-Onset Parkinson's Disease Caused by Mutations in PINK1. Science *304*, 1158-1160.

van den Berge, S.A., van Strien, M.E., Korecka, J.A., Dijkstra, A.A., Sluijs, J.A., Kooijman, L., Eggers, R., Filippis, L., Vescovi, A.L., Verhaagen, J.*, et al.* (2011). The proliferative capacity of the subventricular zone is maintained in the parkinsonian brain. Brain *134*, 3249-3263.

Vernier, P., Moret, F., Callier, S., Snapyan, M., Wersinger, C., and Sidhu, A. (2004). The Degeneration of Dopamine Neurons in Parkinson's Disease: Insights from Embryology and Evolution of the Mesostriatocortical System. Annals of the New York Academy of Sciences *1035*, 231-249.

Vilariño-Güell, C., Wider, C., Ross, O.A., Dachsel, J.C., Kachergus, J.M., Lincoln, S.J., Soto-Ortolaza, A.I., Cobb, S.A., Wilhoite, G.J., Bacon, J.A.*, et al.* (2011). VPS35 Mutations in Parkinson Disease. The American Journal of Human Genetics *89*, 162-167.

Voges, J., Waerzeggers, Y., Maarouf, M., Lehrke, R., Koulousakis, A., Lenartz, D., and Sturm, V. (2006). Deep-brain stimulation: long-term analysis of complications caused by hardware and surgery—experiences from a single centre. Journal of Neurology, Neurosurgery & Psychiatry *77*, 868-872.

Vonk, L.A., de Windt, T.S., Slaper-Cortenbach, I.C.M., and Saris, D.B.F. (2015). Autologous, allogeneic, induced pluripotent stem cell or a combination stem cell therapy? Where are we headed in cartilage repair and why: a concise review. Stem Cell Research & Therapy *6*, 1-11.

Wakabayashi, K., Tanji, K., Mori, F., and Takahashi, H. (2007). The Lewy body in Parkinson's disease: Molecules implicated in the formation and degradation of α-synuclein aggregates. Neuropathology *27*, 494-506.

Wallings, R., Manzoni, C., and Bandopadhyay, R. (2015). Cellular processes associated with LRRK2 function and dysfunction. FEBS Journal *282*, 2806-2826.

Walter, J., Nickels, S., and Schwamborn, J. (2017). Human induced pluripotent stem cell-derived neuronal progenitors are a suitable and effective drug discovery model for neurological mtDNA disorders. Stem Cell Investigation *1*, 101-101.

Wang, Q., Liu, Y., and Zhou, J. (2015a). Neuroinflammation in Parkinson's disease and its potential as therapeutic target. Translational Neurodegeneration *4*, 1-9.

Wang, W., Wang, X., Fujioka, H., Hoppel, C., Whone, A.L., Caldwell, M.A., Cullen, P.J., Liu, J., and Zhu, X. (2015b). Parkinson's disease–associated mutant VPS35 causes mitochondrial dysfunction by recycling DLP1 complexes. Nature Medicine *22*.

Wang, Y., Li, L., Hou, C., Lai, Y., Long, J., Liu, J., Zhong, Q., and Diao, J. (2016). SNARE-mediated membrane fusion in autophagy. Seminars in Cell & Developmental Biology *60*, 97-104.

Wenker, S.D., Casalía, M., Candedo, V.C.C., Casabona, J.C., and Pitossi, F.J. (2015). Cell reprogramming and neuronal differentiation applied to neurodegenerative diseases: Focus on Parkinson's disease. FEBS letters *589*, 3396-3406.

Willett, R., Martina, J.A., Zewe, J.P., Wills, R., Hammond, G.R.V., and Puertollano, R. (2017). TFEB regulates lysosomal positioning by modulating TMEM55B expression and JIP4 recruitment to lysosomes. Nature Communications *8*, 1580.

Williams-Gray, C.H., Foltynie, T., Lewis, S.J.G., and Barker, R.A. (2006). Cognitive Deficits and Psychosis in Parkinson's Disease. CNS Drugs *20*, 477-505.

Williams, E.T., Chen, X., and Moore, D.J. (2017). VPS35, the Retromer Complex and Parkinson's Disease. Journal of Parkinson's Disease *Preprint*, 1-15.

Wilmut, I., Schnieke, A.E., McWhir, J., Kind, A.J., and Campbell, K.H.S. (1997). Viable offspring derived from fetal and adult mammalian cells. Nature *385*.

Woodard, C.M., Campos, B.A., Kuo, S.-H.H., Nirenberg, M.J., Nestor, M.W., Zimmer, M., Mosharov, E.V., Sulzer, D., Zhou, H., Paull, D.*, et al.* (2014). iPSC-derived dopamine neurons reveal differences between monozygotic twins discordant for Parkinson's disease. Cell reports *9*, 1173-1182.

World Health Organization (2011). Global Health and Ageing.

World Health Organization (2015). World report on ageing and health.

World Health Organization (2017). Health workforce for ageing populations.

Wu, S.-L., Liscic, R.M., Kim, S., Sorbi, S., and Yang, Y.-H. (2017). Nonmotor Symptoms of Parkinson's Disease. Parkinson's Disease *2017*, 4382518.

Xie, F., Ye, L., Chang, J.C., Beyer, A.I., Wang, J., Muench, M.O., and Kan, Y. (2014). Seamless gene correction of β-thalassemia mutations in patient-specific iPSCs using CRISPR/Cas9 and piggyBac. Genome Research.

Xilouri, M., Brekk, O., and Stefanis, L. (2016). Autophagy and Alpha-Synuclein: Relevance to Parkinson's Disease and Related Synucleopathies. Movement Disorders *31*, 178-192.

Xu, Z., Chu, X., Jiang, H., Schilling, H., Chen, S., and Feng, J. (2017). Induced dopaminergic neurons: A new promise for Parkinson's disease. Redox Biology *11*, 606-612.

Yalcin-Cakmakli, G., Olgiati, S., Quadri, M., Breedveld, G.J., Cortelli, P., Bonifati, V., and Elibol, B. (2014). A new Turkish family with homozygous FBXO7 truncating mutation and juvenile atypical parkinsonism. Parkinsonism & Related Disorders *20*, 1248-1252.

Yamanaka, S. (2012). Induced Pluripotent Stem Cells: Past, Present, and Future. Cell Stem Cell *10*, 678-684.

Yamano, K., Matsuda, N., and Tanaka, K. (2016). The ubiquitin signal and autophagy: an orchestrated dance leading to mitochondrial degradation. EMBO reports *17*, 300-316.

Yan, Y., Shin, S., Jha, B., Liu, Q., Sheng, J., Li, F., Zhan, M., Davis, J., Bharti, K., Zeng, X.*, et al.* (2013). Efficient and Rapid Derivation of Primitive Neural Stem Cells and Generation of Brain Subtype Neurons From Human Pluripotent Stem Cells. Stem Cells Translational Medicine *2*, 862-870.

Yang, L., Briggs, A.W., Chew, W., Mali, P., Guell, M., Aach, J., Goodman, D., Cox, D., Kan, Y., Lesha, E.*, et al.* (2016). Engineering and optimising deaminase fusions for genome editing. Nature Communications *7*.

Yang, S.-Y., Beavan, M., Chau, K.-Y., Taanman, J.-W., and Schapira, A. (2017). A Human Neural Crest Stem Cell-Derived Dopaminergic Neuronal Model Recapitulates Biochemical Abnormalities in GBA1 Mutation Carriers. Stem Cell Reports *8*, 728-742.

Youle, R.J., and Narendra, D.P. (2011). Mechanisms of mitophagy. Nature reviews Molecular cell biology *12*, 9-14.

Young, P.E., Jew, S., Buckland, M.E., Pamphlett, R., and Suter, C.M. (2017). Epigenetic differences between monozygotic twins discordant for amyotrophic lateral sclerosis (ALS) provide clues to disease pathogenesis. PLOS ONE *12*.

Yusa, K. (2013). Seamless genome editing in human pluripotent stem cells using custom endonuclease–based gene targeting and the piggyBac transposon. Nature Protocols *8*, 2061-2078.

Zhang, C.-W., Hang, L., Yao, T.-P., and Lim, K.-L. (2016). Parkin Regulation and Neurodegenerative Disorders. Frontiers in Aging Neuroscience *7*, 248.

Zhang, S., Tang, M.-b., Luo, H.-y., Shi, C.-h., and Xu, Y.-m. (2017). Necroptosis in neurodegenerative diseases: a potential therapeutic target. Cell Death & Disease *8*.

Zhang, Y.-d., and Zhao, J.-j. (2015). TFEB Participates in the Aβ-Induced Pathogenesis of Alzheimer's Disease by Regulating the Autophagy-Lysosome Pathway. DNA and cell biology *34*, 661-668.

Zhao, Z., Xu, M., Wu, M., Tian, X., Zhang, C., and Fu, X. (2015). Transdifferentiation of Fibroblasts by Defined Factors. Cellular Reprogramming *17*, 151-159.

Zhi, X., Feng, W., Rong, Y., and Liu, R. (2018). Anatomy of autophagy: from the beginning to the end. Cellular and Molecular Life Sciences *75*, 815-831.

6. Appendices

6.1 Manuscripts

6.1.1 Manuscript IV

CRISPR/Cas9 and piggyBac-mediated footprint-free LRRK2-G2019S knock-in reveals neuronal complexity phenotypes and α-Synuclein modulation in dopaminergic neurons

Xiaobing Qing, Jonas Walter, **Javier Jarazo**, Jonathan Arias-Fuenzalida, Anna-Lena Hillje, Jens C. Schwamborn*

University of Luxembourg, Luxembourg Centre for Systems Biomedicine (LCSB), 6, avenue du Swing, L-4367 Belvaux, Luxembourg

Status: The manuscript is published in Stem Cell Research, 24 (2017) 44-50

CRISPR/Cas9 and piggyBac-mediated footprint-free LRRK2-G2019S knock-in reveals neuronal complexity phenotypes and α-Synuclein modulation in dopaminergic neurons

Xiaobing Qing, Jonas Walter, Javier Jarazo, Jonathan Arias-Fuenzalida, Anna-Lena Hillje, Jens C. Schwamborn*

University of Luxembourg, Luxembourg Centre for Systems Biomedicine (LCSB), 6, avenue du Swing, L-4367 Belvaux, Luxembourg

*Correspondence: jens.schwamborn@uni.lu

Abstract

The p.G2019S mutation of the leucine-rich repeat kinase 2 (LRRK2) has been identified as the most prevalent genetic cause of familial and sporadic Parkinson's disease (PD). The Cre-LoxP recombination system has been used to correct the LRRK2-G2019S mutation in patient derived human induced pluripotent stem cells (hiPSCs) in order to generate isogenic controls. However, the remaining LoxP site can influence gene expression. In this study, we report the generation of a footprint-free LRRK2-G2019S isogenic hiPS cell line edited with the CRISPR/Cas9 and piggyBac technologies. We observed that the percentage of Tyrosine Hydroxylase (TH) positive neurons with a total neurite length of more than 2000µm was significantly reduced in LRRK2-G2019S dopaminergic (DA) neurons. The average branch number in LRRK2-G2019S DA neurons was also decreased. In addition, we have shown that *in vitro* TH positive neurons with a total neurite length of more than 2000µm were positive for Serine 129 phosphorylated (S129P) alpha-Synuclein (αS) and we hypothesize that S129P-αS plays a role in the maintenance or formation of long neurites. In summary, our footprint-free LRRK2-G2019S isogenic cell lines allow standardized, genetic background independent, *in vitro* PD modeling and provide new insights into the role of LRRK2-G2019S and S129P-αS in the pathogenesis of PD.

Keywords

LRRK2-G2019S, CRISPR/Cas9, piggyBac, Parkinson's disease, hiPS, α-Synuclein, Serine129 phosphorylated α-Synuclein

Abbreviations

PD: Parkinson's disease; LRRK2: leucine-rich repeat kinase 2; G2019S: Glycine 2019 mutated to Serine; SNpc*:* substantia nigra pars compacta; DA: dopaminergic; LBs: Lewy Bodies; αS: α-Synuclein; S129P-αS: Serine 129 phosphorylated α-Synuclein; hiPSCs: human induced pluripotent stem cells; HR: homologous recombination; hESCs: human embryonic stem cells; HSV-DTK: herpes simplex virus thymidine kinase; DSB: double strand break.

1. Introduction

Parkinson's disease (PD) is the second most common neurodegenerative disorder[1]. One of the main pathological features of PD is the degeneration of the pigmented dopaminergic neurons (DA) in the *substantia nigra pars compacta* (SNpc) of the midbrain. Genetic analysis of PD patients reveals that a fraction of cases can be explained by genetic mutations [2, 3]. So far, 28 loci have been identified as potential risk factors, and of these, leucine-rich repeat kinase 2 (LRRK2) gene related mutations are the most common genetic cause of sporadic and familial PD [4]. Among the LRRK2 mutations, the most common is p.G2019S (c.G6055A). The p.G2019S mutation increases the kinase activity of LRRK2, thereby inducing toxicity [5], and it has been reported as genetically dominant.

Another feature of PD is the appearance of protein aggregates, called Lewy Bodies (LBs), in the remaining SNpc DA neurons [6]. The major component of LBs is the protein α-Synuclein (αS) [7]. Since 90% of αS in LBs is phosphorylated at Serine 129 (S129P) [8], S129P-αS has been implicated as the cause of αS aggregation and SNpc DA neuron degeneration [9]. Additionally, LRRK2 also has been described as component of LBs [10]. The potential function of LRRK2 in LBs and whether LRRK2 is directly phosphorylating αS are still being discussed controversially [11].

Human induced pluripotent stem cells (hiPSCs) have the potential to differentiate into various types of somatic cells and can be used to derive PD-relevant DA neurons from patients [12]. The iPSC technology has been used extensively for PD *in vitro* disease modeling, including the analysis of pathological functions of LRRK2-G2019S. Increased stress sensitivity and reduced neurite complexity have been reported [13, 14]. However, most of these studies on LRRK2-G2019S ignore differences in genetic background between patients and healthy controls. Such differences can hide relevant aspects of PD pathogenesis [15]. Hence, ideal comparisons should evaluate cell lines with an identical genetic background, which differ only in the mutation under investigation, i.e., isogenic cell lines. Several LRRK2-G2019S isogenic cell lines have been generated by other groups using Zinc finger- and Cre/LoxP systems [16]. The major drawback of the Cre/LoxP system is that a 34-bp-long LoxP site is left behind in the chromatin, typically in an intron close to the position where mutations are introduced or corrected. However, leaving this LoxP site in the intron has been reported to affect the expression of the targeted allele [17]. Particularly, for heterozygous mutations like the LRRK2-G2019S this might result in cells that silence the mutant allele and only the wild-type allele is expressed. Additionally, if by chance, the LoxP site was inserted in an unknown regulatory element in the

intron, this may affect the regulation of other genes [18]. These facts clearly highlight the need for the rigorous generation of footprint-free isogenic cell lines.

CRISPR/Cas9 is a newly developed genome editing tool that is superior in its simplicity and efficiency in comparison to Zinc finger nucleases and TALENs [19, 20]. Even though the CRISPR/Cas9 system is highly efficient at inducing double stranded break (DSB) in the genome, the rate-determining step, homologous recombination (HR), is still extremely rare in hiPSCs [21]. Introducing reporter systems or selectable markers greatly facilitates the identification of rare recombination events. Nevertheless, after selection the reporter or selection marker needs to be removed. As an alternative to the Cre/LoxP system, the piggyBac transposon system allows complete removal of selection cassette in a footprint-free manner [22, 23]. In this study, we combined the CRISPR/Cas9 and piggyBac systems to generate footprint-free LRRK2-G2019S knock-in isogenic cell lines in order to assess the contribution of this single mutation to PD cellular phenotypes. We analyzed DA neuron neurite complexity and S129P-αS in our newly generated footprint-free isogenic cell lines as well as another pair of reporter gene-free isogenic cell lines. Our here described model is able to recapitulate PD-specific phenotypes concerning neurite complexity and provides new insights into the role of S129P-αS. Furthermore, we demonstrate that cellular phenotypes can be rescued through pharmacological inhibition of the LRRK2 kinase activity.

2. Materials and Methods

2.1 gRNA and donor vector construction.

The pCas9_GFP plasmid (Addgene 44719) encoding human optimized Cas9 nuclease driven by CAG promoter was obtained from Addgene. gRNA targets with high activity and specificity were designed with the online software from Dr. Zhang Feng's lab (http://crispr.mit.edu) and inserted into gRNA_Cloning vector (Addgene 41824). To speed up the donor vector construction, two Hpa I sites were introduced into the pCAG-puroRDTK.Neo vector provided by Yuet Wai Kan (University of California, San Francisco, USA). The pCAG-puroRDTK.Neo plasmid was constructed from the 5′-PTK-3′ plasmid created by Allen Bradley (The Wellcome Trust Sanger Institute, Cambridge, UK). All primers were designed using Snapgene (GSL Biotech LLC, Chicago, USA).

2.2 hiPS cell culture and characterization.

Two types of hiPS cells were used: iPS1-H with healthy background, a gift from Dr. Bill Skarnes (The Wellcome Trust Sanger Institute, Cambridge, UK) and iPS2-P with the LRRK2-G2019S mutation from a PD

patients provided by Dr. Jared Sterneckert (Technical University of Dresden, Germany) and Dr. Thomas Gasser (German Center for Neurodegenerative Diseases, Tuebingen, Germany) [23] (Table 1). Human iPS cells were cultured on Matrigel in Essential 8 (E8) medium (Thermo Fisher, cat no. A1517001). For passaging, human iPS cells were treated with Accutase (Thermo Fisher, cat no. A1110501) for 5 minutes and seeded on new plate at dilution 1:50 in E8 medium added with 10μM Rock Inhibitor Y-27632 (Merck Chemicals Ltd, cat no. 688000). Molecular karyotyping analysis was performed at Life & Brain Center, Bonn, Germany. For pluripotency tests, spec ific antibodies to Sox2 (ab97959, 1:200, Rb, Abcam), Oct4 (ab19857, 1:300, Ms, Abcam), TRA-1-60 (MAB4360, 1:50, Ms, Millipore) and TRA-1-81 (MAB4381, 1:50, Ms, Millipore) were used.

2.3 hiPS cell nucleofection and genomic DNA extraction.

Log-phase hiPSC colonies were chosen and dissociated into single cells by Accutase (Thermo Fisher, cat no. A1110501). One million cells were collected for nucleofection with 1μg gRNA vector, 1μg Cas9 vector and 1μg donor vector using the 4D Nucleofector system (Lonza), following the human embryonic stem cell (hESC) optimized program. After the nucleofection, cells were washed with pre-warmed E8 medium by 200xg centrifugation, and seeded on a 6-well-plate in E8 medium added with 10μM Rock Inhibitor. Three days after nucleofection, 0.4 μg/ml puromycin was added to select cells that have the integration of selection cassette. Afterwards cells were grown for two weeks to form colonies. Since random integration will also confer puromycin resistance to cells, genotyping methods including 5'/3'-Junction PCR and random integration PCR were performed to exclude imprecise integration. To remove the selection cassette, a piggyBac transposase plasmid kindly provided by Allen Bradley (The Wellcome Trust Sanger Institute, Cambridge, UK) was nucleofected into cells using the same method. For quality checks of integration and cassette excision, 100μl genomic DNA extraction solution from a QuickExtract Kit (EPICENTRE Biotechnologies, Madison, WI, USA) was used to extract DNA from 10, 000 cells (1 well of 96-well-plate). To pick hiPSC colonies, 0.5μM EDTA (Thermo Fisher, cat no. 15575-020) was used to facilitate colonies scratching with pipet tips.

2.4 hNESC and DA neuron differentiation.

1.2 million hiPS single cells were deposited on 1 well of an AggreWell 400 plate (STEMCELL Technologies, Cat no. #27845) and distributed into microwells by 100xg centrifugation. Afterwards they were cultured for 24 hours to form Embryoid bodies (EBs). EBs were detached from the AggreWell by pipetting and transferred to ultra-low attachment plates. The following differentiation steps were done according to a previously published mDA derivation protocol [24].

2.5 Immunofluorescence staining and neurite complexity analysis.

Cells growing on Matrigel-coated coverslips were washed once with 1xPBS and fixed in 4% paraformaldehyde (PFA) (Sigma, Cat no. P6148) for 15 minutes, followed by three 1xPBS wash steps. Fixed cells were permeabilized and blocked by 1xPBS containing 2% FCS and 0.2% Triton X-100 (Carl Roth, Cat no. 3051.3) for 2 hours at room temperature. For immunofluorescence staining, standard protocols were followed. Briefly, fixed coverslips were incubated in primary antibodies diluted in 1xPBS containing and 2% FCS at 4°C overnight, followed by 1 hour incubation with matching secondary antibody solutions additionally containing Hoechst33342 (1:10000, Thermo Fisher, cat no. 62249) for nuclear staining at room temperature. For the characterization of human neuroepithelial stem cells (hNESCs), specific antibodies to Nestin (611659, 1:600, Ms, BD), PAX6 (PRB-278P, 1:300, Rb, Covance), Sox1 (AF3369, 1:100, Goat, R&D systems) and Sox2 (ab97959, 1:200, Rb, Abcam) were used. For mDA neurons, specific antibodies to TH (ab112, 1:500, Rb, Abcam), Tuj1 (ab107216, 1:1000, Chk, Abcam), FOXA2 (sc-101060, 1:100, Ms, Santa Cruz), MAP2 (MAB3418, 1:200, Ms, Millipore), Cleaved Caspase3 (9661, 1:200, Rb, Cell Signalling Technology), S129P-αS (Phospho S129) (ab184674, 1:400, Ms, Abcam) and αS (s3062, 1:500, Rb, Sigma) were used.

Images were acquired by confocal microscopy (LSM 510, Carl Zeiss) and analysed with the NeuronJ plugin of Image J (NIH, Bethesda, MD, USA).

3. Results

3.1 Footprint-free introduction of the LRRK2-G2019S mutation into human iPSCs with the CRISPR/Cas9 and piggyBac transposase systems.

In this study, we used the CRISPR/Cas9 nuclease system together with the piggyBac transposase approach to introduce the heterozygous point mutation LRRK2-G2019S (c.G6055A) into hiPSCs [22, 23, 25]. To mutate c.G6055A on Exon 41 of the hLRRK2 genome locus, we designed a guide RNA target site 4bp away from G6055, and chose a TAAA tetra-nucleotide 8bp away from the double strand break (DSB) site for introduction of a silent mutation to become a TTAA sequence, which is necessary for insertion or release of the piggyBac. We used 742bp (including the c.G6055A mutation) upstream of the TAAA site and 628bp downstream, as homologous arms for the construction of the piggyBac donor vector (**Figure 1A**). The donor vector contains an expression cassette for Puromycin N-acetyl-transferase, which upon integration in the genome renders the cells resistant to Puromycin (**Figure 1A**). The donor vector together with the gRNA and Cas9 vectors were electroporated into an iPSC line from a healthy donor not suffering from PD (iPS1-H). After treating the

electroporated hiPSCs with 0.2µg/ml Puromycin for 2 weeks, we obtained ~100 viable colonies. Of those, 16 colonies were expanded and genotyped. Junction PCR and Sanger sequencing from 14 colonies verified the presence of the specifically integrated selection cassette (**Figure 1A-C**).

3.2 Donor vector random integration screening.

A major concern with the usage of donor-mediated homologous recombination for gene-targeting is random integration of the whole plasmid DNA donor into the host genome [26]. We used primers positioned on the vector backbone to detect random integration events. The vector backbone should be absent from the host genome when correct homologous recombination takes place (**Figure 1A**). As negative controls, we used H_2O and gDNA from hiPSCs before the gene-editing process as templates. In contrast to previous studies using Southern Blotting, the PCR results showed that random integration events very often co-existed together with specific integration (**Figure 1B**). One possible explanation is that the screened colonies are heterogeneous, containing cells with correct gene-editing next to cells where only random integration occurred. Another possibility is that the PCR based detection of random integration events is more sensitive than the conventionally used Southern Blotting method, which is easily affected by deficient hybridization of probes and the amount of genomic DNA used [27].

3.3 Selection cassette removal by the piggyBac transposon.

In order to remove the selection cassette, we transiently expressed the piggyBac transposase in the selected hiPSCs clones (**Figure 1A**). The herpes simplex virus thymidine kinase (HSV-DTK) gene was included as negative selection marker. Two days after electroporation, cultures were seeded at low density as single cells and treated with FIAU. As a substrate of HSV-DTK, FIAU can be phosphorylated and becomes toxic to human cells [23]. Therefore, only cells where the selection cassette has been removed can survive and form new colonies. Surviving colonies were tested by PCR for the absence of PuroDTK. Genomic DNA from cells before transposase overexpression was used as a positive control. 36% of these FIAU-resistant sub-colonies were indeed free of PuroDTK (**Figure S1A**). The high survival rate of cells that still contained PuroDTK might be explainable by insufficient expression of HSV-DTK or their generally rather low FIAU sensitivity. However, since previous reports showed mitochondrial toxicity with higher concentrations or longer treatment of FIAU [28], we decided not to increase the dosage or the treatment time.

3.4 Cas9, gRNA and piggyBac transposase plasmids random integration screening.

In addition to the donor vector, in principle the plasmids for Cas9, gRNA and transposase expression also have the potential to enter the host genome though random integration due to the higher DNA delivery

efficiency of electroporation [29]. Accordingly, we designed primers to detect their potential integration, and appropriate controls were included to rule out false positive or false negative results. In contrast to the results for donor DNA, no random integration of these plasmids was detectable (**Figure S1B**). Furthermore, Sanger sequencing confirmed the introduction of the wanted mutation (**Figure 1C**). In summary, using highly stringent gene editing and genotyping methods, we generated a new isogenic hiPSC line (G2019S-iPS1-H) carrying the heterozygous G2019S mutation without any other detectable residuals.

3.5 Off-target detecting and pluripotency characterization in the LRRK2-G2019S edited hiPSCs.

Although the incidence of CRISPR/Cas9 nuclease-induced off-target indels is rare in human ES or iPS cell lines [30, 31], we performed an unbiased detection of the top 8 potential off-target sites predicted by the COD algorithm (cas9.wicp.net). For each site, we designed products that spanned ~1000bps of the predicted indel region. Sanger sequencing analysis demonstrated the absence of any off-target indels (**Figure S1C**). Immunostaining of selected hiPSCs with Oct4, Sox2, TRA-1-60 and TRA-1-81 indicated that they still preserved their pluripotency after gene editing (**Figure S1D**). Furthermore, no karyotype abnormalities were detected in the edited hiPSCs in comparison to their parental cells (**Figure S2 and S3**).

3.6 Differentiation of isogenic hiPS cell lines into DA neurons.

Subsequently, we compared our isogenic set with a previously described model of LRRK2-G2019S iPSCs (iPS2-P) [16] and determined if the previously described cellular phenotypes can be recapitulated. Previous studies showed that the LRRK2-G2019S mutation leads to reduced neurite complexity in dopaminergic neurons [14, 16, 32]. We have devised a small molecule-mediated differentiation protocol [24] to obtain DA neurons from hiPS cells. One unique feature of our protocol is the generation of human neuroepithelial stem cells (hNESCs) by using a combination of the factors CHIR, SB-431542, dorsomorphin and PMA (**Figure S4A**) firstly and then DA neurons with CHIR, SB-431542, dorsomorphin and PMA (**Figure S4B**). The hNESCs can be expanded for more than 20 passages without losing their capacity for differentiation into DA neurons. This feature of hNESCs could be helpful for high-throughput analysis requiring large numbers of DA neurons in a short time interval. In this study, differentiation included the here newly generated isogenic set from a non-patient background (LRRK2-WT-iPS1-H and LRRK2-G2019S-iPS1-H) and an isogenic set from a PD-patient background (LRRK2-WT-iPS2-P and LRRK2-G2019S-iPS2-P) [16]. The identity of the hNESCs was confirmed by the expression of the neural progenitor markers Pax6, Nestin, Sox1, and Sox2 (**Figure S4C**). The generation of DA neurons was confirmed by staining with Tyrosine Hydroxylase (TH),

Tubulin beta-1 chain (Tuj1), Hepatocyte nuclear factor 3-beta (FOXA2), and Microtubule-associated protein 2 (MAP2) (**Figure S4D**).

3.7 LRRK2-G2019S reduces the neurite complexity of DA neurons.

Firstly the number of neurites per TH^+ neuron was quantified 14 days after differentiation. Assessment of the total number of neurites per cell showed no significant differences for either isogenic pair (**Figure 2A, B**). Treatment with a LRRK2 kinase inhibitor (IN-1) [33] had no significant effect on the number of neurites per cell. Interestingly, however, the total neurite length per TH^+ neuron was significantly reduced in lines carrying the LRRK2-G2019S mutation (**Figure 2A, C**). Importantly, this aberrant shortening could be rescued by treatment with IN-1 (**Figure 2A, C**). The same observed was made for the number of neurite branches per neuron (**Figure 2A, D**). These results indicate that the heterozygous insertion of the p.G2019S mutation in an otherwise healthy background recapitulates cellular phenotypes observed in p.G2019S mutants from a PD background. Furthermore, the phenotypes in DA neurons can be rescued via pharmacological LRRK2 kinase inhibition, validating the use of the engineered lines for drug screening campaigns.

3.8 S129P-αS is necessary for the elongation of DA neuron neurite.

Previous studies showed that LRRK2-G2019S hiPSCs-derived DA neurons express higher levels of total αS [13, 14, 16]. To further test the cellular phenotype of LRRK2-G2019S DA neurons, we evaluated αS level after neuronal differentiation. We stained DA neurons 14 days after differentiation against αS. This revealed that, independent of the genotype, all TH^+ neurons were positive for αS (**Figure S5A-B**). In the next step, we stained with antibodies specific for S129P-αS. Surprisingly, we found that only DA neurons with very long neurites (neurite length >2000µm, maximum length up to 7000µm) were clearly positive for S129P-αS (**Figure 3A, S5A-B**). We did not observe co-staining of these S129P-αS positive neurons with the apoptosis marker cleaved-Caspase-3 (**Figure S6**) and therefore conclude that it is indeed unlikely that S129P-αS is toxic for DA neurons, at least at that stage of differentiation. Strikingly, the fraction of TH^+/S129P-$αS^+$ neurons was significantly reduced in LRRK2-G2019S mutant lines in comparison to their respective isogenic controls. Furthermore, in both cases this reduction was partially rescued by treatment with IN-1 (**Figure 3B**). These results confirm that engineered lines are suitable for the detection of disease related phenotypes as well as for testing drug candidates for phenotypic reversion.

4. Discussion

In the present study, we describe the generation of footprint-free LRRK2-G2019S knock-in hiPSCs. Using our two-step differentiation protocol [24], we generated DA neurons positive for TH, FOXA2, Tuj1 and MAP2. We demonstrated that the LRRK2-G2019S mutation leads to a significant reduction in the length and branching of neurites of DA neurons. This finding is consistent with previous studies [13, 14, 16]. Importantly, we obtain consistent phenotypes in patient specific lines with the mutation and in engineered cells where the mutation was introduced with the CRISPR/Cas9 system. Furthermore, these phenotypes can be rescued by treatment with the LRRK2 kinase inhibitor IN-1 [33].

To date, the function of αS and S129P-αS, and whether the S129P-αS increases or inhibits the aggregation and toxicity of αS remain elusive. Synuclein genes are only present in vertebrates, whose neurons have longer neurites and more neurite branches than invertebrates [34]. It is tempting to speculate that Synuclein proteins might play an important role in the formation or maintenance of the high neurite complexity in vertebrate neurons. DA neurons of the *substantia nigra*, which project to the *striatum*, are among the neurons with the most complex neurite extensions. αS might play a particularly important role in their maintenance. It has been shown that midbrain S129P-αS increases during development and aging in both humans and non-human primates [35, 36]. Analysis of proteins extracted from the SNpc showed that S129P-αS is slightly down-regulated in PD patients [35]. Immunohistochemical analysis of midbrain sections reveals healthy SNpc DA neurons are mostly positive for S129P-αS, while patients are mostly negative [37]. Interestingly, S129P-αS proteins are abnormally aggregated to form LBs in patient SNpc DA neurons [7]. The neural death might be explained by the loss-of-function of S129P-αS which might be trapped in LBs. Overexpression of PLK2, an enzyme that mediates the S129 phosphorylation of αS, can even suppress dopaminergic neurodegeneration *in vivo* [38]. This body of evidence indicates that S129P-αS can have a protective function in SNpc DA neurons and not a detrimental impact as previous thought.

In line with the *in vivo* studies mentioned above, TH^+/S129P-αS^+ neurons derived from our isogenic hiPSCs show significantly longer neurites than those of TH^+/S129P-αS^- neurons. Our results also show higher levels of TH^+/S129P-αS^+ neurons in a wild type LRRK2 context than in mutant LRRK2-G2019S neurons. The mechanisms underlying such phenomena require further investigation. We envision that the use of footprint-free isogenic models such as the one described here will be essential for such studies.

5. Conclusion

In summary, we describe the generation of a footprint-free isogenic LRRK2-G2019S iPSC line using the CRISPR/Cas9 and piggyBac systems. We provide evidence that the LRRK2-G2019S mutation alone leads to a reduction of neurite complexity in dopaminergic neurons. Furthermore, we demonstrate that DA neurons positive for S129P-αS can form neurites longer than 2000µm and that the LRRK2-G2019S mutation inhibits the development of this subtype of DA neurons. Furthermore, we show that introducing the LRRK2-G2019S mutation in a healthy genetic background faithfully recapitulates the cellular phenotypes observed in DA neurons from patients with the LRRK2-G2019S mutation. In addition, we provide evidences that such phenotypes can be rescued by drug treatment. Engineered isogenic lines, with non-pathogenic genetic backgrounds, will prove to be useful tools to evaluate phenotypes in complex genetic diseases that have hitherto been masked or enhanced by diverse genetic or environmental backgrounds, and they will facilitate phenotype-specific drug screening efforts.

Conflict of interest

J.C.S. is shareholder of Braingineering Technologies sarl (www.braingineering.lu).

Acknowledgments

We would like to thank Thea van Wuellen and Inga Brüggemann for excellent technical assistance.

We thank Dr. Jared Sterneckert (Technical University of Dresden, Germany), Dr. Thomas Gasser (German Center for Neurodegenerative Diseases, Tuebingen, Germany) and Dr. Bill Skarnes (The Wellcome Trust Sanger Institute, Cambridge, UK) for human iPSC lines. This project was supported by the LCSB pluripotent stem cell core facility. The JCS lab is supported by the Fonds National de la Recherche (FNR) (CORE, C13/BM/5791363) and by a University Luxembourg Internal Research Project grant (MidNSCs). X.Q., J.W and J.J. are supported by fellowships from the FNR (AFR, Aides à la Formation-Recherche). A.L.H. is supported by the Fonds National de la Recherche (FNR) (INTER/15/10922184/LysoPD_NCL). This is an EU Joint Programme - Neurodegenerative Disease Research (JPND) project (INTER/JPND/14/02; INTER/JPND/15/11092422). Further support comes from the SysMedPD project which has received funding from the European Union's Horizon 2020 research and innovation programme under grant agreement No 668738. We also thank the private donors who support our work at the LCSB.

Figure legend

Fig 1. Generation of footprint-free edited isogenic LRRK2-G2019S hiPS cell line.

(A) Schematic depiction of the footprint-free editing strategy using the CRISPR-Cas9 and piggyBac systems. The positions of the p.G2019S mutation (GGC to AGC), the guide RNA target / PAM and the selection cassette insertion site (TAAA to TTAA) are highlighted at the LRRK2 locus (top). The c.G6055A (p.G2019S) mutation is located on Exon (E) 41.

The targeting donor plasmid includes the backbone (blue), two homologous arms, a CAG driven Puromycin resistance gene and a DTK gene expression cassette (green). Short arrows in the backbone (blue) and arrows in the selection cassette (green) region indicate the positions of primers for detection of random integration (LA, left homologous arm; RA, right homologous arm; BM-Random, in the middle of backbone; 5'-Random-1 or 2, close to the left arm; 3'-Random-1 or 2, close to the right arm). Paired arrows within the LRRK2 locus outside of the homology arms and in the selection cassette (green) indicate the positions of primers for the junction PCR to detect the specific integration (5'-junction, close to the left arm; 3'-junction, close to the right arm); HR, homologous recombination.

(B) Agarose gel of 5'/3'-junction and 5'/3'-random integration PCR products in 16 puromycin resistant hiPSC colonies after electroporation. hiPS-WT and ddH_2O indicate negative controls, and Donor indicates positive controls for random integration.

(C) Sanger sequencing chromatograms confirm the specific integration (upper) and GGC->AGC mutation introduction after excision (bottom). WT, wild type hiPS; Colony 1/13/16, chosen from (B); R, A/G mixture; W, T/A mixture.

Fig 2. LRRK2-G2019S affects neurite complexity in dopaminergic neurons.

(A) Representative immunofluorescence images of Tuj1 (white), TH (red), and Tuj1/TH/DNA (blue) dopaminergic neurons with the indicated genotypes at 14 days of differentiation. Treatment with the LRRK2-IN-1 inhibitor for rescuing is indicated. iPS1-H, healthy background; iPS2-P, PD background.

(B) Quantification of the neurite number per neuron in the different groups.

(C) Quantification of total neurite length per neuron in the different groups.

(D) Quantification of the number of neurite branches per neuron in the different groups.

For each quantification, at least three independent experiments were conducted, for each parameter > 60 neurons per genotype were analyzed. Statistical analysis was done with Student's T test, N.S., not significant; *p < 0.05; **p < 0.01; ***p < 0.001. All scale bars represent 20µm.

Fig 3. LRRK2-G2019S reduces the fraction of S129P-αS positive dopaminergic neurons with long neurites.

(A) Representative immunofluorescence images of TH (red) and S129P-αS (green) in dopaminergic neurons with the indicated genotypes at 14 days of differentiation. The cell body as well as neurites and neurite-terminals are shown. iPS1-H, healthy background; iPS2-P, PD background.

(B) Quantification of the fraction of TH^+/S129P-αS^+ neurons of the total of TH^+ neurons in different groups. Treatment with the LRRK2-IN-1 inhibitor for phenotypic rescue is indicated. Samples were collected on Day 14. Bars represent the mean value.

For each quantification, at least three independent experiments were conducted, for each parameter > 60 neurons per genotype were analyzed. Statistical analysis was done with Student's T test, N.S., not significant; *p < 0.05; **p < 0.01; ***p < 0.001. All scale bars represent 20µm.

Table 1. Cell line information

The iPSC lines used in this study are listed. Information about donor age at sampling, gender, reprogramming method and gene-editing method for generation of isogenic controls is given.

References

[1] L. Bertram, R.E. Tanzi, The genetic epidemiology of neurodegenerative disease, J Clin Invest, 115 (2005) 1449-1457.
[2] W.E. Martin, W.I. Young, V.E. Anderson, Parkinson's disease. A genetic study, Brain, 96 (1973) 495-506.
[3] A. Barbeau, M. Roy, L. Boyer, Genetic studies in Parkinson's disease, Adv Neurol, 40 (1984) 333-339.
[4] C. Sandor, F. Honti, W. Haerty, K. Szewczyk-Krolikowski, P. Tomlinson, S. Evetts, S. Millin, T. Keane, S.A. McCarthy, R. Durbin, K. Talbot, M. Hu, C. Webber, C.P. Ponting, R. Wade-Martins, Whole-exome sequencing of 228 patients with sporadic Parkinson's disease, Sci Rep, 7 (2017) 41188.
[5] J.Q. Li, L. Tan, J.T. Yu, The role of the LRRK2 gene in Parkinsonism, Mol Neurodegener, 9 (2014) 47.
[6] M.S. Pollanen, D.W. Dickson, C. Bergeron, Pathology and biology of the Lewy body, J Neuropathol Exp Neurol, 52 (1993) 183-191.
[7] M.G. Spillantini, M.L. Schmidt, V.M. Lee, J.Q. Trojanowski, R. Jakes, M. Goedert, Alpha-synuclein in Lewy bodies, Nature, 388 (1997) 839-840.
[8] J.P. Anderson, D.E. Walker, J.M. Goldstein, R. de Laat, K. Banducci, R.J. Caccavello, R. Barbour, J. Huang, K. Kling, M. Lee, L. Diep, P.S. Keim, X. Shen, T. Chataway, M.G. Schlossmacher, P. Seubert, D. Schenk, S. Sinha, W.P. Gai, T.J. Chilcote, Phosphorylation of Ser-129 is the dominant pathological modification of alpha-synuclein in familial and sporadic Lewy body disease, J Biol Chem, 281 (2006) 29739-29752.
[9] A. Oueslati, Implication of Alpha-Synuclein Phosphorylation at S129 in Synucleinopathies: What Have We Learned in the Last Decade?, J Parkinsons Dis, 6 (2016) 39-51.
[10] J. Alegre-Abarrategui, O. Ansorge, M. Esiri, R. Wade-Martins, LRRK2 is a component of granular alpha-synuclein pathology in the brainstem of Parkinson's disease, Neuropathol Appl Neurobiol, 34 (2008) 272-283.
[11] I. Martin, V.L. Dawson, T.M. Dawson, Recent advances in the genetics of Parkinson's disease, Annu Rev Genomics Hum Genet, 12 (2011) 301-325.
[12] K. Takahashi, K. Tanabe, M. Ohnuki, M. Narita, T. Ichisaka, K. Tomoda, S. Yamanaka, Induction of pluripotent stem cells from adult human fibroblasts by defined factors, Cell, 131 (2007) 861-872.
[13] H.N. Nguyen, B. Byers, B. Cord, A. Shcheglovitov, J. Byrne, P. Gujar, K. Kee, B. Schule, R.E. Dolmetsch, W. Langston, T.D. Palmer, R.R. Pera, LRRK2 mutant iPSC-derived DA neurons demonstrate increased susceptibility to oxidative stress, Cell stem cell, 8 (2011) 267-280.
[14] A. Sanchez-Danes, Y. Richaud-Patin, I. Carballo-Carbajal, S. Jimenez-Delgado, C. Caig, S. Mora, C. Di Guglielmo, M. Ezquerra, B. Patel, A. Giralt, J.M. Canals, M. Memo, J. Alberch, J. Lopez-Barneo, M. Vila, A.M. Cuervo, E. Tolosa, A. Consiglio, A. Raya, Disease-specific phenotypes in dopamine neurons from human iPS-based models of genetic and sporadic Parkinson's disease, EMBO molecular medicine, 4 (2012) 380-395.
[15] K. Musunuru, Genome editing of human pluripotent stem cells to generate human cellular disease models, Disease models & mechanisms, 6 (2013) 896-904.
[16] P. Reinhardt, B. Schmid, L.F. Burbulla, D.C. Schondorf, L. Wagner, M. Glatza, S. Hoing, G. Hargus, S.A. Heck, A. Dhingra, G. Wu, S. Muller, K. Brockmann, T. Kluba, M. Maisel, R. Kruger, D. Berg, Y. Tsytsyura, C.S. Thiel, O.E. Psathaki, J. Klingauf, T. Kuhlmann, M. Klewin, H. Muller, T. Gasser, H.R. Scholer, J. Sterneckert, Genetic correction of a LRRK2 mutation in human iPSCs links parkinsonian neurodegeneration to ERK-dependent changes in gene expression, Cell Stem Cell, 12 (2013) 354-367.
[17] J. Zou, P. Mali, X. Huang, S.N. Dowey, L. Cheng, Site-specific gene correction of a point mutation in human iPS cells derived from an adult patient with sickle cell disease, Blood, 118 (2011) 4599-4608.
[18] I.D. Meier, C. Bernreuther, T. Tilling, J. Neidhardt, Y.W. Wong, C. Schulze, T. Streichert, M. Schachner, Short DNA sequences inserted for gene targeting can accidentally interfere with off-target gene expression, FASEB J, 24 (2010) 1714-1724.
[19] T. Gaj, C.A. Gersbach, C.F. Barbas, 3rd, ZFN, TALEN, and CRISPR/Cas-based methods for genome engineering, Trends in biotechnology, 31 (2013) 397-405.
[20] M. Jinek, A. East, A. Cheng, S. Lin, E. Ma, J. Doudna, RNA-programmed genome editing in human cells, eLife, 2 (2013) e00471.
[21] T.P. Zwaka, J.A. Thomson, Homologous recombination in human embryonic stem cells, Nature biotechnology, 21 (2003) 319-321.
[22] K. Yusa, R. Rad, J. Takeda, A. Bradley, Generation of transgene-free induced pluripotent mouse stem cells by the piggyBac transposon, Nat Methods, 6 (2009) 363-369.
[23] L. Ye, J. Wang, A.I. Beyer, F. Teque, T.J. Cradick, Z. Qi, J.C. Chang, G. Bao, M.O. Muench, J. Yu, J.A. Levy, Y.W. Kan, Seamless modification of wild-type induced pluripotent stem cells to the natural

CCR5Delta32 mutation confers resistance to HIV infection, Proc Natl Acad Sci U S A, 111 (2014) 9591-9596.
[24] P. Reinhardt, M. Glatza, K. Hemmer, Y. Tsytsyura, C.S. Thiel, S. Hoing, S. Moritz, J.A. Parga, L. Wagner, J.M. Bruder, G. Wu, B. Schmid, A. Ropke, J. Klingauf, J.C. Schwamborn, T. Gasser, H.R. Scholer, J. Sterneckert, Derivation and expansion using only small molecules of human neural progenitors for neurodegenerative disease modeling, PloS one, 8 (2013) e59252.
[25] F.A. Ran, P.D. Hsu, J. Wright, V. Agarwala, D.A. Scott, F. Zhang, Genome engineering using the CRISPR-Cas9 system, Nat Protoc, 8 (2013) 2281-2308.
[26] S. Saito, N. Adachi, Advances in the Development of Gene-Targeting Vectors to Increase the Efficiency of Genetic Modification, Biol Pharm Bull, 39 (2016) 25-32.
[27] R. Vilgalys, M. Hester, Rapid genetic identification and mapping of enzymatically amplified ribosomal DNA from several Cryptococcus species, J Bacteriol, 172 (1990) 4238-4246.
[28] C. Semino-Mora, M. Leon-Monzon, M.C. Dalakas, Mitochondrial and cellular toxicity induced by fialuridine in human muscle in vitro, Lab Invest, 76 (1997) 487-495.
[29] Z. Wang, P.J. Troilo, X. Wang, T.G. Griffiths, S.J. Pacchione, A.B. Barnum, L.B. Harper, C.J. Pauley, Z. Niu, L. Denisova, T.T. Follmer, G. Rizzuto, G. Ciliberto, E. Fattori, N.L. Monica, S. Manam, B.J. Ledwith, Detection of integration of plasmid DNA into host genomic DNA following intramuscular injection and electroporation, Gene Ther, 11 (2004) 711-721.
[30] A. Veres, B.S. Gosis, Q. Ding, R. Collins, A. Ragavendran, H. Brand, S. Erdin, C.A. Cowan, M.E. Talkowski, K. Musunuru, Low incidence of off-target mutations in individual CRISPR-Cas9 and TALEN targeted human stem cell clones detected by whole-genome sequencing, Cell Stem Cell, 15 (2014) 27-30.
[31] K. Suzuki, C. Yu, J. Qu, M. Li, X. Yao, T. Yuan, A. Goebl, S. Tang, R. Ren, E. Aizawa, F. Zhang, X. Xu, R.D. Soligalla, F. Chen, J. Kim, N.Y. Kim, H.K. Liao, C. Benner, C.R. Esteban, Y. Jin, G.H. Liu, Y. Li, J.C. Izpisua Belmonte, Targeted gene correction minimally impacts whole-genome mutational load in human-disease-specific induced pluripotent stem cell clones, Cell Stem Cell, 15 (2014) 31-36.
[32] S.J. Orenstein, S.H. Kuo, I. Tasset, E. Arias, H. Koga, I. Fernandez-Carasa, E. Cortes, L.S. Honig, W. Dauer, A. Consiglio, A. Raya, D. Sulzer, A.M. Cuervo, Interplay of LRRK2 with chaperone-mediated autophagy, Nat Neurosci, 16 (2013) 394-406.
[33] X. Deng, N. Dzamko, A. Prescott, P. Davies, Q. Liu, Q. Yang, J.D. Lee, M.P. Patricelli, T.K. Nomanbhoy, D.R. Alessi, N.S. Gray, Characterization of a selective inhibitor of the Parkinson's disease kinase LRRK2, Nat Chem Biol, 7 (2011) 203-205.
[34] I.J. Siddiqui, N. Pervaiz, A.A. Abbasi, The Parkinson Disease gene SNCA: Evolutionary and structural insights with pathological implication, Sci Rep, 6 (2016) 24475.
[35] G. Muntane, I. Ferrer, M. Martinez-Vicente, alpha-synuclein phosphorylation and truncation are normal events in the adult human brain, Neuroscience, 200 (2012) 106-119.
[36] A.L. McCormack, S.K. Mak, D.A. Di Monte, Increased alpha-synuclein phosphorylation and nitration in the aging primate substantia nigra, Cell Death Dis, 3 (2012) e315.
[37] A. Mamais, M. Raja, C. Manzoni, S. Dihanich, A. Lees, D. Moore, P.A. Lewis, R. Bandopadhyay, Divergent alpha-synuclein solubility and aggregation properties in G2019S LRRK2 Parkinson's disease brains with Lewy Body pathology compared to idiopathic cases, Neurobiology of disease, 58 (2013) 183-190.
[38] A. Oueslati, B.L. Schneider, P. Aebischer, H.A. Lashuel, Polo-like kinase 2 regulates selective autophagic alpha-synuclein clearance and suppresses its toxicity in vivo, Proceedings of the National Academy of Sciences of the United States of America, 110 (2013) E3945-3954.

CRISPR/Cas9 and piggyBac-mediated footprint-free LRRK2-G2019S knock-in reveals neuronal complexity phenotypes and α-Synuclein modulation in dopaminergic neurons

Xiaobing Qing, Jonas Walter, Javier Jarazo, Jonathan Arias-Fuenzalida, Anna-Lena Hillje, Jens C. Schwamborn*

University of Luxembourg, Luxembourg Centre for Systems Biomedicine (LCSB), 6, avenue du Swing, L-4367 Belvaux, Luxembourg

- Supplementary Information -

Supplementary Figure legends

Figure S1. Characterization of the edited hiPS colonies.

(A) Agarose gel of PCR products generated with primers detecting the selection cassette of sub-colonies picked after FIAU selection. hiPS-WT and ddH2O were used as negative controls, DNA from a colony before expression of the transposase was used as positive control.

(B) Agarose gel of PCR products amplified with primers detecting the plasmids of Cas9, gRNA and the Transposase in subclones that have been demonstrated to be "selection cassette-free". hiPS-WT and ddH2O were used as negative control, the plasmids for Cas9, gRNA and Transposase are used as positive controls.

(C) The sequences of predicted potential off-targets. The PAM sequences (blue) and the degree of matching to the gRNA target sequence (yellow) are highlighted. Sequencing revealed no indels of these regions after gene editing. All scale bars represent 20μm.

(D) Representative images of iPSC colonies after the gene-editing process. Expression of the pluripotency markers Oct4, Sox2. TRA-1-60 and TRA-1-81 is shown. DNA is visualized with Hoechst (HE) staining.

Figure S2. Molecular karyotype of LRRK2-WT iPS1-H parental cell line.

Single-nucleotide polymorphism (SNP) genotyping assay shows a normal male karyotype in the iPS1-H cell line. Chr 1-22/X/Y, Chromosome 1-22/X/Y.

Figure S3. Molecular karyotype of LRRK2-G2019S edited iPS1-H cell line.

SNP genotyping assay shows a normal male karyotype in the LRRK2-G2019S iPS1-H cell line edited by CRISPR/Cas9 and piggyBac. Chr 1-22/X/Y, Chromosome 1-22/X/Y.

Figure S4. Derivation of human neural epithelial stem cells (hNESCs) and midbrain DA neurons.

(A) Strategy for hNESC generation. Phase contrast images of single cells precipitated in the microwells of Aggrewell on Day 0 and Day 1 (1000 single human iPS cells per microwell). Phase contrast images of EBs growing in low affinity 6-well plates from Day 2 to Day 7. Phase contrast images of hNESCs culture on Marigel. EBs, embyoid bodies; CHIR, GSK3b inhibitor; SB-431542, ALK5 inhibitor; Dorsomorphin, AMPK inhibitor; PMA, activator of Protein Kinase C (PKC); AA, ascorbic acid.

(B) Strategy for mDA generation. Phase contrast images of hNESC and mDA (Day 6, 14, and 30). 20,000 hNESC single cells were seeded on a well of 24-well plate coated with Matrigel. For the first 6 days, PMA was added to the differentiation medium and afterwards PMA was removed. AA, ascorbic acid; dbcAMP, cAMP analogue dibutyryl, activator of cAMP dependent Protein Kinase A (PKA); hGDNF, Human Glail-Derived Neurotrophic Factor; hBDNF, Human Brain-Derived Neurotrophic Factor; Tgfb3, Transforming growth factor beta-3.

(C) Representative immunostaining images of hNESC colonies. Expression of hNESC markers Sox1, Sox2, Pax6 and Nestin is shown.

(D) Representative immunostaining images of hNESC colonies. Expression of mDA markers TH, Tuj1, MAP2, and FOXA2 shows that the midbrain dopaminergic neurons were generated efficiently.

All scale bars represent 20μm.

Figure S5. Expression pattern of total- and S129P-αS in subtypes of TH^+ neurons.

(A) Representative immunostaining images of subtypes of TH^+ neurons. TH (red), αS (white), S129P-αS (green) and DNA (blue) were shown. > 2000 μm, total neurite length longer than 2000 μm; < 2000 μm, total neurite length shorter than 2000 μm; iPS1-H, healthy background. All scale bars represent 20μm.

(B) Representative immunostaining images of subtypes of TH^+ neurons. TH (red), αS (white), S129P-αS (green) and DNA (blue) were shown. > 2000 μm, total neurite length longer than 2000 μm; < 2000 μm, total neurite length shorter than 2000 μm; iPS2-P, PD background. All scale bars represent 20μm.

Figure S6. S129P-αS doesn't induce apoptosis in neurons.

Representative immunostaining images of **S129P-αS$^+$** neurons. Cleaved Caspase-3 (red), S129P-αS (green) and DNA (blue) were shown. iPS1-H, healthy background; iPS2-P, PD background. All scale bars represent 20μm.

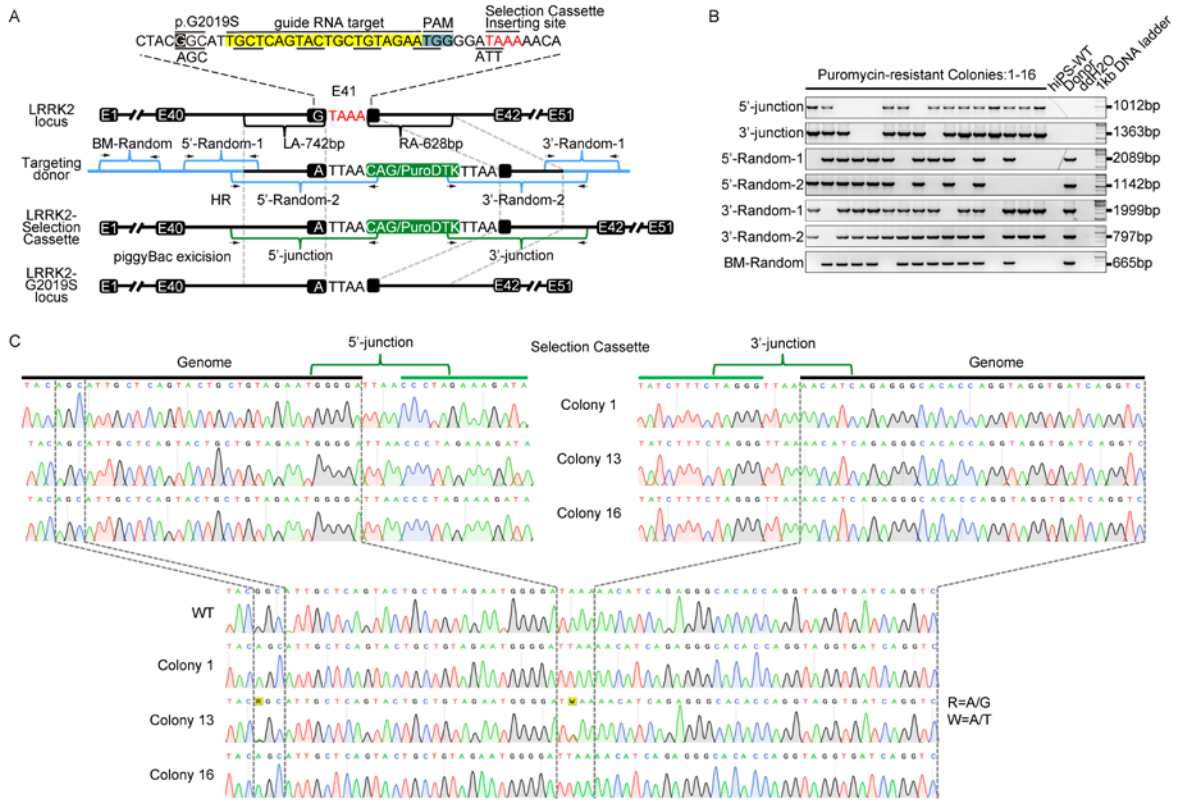

Figure 1

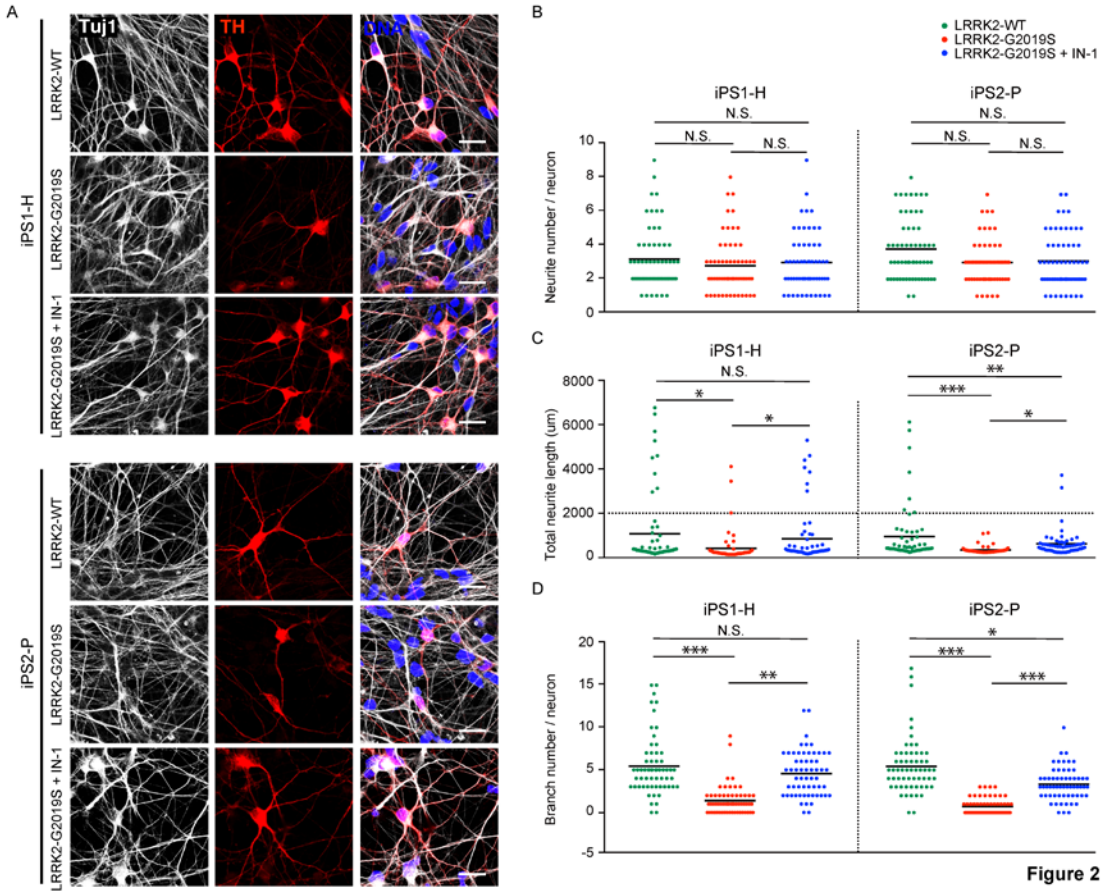

Figure 2

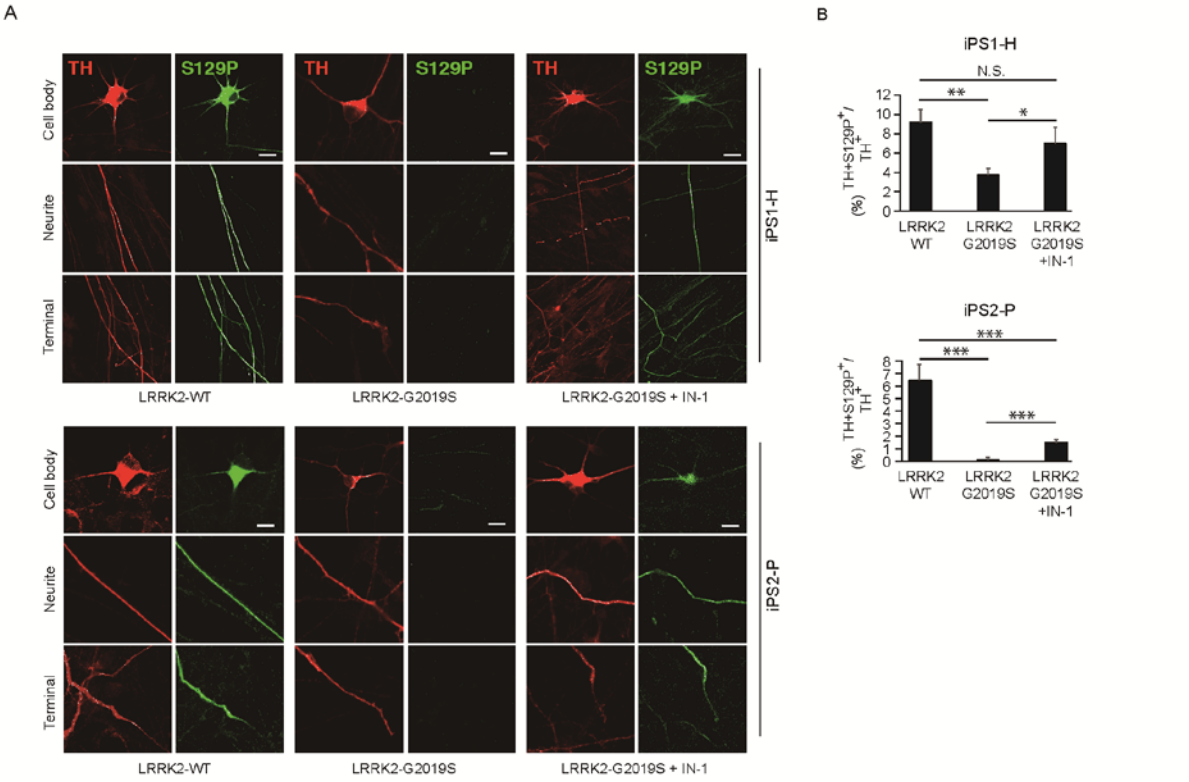

Figure 3

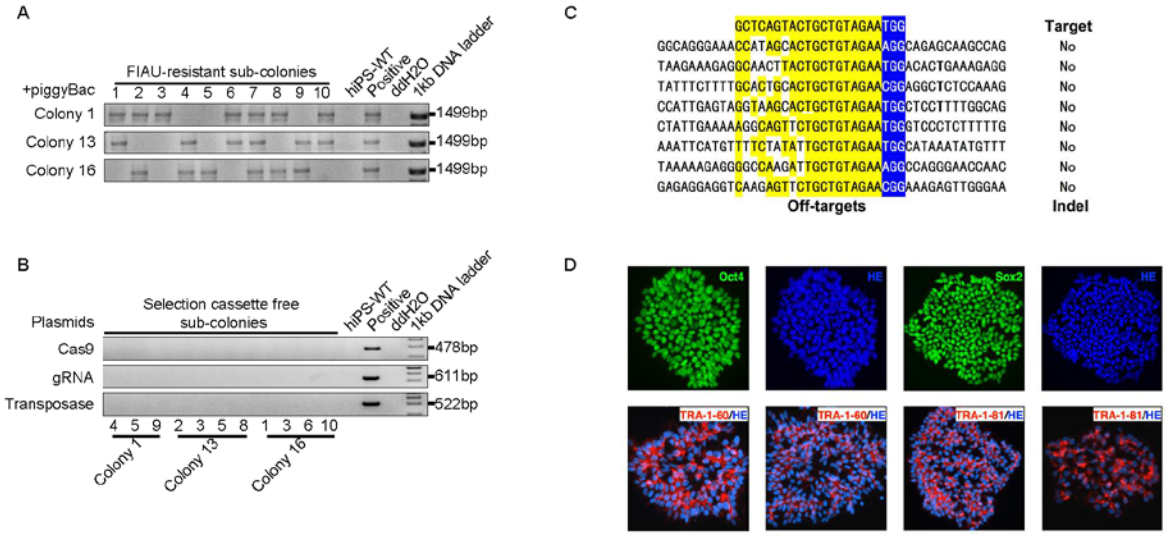

Figure S1

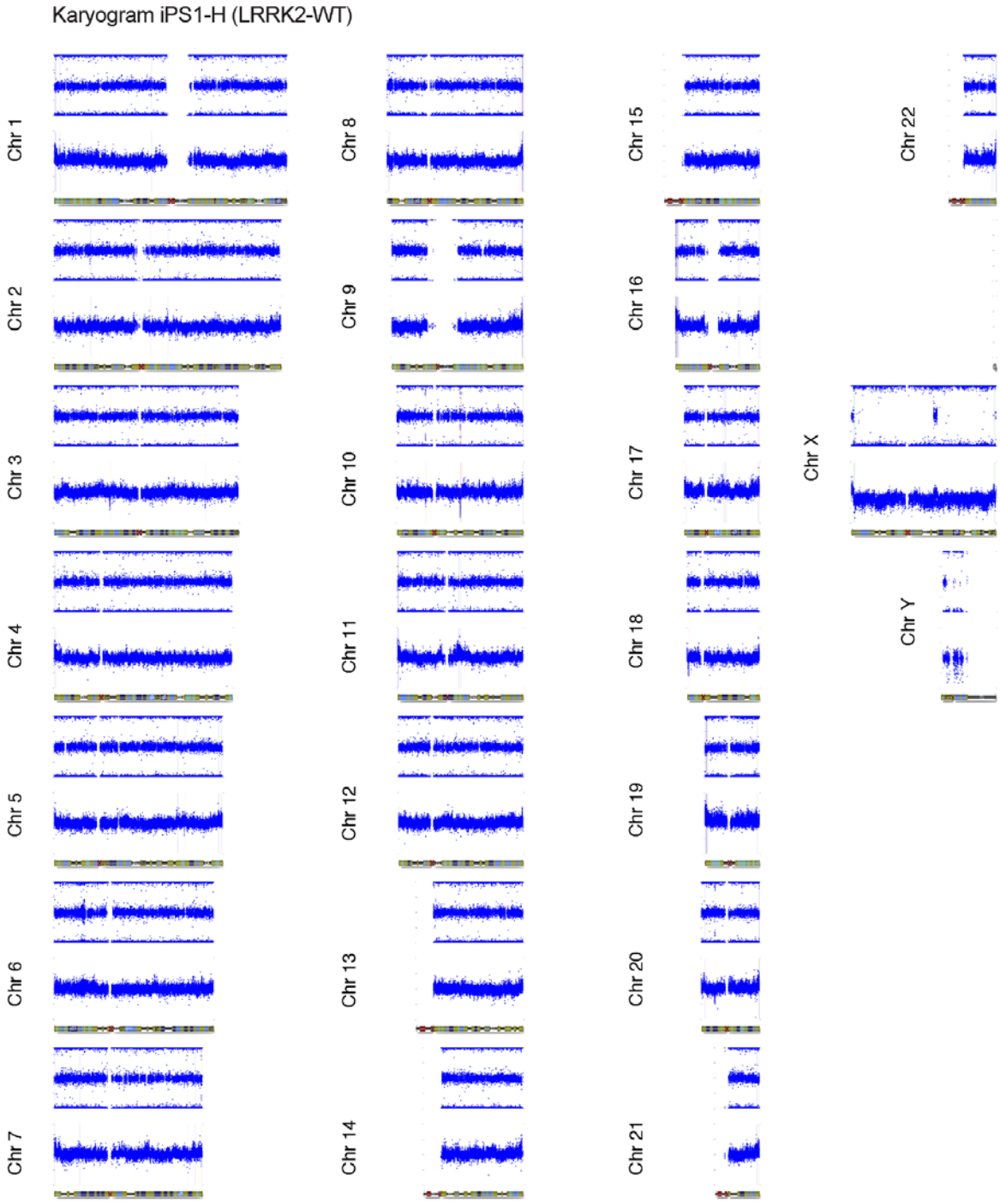
Karyogram iPS1-H (LRRK2-WT)
Chr 1
Chr 2
Chr 3
Chr 4
Chr 5
Chr 6
Chr 7
Chr 8
Chr 9
Chr 10
Chr 11
Chr 12
Chr 13
Chr 14
Chr 15
Chr 16
Chr 17
Chr 18
Chr 19
Chr 20
Chr 21
Chr 22
Chr X
Chr Y

Figure S2

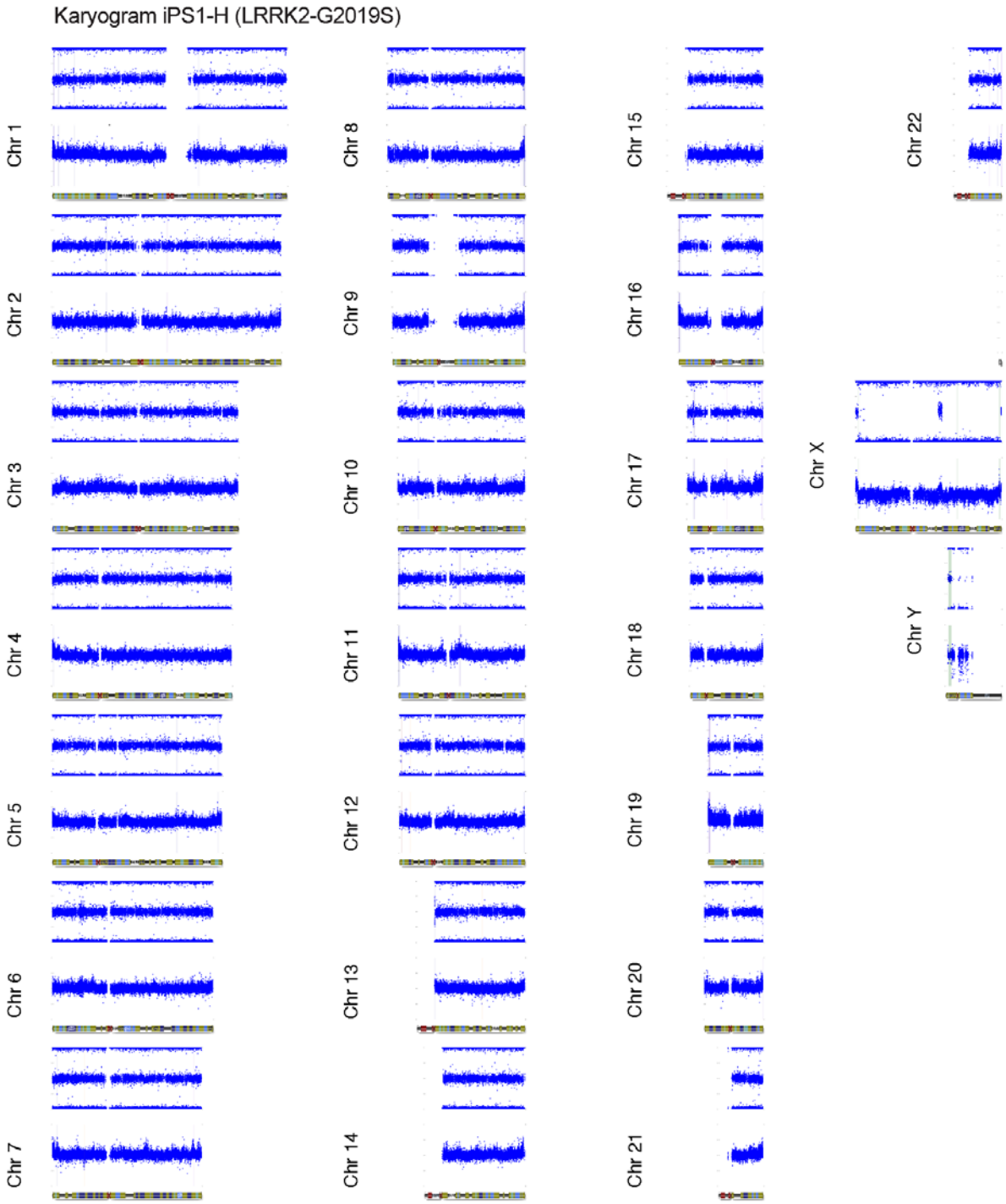
Karyogram iPS1-H (LRRK2-G2019S)
Chr 1
Chr 2
Chr 3
Chr 4
Chr 5
Chr 6
Chr 7
Chr 8
Chr 9
Chr 10
Chr 11
Chr 12
Chr 13
Chr 14
Chr 15
Chr 16
Chr 17
Chr 18
Chr 19
Chr 20
Chr 21
Chr 22
Chr X
Chr Y

Figure S3

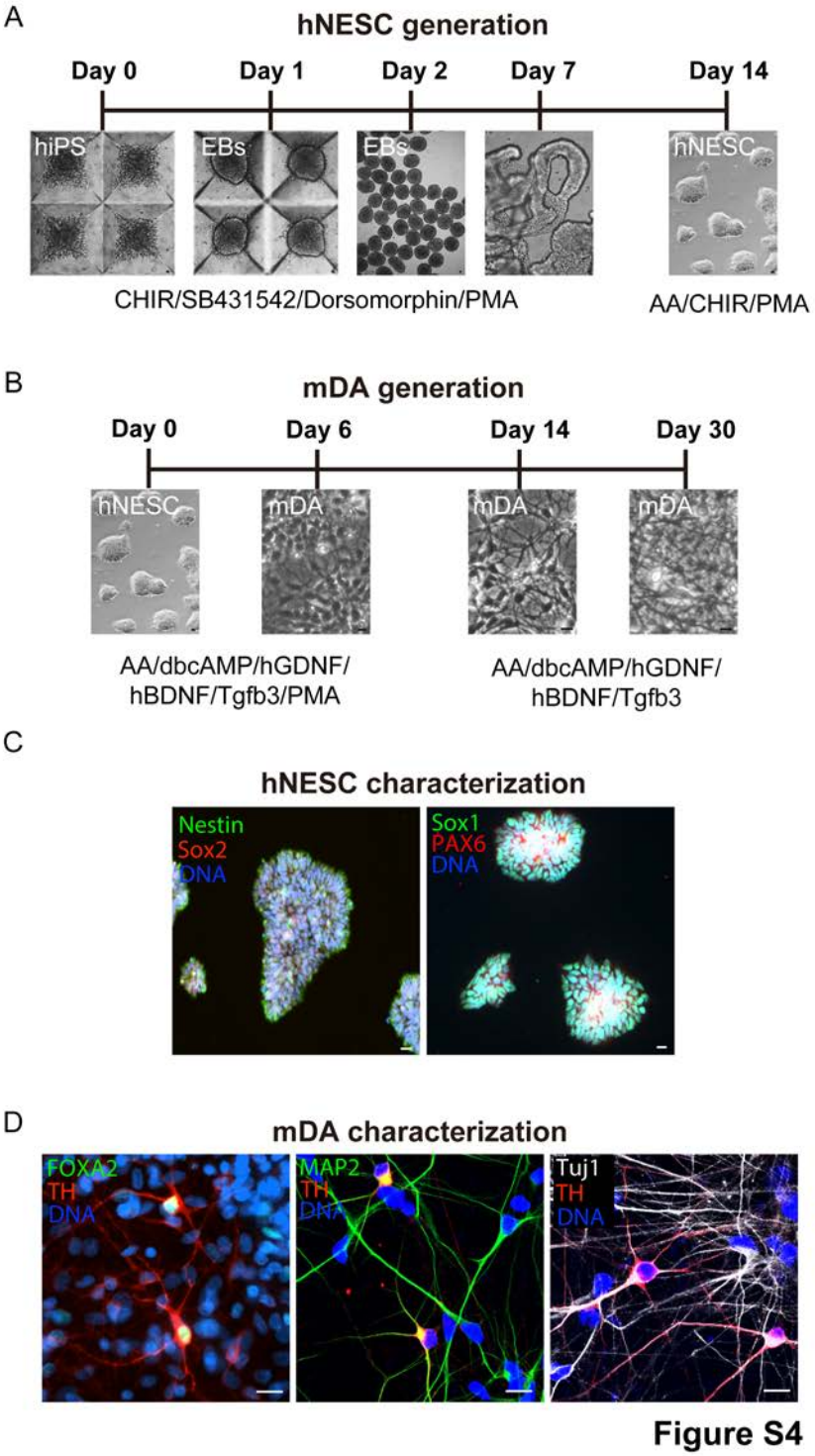
A
hNESC generation
Day 0
Day 1
Day 2
Day 7
Day 14
hiPS
EBs
EBs
hNESC
CHIR/SB431542/Dorsomorphin/PMA
AA/CHIR/PMA
B
mDA generation
Day 0
Day 6
Day 14
Day 30
hNESC
mDA
mDA
mDA
AA/dbcAMP/hGDNF/
hBDNF/Tgfb3/PMA
AA/dbcAMP/hGDNF/
hBDNF/Tgfb3
C
hNESC characterization
Nestin
Sox2
DNA
Sox1
PAX6
DNA
D
mDA characterization
FOXA2
TH
DNA
MAP2
TH
DNA
Tuj1
TH
DNA

Figure S4

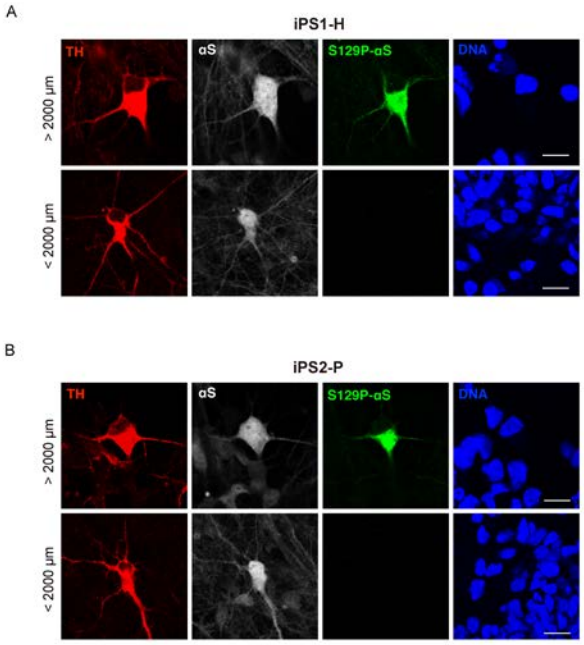

Figure S5

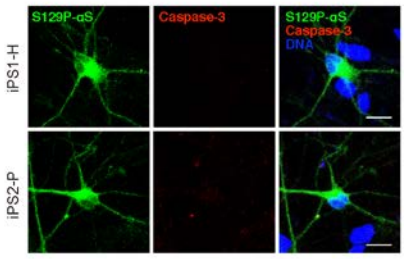

Figure S6

6.1.2 Manuscript V

hiPSC-derived neurons in a 3D microfluidic system as an enabling tool for high content drug screening targeting G2019S LRRK2 mutation

Silvia Bolognin [1], Marie Fossepre [1], Xiaobing Qing [1], **Javier Jarazo** [1], Janez Ščančar [2], Edinson Lucumi Moreno [1], Luis Salamanca [1], Ronan M. T. Fleming [1], Paul Antony [1], Jens C. Schwamborn [1]

[1] University of Luxembourg, Luxembourg Centre for Systems Biomedicine, 6 avenue du Swing, Belvaux, L-4367, Luxembourg.

[2] Department of Environmental Sciences, Jožef Stefan Institute, Jamova 39, 1000 Ljubljana, Slovenia.

Status: The manuscript is submitted to Acta Neuropathologica.

hiPSC-derived neurons in a 3D microfluidic system as an enabling tool for high content drug screening targeting G2019S LRRK2 mutation

Silvia Bolognin[1], Marie Fossepre[1], Xiaobing Qing[1], Javier Jarazo[1], Janez Ščančar[2], Edinson Lucumi Moreno[1], Luis Salamanca[1], Ronan M. T. Fleming[1], Paul Antony[1]*, Jens C. Schwamborn[1*#]

[1]University of Luxembourg, Luxembourg Centre for Systems Biomedicine, 6 avenue du Swing, Belvaux, L-4367, Luxembourg. [2]Department of Environmental Sciences, Jožef Stefan Institute, Jamova 39, 1000 Ljubljana, Slovenia.

Lead contact

*Corresponding authors:

Prof. Dr. Jens C. Schwamborn

Université du Luxembourg LCSB - Luxembourg Centre for Systems Biomedicine

6, Avenue du Swing L-4362 Belvaux, Luxembourg

T. +352 / 4666445536 E. jens.schwamborn@uni.lu

Dr. Paul Antony

Université du Luxembourg LCSB - Luxembourg Centre for Systems Biomedicine

6, Avenue du Swing L-4362 Belvaux, Luxembourg

T. +352 / 4666446986 E. paul.antony@uni.lu

Running title: 3D microfluidic systems exacerbated LRRK2-G2019S dependent toxicity.

Abstract

Stem cells derived neurons are a powerful tool to study disease mechanisms and phenotypes in Parkinson's disease (PD). However, the identification of a robust phenotype in the derived neuronal cultures is often difficult. We optimized the cultivation of PD patient specific neurons carrying the LRRK2-G2019S mutation in 3D microfluidic conditions, combined with automated image analysis to enable pharmaco-phenomics in disease-relevant conditions. This newly established pipeline allowed for high-content data collection, which showed decreased dopaminergic differentiation and branching complexity, altered mitochondrial functionality, and increased cell death in LRRK2-G2019S neurons compared to the isogenic lines in 3D but not in 2D conditions. Treatment with the LRRK2 inhibitor CZC-25146 rescued disease-associated phenotypes. However, a view throughout all analyzed features showed that the genetic background of the PD patients constituted the strongest discriminant between the lines. These data support the use of advanced *in vitro* models for future patient stratification and personalized drug development.

Introduction

The identification of promising drug candidates in pre-clinical research, as well as personalized precision medicine, are hampered by the lack of sufficiently representative *in vitro* models. This is particularly true in the case of Parkinson´s disease (PD), a complex neurodegenerative disorder where the most studied cells, associated to the onset of motor dysfunctions, are the dopaminergic neurons of the *substantia nigra* in the midbrain [35]. PD is a human specific disorder for which animal models are not sufficiently predictive of the human response. The difficulty of capturing the multifactorial nature of the disease in *in vitro* models and the excessive reliance on animal models partly explain the disappointingly high failure rate of new candidate molecules in clinical trials [24, 35]. New technological advancements have failed to translate into successful curative pharmacological options and no definitive disease-modifying therapy is currently available.

In this scenario, human induced pluripotent stem cells (iPSCs) represent a promising tool for the generation of relevant human *in vitro* models, due to their ability to differentiate into any cell type of the body [34, 50]. However, the use of iPSC technology alone is often not sufficient to account for all the limitations of modelling complex diseases in a dish. Standard 2D cell culture systems do not offer an ideal set-up to study highly ramified cells such as neurons. In contrast to physiological conditions, in 2D the dendrites and growth cones are unrealistically flattened, limiting the acquisition of full cellular functionality, and poorly modelling the cellular microenvironment. On the other hand, it has been shown that cells in a 3D *in vitro* settings are subjected to mechano-structural clues which bring them closer to the physiological condition [2]. Surrounded by matrix surrogates, cells experience a more physiological transport and equilibration of soluble factors [2, 37]. Notably, several groups have reported different gene and protein expression profiles when comparing 2D and 3D cultures [1, 29]. Cell cultured in 2D showed approximately 30% of differentially expressed genes compared to cells *in vivo* [4]. It is not surprising that the cellular responses to drug administration in 3D were closer to *in vivo* than 2D cultures [45, 56]. This more metabolic competent system holds the potential to enable pharmacological studies in personalized human derived *in vitro* models at very early stages of the drug discovery pipeline. In the context of Alzheimer's disease, it was reported that the 3D cultivation of gene-edited stem-cell-derived neurons, expressing mutations responsible for the familial form of the pathology, allowed to successfully recapitulate, for the first time in an *in vitro* system, all the key neuronal pathological hallmarks [10].

We have recently shown that iPSCs-derived neuroepithelial stem cells can be used for the generation of midbrain specific dopaminergic neurons in a 3D microfluidics device [27]. The most common pathogenic mutation, causing autosomal-dominant PD, is the G2019S mutation in the leucine-rich-repeat-kinase-2 (*LRRK2*) [32, 57]. LRRK2-associated familial form is pathologically and clinically indistinguishable from idiopathic PD [16]. Remarkably, LRRK2, in its wild-type sequence, was also found to be relevant to the etiology of sporadic PD indicating it can modulate the risk of developing the disease [46]. The mutated LRRK2 has been reported to alter several cellular pathways including cell proliferation, protein trafficking, and cytoskeletal integrity [52]. However, due to its two enzymatic and several interaction domains, the contribution of LRRK2 to the pathogenic mechanism causing neuronal degeneration remains elusive [9, 18].

Here, we demonstrated that 3D, and not 2D, systems elicited the occurrence of time-dependent phenotypes affecting dopaminergic neurons. We also showed that G2019S-LRRK2 caused mitochondrial abnormalities and cell death in young neurons. The administration of the LRRK2 inhibitor 2 (CZC-25146) rescued only the dopaminergic, but not the mitochondrial, defects. The use of isogenic control lines allowed for the analysis of the genetic background contributions to the observed phenotypes (healthy individual or PD patients). The patient specific background turned out to be a major factor of clustering, prior to the G2019S mutation. Our high-content image analysis platform allowed for the identification of key G2019S LRRK2-dependent and independent phenotypes, which can be used to test the effect of potential disease-modifying compounds with a high-throughput approach.

Results

1 Time-dependent alteration of dopaminergic neuron differentiation associated to G2019S-LRRK2

We used hNESC lines from 2 PD patients carrying the G2019S-LRRK2 mutation and from 2 healthy individuals (**Fig S1A**). The pipeline of the study is shown in **Fig 1A**. In the patient lines the mutation was corrected to the wild-type sequence, while in the iPSC lines from healthy individuals the wild-type sequence was replaced by the mutated one (isogenic cell line pairs). Sequencing was also performed to confirm the correct editing (**Fig S1B**). All the different 8 hNESC lines used in the study were checked for the expression of neural stem cell markers SOX1, SOX2, and Nestin (**FigS1C**). As previously reported, the neuronal differentiation protocol generated a mixed population of neural cells, about 30% of those being dopaminergic neurons [27, 40].

Our data showed significant morphometric changes in 3D neuronal cultures, which were not observed in classical 2D cultures (**Fig1B-C, FigS1D**). After 6 weeks of neuronal differentiation in 3D systems, PD specific cultures expressing the LRRK2-G2019S mutation showed a significant degeneration of TH positive dopaminergic neurons. This degeneration was not observed in 2D conditions. Since we used the same Matrigel and media cocktails for the 2D and 3D differentiation protocols, it can be concluded that these differences were due to the spatial culture conditions. We then decided to focus only on 3D cultures and to better resolve the temporal dynamics of the observed defect. We evaluated the branching complexity of TH^+ cells after 2 and 6 weeks of differentiation in the microfluidic device (**Fig1D-E, H**). We observed a significantly increased TH/Tuj1 ratio in the G2019S lines compared to WT after 2 weeks (**Fig1E**). However, after 6 weeks we observed a significant decrease in several TH^+ neuron parameters including volume of the TH^+ cells, *skeleton pixel*, *node count*, and *link count* (**Fig1H**). This highlights a time-dependent selective degeneration of the dopaminergic neurons, accompanied by a reduction of neurite complexity. We also analyzed the levels of α-synuclein phosphorylation at serine 129 (pS129αSNCA) and of LRRK2 at serine 935 (pS935LRRK2) after either 2 or 6 weeks (**Fig1F, 1I**). pS129αSNCA was unchanged at the time points tested but pS935LRRK2 levels were increased after 2 weeks in the LRRK2-G2019S lines.

2 G2019S-LRRK2 induced mitochondrial abnormalities and cell death in developing neurons

As 6 week old neurons showed LRRK2-G2019S-induced alterations in survival and dopaminergic architecture, we were interested in the potentially underlying preceding mechanism. Since mitochondrial alterations are well known to be involved in PD [6, 26, 44], we tested the cultures for signs of mitochondrial abnormalities at earlier time points, 2 and 3 weeks. We performed live imaging with TMRM and MitoTracker Green (**Fig2A-B**). The number of mitochondrial objects (*MitoCount*) was lower at 2 weeks in LRRK2-G2019S than in LRRK2-WT neurons (**Fig2C**). Mitochondrial morphometric features in LRRK2-G2019S such as *skeleton*, *perimeter*, *body pixels*, and complexity of the network (number of *links* and *nodes*) were also decreased compared to WT-LRRK2. After 3 weeks of neuronal differentiation, we observed a progressive further reduction in mitochondrial number, perimeter, and complexity. This underlies a detrimental effect of LRRK2-G2019S on key components of the mitochondrial machinery without impairing the mitochondrial membrane potential, coherently with previous studies in fibroblasts [33]. The ratio between nuclear and cytoplasmic volumes significantly increased in the G2019S-LRRK2 lines. We hypothesized this might be an indicator of nucleus shrinking due to cell death trigger (**Fig2D**). Accordingly, we then sought to analyze the activation of cleaved-caspase 3 (CC3) at the same time points. We observed that the time window for the

increased CC3 activation was at 2 weeks (**Fig2E-F**), meanwhile at 3 weeks the levels between LRRK2-G2019S and WT were comparable (data not shown). The total levels of live cells and dead cells as detected by Calcein and Ethidium Homodimer (EH) were increased when considering the individual masks in the LRRK2-G2019S lines. By normalizing these masks to the Hoechst mask, the total levels of Calcein and EH were unchanged between LRRK2-G2019S and WT lines. However, the levels of CC3 identified in live cells (double staining CC3-Calcein) and the CC3 by the overall nuclei (Hoechst) were both increased in the LRRK2-G2019S compared to WT lines. Additionally, the analysis of chromatin condensation via Hoechst fluorescent intensity showed increased levels of pyknosis in LRRK2-G2019S compared to WT lines. Coherently with the decreased in the nuclear volumes observed at 3 weeks, also the LDH release into the media was increased at that time point in differentiating LRRK2-G2019S neurons as compared to WT (**Fig2G**). The progressive decrease of Zn levels in the media outflow becoming more prominent after 3 weeks further supported the observed reduction in cell viability (**FigS1E**). Taken together, these results indicate that LRRK2-G2019S neurons were more prone to mitochondrial abnormalities and activation of cell death pathways.

3 Kinase inhibitor Inh2 rescued LRRK2-G2019S dependent dopaminergic phenotype

Based on the established assays and observed phenotypes, we ran a proof-of-concept drug testing screen in our 3D system. We tested the rescue effect of the LRRK2 kinase Inh2 to rescue the described phenotypes [38]. After testing concentrations up to 1.5 µM (data not shown), 0.5 µM was selected for all the experiments of this study. The administration of Inh2 for 6 weeks ameliorated many of the dopaminergic features assessed (**Fig 3A-B**). Importantly, the selective degeneration of TH^+ dopaminergic neurons in LRRK2-G2019S lines was completely rescued by Inh2. This effect was enforced by the increase, although not significant, in network elements, comprised of link and node counts, upon Inh2 administration (**Fig3B**). The neuronal volume ($Tuj1^+$ cells) increased after the treatment in the LRRK2-G2019S lines, indicating a general neuroprotective effect also in the non-dopaminergic neurons. Notably, treatment with Inh2 was not effective in rescuing the increased CC3 activation or the mitochondrial defects, suggesting it corrects only part of the alterations produced by the mutation. Focusing on the TH^+ morphometric analysis, we evaluated Inh2 rescue effects posing the LRRK2-G2019S average values equal to 0 and the WT to 100%. Inh2 determined a rescue between 43% and 82.6% of the LRRK2-G2019S phenotypes to the WT condition (**Fig3C**). The same analysis was performed when genetically correcting the patient lines to the WT sequence of LRRK2. As for the pharmacological treatment, gene editing also determined a phenotype amelioration, but of a lower amplitude.

4 Contribution of patient-specific genetic background to the LRRK2-G2019S phenotype

We next stratified the lines for the genetic background of the donors (PD patients or healthy individuals). The clustergram with these groups showed that the PD-patient derived lines are clustering together independently of presence or absence of the mutation (**Fig4A**). This suggests that the genetic background of the cells accounts for most of the differences between the studied cell lines, independently of the pharmacological treatment or the gene editing. A closer analysis of some of the underlying assays showed that PD-patients derived lines (P) presented significantly higher levels of CC3 in live cells and as a ratio of total number of cells than healthy lines (**Fig3B-C**). G2019S-LRRK2 editing rescued CC3 activation. A similar rescue pattern was observed for *mitochondria count* at 3w, *node TH count*, and *link TH counts* at 6w: these features were decreased in P compared to healthy-individual derived lines (H) and a rescued was observed after LRRK2-G2019S correction (PGC lines). The TH pixel count was also affected by the mutation when this was inserted (HMut) and in the patient lines (P).

5 Assay performance based on ROC analysis

To calculate the performance of the single assays with ROC analysis, we performed the following comparisons: LRRK2-G2019S versus WT, and LRRK2-G2019S Inh2 versus WT Inh2. Table S1 indicates the number of samples for each group, as well as the number of features extracted for each of the assays. For cell death at 2w, mitochondrial assay at 2w and 3w, we had a good trade-off between number of samples and features. This was not the case for cell death at 3w, morphometric analysis at 2w and 6w. In the morphometric assay, a large number of features was extracted. In these three cases, we applied the feature selection approach as described in the Methods section: the chosen threshold was the one giving the best results among the values 0.75, 0.8, 0.85 and 0.9. Except for the comparison of LRRK2-G2019S Inh2 vs WT Inh2 for the morphometric assay at 6w, where the threshold was 0.75, for all the other cases the chosen threshold was 0.8. **Table 2** shows the results for the comparison between LRRK2-G2019S and WT. The cell death assays allowed for the higher separation between the 2 conditions, as they provided an AUC of 88.5 for the 2w and 90.1 for 3w with high accuracies, sensitivities, and specificities. The morphometric assays provided reasonable performances (77.9 at 2w and 79.2 at 3w) the reduction of the number of features to 16. Finally, the mitochondrial assays showed low performance to discriminate the 2 conditions despite still providing good values of specificity. Additionally, **Table 3** shows the results for the comparison between LRRK2-G2019S Inh2 and WT Inh2. The cell death assays maintained the highest AUCs, though with a lower

accuracies compared to **Table 2**. For the remaining assays, the AUCs were reduced compared to Table 2, indicating that the addition of Inh2 brought the LRRK2-G2019S closer to the WT lines.

Discussion

Recapitulating the key cellular hallmarks of LRRK2-associated toxicity in patient derived cells is a requirement to set-up *in vitro* assays, which can drive personalized medicine approaches. Here, we developed a platform based on hNESC-derived neurons from PD patients carrying the LRRK2-G2019S mutation. This platform recapitulates the key features of PD, including degeneration of dopaminergic neurons and preceding mitochondrial impairments. Chronic treatment with the LRRK2 specific inhibitor, Inh2, restored the neurodegeneration and neurite complexity phenotypes without fully reversing mitochondrial abnormalities. When looking at the overall assays at all the time points, the genetic background of the patients turned out to be a major discriminating factor between the lines.

Cells in a 3D *in vitro* setting are subjected to structural clues, which bring them closer to the physiological condition [42]. This more confined microenvironment seems to fasten cell-cell contact and extracellular matrix (ECM) protein synthesis [8]. Unlike 2D cultures, 3D microenvironments showed gene expression patterns and cellular phenotypes that resemble the *in vivo* condition [3, 54]. This more metabolic competent system, combined with stem cell technology tools, holds the potential to leverage the assessment of drug effects to a human derived model at a very early stage. Classical *in vitro* models for PD mainly comprises of PD patient fibroblasts or immortalized cells (*e.g.* SH-SY5Y) with all the associated drawbacks including different gene expression compared to neurons and instability respectively [55]. The successful use of 3D and hNESC-derived neurons for phenotype assessment has been shown in Alzheimer's Disease [10]. As in 2D cultures paracrine factors diffuse rapidly into large media volumes, we hypothesized that neurons cultivated in 3D exacerbated LRRK2-G2019S toxicity by providing a brain tissue-like environment. We chose Matrigel as a 3D support matrix as it contains high levels of brain extracellular matrix proteins such as laminin, collagen, and heparin sulfate proteoglycans [17]. The 3D scaffold given by Matrigel, but also other hydrogels such as collagen and alginate gels, has shown to accelerate neuronal network formation [10, 20, 21, 31, 49]. More importantly, the support of the matrix allows vertical growth, which is completely lacking in 2D cultures resulting in unwanted apical-basal polarity [2]. The 3D environment is also able to trigger mechanical clues, which can be converted into biochemical signals not achievable in conventional flat cultures. Building on that, several brain organoids recapitulating cortical [19] and midbrain [25] identities have been recently developed

and demonstrated the huge potential of 3D systems to recapitulate disease-relevant features. The derivation of dopaminergic neurons in the described 3D set-up has also the advantage of using low volumes of media and the option for multiplexing and automated screening activities [15, 51]. Beyond enabling larger throughput than manual approaches, the automation also improves reproducibility, and the depth of available phenomic data, allowing to gain a systems-level understanding of the multiple contributions of LRRK2 in determining the neuronal phenotype. A deeper understanding of the role of LRRK2 in PD is of interest as the same pathways might be shared with idiopathic PD [11].

Our results are consistent with a series of past observations describing reduced neurite outgrowth speed in LRRK2-G2019S mutant neurons within 30 minutes recording in bright field microscopy [41]. LRRK2-G2019S or Y1699C-LRRK2 expression led to shorter total neurite lengths compared to wild-type rat primary neurons [47]. However, in contrast to previous reports, here we were able to show a progressive time-dependent degeneration of TH^+ neurons carrying LRRK2-G2019S, which is reproducing what occurs in patients. Interestingly, at 2 weeks we observed an increased TH/Tuj1 ratio, which we hypothesize, might respond to an attempt to accelerate dopaminergic differentiation to try to counteract LRRK2-induced defects. This compensatory mechanism has often been described in other pathological contexts, for instance in Alzheimer's disease brain samples, where the synaptic protein synaptophysin is increased in autoptic brain stages 3 and 4 and later decreased in Braak stage 5-6 [28].

The hypothesis of mitochondrial dysfunction being a key event in PD pathogenesis has been proposed in several studies [43, 44]. Interestingly, LRRK2 seems to control mitochondrial homeostasis via the dynamin-like protein DLP1 [53]. We have confirmed the compromised mitochondrial function of LRRK2-G2019S [33, 53], but also broadened its characterization in hNESC-derived neurons. It has been reported that the overexpression of LRRK2- G2019S in SH-SY5Y cells caused reduced membrane potential in the absence mitochondrial morphology changes [33]. In contrast, 2D derived LRRK2-G2019S iPSC-derived neurons showed unaltered electron transport chain but susceptibility to stress after chemical stressors [12]. These differences can be reconciled in our model, where no tumoral lines were used and no chemical stressors were applied. The 3D condition was the only factor triggering a striking alteration in mitochondrial number and network complexity. LRRK2 controls microtubule stability, which is essential for the trafficking of mitochondria to every distal area in branched cells. It has also been shown that LRRK2-G2019S increased phosphorylation of tubulin alters the microtubule dynamics [13], destabilizing the mitochondrial network as well.

In contrast to previous studies [7, 23, 30], we also showed the occurrence of neuronal cell death without using neurotoxins. Only a modest increase in CC3 was previously observed in 2D cultures even after treatments with H_2O_2 or 6-OHDA [30]. The increased CC3 levels and LDH release observed here highlight the intrinsic vulnerability of neurons carrying LRRK2-G2019S. A reason for the increased cell death in LRRK2-G2019S neurons might lie in its interaction with 14-3-3s, a family of proteins that has a role in cell survival [36]. Mutations of the residues S910/S935 to alanine in LRRK2 decreased its interaction with 14-3-3, causing toxic cellular redistribution of LRRK2 in HEK293 cells [36].

Due to its involvement in familial and sporadic PD and the presence of a drugable kinase domain, LRRK2 has become an attractive pharmacological target. Initial studies focused on LRRK2 kinase activity as a pathological trigger [14, 48]. Subsequent investigations pointed also to the protein expression levels, focusing on posttranslational modification such as the phosphorylation at serine residues Ser910 and Ser935, located prior to the leucine-rich domain of LRRK2 [48]. With a view on therapeutical application, we use Inh2 as a proof of concept to gain some mechanistic insights. In our set-up, Inh2 rescued the dopaminergic impairment but not the mitochondrial and viability abnormalities. The fact that LRRK2-G2019S, the most active mutation in increasing kinase activity [48], is not fully penetrant suggests that its pathological function comprises of additional pathways. Permissive genetic background, due to cumulative genetic variants, highlights how other players might mediate and enhance LRRK2-induced neurodegeneration. From this perspective, proper patient stratification is essential for the identification of therapeutic choices with maximized effect probability. For example, trafficking of dopamine receptor 1 and 2 seems to be affected by LRRK2-G2019S leading to an alteration in signal transduction [39]. This might result in resistance to the neurotrophic effect of dopamine receptor antagonist that could be preliminary tested for therapy prioritization. The possibility of using 3D *in vitro* testing to stratify PD patients for proper drug administration is a key opportunity to bring the present work to clinical application.

Despite its advantages, 3D microfluidic systems still present several limitations including the proper control of critical factors such as oxygen tension, pH, and gradient-dependent effects within the matrix. Thus, the applicability for drug screening purposes is currently still a proof-of-concept, which needs to be further validated. Moreover, in our current set-up only neurons were assessed, but other cell types might likely be affected and contribute to PD pathology [5]. Co-cultures of different iPSC-derived neural cells will be important to assess cell and non-cell autonomous effects. hNESC-derived neurons successfully recapitulate hallmarks of LRRK2 pathogenesis including degeneration, cell loss, and mitochondria impairment. However,

we did not observe α-synuclein accumulation as previously observed [41]. The improved microenvironment seems not to be sufficient to overcome the limitation of mirroring robust α-synuclein accumulation within 6 weeks. A major challenge is to recapitulate comprehensively PD pathology *in vitro* over a short time-course, while *in vivo* this takes decades. A more thorough recapitulation might come with the administration of aging-associated stressors such as DNA damaging agents or oxidative stress triggers [22]. Further studies may be necessary in this direction and will certainly fuel our understanding of disease pathogenesis and options for drug discovery.

Materials and Methods

Cell lines

The hiPSC-derived hNESCs were generated and cultured as previously described [40]. For the line Healthy 2, the footprint-free isogenic LRRK2-G2019S cell pair was established using CRISPR/Cas9 and piggyBac. Besides the p.G2019S (c.G6055A) mutation inserted into the wild type LRRK2 locus, we also introduced a silent mutation (c.A6087T) to convert TAAA into TTAA that is needed for piggyBac inserting and releasing. To make the wild type control an authentically isogenic control, we introduced silent mutation (c.A6087T) into wild type hiPSC as well, but without the p.G2019S mutation. The described LRRK2-G2019S isogenic cell differed only by LRRK2-G2019S from the Healthy2 line and the pair underwent the same procedure of editing and subcloning.

For cultivation, the hNESC derived from iPSC of 2 PD patients and 2 healthy individuals and their isogenic controls were cultured in N2B27 medium: DMEM-F12 (Gibco) /Neurobasal (Gibco) 50:50 supplemented with 1:200 N2 (Invitrogen), 1:100 B27 lacking vitamin A (Invitrogen), penicillin/streptomycin and glutamine (Invitrogen). 3 μM CHIR 99021 (Axon), 0.5 μM purmorphamin, PMA, (Enzo Life Science), and 150 μM ascorbic acid (Sigma) were added. Cells were maintained in Matrigel coated plates. At a confluence of 70-80% cells were detached using Accutase (Life Technologies) for 3 minute, collected by centrifugation and re-suspended in 80% Matrigel (BD Bioscience). 27,000 cells were loaded in microfluidic OrganoPlates (Mimetas) in 0.8μl per bioreactor. The media perfusion was achieved by gravity, with an average fluid flow of 1.5μl/h.

To achieve neuronal differentiation, cell were cultured in N2B27 medium supplemented with 10 ng/mL BDNF (Peprotech), 10 ng/mL GDNF (Peprotech), 1 ng/mL TGF-β3 (Peprotech), 200 μM ascorbic acid and 500 μM

dbcAMP (Sigma Aldrich). For the first 6 days, 1µM PMA was also added and the media was changed every second day. From day 7 onwards, the media without PMA was changed every 4th day (**Fig 1A**).

For 2D neuronal differentiation, 10,000 cells per well were seeded on Matrigel-coated 96 well cell carrier plate (PerkinElmer). The same differentiation protocol used in the OrganoPlates was applied.

For drug treatments, differentiation media containing 0.5 µM LRRK2 Inhibitor 2 (Merck Chemicals) or DMSO (Sigma) as vehicle were added at every media changed [38]. The final DMSO concentration in the media was 0.1% for the Inh2 and vehicle. In this paper, cells treated with DMSO were labelled as LRRK2-G2019S or WT.

Mitochondria live imaging

Mitochondrial membrane potential ($\Delta\Psi$) was assessed with TMRM (Thermo Scientific). Neurons differentiated for 2 and 3 weeks in the OrganoPlates were analyzed for their mitochondrial membrane potential with TMRM (4 nM), along with MitoTracker (1:10,000) Green (Invitrogen). In addition, cells were co-stained with Hoechst (1:1000) and Cell Mask (1:5000) to visualize nuclei and cell bodies respectively (Invitrogen). Cells were incubated for 30 min at 37 °C. Fluorescence images were acquired on Opera confocal microscope (Perkin Elmer).

Immunofluorescence staining

In 3D and 2D, neuronal cultures were fixed with 4% paraformaldehyde (PFA) in 1x phosphate buffer (PBS) overnight at 4 °C. After 3 washes in PBS, cells were permeabilized 15min in 0,3% Triton-X100 in PBS at RT. After blocking for 1h (2% fetal bovine serum, 2% bovine serum albumin, 0.1% Triton-X100), the first antibodies were incubated overnight at room temperature. The combination of the appropriate secondary antibodies (Invitrogen) was then added for an additional 2h at room temperature. Cells were analyzed by the neuronal marker Tuj1 (Millipore), the dopaminergic marker TH (Santa Cruz Biotechnology), and the dye Hoechst. The semi-quantitative expression of the LRRK2 phosphorylated at the serine 935 (pS935) (Abcam) and α-synuclein phosphorylated at the serine 129 (pS129) (Abcam) was assessed.

For assessing cell viability in 3D, Calcein and Ethidium Homodimer co-staining was used (Life Technology). Neurons were incubated for 45 minutes and subsequently fixed with 4% PFA overnight at 4 °C to perform CC3 (Cell Signaling Technology). Fluorescence images were acquired on Opera confocal microscope (Perkin Elmer) with a 20x Objective.

Image analysis for the morphometric assays

Immunofluorescence 4 channel 3D images of hNESC derived neuronal cultures in OrganoPlates were analyzed in Matlab (2017a, Mathworks). The developed custom image analysis algorithm automates 4 major steps, namely: mosaic stitching, segmentation of the bioreactors, segmentation of nuclei and neurons, and feature extraction.

For *stitching*, the normalized cross correlation between overlapping image sections was computed and the positions of local maxima were used to return x and y offsets. The positioning of the images in the mosaic was implemented accordingly, using translation.

The bioreactors were segmented based on the fluorescence intensities in the Hoechst, Alexa488, Alexa568, and Alexa647 channels. For preprocessing, each of these channels was average filtered with a square shaped structuring element of side length 5 and maximum projected. A first rough bioreactor segmentation to refine the bioreactor mask was used to remove false positive pixels and to leverage the detection of vertical linear structures in the microfluidic device. To remove sparse cellular structures, the rough bioreactor mask was eroded with a disk shaped structuring element of radius 5. Connected components with less than 1000 pixels were removed. To enlarge the bioreactor mask, a dilatation with a disk shaped structuring element of radius 20 was applied. To close vertical gaps, the mask was dilated with a vertical rod shaped structuring element with a height 101 and width 1. To remove potentially remaining false positive structures in the microfluidic channels, an erosion with a vertical rod shaped structuring element of height 501 and width 1 was applied. Clipped objects with less than 100.000 pixels were removed. To detect the phase guide, the connected components were identified using the function bwconncomp - resulting in three blocks indexed ascendingly from left to right. The middle block with index 2 was defined as phase guide. Next, the 2D bioreactor mask was projected to all the planes of the 3D bioreactor mask and the phaseguide was clipped to the lower 8 planes. The segmentation of matrigel channel (MC) and perfusion channel (PC) was based on the fact the matrigel channel is located at the left of the phaseguide while the perfusion channel is located at the right side. The tool used for this step is the Matlab function regionprops, which reconstructs objects within a limiting mask, provided that they contain corresponding pixels in a seed mask. The limiting mask in both cases was the complement of the bioreactor mask. For reconstructing the matrigel channel, the seed mask was created by dilating the phaseguide mask with the structuring element [1 1 0]. Similarly, dilatation with the structuring element [0 1 1] was used to create a seed mask for the reconstruction of the perfusion channel.

After segmenting the bioreactor, also nuclei and neurons were segmented. Image preprocessing for the segmentation of nuclei was done via a difference of gaussians. Briefly, a foreground image was computed by convolving the raw Hoechst channel with a gaussian filter of size 10 and standard deviation 2. Similarly, for the background image, a gaussian filter of size 60 and standard deviation 20 was used. The difference was computed by substracting the background from the foreground. The first rough nuclei mask was defined by those pixels with graytone values larger than 10. To refine the nuclei mask, pixels overlapping with the OrganoPlate mask were removed and only connected components with at least 200 pixels were retained. To classify nuclei pixels based on their fluorescence intensity, the raw Hoechst channel was preprocessed via average filtering with a square shaped structuring element of side length 5. Pixels overlapping with the nuclei mask and with values above 400 were assigned to the pyknotic nuclei mask. The remaining nuclei mask pixels were assigned to the normal nuclei mask.

For the segmentation of neurons, a strategy combining global and local thresholding was implemented. For global thresholding, image preprocessing was done via low pass filtering. For this purpose, the raw Tuj1 channel was convolved with a gaussian filter of size 10 and standard deviation 3. The global neuronal mask is defined by threshold 150. For local thresholding, a difference of gaussians was applied in the preprocessing step. Precisely, the background defined via convolution with a gaussian filter of size 20 and standard deviation 6 was substracted from the foreground defined via convolution with a gaussian filter of size 10 and standard deviation 3. The local neuronal mask is defined by those pixels with values larger than 3. The concepts of global and local thresholding were combined by retaining those pixels in the neuronal mask, which were detected by at least one of these methods. For refining the neuronal mask, connected components with less than 200 pixels were removed.

To analyze neuronal fragmentation, the concept of erosion was used. Indeed, the surface of fragmented objects is larger than the surface of non-fragmented objects as compared to their cumulated volumes. For the analysis of fragmentation in the TH channel, an additional mask was defined by preprocessing the raw TH channel via convolution with a gaussian filter of size 10 and standard deviation 1, and thresholding of this image by pixel value 100. Both masks were eroded with a 3D structuring element corresponding to a center pixel and its 6 connected neighbourhood. Furthermore, the surface masks were computed by substracting the eroded masks from the corresponding original masks.

For further analysis, based on fluorescence quantification, the analysis of raw measured fluorescence in the above defined masks was backed up with spectral unmixing. Indeed, the used fluorophores were chosen in order to minimize spectral overlap. To determine the parameters for spectral unmixing, samples with single secondary antibody staining were measured as described above in the microscopy section. Spectral unmixing was applied according to the formula $I = \sum_i f_i C_i$ where I is the average measured intensity, C the contribution of a given fluorophore to the measured intensity, and f the proportional contribution of a fluorophore to I. Noteworthy, i was 3 as the fluorophores Alexa488, Alexa568, and Alexa647 were considered. Hoechst was excluded from spectral unmixing, as the segmentation steps above excluded Hoechst positive pixels already from the neuronal analysis. Some of the extracted features are summarized in **Table 1.**

Image analysis for the mitochondrial assays

The custom image analysis algorithm developed for the processing of TMRM assays automates the same key steps as above. Since a different staining was used as compared to the morphometric assays, the first raw segmentation of the OrganoPlates was based on the rule OrganoPlate Mask = 10 < $TMRM_{max}$ < 30 or 30 < $Hoechst_{max}$ < 200 and $MitoTrackerGreenFM_{max}$ > 15, where subscript max refers to maximum projections of size 5 average filtered raw images. The refinement of the OrganoPlate mask was done as described above.

The nucleus mask was defined by global thresholding (> 100) in the raw Hoechst channel. Pixels which were not included in the OrganoPlate mask were removed. The CellMask was defined via a combination of local and global thresholding. Large and bright cellular structures were identified via thresholding on the raw CellMask channel (> 400). Smaller cellular structures were detected via local thresholding by applying a difference of gaussians to the raw CellMask channel. The foreground image was computed via gaussian convolution with size 100 and standard deviation 5. The substracted background image was defined via gaussian convolution of size 100 and standard deviation 30. The cell mask was defined via thresholding of this difference of gaussians (>10) and by removing pixels assigned to the OrganoPlate mask. The mitochondrial mask was defined via a difference of gaussians. For the foreground image, the gaussian size was set to 10 and the standard deviation to 1. For the subtracted background, a gaussian of size 10 and standard deviation 3 was used. A first raw mitochondria mask was defined via thresholding of this difference of gaussians (>30). To refine the mitochondria mask, connected components with less than 5 or more than 500 pixels, and the OrganoPlate mask were removed.

In order to leverage the morphometric analysis of mitochondria, the surface of mitochondrial connected components and the corresponding mitochondrial bodies were defined via erosion of the mitochondria mask with a 3D structuring element corresponding to a pixel and its 6 connected neighborhood. The skeletonization of the mitochondrial mask was performed using established methods. The extracted features are summarized in Table 1.

Image analysis for the cell death assays

The custom image analysis algorithm developed for the analysis of Live/Dead assays automates the same key steps as above. The first raw segmentation of OrganoPlate bioreactors was based on the rule OrganoPlate Mask = 50 < $Calcein_{max}$ < 300, where subscript max refers to the maximum projection of size 5 average filtered raw Calcein images. For the refinement of the OrganoPlate mask the size of the structuring element used for closing vertical gaps, was set to height 201 and width 1 and the size of the structuring element used for the subsequent erosion was set to height 3001 and width 1. In addition, the mask was opened with the function *imopen,* using a disk shaped structuring element of radius 20 and dilated using a disk shaped structuring element of radius 22.

The segmentation of the nuclei was based on global thresholding on a difference of gaussians of the Hoechst channel. The foreground image of the difference of gaussians was computed via a gaussian kernel of size 10 and standard deviation 2. The subtracted background image was returned from gaussian convolution using size 60 and standard deviation 20. The nuclei mask was defined via thresholding (> 50). Next, the nuclei mask was refined by excluding pixels from the OrganoPlate mask and by removing connected components with less than 200 pixels. For defining the mask of EH positive pixels, the corresponding channel was low pass filtered using a gaussian filter of size 10 and standard deviation 3. Next, thresholding was applied (>500) and pixels overlapping with the OrganoPlate were excluded. For detecting CC3 positive pixels, the raw CC3 channel was low pass filtered with a gaussian of size 10 and standard deviation 3. The threshold was set to 250 and in the resulting mask, pixels overlapping with the OrganoPlate or nucleus masks, were excluded. Furthermore, connected components with less than 20 pixels were removed. For the detection of Calcein positive pixels, an approach combining global and local thesholding was used. For global thresholding the raw Calcein channel was low pass filtered with a gaussian of size 10 and standard deviation 1, and the threshold was set to 50. For local thesholding a difference of gaussians was computed on the Calcein channel. The foreground gaussian was set to size 20 and standard deviation 1. The background

gaussian was set to size 20 and standard deviation 5. The threshold was set to 10. The local and global Calcein masks were combined via Boolean OR operation and pixels overlapping with the nuclei mask or the OrganoPlate mask were removed from the Calcein mask. The live mask was defined by excluding the nuclei mask from the Calcein mask and by removing connected components with less than 200 pixels. The CC3 live mask was defined via Boolean operations using the Calcein mask, the not nuclei mask, and the CC3 mask. Extracted features are shown in **Table 1.**

LDH viability test

Cell death was assessed in 3D microfluidic devices at 3 weeks of neuronal differentiation by measuring the amount of lactate dehydrogenase (LDH) released into the cell culture media by plasma membrane damaged cells. The assay was conducted following manufacturer's instructions (Thermo Scientific).

Zn metal analysis

200 µl of media outflow was collected for each condition at each time point and treated with 20 ml of nitric acid (HNO_3) 65%. The content of Zn in the digested supernatant samples was determined by inductively coupled plasma mass spectrometry. Prior analysis, 200 µL of 1 + 1 mixture of 30 % H_2O_2 s.p. and 65 % HNO_3 s.p. (Merck, Darmstadt, Germany) was added to 200 µL sample aliquots, which were kept in 2 mL polypropylene vials (Nalgene cryogenic vials, Merck). Samples were then digested at 60 °C for 48 hours. The clear solutions obtained were diluted with milliQ water up to 2 mL. The concentrations of Zn was determined on Agilent 7900 series ICP-MS instrument (Agilent, Tokyo, Japan) under the following operating parameters: forward power 1550W, plasma gas flow 15.0 L min^{-1}, carrier gas flow 0.95 L min^{-1}, dilution gas flow 0.1 L min^{-1}, sample depth 8.0 mm, He gas flow 4.5 mL min^{-1}, energy discrimination 5V. The isotope monitored was Zn^{66} and the isotopes of internal standards ^{103}Rh, ^{193}Ir.

Multivariate classification methods

To study the potential of the described assays to robustly discriminate the different groups, multivariate classification methods were used. The performance was first measured in terms of accuracy in the classification, sensitivity, and specificity. However, since the dataset includes different numbers of samples for each group, a receiver operating characteristic (ROC) analysis was additionally performed, measuring the true-positive rate (sensitivity) against the false-positive rate (specificity). From the provided ROC curves, the area under the ROC curve (AUC) was computed. AUC is a reliable measure of the performance that takes into account the skewness in the sample distribution. For the binary classification between the groups of

interest, support vector machine (SVM) technique with a radial basis function (RBF) kernel to boost the accuracy was implemented. The results were computed with a 5-fold cross validation. We randomly split the set of LRRK2-G2019S and WT samples in two subsets: a training one that comprises 4/5 of the samples, and a test subset with the remaining 1/5 samples. Then, the classifier was trained using the training set, and its accuracy was obtained by testing its performance on the test set. This was run for the 5 different combinations of training and test sets. This process was repeated 200 times, this aiming at ensuring statistical robustness for both the accuracy and the AUC. We also tackled the tendency of the RBF kernel to over fit during the training process. Hence, we additionally trained the classifier using a wide range of values of the 2 parameters the classifier depends on. For the parameter that controls the overfitting, we generated 21 values ranging from 10^{-5} to 10^{5}, and for the parameters that scales the RBF kernel, 10 values between 10^{-3} and 10, in both cases logarithmically equally spaced. For the two comparisons presented in the current paper, LRRK2-G2019S versus WT and LRRK2-G2019S Inh2 versus WT Inh2, all the considerations previously stated helped ensuring the validity of the obtained results for the cell death and mitochondrial assays, and their two time points, since there was a fair trade-off between number of samples and number of features. Nevertheless, for the he morphometric analysis assay, the number of samples for each comparison was insufficient compared to the number of features, which might have lead to strong overfitting. Therefore, we decided to additionally proceed with a stage of feature selection before the classification. We took advantage of the existing high correlation between some of the designed features in the morphometric assay. We proceeded removing one of each pair of highly correlated features at a time, repeated this process iteratively until the remaining features had cross-correlations below the given threshold. For the generation of the results, we used Matlab (R2017a). The SVM algorithm used was the one implemented in the *LIBSVM* library

Statistics

All quantified data represent an average of all the technical replicates performed over 4-8 independent experiment per cell line. Automated outlier removal was performed using Matlab. The statistical analysis was performed using two-tailed Student's *t*-test (unpaired or Mann Whitney according to normality test D'Agostino&Pearson) or one-way ANOVA followed by an appropriate post hoc test (Dunett's or Turkey's according to normality test D'Agostino&Pearson) in GraphPad Prism software. Levels of significance are as follows: **p*<0.05, ***p*<0.01, *p****<0.001, p****<0.0001. Data are expressed as mean values ± S.E.M. In all box-plots the whiskers represent the minimum and maximum value of the distribution. When dysplayed, the

points represent the single experimental value. To analyze the rescue size effect given by Inh2 or gene editing, a bootstrap method with $1x10^5$ iterations and 10 randomly chosen samples per iteration was used.

Supplementary Materials

Supplementary Figures: FigS1, FigS2, FigS3, TableS1.

Acknowledgments. We thank Prof. Dr. Hans R. Schöler from the Max-Planck-Gesellschaft and Dr. Jared Sterneckert from the CRTD for providing us with cell lines.

Funding. The JCS lab is supported by the Fonds National de la Recherché (FNR) (CORE, C13/BM/5791363 and Proof-of-Concept program PoC15/11180855 & PoC16/11559169). This is an EU Joint Programme - Neurodegenerative Disease Research (JPND) project (INTER/JPND/14/02; INTER/JPND/15/11092422). Further support comes from the SysMedPD project which has received funding from the European Union's Horizon 2020 research and innovation programme under grant agreement No 668738. JJ, ELM and XQ are supported by fellowships from the FNR (AFR, Aides à la Formation-Recherche). Finally, we also thank the private donors who support our work at the Luxembourg Centre for Systems Biomedicine. ELM was also supported by an Aides à la Formation-Recherché training allowance from FNR.

Author contributions. JCS conceived the project. SB, and MF performed the experiments. SB, and JCS designed the experiments and wrote the paper. XQ introduced the LRRK2-G2019S mutation in the Healthy2 line. PA wrote and conceived the algorithms for image analysis. JJ contributed to the image analysis optimization. ELM contributed to the optimization of the microfluidic culture system. RMTF provided critical reading and scientific discussion. JS performed Zn analysis. LS performed the ROC and AUC analysis.

Competing interests. SB and JCS are co-founders and shareholders of Braingineering Technologies.

Figure legends

Fig. 1. LRRK2-G2019S dependent phenotype was enhanced in 3D conditions. (**A**) Schematic representation of the experimental pipeline used in the study. Image acquisition, segmentation, feature extraction, and data analysis were all automated. (**B**) Amount of TH/Tuj1, and Hoechst pixel per volume in 2D and 3D cultures after 6 weeks of neuronal differentiation was quantified as percentage of the WT cells (n=3-8 per cell line), p*=0.045. (**C**) Representative maximum intensity projection of confocal images of WT and LRRK2-G2019S neurons after 6 weeks showing Tuj1 row data, the perimeter of the Tuj1 mask after segmentation (red line) superimposed on Tuj1 row channel, and Hoechst raw channel superimposed on the nuclei mask (blue line). Representative confocal images of TH^+ cells and consequent TH skeleton mask and branching rendering after (**D**) 2 and (**G**) 6 weeks. Radar plots showing several features extracted from TH segmentation after 2 (**E**) and 6 (**H**) weeks. Semi-quantitative expression levels of pS935LRRK2 and pS129αSNCA after 2 (**F**) and 6 (**I**) weeks. Scale bar 100 µm. Values represent means with whiskers from min to max. *p<0.05, **p<0.01. Statistical analysis was performed using Student's *t* test.

Fig. 2. LRRK2-G2019S induced early mitochondrial dysfunction and cell death. Representative maximum intensity projection of confocal images of WT and LRRK2-G2019S neurons after 2 (**A**) and 3 (**B**) weeks showing TMRM row channel, and segmented mitochondria (red line) superimposed on Mitotracker green channel. Radar plots showing several features extracted from the nuclear and mitochondrial segmentation after (**C**) 2 and (**D**) 3 weeks. (**E**) Effects of the mutations on EH, Calcein, and CC3 pixel per volume after 2 weeks. (**F**) Representative maximum intensity projection of confocal images of WT and LRRK2-G2019S neurons after 2 weeks showing staining for Calcein/CC3, and EH/CC3. Each dot represents a technical replicate, n=4-8 per cell line. (**G**) LDH increased release in G2019S compared to WT lines after 3 weeks, values represent means with whiskers from min to max, 3 technical replicates were performed per each of the 4 independent experiments. Scale bar 100 µm. *p<0.05, **p<0.01, ***p<0.001. Statistical analysis was performed using Student's *t* test.

Fig. 3. Pharmacological rescue of LRRK2-G2019S induced morphometric defects.

(**A**) Radar plot showing the rescue of LRRK2-G2019S-induced phenotype following 6 week Inh2 administration. Inh2 restored TH levels back to the WT situation and ameliorated branching complexity. (**B**) Bar graphs showing neuronal volume, TH volume, network elements, TH link count, and TH node count after 6 weeks. CC3 in live cells after 2 weeks and mitochondrial count after 3 weeks is shown. Bars represent

means ± SEM, each dot represents a technical replicate, n=4-8 per cell line. (**C**) Bar graphs showing the rescue of selected features achieved with gene editing or Inh2 administration performed by bootstrapping. Statistical analysis was performed using Kruskal-Wallis test followed by post hoc Dunn's test.

Fig. 4. Contribution of the genetic background to LRRK2-G2019S induced neuronal abnormalities. (**A**) Heatmap comprising of all the assay combined, showing a clear clustering of the lines according to the genetic background. Bar graphs showing (**B**) CC3 in live cells, (**C**) CC3 by nuclei after 2 weeks; (**D**) mitochondrial count after 3 weeks; and (**E**) TH node count, (**F**) TH link count, and (**G**) TH pixels after 6 weeks. Bars represent means ± SEM, each dot represents a technical replicate, n=4-8 per cell line. Statistical analysis was performed using Kruskal-Wallis test followed by post hoc Dunn's test except in G where Turkey's MC test was performed as the data were normally distributed. In B, Mann-Whitney *t* test when comparing P versus PG is indicated. * compared to H, # compared to HMut.

References

1 Baharvand H, Hashemi SM, Kazemi Ashtiani S, Farrokhi A (2006) Differentiation of human embryonic stem cells into hepatocytes in 2D and 3D culture systems in vitro. The International journal of developmental biology 50: 645-652 Doi 10.1387/ijdb.052072hb

2 Baker BM, Chen CS (2012) Deconstructing the third dimension: how 3D culture microenvironments alter cellular cues. Journal of cell science 125: 3015-3024 Doi 10.1242/jcs.079509

3 Barker N, Huch M, Kujala P, van de Wetering M, Snippert HJ, van Es JH, Sato T, Stange DE, Begthel H, van den Born Met al (2010) Lgr5(+ve) stem cells drive self-renewal in the stomach and build long-lived gastric units in vitro. Cell Stem Cell 6: 25-36 Doi 10.1016/j.stem.2009.11.013

4 Birgersdotter A, Sandberg R, Ernberg I (2005) Gene expression perturbation in vitro--a growing case for three-dimensional (3D) culture systems. Seminars in cancer biology 15: 405-412 Doi 10.1016/j.semcancer.2005.06.009

5 Booth HDE, Hirst WD, Wade-Martins R (2017) The Role of Astrocyte Dysfunction in Parkinson's Disease Pathogenesis. Trends in neurosciences 40: 358-370 Doi 10.1016/j.tins.2017.04.001

6 Bose A, Beal MF (2016) Mitochondrial dysfunction in Parkinson's disease. Journal of neurochemistry 139 Suppl 1: 216-231 Doi 10.1111/jnc.13731

7 Byers B, Cord B, Nguyen HN, Schule B, Fenno L, Lee PC, Deisseroth K, Langston JW, Pera RR, Palmer TD (2011) SNCA triplication Parkinson's patient's iPSC-derived DA neurons accumulate alpha-synuclein and are susceptible to oxidative stress. PLoS One 6: e26159 Doi 10.1371/journal.pone.0026159

8 Caiazzo M, Tabata Y, Lutolf M (2017) Generation of Induced Pluripotent Stem Cells in Defined Three-Dimensional Hydrogels. Methods Mol Biol 1612: 65-78 Doi 10.1007/978-1-4939-7021-6_5

9 Chan SL, Tan EK (2017) Targeting LRRK2 in Parkinson's disease: an update on recent developments. Expert opinion on therapeutic targets 21: 601-610 Doi 10.1080/14728222.2017.1323881

10 Choi SH, Kim YH, Hebisch M, Sliwinski C, Lee S, D'Avanzo C, Chen H, Hooli B, Asselin C, Muffat Jet al (2014) A three-dimensional human neural cell culture model of Alzheimer's disease. Nature 515: 274-278 Doi 10.1038/nature13800

11 Cookson MR, Bandmann O (2010) Parkinson's disease: insights from pathways. Hum Mol Genet 19: R21-27 Doi 10.1093/hmg/ddq167

12 Cooper O, Seo H, Andrabi S, Guardia-Laguarta C, Graziotto J, Sundberg M, McLean JR, Carrillo-Reid L, Xie Z, Osborn Tet al (2012) Pharmacological rescue of mitochondrial deficits in iPSC-derived neural cells from patients with familial Parkinson's disease. Sci Transl Med 4: 141ra190 Doi 10.1126/scitranslmed.3003985

13 Gillardon F (2009) Leucine-rich repeat kinase 2 phosphorylates brain tubulin-beta isoforms and modulates microtubule stability--a point of convergence in parkinsonian neurodegeneration? Journal of neurochemistry 110: 1514-1522 Doi 10.1111/j.1471-4159.2009.06235.x

14 Greggio E (2012) Role of LRRK2 kinase activity in the pathogenesis of Parkinson's disease. Biochemical Society transactions 40: 1058-1062 Doi 10.1042/BST20120054

15 Halldorsson S, Lucumi E, Gomez-Sjoberg R, Fleming RM (2015) Advantages and challenges of microfluidic cell culture in polydimethylsiloxane devices. Biosensors & bioelectronics 63: 218-231 Doi 10.1016/j.bios.2014.07.029

16 Healy DG, Falchi M, O'Sullivan SS, Bonifati V, Durr A, Bressman S, Brice A, Aasly J, Zabetian CP, Goldwurm Set al (2008) Phenotype, genotype, and worldwide genetic penetrance of LRRK2-associated Parkinson's disease: a case-control study. Lancet Neurol 7: 583-590 Doi 10.1016/S1474-4422(08)70117-0

17 Hughes CS, Postovit LM, Lajoie GA (2010) Matrigel: a complex protein mixture required for optimal growth of cell culture. Proteomics 10: 1886-1890 Doi 10.1002/pmic.200900758

18 Islam MS, Moore DJ (2017) Mechanisms of LRRK2-dependent neurodegeneration: role of enzymatic activity and protein aggregation. Biochemical Society transactions 45: 163-172 Doi 10.1042/BST20160264

19 Lancaster MA, Knoblich JA (2014) Generation of cerebral organoids from human pluripotent stem cells. Nat Protoc 9: 2329-2340 Doi 10.1038/nprot.2014.158

20 Li H, Wijekoon A, Leipzig ND (2012) 3D differentiation of neural stem cells in macroporous photopolymerizable hydrogel scaffolds. PLoS One 7: e48824 Doi 10.1371/journal.pone.0048824

21 Liedmann A, Frech S, Morgan PJ, Rolfs A, Frech MJ (2012) Differentiation of human neural progenitor cells in functionalized hydrogel matrices. Biores Open Access 1: 16-24 Doi 10.1089/biores.2012.0209

22 Liu GH, Ding Z, Izpisua Belmonte JC (2012) iPSC technology to study human aging and aging-related disorders. Curr Opin Cell Biol 24: 765-774 Doi 10.1016/j.ceb.2012.08.014

23 Liu GH, Qu J, Suzuki K, Nivet E, Li M, Montserrat N, Yi F, Xu X, Ruiz S, Zhang Wet al (2012) Progressive degeneration of human neural stem cells caused by pathogenic LRRK2. Nature 491: 603-607 Doi 10.1038/nature11557

24 Meissner WG, Frasier M, Gasser T, Goetz CG, Lozano A, Piccini P, Obeso JA, Rascol O, Schapira A, Voon Vet al (2011) Priorities in Parkinson's disease research. Nature reviews Drug discovery 10: 377-393 Doi 10.1038/nrd3430

25 Monzel AS, Smits LM, Hemmer K, Hachi S, Moreno EL, van Wuellen T, Jarazo J, Walter J, Bruggemann I, Boussaad Iet al (2017) Derivation of Human Midbrain-Specific Organoids from Neuroepithelial Stem Cells. Stem cell reports 8: 1144-1154 Doi 10.1016/j.stemcr.2017.03.010

26 Moon HE, Paek SH (2015) Mitochondrial Dysfunction in Parkinson's Disease. Experimental neurobiology 24: 103-116 Doi 10.5607/en.2015.24.2.103

27 Moreno EL, Hachi S, Hemmer K, Trietsch SJ, Baumuratov AS, Hankemeier T, Vulto P, Schwamborn JC, Fleming RM (2015) Differentiation of neuroepithelial stem cells into functional dopaminergic neurons in 3D microfluidic cell culture. Lab on a chip 15: 2419-2428 Doi 10.1039/c5lc00180c

28 Mukaetova-Ladinska EB, Garcia-Siera F, Hurt J, Gertz HJ, Xuereb JH, Hills R, Brayne C, Huppert FA, Paykel ES, McGee Met al (2000) Staging of cytoskeletal and beta-amyloid changes in human isocortex reveals biphasic synaptic protein response during progression of Alzheimer's disease. Am J Pathol 157: 623-636

29 Nelson CM, Bissell MJ (2005) Modeling dynamic reciprocity: engineering three-dimensional culture models of breast architecture, function, and neoplastic transformation. Seminars in cancer biology 15: 342-352 Doi 10.1016/j.semcancer.2005.05.001

30 Nguyen HN, Byers B, Cord B, Shcheglovitov A, Byrne J, Gujar P, Kee K, Schule B, Dolmetsch RE, Langston Wet al (2011) LRRK2 mutant iPSC-derived DA neurons demonstrate increased susceptibility to oxidative stress. Cell Stem Cell 8: 267-280 Doi 10.1016/j.stem.2011.01.013

31 Ortinau S, Schmich J, Block S, Liedmann A, Jonas L, Weiss DG, Helm CA, Rolfs A, Frech MJ (2010) Effect of 3D-scaffold formation on differentiation and survival in human neural progenitor cells. Biomed Eng Online 9: 70 Doi 10.1186/1475-925X-9-70

32 Paisan-Ruiz C, Jain S, Evans EW, Gilks WP, Simon J, van der Brug M, Lopez de Munain A, Aparicio S, Gil AM, Khan Net al (2004) Cloning of the gene containing mutations that cause PARK8-linked Parkinson's disease. Neuron 44: 595-600 Doi 10.1016/j.neuron.2004.10.023

33 Papkovskaia TD, Chau KY, Inesta-Vaquera F, Papkovsky DB, Healy DG, Nishio K, Staddon J, Duchen MR, Hardy J, Schapira AHet al (2012) G2019S leucine-rich repeat kinase 2 causes uncoupling protein-mediated mitochondrial depolarization. Hum Mol Genet 21: 4201-4213 Doi 10.1093/hmg/dds244

34 Parr CJC, Yamanaka S, Saito H (2017) An update on stem cell biology and engineering for brain development. Molecular psychiatry 22: 808-819 Doi 10.1038/mp.2017.66

35 Poewe W, Seppi K, Tanner CM, Halliday GM, Brundin P, Volkmann J, Schrag AE, Lang AE (2017) Parkinson disease. Nature reviews Disease primers 3: 17013 Doi 10.1038/nrdp.2017.13

36 Porter GW, Khuri FR, Fu H (2006) Dynamic 14-3-3/client protein interactions integrate survival and apoptotic pathways. Seminars in cancer biology 16: 193-202 Doi 10.1016/j.semcancer.2006.03.003

37 Ramanujan S, Pluen A, McKee TD, Brown EB, Boucher Y, Jain RK (2002) Diffusion and convection in collagen gels: implications for transport in the tumor interstitium. Biophysical journal 83: 1650-1660 Doi 10.1016/S0006-3495(02)73933-7

38 Ramsden N, Perrin J, Ren Z, Lee BD, Zinn N, Dawson VL, Tam D, Bova M, Lang M, Drewes Get al (2011) Chemoproteomics-based design of potent LRRK2-selective lead compounds that attenuate Parkinson's disease-related toxicity in human neurons. ACS Chem Biol 6: 1021-1028 Doi 10.1021/cb2002413

39 Rassu M, Del Giudice MG, Sanna S, Taymans JM, Morari M, Brugnoli A, Frassineti M, Masala A, Esposito S, Galioto Met al (2017) Role of LRRK2 in the regulation of dopamine receptor trafficking. PLoS One 12: e0179082 Doi 10.1371/journal.pone.0179082

40 Reinhardt P, Glatza M, Hemmer K, Tsytsyura Y, Thiel CS, Hoing S, Moritz S, Parga JA, Wagner L, Bruder JMet al (2013) Derivation and expansion using only small molecules of human neural progenitors for neurodegenerative disease modeling. PLoS One 8: e59252 Doi 10.1371/journal.pone.0059252

41 Reinhardt P, Schmid B, Burbulla LF, Schondorf DC, Wagner L, Glatza M, Hoing S, Hargus G, Heck SA, Dhingra Aet al (2013) Genetic correction of a LRRK2 mutation in human iPSCs links parkinsonian neurodegeneration to ERK-dependent changes in gene expression. Cell Stem Cell 12: 354-367 Doi 10.1016/j.stem.2013.01.008

42 Sbrana T, Ahluwalia A (2012) Engineering Quasi-Vivo in vitro organ models. Adv Exp Med Biol 745: 138-153 Doi 10.1007/978-1-4614-3055-1_9

43 Schapira AH (2007) Mitochondrial dysfunction in Parkinson's disease. Cell Death Differ 14: 1261-1266 Doi 10.1038/sj.cdd.4402160

44 Schapira AH, Gegg M (2011) Mitochondrial contribution to Parkinson's disease pathogenesis. Parkinson's disease 2011: 159160 Doi 10.4061/2011/159160

45 Shield K, Ackland ML, Ahmed N, Rice GE (2009) Multicellular spheroids in ovarian cancer metastases: Biology and pathology. Gynecologic oncology 113: 143-148 Doi 10.1016/j.ygyno.2008.11.032

46 Simon-Sanchez J, Schulte C, Bras JM, Sharma M, Gibbs JR, Berg D, Paisan-Ruiz C, Lichtner P, Scholz SW, Hernandez DGet al (2009) Genome-wide association study reveals genetic risk underlying Parkinson's disease. Nature genetics 41: 1308-1312 Doi 10.1038/ng.487

47 Skibinski G, Nakamura K, Cookson MR, Finkbeiner S (2014) Mutant LRRK2 toxicity in neurons depends on LRRK2 levels and synuclein but not kinase activity or inclusion bodies. J Neurosci 34: 418-433 Doi 10.1523/JNEUROSCI.2712-13.2014

48 Smith WW, Pei Z, Jiang H, Dawson VL, Dawson TM, Ross CA (2006) Kinase activity of mutant LRRK2 mediates neuronal toxicity. Nature neuroscience 9: 1231-1233 Doi 10.1038/nn1776

49 Suga H, Kadoshima T, Minaguchi M, Ohgushi M, Soen M, Nakano T, Takata N, Wataya T, Muguruma K, Miyoshi Het al (2011) Self-formation of functional adenohypophysis in three-dimensional culture. Nature 480: 57-62 Doi 10.1038/nature10637

50 Takahashi K, Yamanaka S (2006) Induction of pluripotent stem cells from mouse embryonic and adult fibroblast cultures by defined factors. Cell 126: 663-676 Doi 10.1016/j.cell.2006.07.024

51 Trietsch SJ, Israels GD, Joore J, Hankemeier T, Vulto P (2013) Microfluidic titer plate for stratified 3D cell culture. Lab on a chip 13: 3548-3554 Doi 10.1039/c3lc50210d

52 Wallings R, Manzoni C, Bandopadhyay R (2015) Cellular processes associated with LRRK2 function and dysfunction. FEBS J 282: 2806-2826 Doi 10.1111/febs.13305

53 Wang X, Yan MH, Fujioka H, Liu J, Wilson-Delfosse A, Chen SG, Perry G, Casadesus G, Zhu X (2012) LRRK2 regulates mitochondrial dynamics and function through direct interaction with DLP1. Hum Mol Genet 21: 1931-1944 Doi 10.1093/hmg/dds003

54 Yamada KM, Cukierman E (2007) Modeling tissue morphogenesis and cancer in 3D. Cell 130: 601-610 Doi 10.1016/j.cell.2007.08.006

55 Zhao P, Luo Z, Tian W, Yang J, Ibanez DP, Huang Z, Tortorella MD, Esteban MA, Fan W (2014) Solving the puzzle of Parkinson's disease using induced pluripotent stem cells. Exp Biol Med (Maywood) 239: 1421-1432 Doi 10.1177/1535370214538588

56 Zietarska M, Maugard CM, Filali-Mouhim A, Alam-Fahmy M, Tonin PN, Provencher DM, Mes-Masson AM (2007) Molecular description of a 3D in vitro model for the study of epithelial ovarian cancer (EOC). Molecular carcinogenesis 46: 872-885 Doi 10.1002/mc.20315

57 Zimprich A, Biskup S, Leitner P, Lichtner P, Farrer M, Lincoln S, Kachergus J, Hulihan M, Uitti RJ, Calne DBet al (2004) Mutations in LRRK2 cause autosomal-dominant parkinsonism with pleomorphic pathology. Neuron 44: 601-607 Doi 10.1016/j.neuron.2004.11.005

hiPSC-derived neurons in a 3D microfluidic system as an enabling tool for high content drug screening targeting G2019S LRRK2 mutation

Supplementary Information

Supplementary Figure Legends

Fig. S1. Quality controls of hNESC and 2D neurons. (**A**) Table illustrating the characteristics of the cell lines used in the study. (**B**) Genomic sequencing confirming the insertion of LRRK2-G2019S mutation in the healthy cell lines, and the correction of the mutation in the PD cell lines. (**C**) Representative confocal pictures of the hNESC stained against the stem cell markers SOX1, SOX2, and Nestin as a quality control of the cultures. (**D**) Representative confocal pictures of 6 week old 2D cultures showing Tuj1 row images, perimeter of the Tuj1 segmented images (red lines) superimposed on the Tuj1 row images, and perimeter of the TH segmented images (red lines) superimposed on the TH row images. Scale bars 100 µm. (**E**) Time-dependent quantification of Zn expressed as ng/ml in the flow-through of the 3D cultures expressed as means ± SEM (n=3).

Fig. S2. Key steps of the image analysis segmentation. (**A**) For the segmentation of neurons, a strategy combining global and local thresholding was implemented. For global thresholding, image preprocessing was done via low pass filtering (Tuj1LP). The raw Tuj1 channel was convolved with a gaussian filter and the global neuronal mask was defined by threshold 150 (Tuj1GlobalMask). A difference of gaussians was applied in the preprocessing step (Tuj1DoG). The local neuronal mask was defined by those pixels with values larger than 3 (Tuj1LocalMask). The concepts of global and local thresholding were combined by retaining those pixels in the neuronal mask which were detected by at least one of these methods (NeuroMask).

For the analysis of the TH channel, an additional mask was defined by preprocessing the raw TH channel via convolution (THLP), and thresholding by pixel value 100 (THMask). Image preprocessing for the segmentation of nuclei was done via a difference of gaussians (NucleiDoG). The first rough nuclei mask was defined by those pixels with graytone values larger than 10 (NucleiDoGmask). Only connected components with at least 200 pixels were retained (NucleiMask). (**B**) For the mitochondrial segmentation, Mitotracker green channel was convolved with a Gaussian filter (MitoDoGmask), and a thresholding was applied (MitoMask).

Fig. S3. ROC analysis. (**A**) ROC analysis for the comparison LRRK2-G2019S versus WT and **(B)** for the comparison LRRK2-G2019S Inh2 versus WT Inh2 for all the different assays at all time-points. The area under the curve (AUC) is indicated.

Supplementary Table

Table S1: number of samples for the different subgroups in the different assays.

Assay and time point	***# samples Vehicle (G2019S/WT)***	***# samples Inh2 (G2019S/WT)***	***# initial features***
Cell death 2w	**68/66**	**71/64**	11
Cell death 3w	18/22	24/26	11
Mitochondrial assay 2w	**60/68**	**62/54**	21
Mitochondrial assay 3w	**58/63**	**64/53**	21
Morphometric analysis 2w	30/28	29/29	46
Morphometric analysis 6w	32/41	59/45	46

Table 1. Features from image analysis

Feature	***Description***
Morphometric assay	
Hoechst	Count of nuclear mask pixels
Tuj1	Count of neuronal mask pixels
TH/Tuj1	Sum of TH pixel intensities / sumTuj1
pS935LRRK2	Sum of pS935LRRK2 pixel intensities / sumTuj1
pS129αSNCA	Sum of pS129αSNCA pixel intensities / sumTuj1
NucHigh	Sum pyknotic nuclear mask / sumHoechst
NucLow	Sum normal nuclear mask / sumHoechst
TH Mask	TH positive pixels
Skeleton Pixel TH	Count of TH Skeleton Pixel
Node Count TH	Total number of branch and end-points in the TH skeleton
Link Count TH	Total number of links in the TH skeleton
Network Elements	Sum of all the node and link elements
TH	Sum of raw TH pixel values within the Tuj1 mask
TH Fragmentation	Surface to Volume ratio of TH Mask
Mitochondrial assay	
CountMito	Count of mitochondria per image
TMRMinMask	Background pixels were set to zero by multiplying the raw TMRM channel with the mitochondria mask. TMRMinMask corresponds to the sum of pixel values in this image divided by the count of mitochondrial pixels
TMRMinCC	For each mitochondrium the mean TMRM intensity was extracted. TMRMinCC corresponds to the unweighted mean of mean TMRM intensities among all mitochondria in an image
MitoskelPixels	Count of mitochondrial skekleton pixels within an image
MitoPerimPixels	Count of mitochondrial perimeter/surface pixels per image
MitoBodyPixels	Count of mitochondrial body pixels per image
MitobodyCount	Count of mitochondrial bodies as observed after erosion of the mitochondrial mask
Node Count	Count of nodes
Link Count	Count of links
MedianNodeDegree	Median number of pixels in the mitochondrial skeleton image connecting adjacent nodes
CellVolume_by_NucVolume	CellVolume / NucVolume
Cell death assay	
NucMask	Count of nuclear mask pixels
CC3Mask	Count of cleaved-caspase 3 mask pixels

CC3ByNuc	Cleaved-caspase 3Mask / NucMask
EthidMask	Count of ethidiumhomodimer mask pixels
EthidByNuc	EthidMask / NucMask
CalceinMask	Count of calcein mask pixels
CalceinByNuc	CalceinMask / NucMask
CalceinMask	Count of Calcein mask pixels
CalceinByNuc	CalceinMask / NucMask
CC3inLiveCells	Count of cleaved-caspase 3 live mask pixels

Table 2. Results for the comparison between LRRK2-G2019S and WT

Assay and time point	*Features after selection*	*AUC (mean±std)*	*Accuracy (%)*	*Sensitivity (%)*	*Specificity (%)*
Cell death 2w	11	**88,5±2,2**	**81**	81,9	80,1
Cell death 3w	**6**	**90,1±3,9**	**85,8**	81,6	89,3
Mitochondrial assay 2w	21	63,4±4	59,8	46,5	**71,5**
Mitochondrial assay 3w	21	56,5±4,9	54,9	39,4	**69,1**
Morphometric analysis 2w	**16**	**77,9±3,3**	**70,6**	70,4	70,8
Morphometric analysis 6w	**16**	**79,2±3,5**	**75,1**	63,1	84,5

Table 3. Results for the comparison between LRRK2-G2019S Inh2 and WT Inh2

Assay and time point	*Features after selection*	*AUC (mean±std)*	*Accuracy (%)*	*Sensitivity (%)*	*Specificity (%)*
Cell death 2w	11	**81,1±2,4**	67,9	66,1	70
Cell death 3w	6	**74,1±4,1**	67,5	67	68
Mitochondrial assay 2w	21	71,7±3,1	66,7	**84,6**	46,2
Mitochondrial assay 3w	21	65,1±3,7	62,2	**83,8**	36,1
Morphometric analysis 2w	20	52,2±5,7	54,1	54,7	53,6
Morphometric analysis 6w	14	67,7±4,1	62,4	**80,5**	38,5

Figure 1

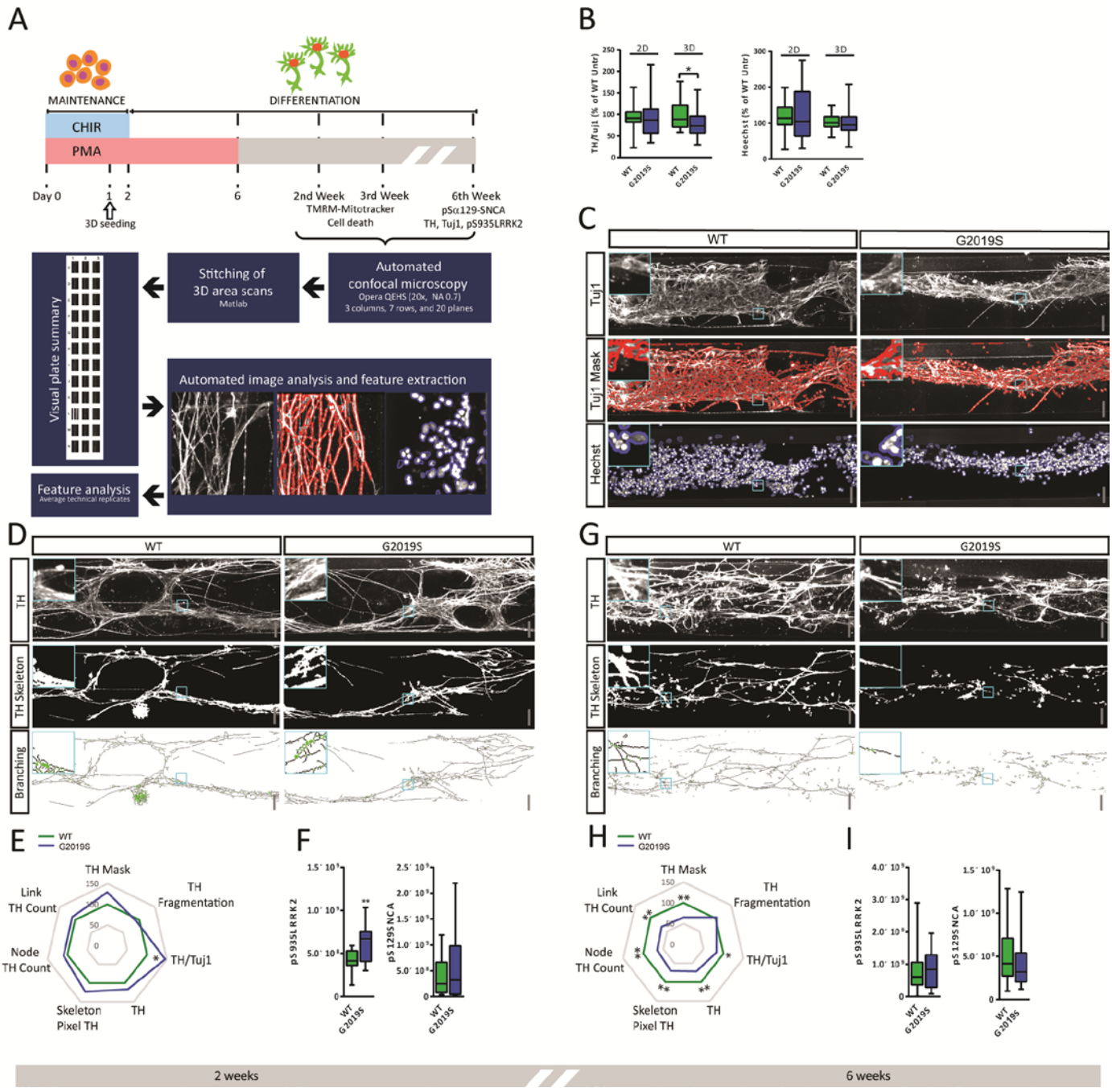
A
MAINTENANCE
DIFFERENTIATION
CHIR
PMA
Day 0
1
2
6
2nd Week
3rd Week
6th Week
3D seeding
TMRM-Mitotracker
Cell death
pSα129-SNCA
TH, Tuj1, pS935LRRK2
Visual plate summary
Stitching of 3D area scans
Matlab
Automated confocal microscopy
Opera QEHS (20x, NA 0.7)
3 columns, 7 rows, and 20 planes
Automated image analysis and feature extraction
Feature analysis
Average technical replicates
B
2D
3D
TH/Tuj1 (% of WT Untr)
Hoechst (% of WT Untr)
WT
G2019S
C
WT
G2019S
Tuj1
Tuj1 Mask
Hechst
D
TH
TH Skeleton
Branching
G
E
F
H
I
TH Mask
TH Fragmentation
TH/Tuj1
TH
Skeleton Pixel TH
Node TH Count
Link TH Count
pS 935LRRK2
pS 1295NCA
2 weeks
6 weeks

Figure 2

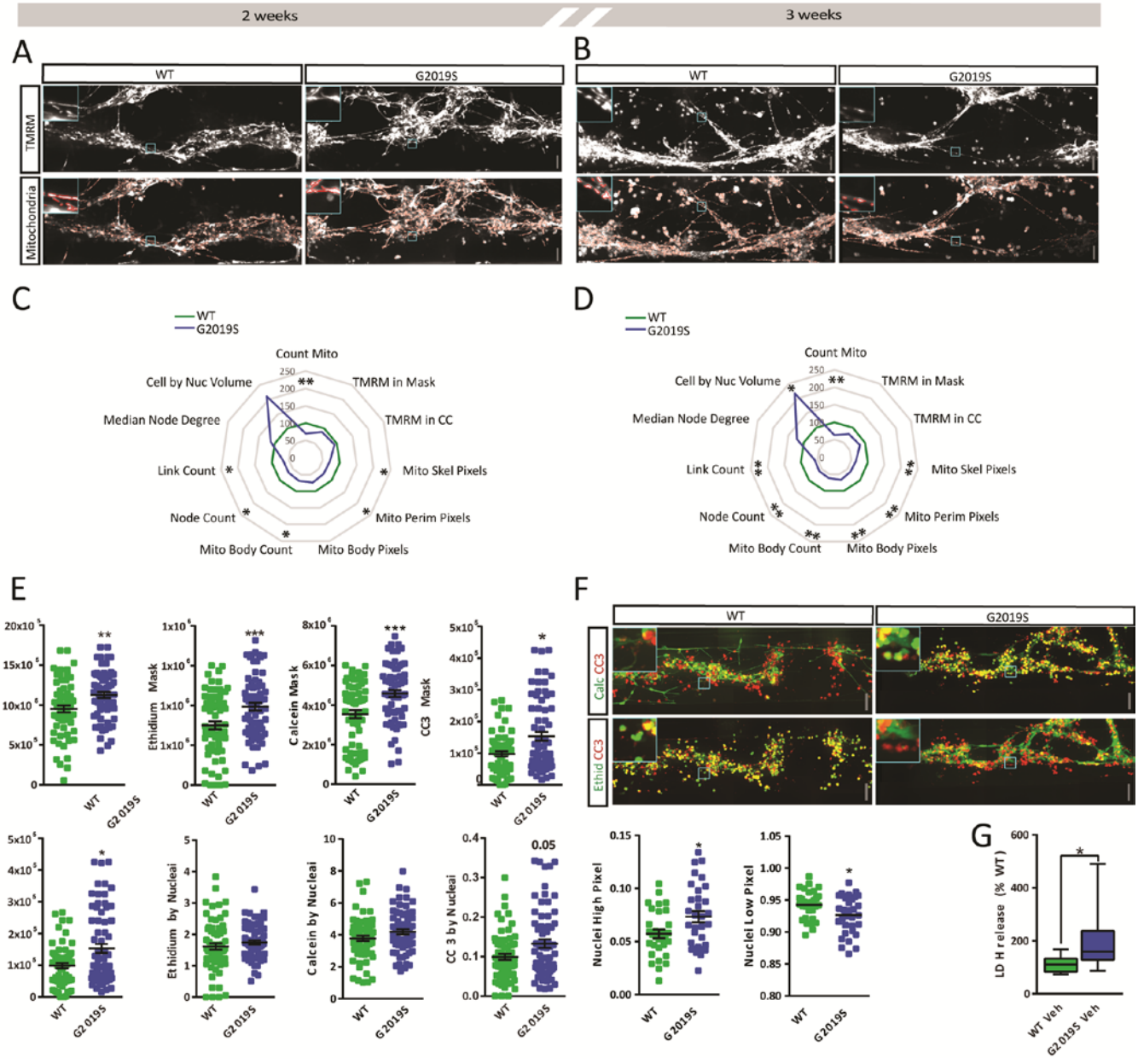
2 weeks
3 weeks
A
B
WT
G2019S
TMRM
Mitochondria
C
D
WT
G2019S
Count Mito
TMRM in Mask
TMRM in CC
Mito Skel Pixels
Mito Perim Pixels
Mito Body Pixels
Mito Body Count
Node Count
Link Count
Median Node Degree
Cell by Nuc Volume
E
F
Calc CC3
Ethid CC3
G
LDH release (% WT)
WT Veh
G2019S Veh

Figure 3

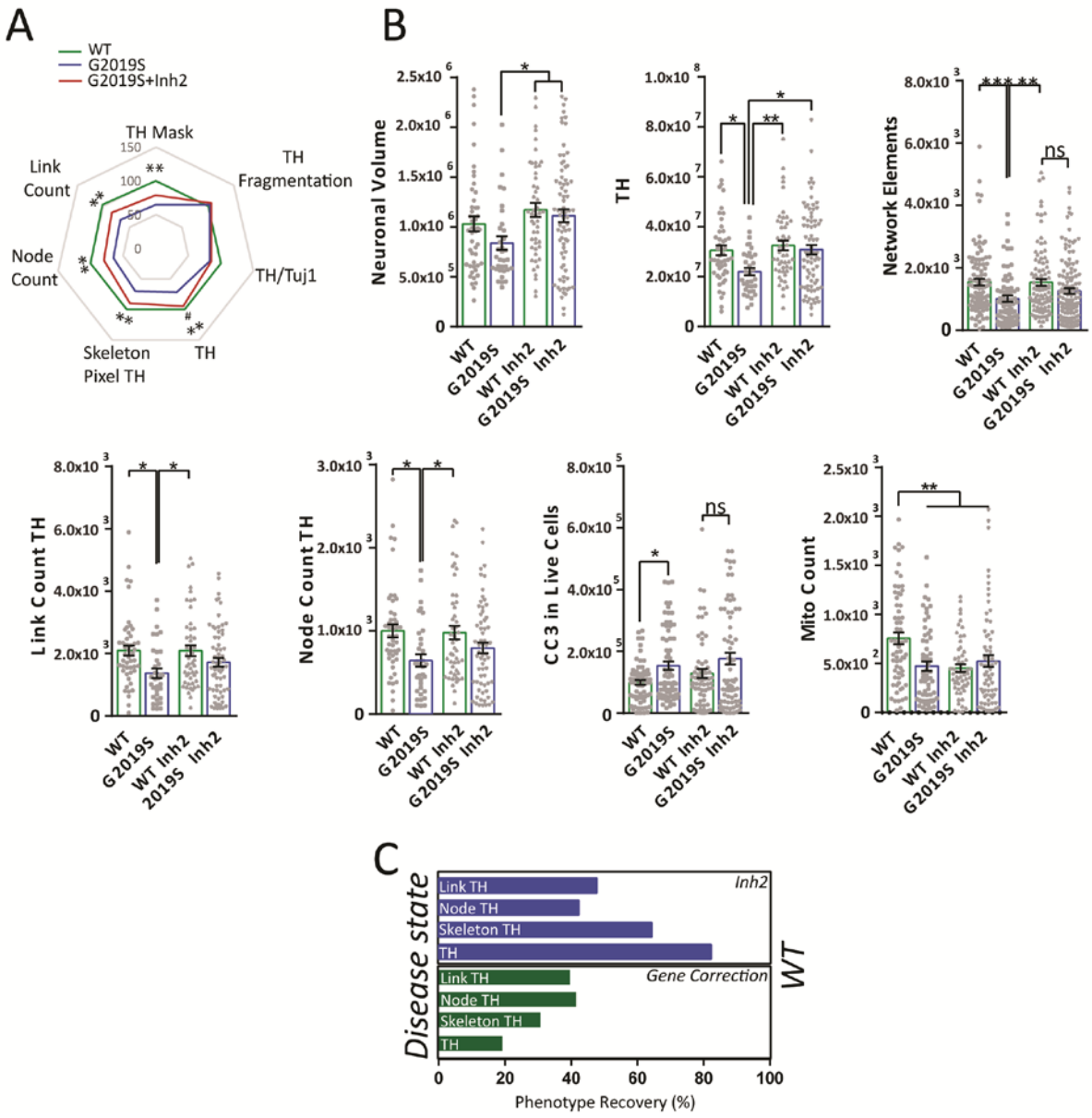
A
WT
G2019S
G2019S+Inh2
TH Mask
TH Fragmentation
TH/Tuj1
TH
Skeleton Pixel TH
Node Count
Link Count
B
Neuronal Volume
TH
Network Elements
Link Count TH
Node Count TH
CC3 in Live Cells
Mito Count
WT
G2019S
WT Inh2
G2019S Inh2
ns
C
Disease state
Inh2
Gene Correction
WT
Link TH
Node TH
Skeleton TH
TH
Phenotype Recovery (%)

Figure 4

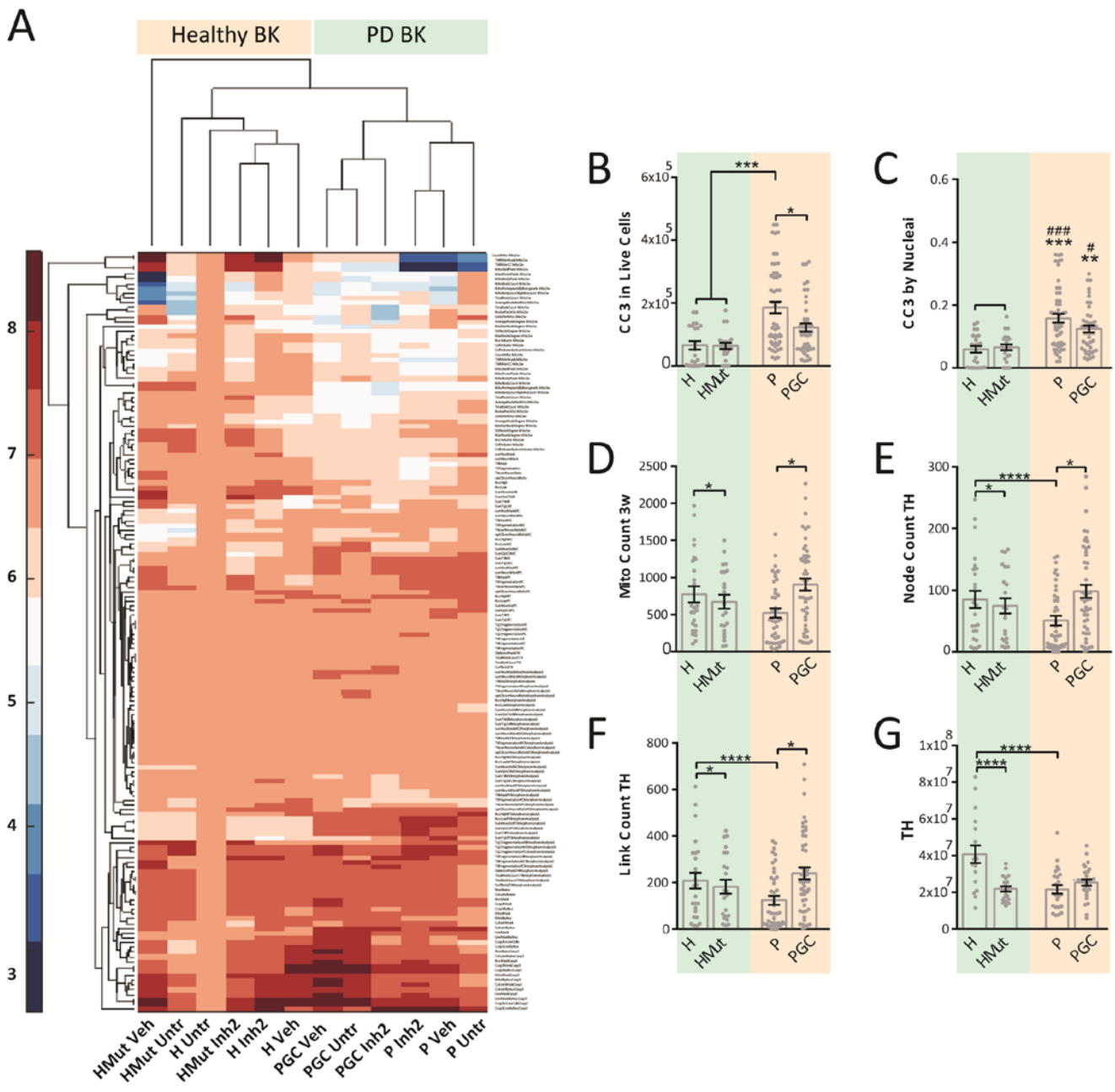
A
Healthy BK
PD BK
8
7
6
5
4
3
HMut Veh
HMut Untr
H Untr
HMut Inh2
H Inh2
H Veh
PGC Veh
PGC Untr
PGC Inh2
P Inh2
P Veh
P Untr
B
CC3 in Live Cells
C
CC3 by Nucleai
D
Mito Count 3w
E
Node Count TH
F
Link Count TH
G
TH
H
HMut
P
PGC

Figure S1

A

Line	Age of sampling	Gender	Reference
Healthy1	81	F	Reinhardt et al., 2013
Healthy2	46	M	BOBSC-T6/8 B1 Cambridge
PD1	81	F	Reinhardt et al., 2013
PD2	54	F	Reinhardt et al., 2013

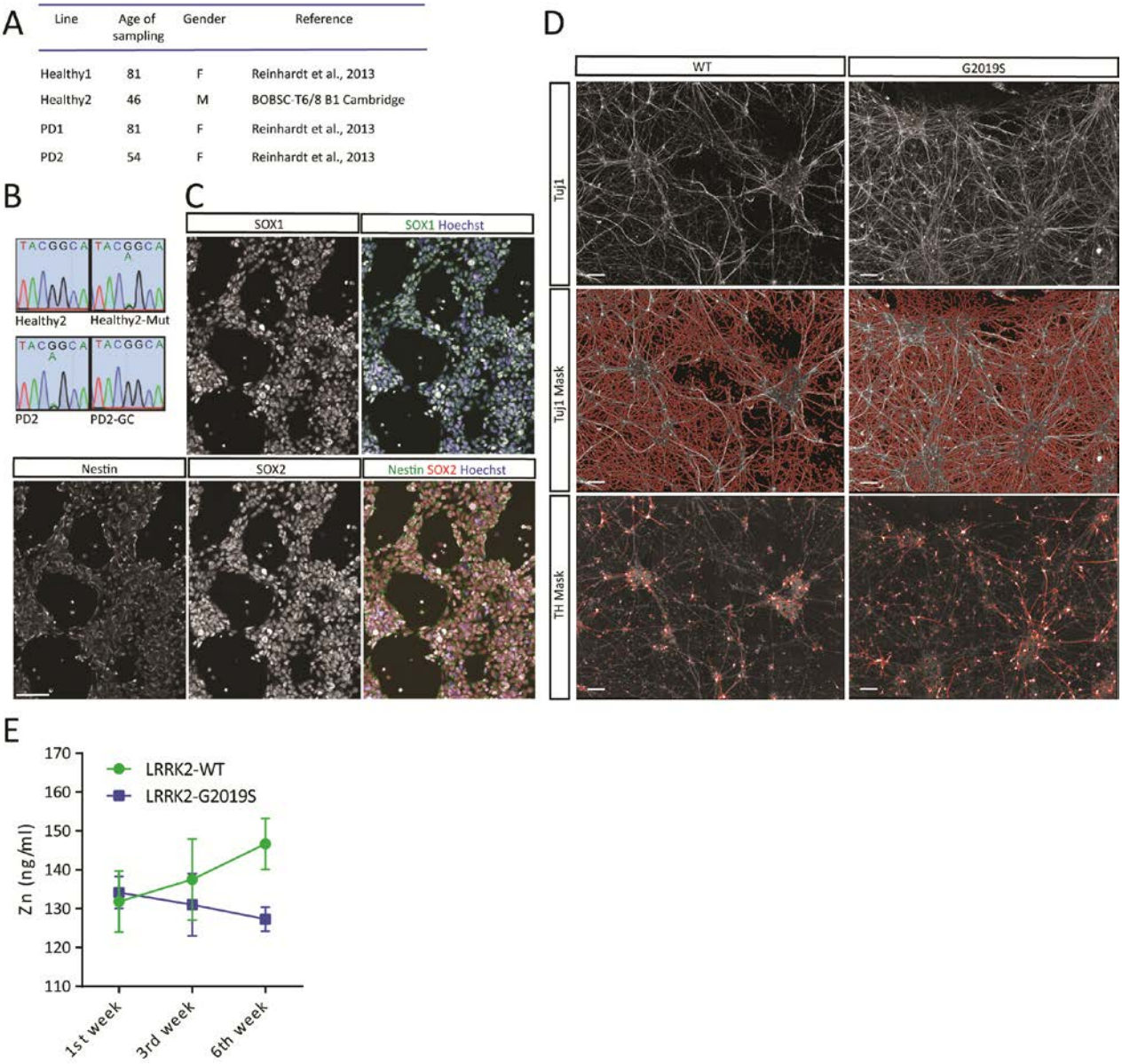

Figure S2

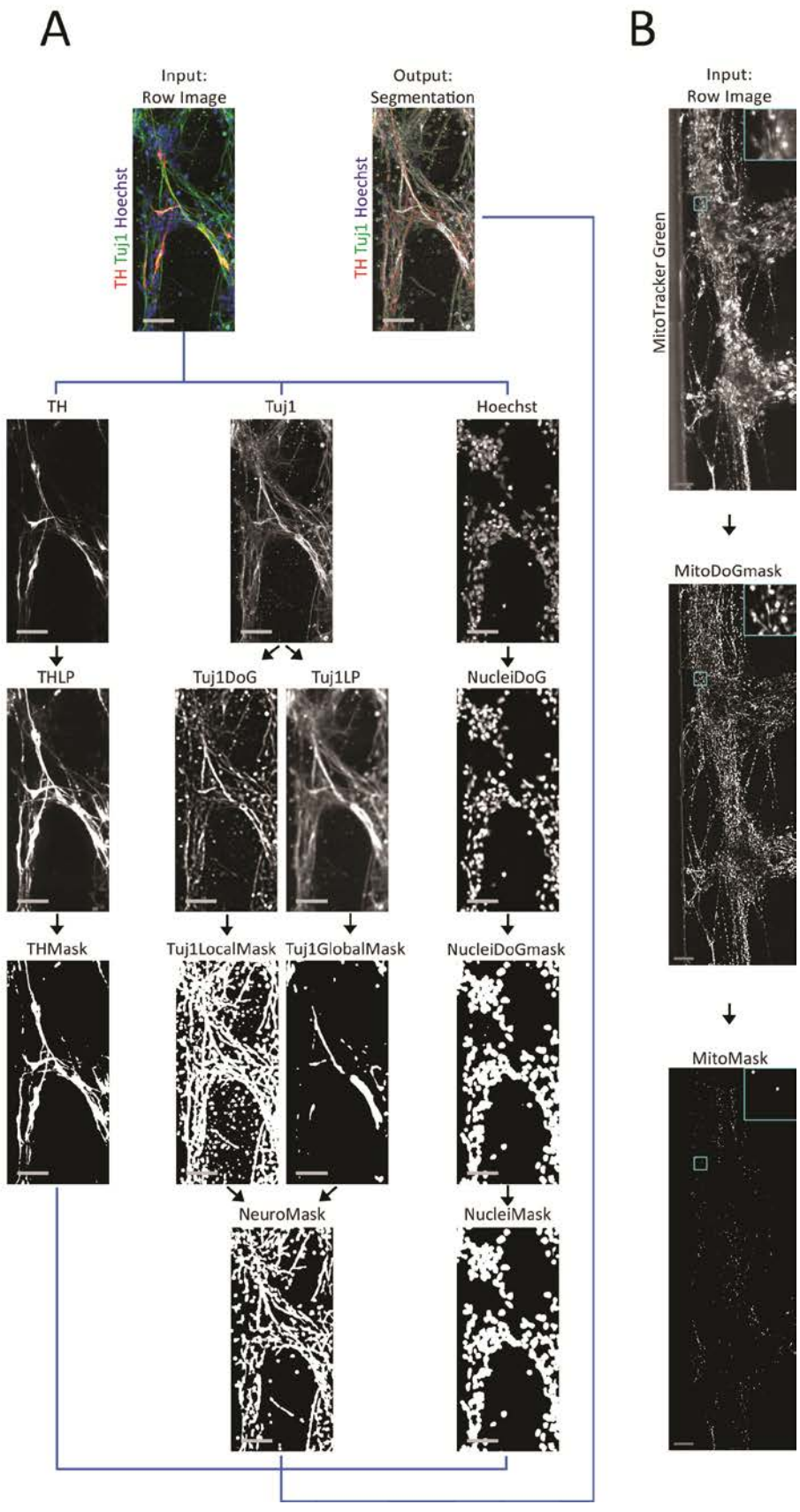
A
Input:
Row Image
TH Tuj1 Hoechst
Output:
Segmentation
TH Tuj1 Hoechst
TH
Tuj1
Hoechst
THLP
Tuj1DoG
Tuj1LP
NucleiDoG
THMask
Tuj1LocalMask
Tuj1GlobalMask
NucleiDoGmask
NeuroMask
NucleiMask
B
Input:
Row Image
MitoTracker Green
MitoDoGmask
MitoMask

Figure S3

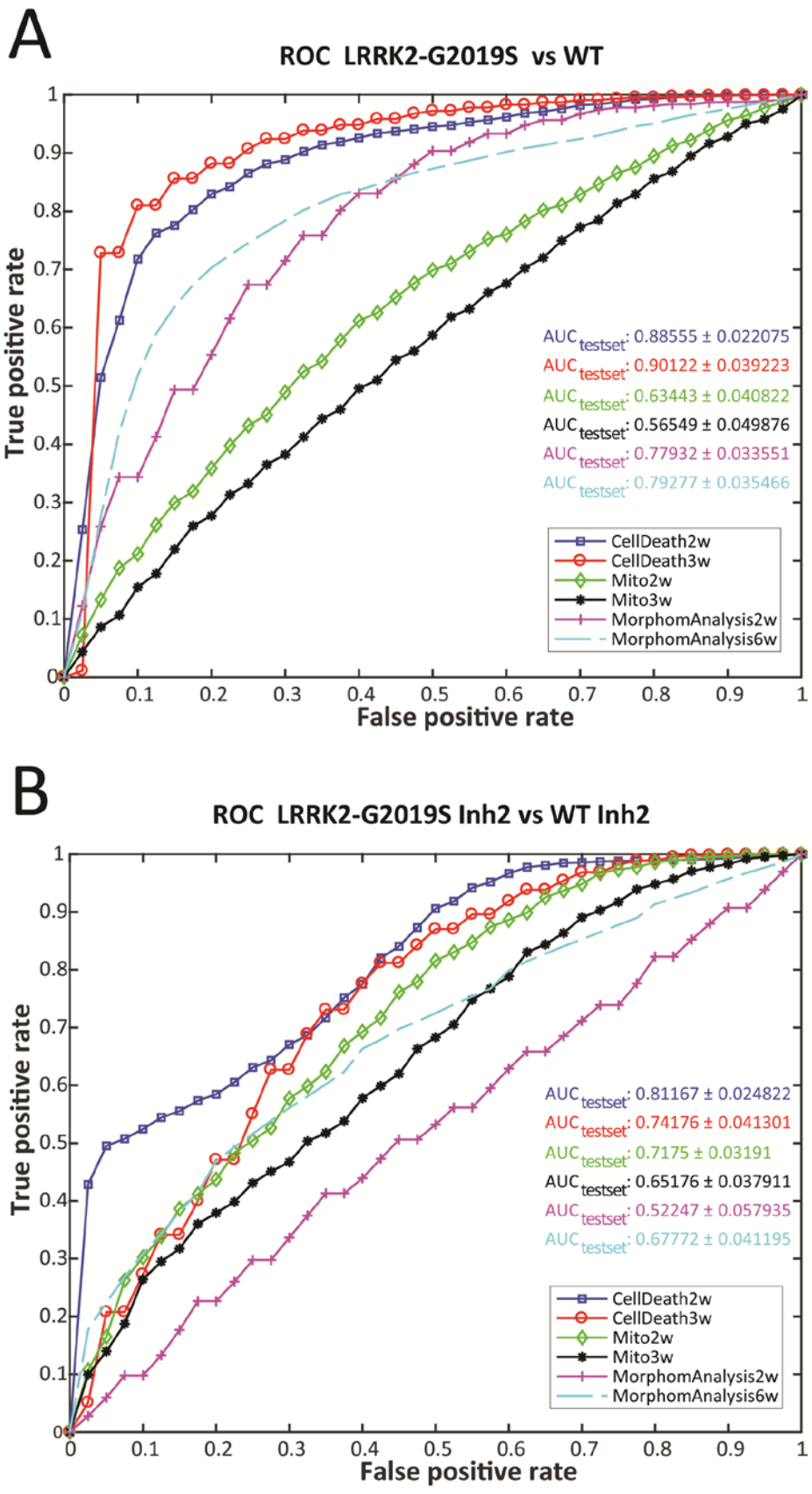
A
ROC LRRK2-G2019S vs WT
True positive rate
False positive rate
AUC testset: 0.88555 ± 0.022075
AUC testset: 0.90122 ± 0.039223
AUC testset: 0.63443 ± 0.040822
AUC testset: 0.56549 ± 0.049876
AUC testset: 0.77932 ± 0.033551
AUC testset: 0.79277 ± 0.035466
CellDeath2w
CellDeath3w
Mito2w
Mito3w
MorphomAnalysis2w
MorphomAnalysis6w
B
ROC LRRK2-G2019S Inh2 vs WT Inh2
True positive rate
False positive rate
AUC testset: 0.81167 ± 0.024822
AUC testset: 0.74176 ± 0.041301
AUC testset: 0.7175 ± 0.03191
AUC testset: 0.65176 ± 0.037911
AUC testset: 0.52247 ± 0.057935
AUC testset: 0.67772 ± 0.041195
CellDeath2w
CellDeath3w
Mito2w
Mito3w
MorphomAnalysis2w
MorphomAnalysis6w

6.1.3 Manuscript VI

Derivation of human midbrain-specific organoids from neuroepithelial stem cells

Anna S. Monzel [1#] , Lisa M. Smits [1#] , Kathrin Hemmer [1#], Siham Hachi [2], Edinson Lucumi Moreno [2], Thea van Wuellen [1], **Javier Jarazo** [1], Jonas Walter [1], Inga Brüggemann [1], Ibrahim Boussaad [3], Emanuel Berger [1], Ronan M.T. Fleming [2], Silvia Bolognin [1], Jens C. Schwamborn [1*]

[1] Luxembourg Centre for Systems Biomedicine (LCSB), Developmental and Cellular Biology, University of Luxembourg, L-4362 Esch-sur-Alzette Luxembourg

[2] Luxembourg Centre for Systems Biomedicine (LCSB), Systems Biochemistry, University of Luxembourg, L-4362 Esch-sur-Alzette Luxembourg

[3] Luxembourg Centre for Systems Biomedicine (LCSB), Clinical & Experimental Neuroscience, University of Luxembourg, L-4362 Esch-sur-Alzette Luxembourg

*Correspondence: Jens C. Schwamborn, Luxembourg Centre for Systems Biomedicine (LCSB), University of Luxembourg, 7, avenue des Hauts-Fourneaux, L-4362 Esch-sur-Alzette Luxembourg; E-mail: jens.schwamborn@uni.lu

#Co-first author

Status: The manuscript is published in Stem Cell Reports, 8 (2017) 1144-1154

Derivation of human midbrain-specific organoids from neuroepithelial stem cells

Anna S. Monzel[1#], Lisa M. Smits[1#], Kathrin Hemmer[1#], Siham Hachi[2], Edinson Lucumi Moreno[2], Thea van Wuellen[1], Javier Jarazo[1], Jonas Walter[1], Inga Brüggemann[1], Ibrahim Boussaad[3], Emanuel Berger[1], Ronan M.T. Fleming[2], Silvia Bolognin[1], Jens C. Schwamborn[1*]

[1]Luxembourg Centre for Systems Biomedicine (LCSB), Developmental and Cellular Biology, University of Luxembourg, L-4362 Esch-sur-Alzette Luxembourg

[2]Luxembourg Centre for Systems Biomedicine (LCSB), Systems Biochemistry, University of Luxembourg, L-4362 Esch-sur-Alzette Luxembourg

[3]Luxembourg Centre for Systems Biomedicine (LCSB), Clinical & Experimental Neuroscience, University of Luxembourg, L-4362 Esch-sur-Alzette Luxembourg

*Correspondence: Jens C. Schwamborn, Luxembourg Centre for Systems Biomedicine (LCSB), University of Luxembourg, 7, avenue des Hauts-Fourneaux, L-4362 Esch-sur-Alzette Luxembourg; E-mail: jens.schwamborn@uni.lu

#Co-first author

Running Title: Generation of midbrain organoids.

Summary

Research on human brain development and neurological diseases is limited by the lack of advanced experimental *in vitro* models that truly recapitulate the complexity of the human brain. Here, we describe a robust human brain organoid system that is highly specific to the midbrain derived from regionally patterned neuroepithelial stem cells. These human midbrain organoids contain spatially organized groups of dopaminergic neurons, which make them an attractive model to study Parkinson's disease. Midbrain organoids are characterized in detail for neuronal, astroglia and oligodendrocyte differentiation. Furthermore, we show the presence of synaptic connections and electrophysiological activity. The complexity of this model is further highlighted by the myelination of neurites. The present midbrain organoid system has the potential to be used for advanced *in vitro* disease modeling and therapy development.

Introduction

With the development of methods to generate induced pluripotent stem cells (iPSCs) from somatic cells (Takahashi and Yamanaka, 2006; Yu et al., 2007), human cells with the potential to generate all body cell types *in vitro* became available. This advance led to tremendous progress in the development of protocols for the differentiation of iPSCs into various human cell types. Additionally, disease-specific human iPSCs and their derived cell types are now widely used for *in vitro* disease modeling. However, particularly with regard to neuronal diseases, it is of importance to consider that the human brain is an extremely complex, three-dimensional (3D) structure. Consequently, the investigation of its development and modeling of disease processes in traditional, two-dimensional cultures has strong limitations. It has been demonstrated that the presence of a 3D matrix promotes many biologically relevant functions, such as differentiation capability (Baharvand et al., 2006; Greiner et al., 2013; Tanaka et al., 2004; Tian et al., 2008), cellular signaling, and lineage specification (Engler et al., 2006; Greiner et al., 2013; McBeath et al., 2004). Additionally, 3D culture systems are more physiological concerning cell-cell and cell-matrix interactions (Lee et al., 2007). These observations have, in recent years, prompted the use of human iPSCs for the generation of 3D *in vitro* models of complete organs, the so-called organoids.

These organoid technologies have been pioneered for the small intestine (Sato et al., 2009) and later extended also to other organs or parts of organs (Nakano et al., 2012). Recently, protocols for the generation of human brain-like organoids have been developed, including protocols for cerebral (Lancaster et al., 2013), cerebellar (Muguruma et al., 2015), midbrain-like (Jo et al., 2016) and forebrain organoids (Qian et al., 2016). These organoids provide a proof-of-concept that human iPSCs can indeed differentiate into various cell types and even self-organize with a specific spatial orientation, which recapitulates key features of the human brain. These brain organoids have been used successfully to model a genetic form of microcephaly (Lancaster et al., 2013) as well as Zika virus-induced microcephaly (Qian et al., 2016). Importantly, thus far, all brain organoids have been generated directly from iPSCs; however, evidence suggesting that these organoids could also be derived from more fate-restricted neural stem cells is lacking. The utilization of neural stem cells as the starting population has the advantage that already patterned cells might differentiate into the desired structures more efficiently (cheaper, faster cell doublings, ease of handling, etc.). Furthermore, while the generation of certain brain structures, such as the cerebral cortex or cerebellum, is meanwhile well described, a higher degree of pre-patterning seems to be required for the generation of other highly

specialized structures. This is particularly true for brain regions severely affected in neurodegenerative disorders, such as Alzheimer's disease (AD, hippocampus) or Parkinson's disease (PD, substantia nigra). To address these challenges, we used our previously described human neuroepithelial stem cell (NESC) culture system (Reinhardt et al., 2013) and differentiated these NESCs under dynamic conditions into human midbrain-specific organoids.

Results

Generation of human midbrain-specific organoids

Previously described NESCs (Reinhardt et al., 2013) were used as the starting population for the generation of human midbrain organoids (hMOs). Compared to iPSCs as a starting population, NESCs are already patterned towards midbrain/hindbrain identity. Therefore, an efficient differentiation into hMOs was expected. Typically, NESCs express the neural progenitor markers SOX1, SOX2, PAX6, and NESTIN prior to organoid generation (Figure S1A). Cells were seeded on round-bottom ultralow adhesion 96-well plates enabling the cells to form 3D colonies. They were cultured in the presence of the GSK3b inhibitor CHIR99021 to stimulate the canonical WNT signaling pathway, and the SHH pathway was activated using purmorphamine (PMA). The 3D NESC colonies were embedded into droplets of Matrigel for structural support, and two days after, differentiation into hMOs was initiated. We kept the organoids on an orbital shaker rotating at 80 rpm (Figure 1A). All experiments were conducted with four different and independent NESC lines, individually derived from four different and independent human iPSC lines (Table S1).

During the first 12 days of culture, the hMOs rapidly increased in size, and reached a mean core size of 1.26 mm (± 0.06 mm, n=4) in diameter after 20 days (Figure 1B). Consistent with the finding that organoids increased in size after starting the differentiation, we observed expression of the cell proliferation marker KI67 at day 27 (referred to as early stage hMOs), which significantly decreased upon maturation until day 61 (late stage hMOs) from 2.32 % (± 0.7 %, n=4) to 0.13 % (± 0.08 %, n=4) (Figures 1C, 1E, 1G). Furthermore, young hMOs expressed the neural progenitor marker SOX2, which also significantly decreased during maturation from 35 % (± 3%, n=4, day 27) to 18.4 % (± 1.7 %, n=4, day 61). Interestingly, the localization of SOX2-positive cells became more regionally restricted by day 61, resembling the formation of a stem cell niche (Figures 1D, 1F, 1G). Although consistent with previous findings (Lancaster and Knoblich, 2014; Lancaster et al., 2013), we found substantial cell death in the core of the hMOs, which resulted from the lack of nutrient support in the center of the organoid. In general, we did not observe high levels of apoptotic cell death, revealed by staining of the marker cleaved caspase-3 (CC3). The basic level of apoptosis that was detectable did not change during the course of differentiation (Figure S1B). Importantly, we were able to reproduce the generation of hMOs from NESCs, which were previously derived from four independent iPSC lines.

Neuronal differentiation and self-organization of NESC-derived hMOs

After showing a decrease of proliferation and stem cell identity, we assessed neuronal differentiation. Because we are particularly interested in the future utilization of hMOs for *in vitro* modeling of PD, we also

investigated the differentiation of midbrain dopaminergic neurons (mDNs). We were able to see robust differentiation into TUJ1-positive neurons and tyrosine hydroxylase- (TH) positive mDNs. These stainings revealed the formation of a complex neuronal network (Figures 2A, 2B, S2A, S2B).

We further examined whether the organoids undergo differentiation into mDNs with midbrain identity. We observed a large population of TH-, LMX1A-, and FOXA2-positive neurons in late stage hMOs (Figure 2C). Flow cytometry analysis of late stage hMOs revealed that 64 % (± 2,4 %, n=4) of the cells were triple-positive for TH, LMX1A and FOXA2 (Figure 2D). To further confirm the regional identity of the hMOs, we stained for the orphan nuclear receptor NURR1, which is widely expressed in mDNs. NURR1 expression was observed in early and late stage hMOs. We identified cells that co-expressed NURR1 with the midbrain-specific transcription factor OTX2 (Figure 2E) and with the mDN marker TH (Figure S2C). We further found cells that co-expressed NURR1 with the ventral marker NKX6-1 (Figures 2F, S2D). We next examined the expression of PITX3, an important transcription factor for the differentiation and maintenance of mDN during development. We found cells co-expressing PITX3 with TH in the late stage hMOs (Figure S2E), as well as a small population of cells co-expressing PITX3 with NKX6-1 (Figure S2F). Taken together these results indicate a differentiation towards ventral midbrain identity in the here described hMOs.

To further address the identity of mDNs in these organoids, we stained for the dopamine transporter (DAT), which is a defining marker for mDNs. In late stage hMOs we identified cells co-expressing TH and DAT (Figure 1G), as well as cells positive for FOXA2/DAT (Figure S2G) and for TH/dopamine decarboxylase (DDC) (Figure S2H). qRT-PCR further confirmed the upregulation of the three mDN differentiation marker *th*, *dat* and *ddc* in late stage hMOs (Figure 2H). Previously, expression of PAX6 in the midbrain but not in mDNs has been shown (Schwarz et al., 1999; Duan et al., 2013). To further confirm the identity of the mDNs, we stained for PAX6 and TH. We could not identify TH-positive mDNs co-expressing PAX6, further supporting that the hMOs contain authentic mDNs (Figure S2I). Intriguingly, we observed robust co-expression of GIRK2 with TH in late stage hMOs, revealing the presence of the A9 subtype mDNs (Figure 2I) but we also observed cells double-positive for CALBINDIN (CALB) and TH in late stage hMOs, indicating the presence of A10 subtype mDNs (Figure 2J). These data confirm that our hMOs contain A9 and A10 subtype mDNs.

In previous studies, it has been repeatedly shown that stem cells exhibit an enormous potential to self-organize into complex heterogeneous brain organoids (Eiraku and Sasai, 2012; Eiraku et al., 2008; Lancaster et al., 2013; Muguruma et al., 2015). To examine the degree of spatial organization in hMOs, we evaluated the distribution pattern of the mDN markers TUJ1/TH and depicted the results using surface plots. Strikingly,

we found that mDNs formed clearly specified clusters within hMOs (Figures 2K, 2L). To further demonstrate the identity of TH-positive neurons as dopaminergic, we analyzed their ability to produce the neurotransmitter dopamine (DA). Immunostainings of mature hMOs demonstrated the presence of DA, TH and MAP2 triple-positive cells (Figure 2M). Intriguingly, we occasionally even observed the formation of Fontana Masson staining-positive neuromelanin granules in the hMO cultures (Figure S2J).

Altogether these results indicate that mDNs of NESC-derived organoids self-organize into a complex, spatially patterned neuronal tissue.

Glia differentiation in hMOs

During the development of the fetal human brain, neural tube-derived cells not only differentiate into neurons but also into glia cells, including astrocytes and oligodendrocytes. Therefore, we investigated the presence of these glia cells in the hMOs. In good agreement with brain development, where glia differentiation temporally follows neuronal differentiation, we were unable to detect significant amounts of glia cells in young hMOs (day 27). However, in more mature organoids (day 61), we observed a significant increase of S100β-positive astrocytes (up to 4 %) (Figure 3A). We confirmed astrocyte identity by co-staining of S100β with the astrocyte markers AQUAPORIN (AQP4) and VIMENTIN (VIM) (Figure 3B). Moreover, we detected a fraction of cells that differentiated into O4-positive oligodendrocytes (Figure S3A). In the central nervous system, mature oligodendrocytes form myelin sheaths that enwrap axons to accelerate the transmission of action potentials along axons. To analyze if the oligodendrocytes within the hMOs are able to execute their actual function, i.e., formation of myelin sheets, we performed IF staining against CNPase, a myelin-associated enzyme, together with the neuronal marker TUJ1. A 3D surface reconstruction of these stainings revealed numerous TUJ1-positive neurites that were ensheathed by myelin sheets of CNPase-positive oligodendrocytes (Figures 3C, S3B, S3C). Interestingly, these neurites often showed gaps of ensheathment, resembling the formation of nodes of Ranvier (Figure 3C) that allow for saltatory fast neuronal transmission. Moreover, CNPase-positive oligodendrocytes that ensheath TUJ1-positive neurites were also positive for the mature oligodendrocyte marker myelin basic protein (MBP) (Figure 3D). Quantification revealed that 29.6 % (± 2.4 %, n=4) of TUJ1-positive neurites were ensheathed by oligodendrocytes as confirmed by image analysis using MBP and TUJ1 masks.

Functionality of hMOs

One important requirement for neuronal transmission is the development of a mature neuronal network via the formation of synaptic connections. Therefore, synaptic connectivity was investigated using IF staining

against the presynaptic marker SYNAPTOPHYSIN and the postsynaptic marker PSD95 at day 61. To assess the presynaptic and postsynaptic density in hMOs, the number of presynaptic and postsynaptic counts per μm^2 was quantified to an amount of 0.031 (± 0.003; n=4) and 0.016 (± 0.004; n=4), respectively. A subsequent 3D surface reconstruction demonstrated not only the formation of numerous pre- and postsynaptic puncta but also multiple synaptic connections (Figures 3E, S3D). Synaptic connections have been developed between different neurites, indicated by the direct contact of SYNAPTOPHYSIN-positive presynapses with PSD95-positive postsynapses (Figure 3F). Accordingly, hMOs fulfill the prerequisite to forward signals via synaptic connections and thus for being electrophysiologically functional.

To further address functionality and neuronal network activity, we performed Fluo-4AM calcium imaging on whole organoids. We measured the spontaneous neuronal activity of 6 hMOs based on calcium transients evoked by action potentials (Figures 4A, 4B, S4 and Movie S1). Notably, some of the fluorescent traces showed regular firing patterns, which were indicative of tonic electrophysiological activity and resembled the pacemaker activity of mDNs (Hartfield et al., 2014; Moreno et al., 2015). We quantified that 64% (± 18%, n=3) of the cells were actively firing. In addition to calcium imaging, a multielectrode array (MEA) system was used to examine the electrophysiological activity. This methodology allows non-invasive recordings of extracellular field potentials generated by action potentials. At day 82-84, the hMOs were placed on a grid of 16 electrodes in a 48-well tissue culture plate (Figure 4C). Spontaneous activity was detected over several days by individual electrodes in the form of mono- and biphasic spikes (96.13 ± 66.8 spikes/active electrode/measurement (n≥4), Figures 4D, 4E). Furthermore, spikes occurred close in time on multiple electrodes, which represents neuronal network synchronicity (Figure 4F). To further address functionality, we treated the hMOs with the dopamine D2/D3 receptor agonist quinpirole (5 µM). Indeed, after the treatment neuronal activity was reduced (Figure 4G) confirming the presence of functional dopamine receptors in the described hMOs. Together these findings indicate that hMOs develop functional synaptic connections and show spontaneous neuronal activity.

Discussion

One of the main limitations in neuroscience and the modeling of neurological diseases is the lack of advanced experimental *in vitro* models that truly recapitulate the complexity of the human brain. Here, we have presented a human brain organoid system that is highly specific to the midbrain. These hMOs contain spatially patterned groups of dopaminergic neurons which make them an attractive model for the study of PD. hMOs are characterized in detail with regard to neuronal differentiation and activity as well as for astroglia and oligodendrocyte differentiation.

The presence of astrocytes is crucial for the formation of synapses and regular neuronal activity (Chung et al., 2015). Astrocytes are specified later in development than neurons (Chaboub and Deneen, 2013; Molofsky et al., 2012). Accordingly, hMOs show a robust astrocyte immunoreactivity only after 61 days of differentiation. Furthermore, synaptic connections, consisting of a direct contact between pre- and post-synapses, are detectable in the hMOs. These synaptic contacts are the prerequisite for electrophysiological and neuronal network functionality, which we indeed detected in the hMOs by Ca2+ imaging and multi-electrode array measurements. Additionally, fast information transmission between neurons depends on axonal myelination, which is achieved by oligodendrocytes. In most stem cell based differentiation protocols, the differentiation into oligodendrocytes is extremely inefficient (Bunk et al., 2016; Jablonska et al., 2010). However, in the present approach, we achieved a robust differentiation into oligodendrocytes and a high degree of neurite myelination. Neurites in these hMOs are ensheathed by oligodendrocytes and even structures, such as the nodes of Ranvier that are of critical importance for saltatory transmission of signals in axons (Faivre-Sarrailh and Devaux, 2013), become apparent.

Compared to other pioneering human brain organoid systems, we are able to generate organoids of a remarkable size (up to 2mm in diameter) with a high reproducibility. Importantly it was possible to reproducibly generate hMOs based on iPSC lines that come from different origins such as cord blood and fibroblasts. Additionally, these fibroblasts have been sampled from individuals at ages from 53 years to 81 years (Table S1). Importantly, in contrast to all other human brain organoid systems, our starting population of cells are not iPSCs but NESCs (Reinhardt et al., 2013), which allows us to achieve an efficient directed differentiation. Our approach is fully focused on the midbrain, as shown by the abundant presence of neurons with mDN identity. These neurons are asymmetrically distributed in a discrete cluster. This asymmetry mirrors a unique feature of the human brain where the soma of mDNs reside in the substantia nigra. Furthermore, the presence of neuromelanin, which is a unique feature of the primate brain, is an interesting finding.

The presented hMOs have a great potential to be used for *in vitro* modeling of diseases that strongly affect the human midbrain, particularly PD (Michel et al., 2016). Patient-specific hMOs might reveal specific phenotypes that are not abundant in 2D cultures and therefore may be used for mechanistic studies and drug testing. Importantly, such a pipeline would be fully suitable for approaches in personalized medicine (Bu et al., 2016; Hillje and Schwamborn, 2016).

Neurodegenerative disorders, such as PD, are typically considered to be age-associated diseases (Sepe et al., 2016; Xu et al., 2016). However, there is accumulating evidence that PD has a strong neurodevelopmental component that probably defines the susceptibility to develop the disease (Garcia-Reitboeck et al., 2013; Le Grand et al., 2014). This finding supports the importance of human brain development models to investigate the disease underlying mechanisms.

Major limitations of the here presented hMOs, as well as for other published brain organoid systems, is the absence of immune cells (microglia) and vasculature. The absence of vasculature might limit the growth of organoids beyond a certain size and the appearance of dead cells in the center of the organoids. While the absence of microglia is a major disadvantage for disease modeling. Another option to reduce the problem of the dead cells in the center of organoids might be to produce smaller organoids. However, it seems likely that there is a minimal size of an organoid required to achieve key characteristics like spatial asymmetry. Despite these limitations, the here presented hMO system along with other models may be a first step towards a more human patient specific, probably even personalized, era of advanced disease modeling and therapy development.

Experimental Procedures

For hMO generation 9000 human neuroepithelial stem cells were plated in each well of an ultra-low attachment 96-well round bottom plate (Corning) and cultured in N2B27 media (DMEM-F12 (Invitrogen)/Neurobasal (Invitrogen) 50:50 with 1:200 N2 supplement (Invitrogen), 1:100 B27 supplement lacking Vitamin A (Invitrogen), 1 % L-glutamine and 1 % penicillin/streptomycin (Invitrogen)) containing 3 μM CHIR-99021 (Axon Medchem), 0.75 μM purmorphamine (Enzo Life Science) and 150 μM ascorbic acid (Sigma) (referred to as N2B27 maintenance media) . After 6 days, the colonies were transferred to ultra-low attachment 24-well plates (Corning) and cultured in N2B27 maintenance media. On day 8, the 3D colonies were transferred to droplets of hESC-qualified Matrigel (BD Bioscience) as previously described ((Lancaster and Knoblich, 2014). Droplets were cultured in N2B27 maintenance media for two more days. On day 10, differentiation was initiated with N2B27 media supplemented with 10 ng/ml hBDNF, 10 ng/ml hGDNF, 500 μM dbcAMP (Peprotech), 200 μM ascorbic acid (Sigma), and 1 ng/ml TGF-β3 (Peprotech). Additionally, 1 μM purmorphamine (Enzo Life Science) was added to this medium for an additional 6 days. On day 14 of the organoid culture, the plates were placed on an orbital shaker (IKA), rotating at 80 rpm, in an incubator and the organoids were kept in culture with media changes every second or third day. A detailed description of the experimental procedures can be found in the supplemental information.

Author contributions

A.S.M., L.M.S., K.H., R.M.T.F., S.B., and J.C.S designed the study; A.S.M., L.M.S., K.H., S.H., E.L.M., T.v.W., J.J., and J.W. conducted the research; A.S.M., L.M.S., K.H., S.H., E.L.M., I.B., I.B., E.B., S.B., and J.C.S. analyzed the data; and A.S.M., L.M.S., K.H., S.H., E.L.M., E.B., R.M.T.F., S.B., and J.C.S. wrote the paper. A.S.M., L.M.S., and K.H. contributed equally.

Acknowledgements

This project was supported by the LCSB pluripotent stem cell core facility. The JCS lab is supported by the Fonds National de la Recherche (FNR) (CORE, C13/BM/5791363) and by a University Luxembourg Internal Research Project grant (MidNSCs). ASM, LMS, SH and ELM are supported by fellowships from the FNR (AFR, Aides à la Formation-Recherche). This is an EU Joint Programme - Neurodegenerative Disease Research (JPND) project (INTER/JPND/14/02; INTER/JPND/15/11092422). Further support comes from the SysMedPD project which has received funding from the European Union's Horizon 2020 research and innovation programme under grant agreement No 668738. Finally, we also thank the private donors who support our work at the Luxembourg Centre for Systems Biomedicine.

References

Baharvand, H., Hashemi, S.M., Kazemi Ashtiani, S., and Farrokhi, A. (2006). Differentiation of human embryonic stem cells into hepatocytes in 2D and 3D culture systems in vitro. Int J Dev Biol *50*, 645-652.
Bu, L.L., Yang, K., Xiong, W.X., Liu, F.T., Anderson, B., Wang, Y., and Wang, J. (2016). Toward precision medicine in Parkinson's disease. Annals of translational medicine *4*, 26.
Bunk, E.C., Ertaylan, G., Ortega, F., Pavlou, M.A., Gonzalez Cano, L., Stergiopoulos, A., Safaiyan, S., Vols, S., van Cann, M., Politis, P.K., *et al.* (2016). Prox1 is required for oligodendrocyte cell identity in adult neural stem cells of the subventricular zone. Stem cells (Dayton, Ohio).
Chaboub, L.S., and Deneen, B. (2013). Astrocyte form and function in the developing central nervous system. Seminars in pediatric neurology *20*, 230-235.
Chung, W.S., Welsh, C.A., Barres, B.A., and Stevens, B. (2015). Do glia drive synaptic and cognitive impairment in disease? Nature neuroscience *18*, 1539-1545.
Eiraku, M., and Sasai, Y. (2012). Self-formation of layered neural structures in three-dimensional culture of ES cells. Curr Opin Neurobiol *22*, 768-777.
Eiraku, M., Watanabe, K., Matsuo-Takasaki, M., Kawada, M., Yonemura, S., Matsumura, M., Wataya, T., Nishiyama, A., Muguruma, K., and Sasai, Y. (2008). Self-organized formation of polarized cortical tissues from ESCs and its active manipulation by extrinsic signals. Cell stem cell *3*, 519-532.
Engler, A.J., Sen, S., Sweeney, H.L., and Discher, D.E. (2006). Matrix elasticity directs stem cell lineage specification. Cell *126*, 677-689.
Faivre-Sarrailh, C., and Devaux, J.J. (2013). Neuro-glial interactions at the nodes of Ranvier: implication in health and diseases. Frontiers in cellular neuroscience *7*, 196.
Garcia-Reitboeck, P., Anichtchik, O., Dalley, J.W., Ninkina, N., Tofaris, G.K., Buchman, V.L., and Spillantini, M.G. (2013). Endogenous alpha-synuclein influences the number of dopaminergic neurons in mouse substantia nigra. Experimental neurology *248*, 541-545.
Greiner, J., Kaltschmidt, B., Kaltschmidt, C., and Widera, D. (2013). Going 3D – Cell Culture Approaches for Stem Cell Research and Therapy. Current Tissue Engineering *2(1):8–19*.
Hartfield, E.M., Yamasaki-Mann, M., Ribeiro Fernandes, H.J., Vowles, J., James, W.S., Cowley, S.A., and Wade-Martins, R. (2014). Physiological characterisation of human iPS-derived dopaminergic neurons. PloS one *9*, e87388.
Hillje, A.L., and Schwamborn, J.C. (2016). Utilization of stem cells to model Parkinson's disease – current state and future challenges. Future Neurology *11*, 171-186.
Jablonska, B., Aguirre, A., Raymond, M., Szabo, G., Kitabatake, Y., Sailor, K.A., Ming, G.L., Song, H., and Gallo, V. (2010). Chordin-induced lineage plasticity of adult SVZ neuroblasts after demyelination. Nature neuroscience *13*, 541-550.
Lancaster, M.A., and Knoblich, J.A. (2014). Generation of cerebral organoids from human pluripotent stem cells. Nature protocols *9*, 2329-2340.
Lancaster, M.A., Renner, M., Martin, C.A., Wenzel, D., Bicknell, L.S., Hurles, M.E., Homfray, T., Penninger, J.M., Jackson, A.P., and Knoblich, J.A. (2013). Cerebral organoids model human brain development and microcephaly. Nature *501*, 373-379.
Le Grand, J.N., Gonzalez-Cano, L., Pavlou, M.A., and Schwamborn, J.C. (2014). Neural stem cells in Parkinson's disease: a role for neurogenesis defects in onset and progression. Cellular and molecular life sciences : CMLS.
Lee, G.Y., Kenny, P.A., Lee, E.H., and Bissell, M.J. (2007). Three-dimensional culture models of normal and malignant breast epithelial cells. Nature methods *4*, 359-365.
McBeath, R., Pirone, D.M., Nelson, C.M., Bhadriraju, K., and Chen, C.S. (2004). Cell shape, cytoskeletal tension, and RhoA regulate stem cell lineage commitment. Developmental cell *6*, 483-495.
Michel, P.P., Hirsch, E.C., and Hunot, S. (2016). Understanding Dopaminergic Cell Death Pathways in Parkinson Disease. Neuron *90*, 675-691.
Molofsky, A.V., Krencik, R., Ullian, E.M., Tsai, H.H., Deneen, B., Richardson, W.D., Barres, B.A., and Rowitch, D.H. (2012). Astrocytes and disease: a neurodevelopmental perspective. Genes & development *26*, 891-907.
Moreno, E.L., Hachi, S., Hemmer, K., Trietsch, S.J., Baumuratov, A.S., Hankemeier, T., Vulto, P., Schwamborn, J.C., and Fleming, R.M. (2015). Differentiation of neuroepithelial stem cells into functional dopaminergic neurons in 3D microfluidic cell culture. Lab on a chip *15*, 2419-2428.
Muguruma, K., Nishiyama, A., Kawakami, H., Hashimoto, K., and Sasai, Y. (2015). Self-organization of polarized cerebellar tissue in 3D culture of human pluripotent stem cells. Cell reports *10*, 537-550.
Nakano, T., Ando, S., Takata, N., Kawada, M., Muguruma, K., Sekiguchi, K., Saito, K., Yonemura, S., Eiraku, M., and Sasai, Y. (2012). Self-formation of optic cups and storable stratified neural retina from human ESCs. Cell stem cell *10*, 771-785.

Qian, X., Nguyen, H.N., Song, M.M., Hadiono, C., Ogden, S.C., Hammack, C., Yao, B., Hamersky, G.R., Jacob, F., Zhong, C., *et al.* (2016). Brain-Region-Specific Organoids Using Mini-bioreactors for Modeling ZIKV Exposure. Cell *165*, 1238-1254.
Reinhardt, P., Glatza, M., Hemmer, K., Tsytsyura, Y., Thiel, C.S., Hoing, S., Moritz, S., Parga, J.A., Wagner, L., Bruder, J.M., *et al.* (2013). Derivation and expansion using only small molecules of human neural progenitors for neurodegenerative disease modeling. PloS one *8*, e59252.
Sato, T., Vries, R.G., Snippert, H.J., van de Wetering, M., Barker, N., Stange, D.E., van Es, J.H., Abo, A., Kujala, P., Peters, P.J., *et al.* (2009). Single Lgr5 stem cells build crypt-villus structures in vitro without a mesenchymal niche. Nature *459*, 262-265.
Sepe, S., Milanese, C., Gabriels, S., Derks, K.W., Payan-Gomez, C., van, I.W.F., Rijksen, Y.M., Nigg, A.L., Moreno, S., Cerri, S., *et al.* (2016). Inefficient DNA Repair Is an Aging-Related Modifier of Parkinson's Disease. Cell reports *15*, 1866-1875.
Takahashi, K., and Yamanaka, S. (2006). Induction of pluripotent stem cells from mouse embryonic and adult fibroblast cultures by defined factors. Cell *126*, 663-676.
Tanaka, H., Murphy, C.L., Murphy, C., Kimura, M., Kawai, S., and Polak, J.M. (2004). Chondrogenic differentiation of murine embryonic stem cells: effects of culture conditions and dexamethasone. J Cell Biochem *93*, 454-462.
Tian, X.F., Heng, B.C., Ge, Z., Lu, K., Rufaihah, A.J., Fan, V.T., Yeo, J.F., and Cao, T. (2008). Comparison of osteogenesis of human embryonic stem cells within 2D and 3D culture systems. Scandinavian journal of clinical and laboratory investigation *68*, 58-67.
Xu, Y., Yang, J., and Shang, H. (2016). Meta-analysis of risk factors for Parkinson's disease dementia. Translational neurodegeneration *5*, 11.
Yu, J., Vodyanik, M.A., Smuga-Otto, K., Antosiewicz-Bourget, J., Frane, J.L., Tian, S., Nie, J., Jonsdottir, G.A., Ruotti, V., Stewart, R., *et al.* (2007). Induced pluripotent stem cell lines derived from human somatic cells. Science (New York, NY) *318*, 1917-1920.

Figure Titles and Legends

Figure 1. Derivation of hMOs from human NESCs.

(A) Procedure of hMO culture system. Details are described in the supplemental experimental procedures section. hNESC, human neuroepithelial stem cell; AA, ascorbic acid, PMA, purmorphamine.

(B) Growth of hMOs from day 4 to day 20. The diameter size of six organoids (two independent cultures) per organoid line was measured on day 4, 8, 12, 16 and 20 of the organoid culture and the mean was calculated. Error bars represent mean + SEM.

(C) IF staining of the cell proliferation marker KI67 at day 27 and day 61 of the organoid culture.

(D) IF staining at day 27 and day 61 of the neural stem cell marker SOX2.

(E) Quantification of the percentage of KI67+ cells at day 27 and day 61 by cell counting. KI67+ cells were normalized to Hoechst+ cells. A total of 3549 Hoechst+ cells (day 27) and 3309 Hoechst+ cells (day 61) of eight independent organoid cultures derived from four independent lines was counted. Error bars represent mean + SEM (n=4, ***p<0.0001).

(F) Quantification of the percentage of SOX2+ cells at day 27 and day 61 by cell counting. SOX2+ cells were normalized to Hoechst+ cells. A total of 3549 Hoechst+ cells (day 27) and 3309 Hoechst+ cells (day 61) of eight independent organoid cultures derived from four independent lines was counted. Error bars represent mean + SEM (n=4, ***p<0.0001).

(G) Representative image of KI67+/SOX2+ proliferative neural progenitor cells at day 27. Scale bars, 200 μm (C, D), 20 μm (G). Dashed lines indicate the perimeter of the organoid.

Figure 2. Neuronal differentiation and self-organization in hMOs.

(A) Whole-mount IF staining of an organoid at day 27 for the mDN markers TUJ1 and TH.

(B) IF staining of the mDN markers TUJ1 and TH in a 50 μm section at day 30.

(C) IF staining of the mDA neuron markers FOXA2, LMX1A and TH at day 61.

(D) Representative flow cytometry analysis of cells dissociated from hMO1 at day 61 (six organoids) to quantify TH, LMX1A and FOXA2-positive cells.

(E) IF staining of NURR1 and midbrain marker OTX2 in late stage hMOs (D61).

(F) IF staining of NKX6-1 and NURR1 in early stage hMOs (day 30).

(G) IF staining of DAT co-stained with TH in late stage hMOs (day 61).

(H) qRT-PCR analysis for the mDN markers *th*, *dat* and *ddc*. Data obtained from four independent NESC lines and thereof derived hMOs. For each hMO culture, five organoids were pooled for RNA isolation. Error bars indicate mean + SEM (n=4, $*p_{(TH)}$=0.0286, $*p_{(DAT)}$=0.0286, $*p_{(DDC)}$=0.0571).

(I) IF staining of A9 mDN marker GIRK2 co-stained with TH in late stage hMOs (day 61)

(J) IF staining of A10 mDN marker Calbindin and TH in late stage hMOs (day 61). Arrowheads show cells that are positive for both markers.

(K-L) Asymmetry analysis of mDNs. Immunostaining of mDNs for TUJ1 and TH. (K) was analyzed based on fluorescence intensities using a 3D surface plot (L).

(M) IF staining for dopamine (DA), MAP2 and TH at day 50.

100 µm section (F), 150 µm section (K). Scale bars, 200 µm (A, K), 20 µm (B, C, E, F, G, I, J), 10 µm (M).

Figure 3. Differentiation into glia cells and formation of synaptic connections.

(A) IF staining for the astroglia marker S100β in early (day 27) and late stage (day 61) hMOs. Dashed lines indicate the perimeter of the organoid.

(B) IF staining for the astrocyte markers S100β, AQP4 and VIM.

(C) IF staining of an organoid at day 61 revealing differentiation into CNPase- and MBP-positive oligodendrocytes. 3D surface reconstructions of confocal z-stacks visualize the formation of myelin sheaths that enwrap TUJ1-positive neurites (arrowheads) as well as the formation of nodes of Ranvier that are suggested by the presence of gaps of CNPase-positive ensheathment.

(D) 3D surface reconstruction of a confocal z-stack of an IF staining of co-stained MBP and CNPase enwrapping a TUJ1-positive neurite.

(E) IF staining of the presynaptic marker SYNAPTOPHYSIN and the postsynaptic marker PSD95 at day 61. Arrowheads indicate a direct contact between a pre- and a postsynapse. Dashed box indicates the region of magnification. Images show the 3D view of a confocal z-stack.

(F) 3D surface reconstructions of confocal z-stacks demonstrate the formation of synaptic connections between different neurites of an organoid as indicated by several direct contacts (arrowheads) between the pre- and postsynaptic markers SYNAPTOPHYSIN and PSD95, respectively. Lower panels show high magnifications of a 3D view of a confocal z-stack and the corresponding 3D surface reconstruction of several synaptic connections. Scale bars, 200 µm (A), 20 µm (B, C upper panel, C lower panel left, E/F upper panel left/middle), 10 µm (C lower panel, D) 2 µm (C upper panel right, F upper panel right, F lower panel).

Figure 4. hMOs reveal electrophysiological activity

A)-B) Monitoring of the spontaneous electrophysiological activity in an organoid using Fluo-4AM-based calcium imaging.

A) Mean fluorescence frame of a calcium imaging dataset of a midbrain organoid with two segmented neurons expressing spontaneous activity. Scale bar, 20 µm.

B) Fluorescence traces corresponding to the segmented cell bodies in (A) showing firing patterns with pacemaking-like shape.

C)-F) Evaluation of the spontaneous activity in 16 hMOs of four organoid lines (n=4) after 82-84 days using a MEA system.

C) Representative scheme of positioned midbrain organoid on a 16-electrode array in a 48-well tissue culture plate.

D) Representative image of the activity map.

E) Examples of mono- and biphasic spikes detected by individual electrodes.

F) Representative image of a spike raster plot showing neuronal network activity in time and space. Spikes occurring on multiple electrodes, closely in time, represent network synchrony, indicated by pink lines.

G) Representative raw data trace (i) and spike raster plots (ii) for single electrodes and the effect of quinpirole on firing frequency of mDNs 30 min after treatment.

Supplemental Material

Graphical abstract

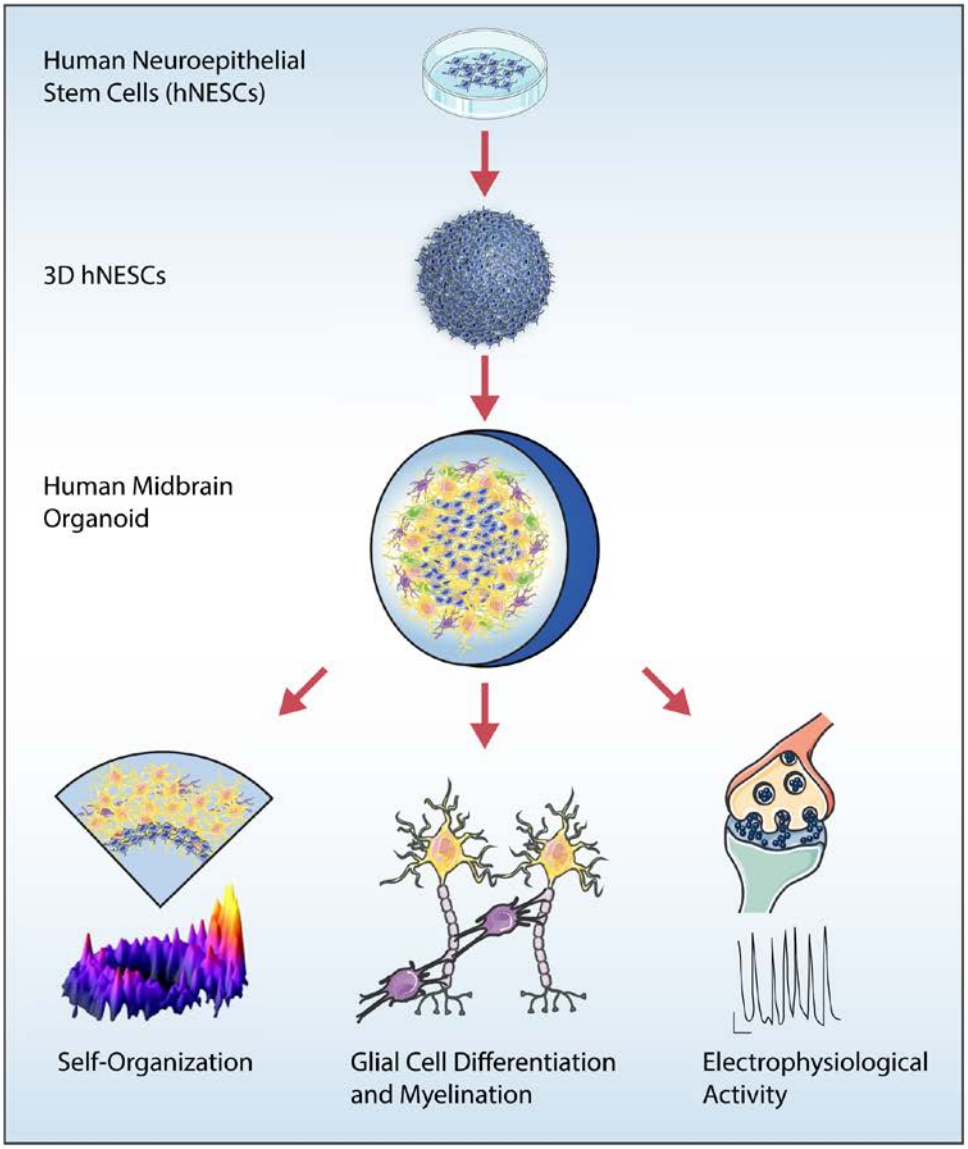

Figure 1

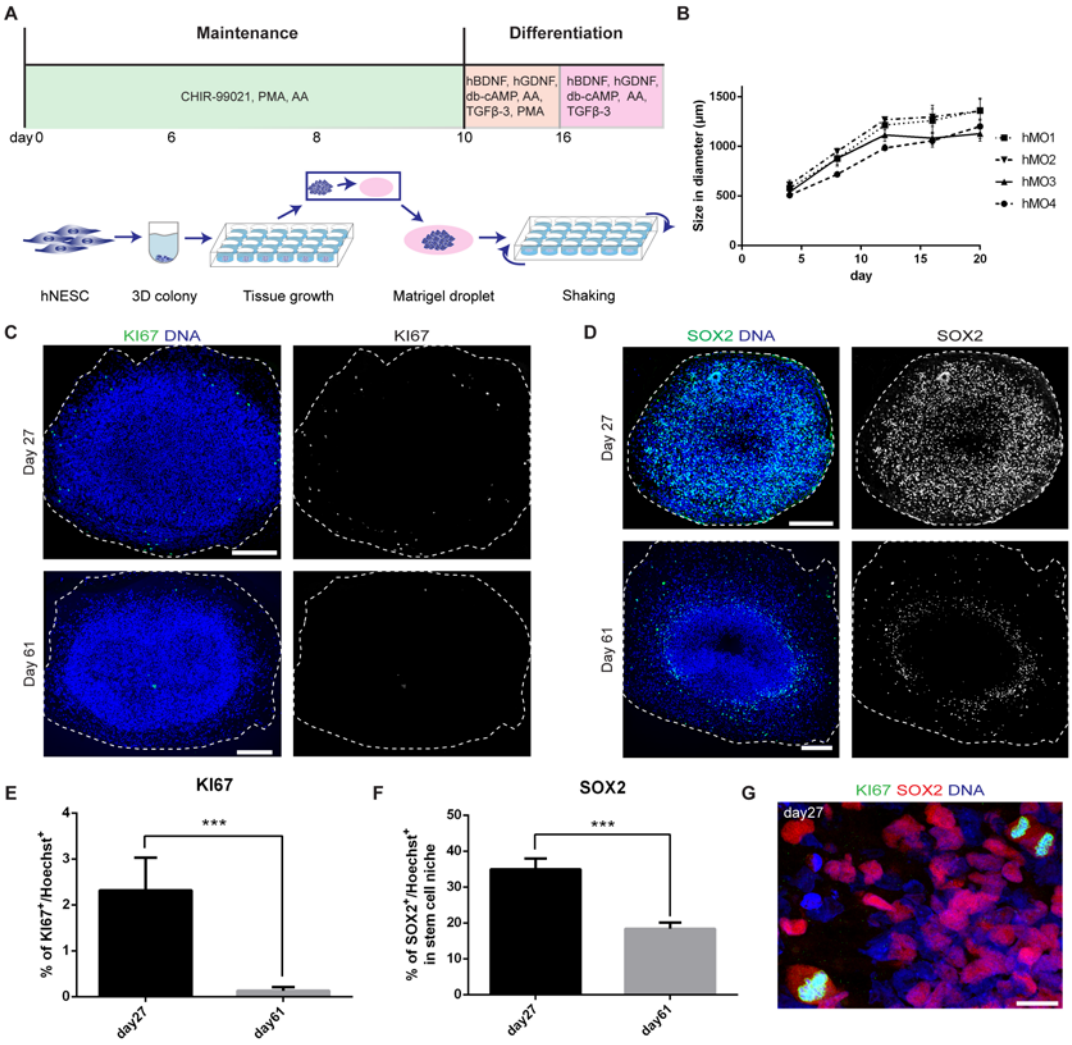
A
Maintenance
Differentiation
CHIR-99021, PMA, AA
hBDNF, hGDNF, db-cAMP, AA, TGFβ-3, PMA
hBDNF, hGDNF, db-cAMP, AA, TGFβ-3
day 0
6
8
10
16
hNESC
3D colony
Tissue growth
Matrigel droplet
Shaking
B
Size in diameter (µm)
day
hMO1
hMO2
hMO3
hMO4
C
KI67 DNA
KI67
Day 27
Day 61
D
SOX2 DNA
SOX2
Day 27
Day 61
E
KI67
% of KI67+/Hoechst+
***
day27
day61
F
SOX2
% of SOX2+/Hoechst+ in stem cell niche
***
day27
day61
G
KI67 SOX2 DNA
day27

Figure 2

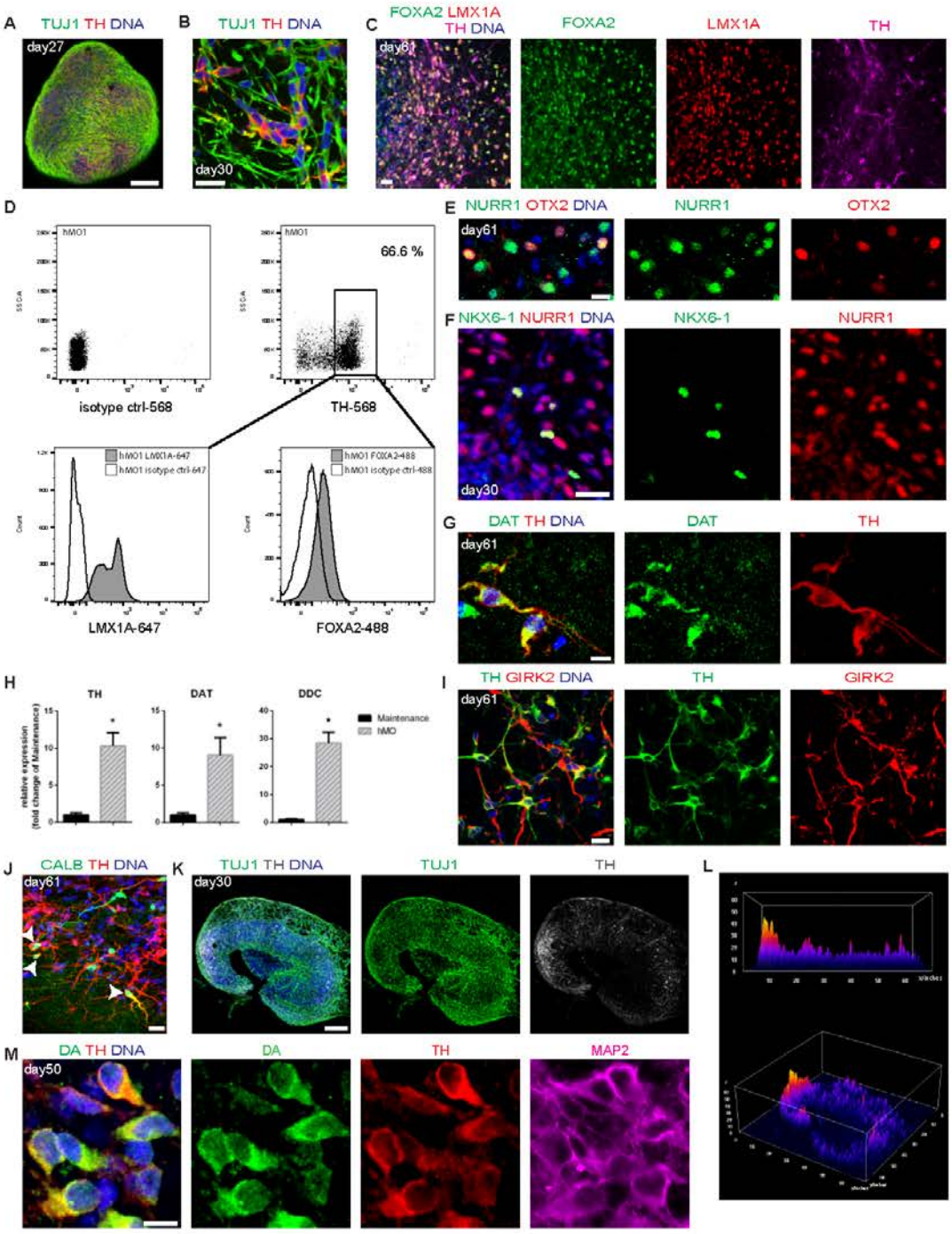
A
TUJ1 TH DNA
day27
B
TUJ1 TH DNA
day30
C
FOXA2 LMX1A
TH DNA
day61
FOXA2
LMX1A
TH
D
hMO1
66.6 %
isotype ctrl-568
TH-568
hMO1 LMX1A-647
hMO1 isotype ctrl-647
hMO1 FOXA2-488
hMO1 isotype ctrl-488
LMX1A-647
FOXA2-488
E
NURR1 OTX2 DNA
day61
NURR1
OTX2
F
NKX6-1 NURR1 DNA
day30
NKX6-1
NURR1
G
DAT TH DNA
day61
DAT
TH
H
TH
DAT
DDC
relative expression
(fold change of Maintenance)
Maintenance
hMO
I
TH GIRK2 DNA
day61
TH
GIRK2
J
CALB TH DNA
day61
K
TUJ1 TH DNA
day30
TUJ1
TH
L
M
DA TH DNA
day50
DA
TH
MAP2

Figure 3

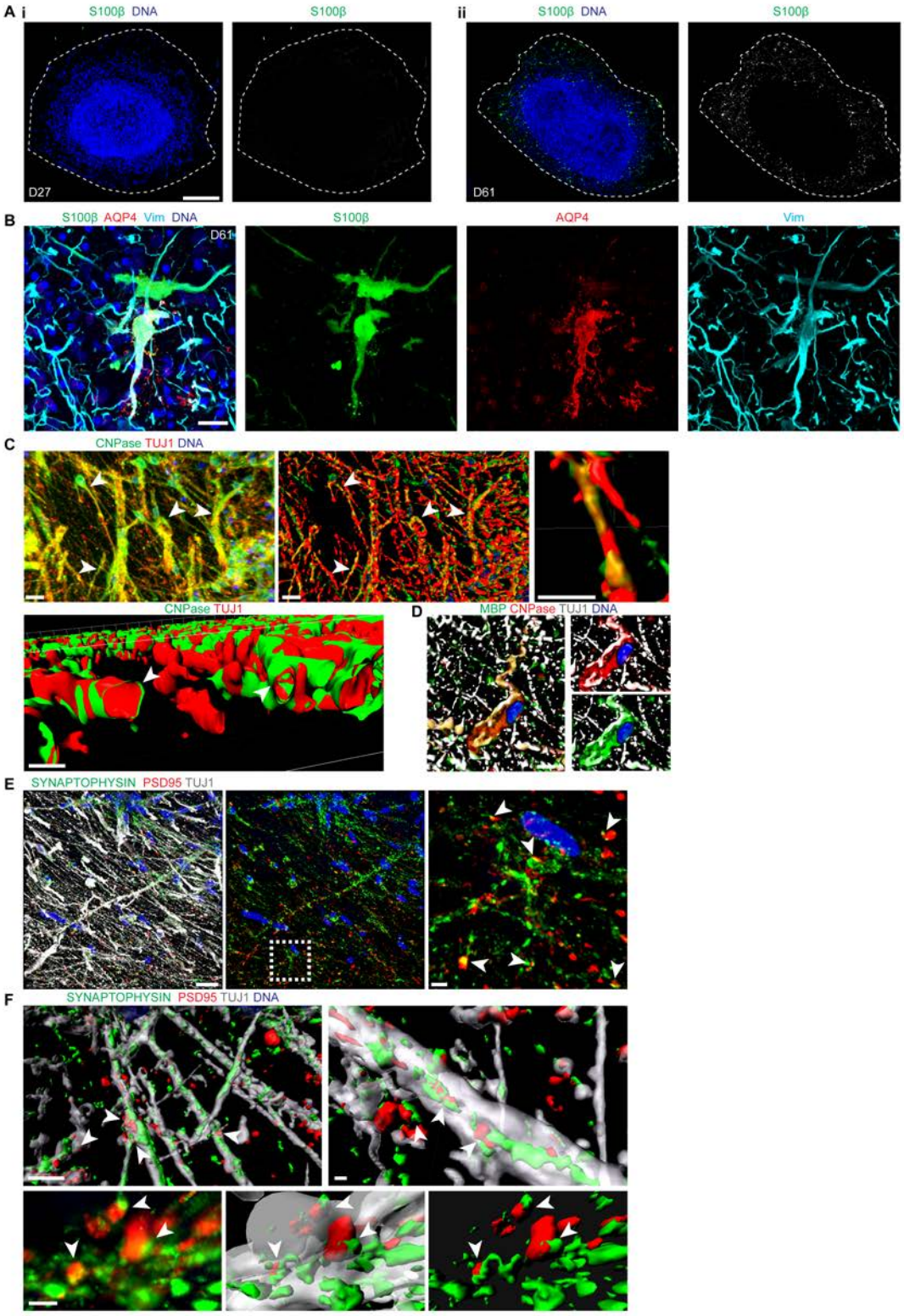
A i
S100β DNA
S100β
D27
ii
S100β DNA
S100β
D61
B
S100β AQP4 Vim DNA
D61
S100β
AQP4
Vim
C
CNPase TUJ1 DNA
CNPase TUJ1
D
MBP CNPase TUJ1 DNA
E
SYNAPTOPHYSIN PSD95 TUJ1
F
SYNAPTOPHYSIN PSD95 TUJ1 DNA

Figure 4

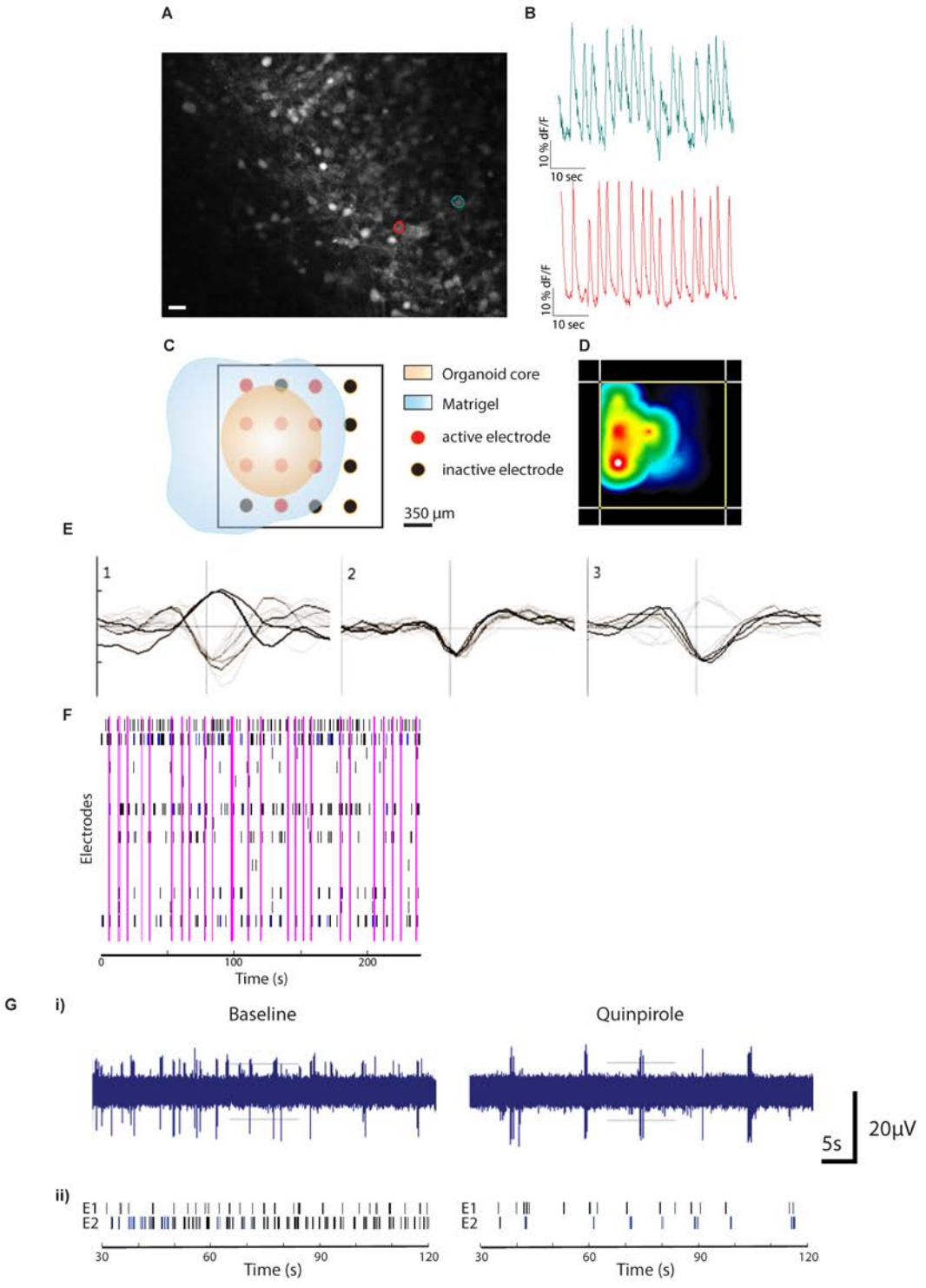
A
B
10 % dF/F
10 sec
10 % dF/F
10 sec
C
Organoid core
Matrigel
active electrode
inactive electrode
350 µm
D
E
1
2
3
F
Electrodes
0
100
200
Time (s)
G
i)
Baseline
Quinpirole
5s
20µV
ii)
E1
E2
30
60
90
120
Time (s)
E1
E2
30
60
90
120
Time (s)

Supplementary Fig. S1

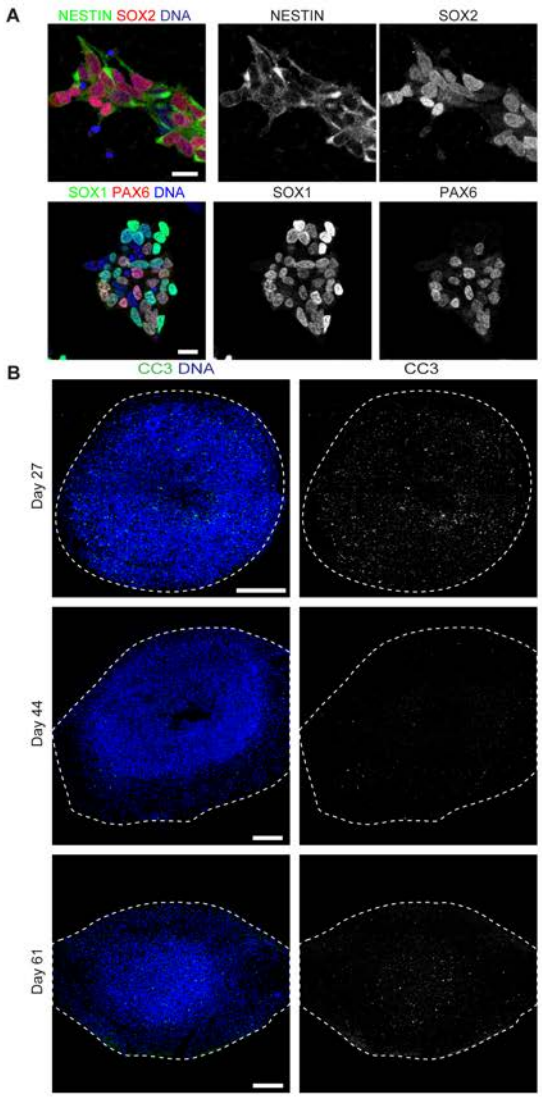

Supplementary Fig. S2

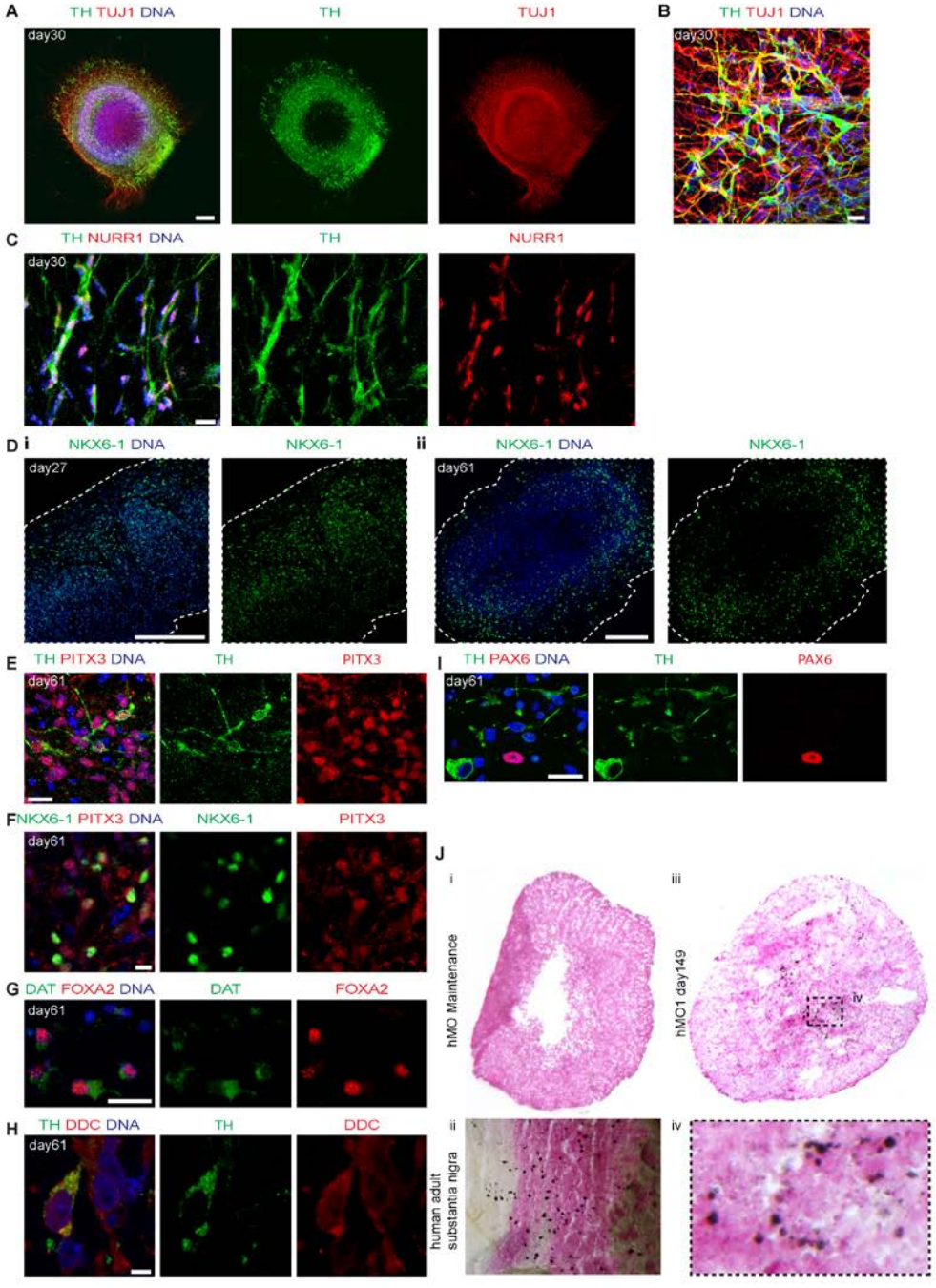

Supplementary Fig. S3

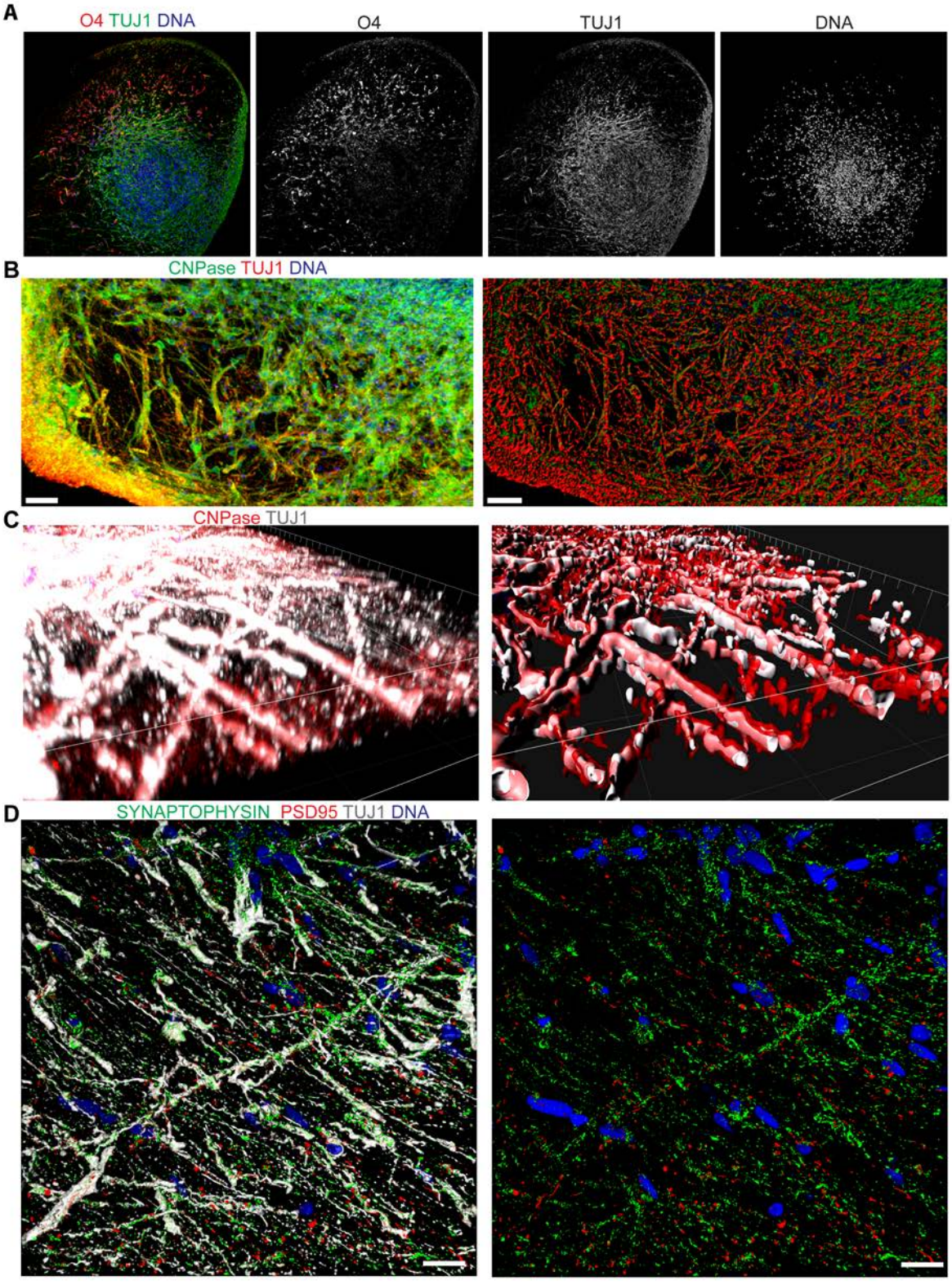

Supplementary Fig. S4

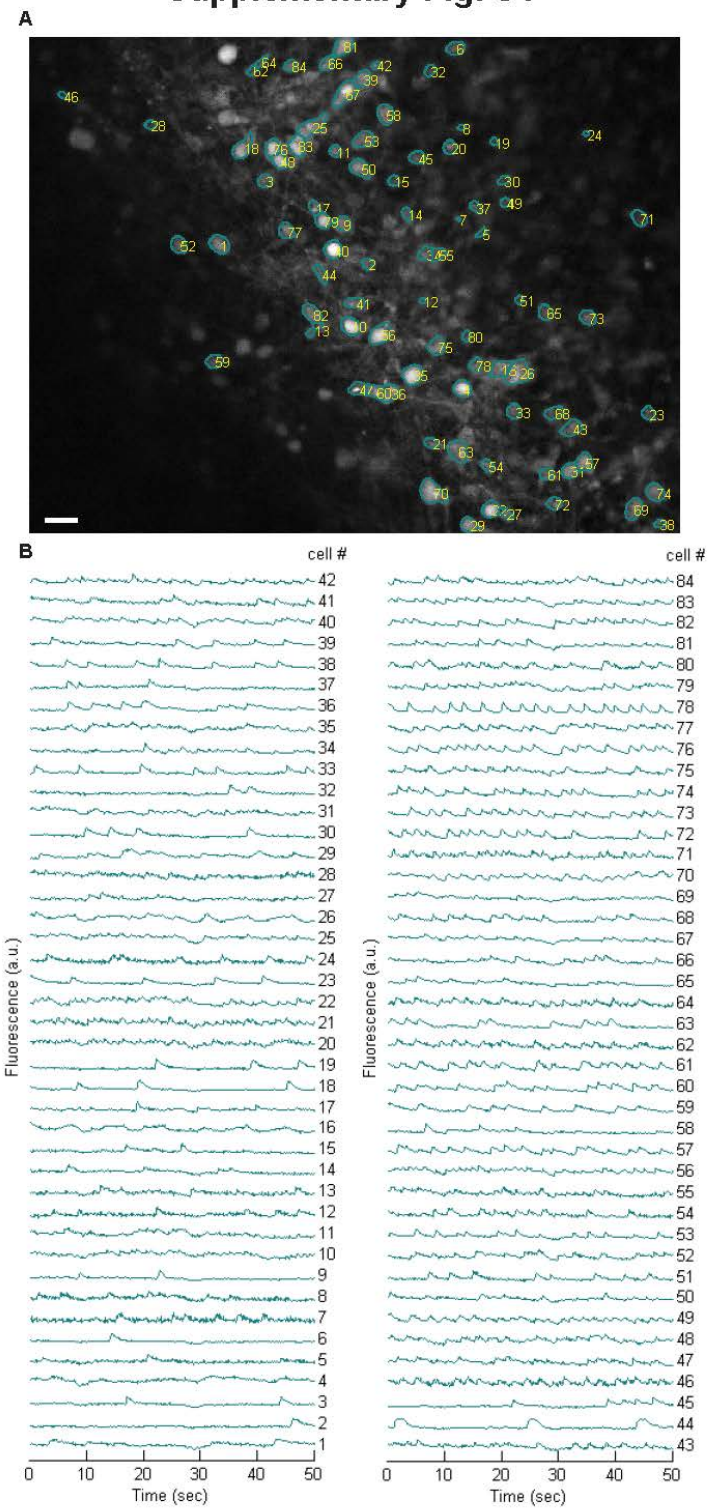

Table S1

Source of hiPSCs	Age at sampling	Gender	hNESC ID	Corresponding human midbrain organoid culture
Reinhardt et al. 2013	81	♀	3.0.0.10.0	hMO1
Reinhardt et al. 2013	53	♀	3.0.0.14.0	hMO2
Coriell (ND34769)	68	♀	3.0.0.24.1	hMO3
Gibco (A13777)	Cord Blood	♀	3.0.0.15.0	hMO4

Table S2

Antibody	Species	Source	Ref.-No.	Dilution
AQP4	rabbit	Santa Cruz	sc-20812	1:100
Calbindin	mouse	swant	300	1:500
CC3	rabbit	Cell Signaling Technology	9661	1:200
CNPase	mouse	Abcam	ab6319	1:200
DAT	rat	Abcam	ab5981	1:500
DDC	rabbit	Thermo Scientific	PA5-25450	1:25
Dopamine	rabbit	ImmuSmol	IS1005	1:500
FOXA2	mouse	Santa Cruz	sc-101060	1:250
GIRK2	goat	Abcam	ab65096	1:200
IgG control	rabbit	Santa Cruz	sc-3888	1:100
IgG2a κ isotype control	mouse	BioLegend	401502	1:300
IgY control	chicken	RnD	AB-101-C	1:50
KI67	mouse	BD Biosciences	550609	1:200
LMX1A	rabbit	Abcam	ab139726	1:200
MAP2	mouse	Millipore	MAB3418	1:200
MBP	rat	Abcam	ab7349	1:200
Nestin	mouse	BD Bioscience	611659	1:200
NKX6-1	mouse	DSHB	F55A10	1:50
NURR1	rabbit	Santa Cruz	sc-991	1:250
O4	mouse	Sigma-Aldrich	O7139	1:400
OTX2	goat	R&D	AF1979	1:200
PAX6	rabbit	Covance	PRB-278P	1:300
PAX6	mouse	DSHB	1-223	1:200
PITX3	rabbit	Millipore	AB5722	1:200
PSD-95	rabbit	Invitrogen	51-6900	1:300
S100B	mouse	Sigma-Aldrich	S2532	1:1000
SOX1	goat	R&D systems	AF3369	1:100
SOX2	goat	R&D systems	AF2018	1:200
SOX2	rabbit	Abcam	ab97959	1:100
SYP	mouse	Abcam	ab8049	1:50
TH	chicken	Abcam	ab76442	1:1000
TH	rabbit	Abcam	ab112	1:1000
TH	rabbit	Santa Cruz	sc-14007	1:1000
TUJ1	mouse	BioLegend	801201	1:600
TUJ1	rabbit	Covance	PRB-435P-0100	1:600
TUJ1	chicken	Millipore	AB9354	1:600
Vimentin	chicken	Abcam	ab24525	1:200

6.2 Patent

LE GOUVERNEMENT
DU GRAND-DUCHÉ DE LUXEMBOURG
Ministère de l'Économie

Le Ministre de l'Économie,

Vu la loi du 20 juillet 1992 portant modification du régime des brevets d'invention, telle que modifiée ;

Vu le règlement grand-ducal du 17 novembre 1997 concernant la procédure et les formalités administratives en matière de brevets d'invention ;

Vu le dépôt de la demande de brevet luxembourgeois daté du : **28/01/2016 ;**

Arrête :

Art. 1er.- Il est délivré à la (aux) personne(s) mentionnée(s) sur le tableau des données bibliographiques attaché au présent arrêté, sous le numéro de code 73, un

BREVET D'INVENTION N° 92964

pour : Means and methods for selecting transformed cells
tel que décrit dans les duplicata des pièces techniques joints en annexe.

Art. 2.- Le brevet est délivré sans examen préalable de la brevetabilité de l'invention, sans garantie de l'exactitude de la description et aux risques et périls des demandeurs.

Art. 3.- Le présent arrêté, qui constitue le titre de protection, est expédié au(x) mandataire(s) agréé(s), mentionné(s) sur le tableau des données bibliographiques attaché au présent arrêté, sous le numéro de code 74 ou, à défaut, à la (aux) personne(s) visées(s) à l'article 1er, pour servir de document probant à celle(s)-ci.

Luxembourg, le **07/08/2017**

Pour le Ministre de l'Économie,

Lex Kaufhold
Chargé de direction
Office de la propriété intellectuelle

(19) LE GOUVERNEMENT
DU GRAND-DUCHÉ DE LUXEMBOURG
Ministère de l'Économie

(11) N° de publication : 92964

(12) **BREVET D'INVENTION** B1

(21) N° de dépôt: 92964

(51) Int. Cl.:
C12N 15/65, C12N 15/90

(22) Date de dépôt: 28/01/2016

(30) Priorité:

(43) Date de mise à disposition du public: 07/08/2017

(47) Date de délivrance: 07/08/2017

(73) Titulaire(s):
UNIVERSITÉ DU LUXEMBOURG –
1511 LUXEMBOURG (Luxembourg)

(72) Inventeur(s):
FUENZALIDA JONATHAN ARIAS – 4367
BELVAUX (Luxembourg), JARAZO JAVIER – 4367
BELVAUX (Luxembourg), SCHWAMBORN JENS – 4367
BELVAUX (Luxembourg), XIAOBING QING – 4367
BELVAUX (Luxembourg)

(74) Mandataire(s):
SCHIWECK WEINZIERL KOCH GBR EUROPEAN PATENT
ATTORNEYS – 80339 MÜNCHEN (Allemagne)

(54) **Means and methods for selecting transformed cells.**

(57) ABSTRACT: The present invention relates to a nucleic acid molecule at least one nucleotide sequence encoding a selection marker indicating homologous recombination in a eukaryotic cell and at least one nucleotide sequence encoding a selection marker indicating heterologous recombination in said eukaryotic cell. The present invention also relates to a composition of matter comprising at least two nucleic acid molecules of the invention. The present invention further relates to in vitro methods for enriching or producing eukaryotic cells which are modified by homologous recombination. 92964

Figure 1

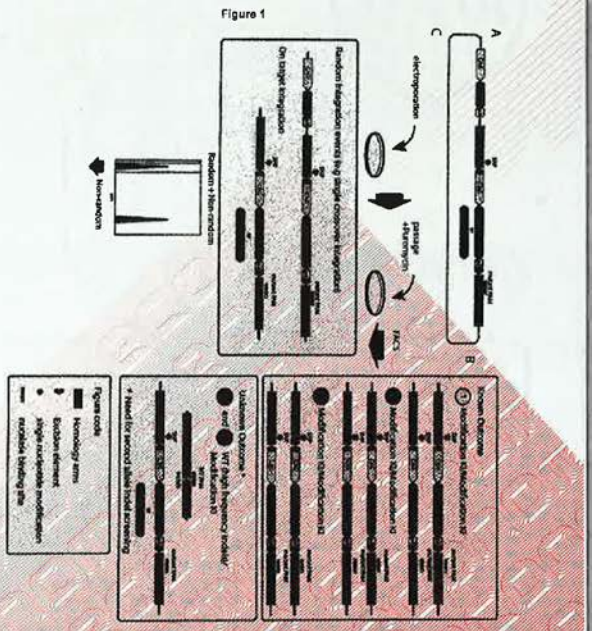

(12) INTERNATIONAL APPLICATION PUBLISHED UNDER THE PATENT COOPERATION TREATY (PCT)

(19) World Intellectual Property Organization
International Bureau

(43) International Publication Date
3 August 2017 (03.08.2017)

WIPO | PCT

(10) International Publication Number
WO 2017/129811 A1

(51) International Patent Classification:
C12N 15/65 (2006.01) *C12N 15/90* (2006.01)

(21) International Application Number:
PCT/EP2017/051889

(22) International Filing Date:
30 January 2017 (30.01.2017)

(25) Filing Language: English

(26) Publication Language: English

(30) Priority Data:
92964 28 January 2016 (28.01.2016) LU

(71) Applicant: **UNIVERSITÉ DU LUXEMBOURG** [LU/LU]; 162 a, Avenue de la Faiencerie, 1511 Luxembourg (LU).

(72) Inventors: **FUENZALIDA, Jonathan Arias**; c/o LCSB, 6, avenue du Swing, 4367 Belvaux (LU). **JARAZO, Javier**; c/o LCSB, 6, avenue du Swing, 4367 Belvaux (LU). **SCHWAMBORN, Jens**; c/o LCSB, 6, avenue du Swing, 4367 Belvaux (LU). **QING, Xiaobing**; c/o LCSB, 6, avenue du Swing, 4367 Belvaux (LU).

(74) Agents: **WEINZIERL, Gerhard Dr.** et al.; Schiweck Weinzierl Koch, European Patent Attorneys, Landsberger Strasse 98, 80339 Munich (DE).

(81) Designated States *(unless otherwise indicated, for every kind of national protection available)*: AE, AG, AL, AM, AO, AT, AU, AZ, BA, BB, BG, BH, BN, BR, BW, BY, BZ, CA, CH, CL, CN, CO, CR, CU, CZ, DE, DJ, DK, DM, DO, DZ, EC, EE, EG, ES, FI, GB, GD, GE, GH, GM, GT, HN, HR, HU, ID, IL, IN, IR, IS, JP, KE, KG, KH, KN, KP, KR, KW, KZ, LA, LC, LK, LR, LS, LU, LY, MA, MD, ME, MG, MK, MN, MW, MX, MY, MZ, NA, NG, NI, NO, NZ, OM, PA, PE, PG, PH, PL, PT, QA, RO, RS, RU, RW, SA, SC, SD, SE, SG, SK, SL, SM, ST, SV, SY, TH, TJ, TM, TN, TR, TT, TZ, UA, UG, US, UZ, VC, VN, ZA, ZM, ZW.

(84) Designated States *(unless otherwise indicated, for every kind of regional protection available)*: ARIPO (BW, GH, GM, KE, LR, LS, MW, MZ, NA, RW, SD, SL, ST, SZ, TZ, UG, ZM, ZW), Eurasian (AM, AZ, BY, KG, KZ, RU, TJ, TM), European (AL, AT, BE, BG, CH, CY, CZ, DE, DK, EE, ES, FI, FR, GB, GR, HR, HU, IE, IS, IT, LT, LU, LV, MC, MK, MT, NL, NO, PL, PT, RO, RS, SE, SI, SK, SM, TR), OAPI (BF, BJ, CF, CG, CI, CM, GA, GN, GQ, GW, KM, ML, MR, NE, SN, TD, TG).

Published:

— *with international search report (Art. 21(3))*

WO 2017/129811 A1

(54) Title: MEANS AND METHODS FOR SELECTING TRANSFORMED CELLS

(57) Abstract: The present invention relates to a nucleic acid molecule at least one nucleotide sequence encoding a selection marker indicating homologous recombination in a eukaryotic cell and at least one nucleotide sequence encoding a selection marker indicating heterologous recombination in said eukaryotic cell. The present invention also relates to a composition of matter comprising at least two nucleic acid molecules of the invention. The present invention further relates to in vitro methods for enriching or producing eukaryotic cells which are modified by homologous recombination.

Means and methods for selecting transformed cells

[0001] Targeted gene inactivation via homologous recombination is a powerful method capable of providing conclusive information for evaluating gene function. However, the use of this technique has been hampered by several factors, including the low efficiency at which engineered constructs are correctly inserted into the chromosomal target site, the need for time-consuming and labor-insensitive selection/screening strategies, and the potential for adverse mutagenic effects.

[0002] However, meganucleases, Zinc-finger nucleases (ZFNs) and transcription activator-like effector nucleases (TALENs) comprise a powerful class of tools that are redefining the boundaries of biological research. These chimeric nucleases are composed of programmable, sequence-specific DNA-binding modules linked to a non-specific DNA cleavage domain. ZFNs and TALENs enable a broad range of genetic modifications by inducing DNA double-strand breaks that stimulate error-prone non-homologous end joining (NHEJ) or homology-directed repair (HDR) at specific genomic locations. The emergence of clustered regulatory interspaced short palindromic repeat (CRISPR)/Cas-based RNA-guided DNA endonucleases has even broadened the tool box for genome editing.

[0003] Meganucleases, ZFNs and TALENs are based on the use of engineered nucleases composed of sequence-specific DNA-binding domains fused to a non-specific DNA cleavage module. These chimeric nucleases enable efficient and precise genetic modifications by inducing targeted DNA double-strand breaks (DSBs) that stimulate the cellular DNA repair mechanisms, including NHEJ and HDR. The versatility of this approach is facilitated by the programmability of the DNA-binding domains that are derived from zinc-finger and transcription activator-like effector (TALE) proteins. This combination of simplicity and flexibility has catapulted ZFNs and TALENs to the forefront of genetic engineering. Nowadays, because of its fast and convenient applicability CRISPR/Cas has become the front-running technology for genome editing.

[0004] However, though the genome editing technology is widely and efficiently applicable, the screening and selection of desired clones is nevertheless labor-and time-sensitive requiring, e.g. PCR techniques, sequencing or the like in order to verify desired clones. In fact, the current protocols to derive genome edited lines require the screening of a great number of clones to obtain one lacking random integration or on locus NHEJ

containing alleles (Ran et al., Nat. Protoc. 8, 2281–2308 (2013), Sander and Joung, Nat. Biotechnol. 32, 347–355 (2014)).

[0005] There is thus still a need for means and methods allowing the selection of transformed cells having the desired genotype. The present application addresses this need and thus provides means and methods for selecting transformed cells having the desired genotype.

[0006] Specifically, the present application provides means and methods for streamlining the gene editing process by incorporating reporters to reduce hands on time by automating/simplifying the screening process. Accordingly, the present application makes use of a negative and positive selection module. While the negative selection module allows screening and sorting out undesired random/off-site modified transformed cells, the positive selection module allows the identification of desired on-site modified cells.

[0007] By way of example, fluorescent proteins are used as selection markers on the nucleic acid molecule used in gene editing as a donor DNA molecule, wherein different fluorescent proteins are used for positive and negative selection such that both fluorescent proteins are optically discriminable, e.g. in Fluorescent-activated cell sorting (FACS), flow cytometry or fluorescence microscopy. The marker used for positive selection is flanked 5' and 3' by nucleotide sequences that are homologous to nucleotide sequences of a nucleic acid sequence of interest comprised by eukaryotic cells, such as mammalian cells or plant cells (homology arms) and thus is indicative of homologous recombination as it is integrated together with the flanking homology arms. A cell comprising the positive selection marker is therefore likely to be a desired on-site (or in locus) modified cells. The marker used for negative selection, not comprised in the region flanked 5' and 3' by homology arms, is likely to be integrated in the cellular genome upon heterologous recombination, only, and thus indicates an unwanted genetic modification, allowing to detect off-site (or out-of locus) modified cells.

[0008] A preferred embodiment of the technique described herein is sometimes called Fluorescence Assisted Genome Editing (FAGE). FAGE allows to derive correctly edited clones carrying a positive selection fluorescent marker and to exclude non-edited, random integrations and on-target allele NHEJ-containing cells from the correctly edited polyclonal population. Specifically, the combined use of two nucleic acid molecules each comprising different nucleotide sequences encoding different fluorescent proteins in the positive selection modules loaded onto specific homology arms (mutant/mutant, wild-type/wild-type or mutant/wild-type) allows to deterministically predict the

outcome of the modification as designed, thereby giving rise to bi-allelically targeted homozygotes and heterozygote cell populations.

[0009] Accordingly, The means and methods of the present application allow the cell population, polyclones or clones that have undergone removal of the positive selection module to be enriched by the selection of cells that lost the optical, e.g. fluorescence signal by, e.g. FACS. After the removal of the positive selection module, e.g. homozygous gene corrected edited lines, homozygous mutant genome edited lines, heterozygous mutant genome edited lines or heterozygous gene corrected edited lines can be subcloned or used for phenotypic characterization, drug screening or cell therapy.

***

[0010] It must be noted that as used herein, the singular forms “a”, “an”, and “the”, include plural references unless the context clearly indicates otherwise. Thus, for example, reference to “an expression cassette” includes one or more of the expression cassettes disclosed herein and reference to “the method” includes reference to equivalent steps and methods known to those of ordinary skill in the art that could be modified or substituted for the methods described herein.

[0011] Unless otherwise indicated, the term "at least" preceding a series of elements is to be understood to refer to every element in the series. Those skilled in the art will recognize, or be able to ascertain using no more than routine experimentation, many equivalents to the specific embodiments of the invention described herein. Such equivalents are intended to be encompassed by the present invention.

[0012] Throughout this specification and the claims which follow, unless the context requires otherwise, the word “comprise”, and variations such as “comprises” and “comprising”, will be understood to imply the inclusion of a stated integer or step or group of integers or steps but not the exclusion of any other integer or step or group of integer or step. When used herein the term “comprising” can be substituted with the term “containing” or sometimes when used herein with the term “having”.

[0013] When used herein “consisting of" excludes any element, step, or ingredient not specified in the claim element. When used herein, "consisting essentially of" does not exclude materials or steps that do not materially affect the basic and novel characteristics of the claim. In each instance herein any of the terms "comprising", "consisting essentially of" and "consisting of" may be replaced with either of the other two terms.

[0014] The term "about" or "approximately" as used herein means within 20%, preferably within 10%, and more preferably within 5% of a given value or range. It includes also the concrete number, e.g., about 20 includes 20.

[0015] Unless otherwise defined herein, scientific and technical terms used in connection with the present invention shall have the meanings that are commonly understood by those of ordinary skill in the art. Further, unless otherwise required by context, singular terms shall include pluralities and plural terms shall include the singular. The methods and techniques of the present invention are generally performed according to conventional methods well-known in the art. Generally, nomenclatures used in connection with techniques of biochemistry, enzymology, molecular and cellular biology, microbiology, genetics and protein and nucleic acid chemistry and hybridization described herein are those well-known and commonly used in the art.

[0016] The methods and techniques of the present invention are generally performed according to conventional methods well-known in the art and as described in various general and more specific references that are cited and discussed throughout the present specification unless otherwise indicated. See, e. g., Sambrook et al., Molecular Cloning: A Laboratory Manual, 3rd ed., Cold Spring Harbor Laboratory Press, Cold Spring Harbor, N. Y. (2001); Ausubel et al., Current Protocols in Molecular Biology, J, Greene Publishing Associates (1992, and Supplements to 2002); Handbook of Biochemistry: Section A Proteins, Vol I 1976 CRC Press; Handbook of Biochemistry: Section A Proteins, Vol II 1976 CRC Press. The nomenclatures used in connection with, and the laboratory procedures and techniques of, molecular and cellular biology, protein biochemistry, enzymology and medicinal and pharmaceutical chemistry described herein are those well-known and commonly used in the art.

[0017] The present invention provides a nucleic acid molecule comprising at least one nucleotide sequence encoding a selection marker indicating homologous recombination when integrated in the sequence of interest comprised in a eukaryotic cell, such as a mammalian or plant cell, and at least one nucleotide sequence encoding a selection marker indicating heterologous recombination when not integrated in the sequence of interest comprised in said eukaryotic cell, wherein the selection markers when being expressed are optically discriminable, e.g. in FACS or any fluorescence guided capture, and wherein the nucleotide sequence encoding a selection marker indicating homologous recombination in a eukaryotic cell is flanked 5' and 3' by nucleotide sequences that are homologous to nucleotide sequences of a nucleic acid sequence of interest comprised by eukaryotic cell.

[0018] A eukaryotic cell when used herein may preferably be a mammalian cell or plant cell. A mammalian cell may preferably be a cell from a human, dog, cat, cow, swine, horse, sheep, goat, rabbit, mouse or rat, with human being preferred. A preferred human cell is a stem cell or induced pluripotent stem cell. The human cells may be obtained from a healthy human or a human suffering from a disease, such as Parkinson disease (PD) or Alzheimer disease (AD). The human cell and any other mammalian cell may be from a cell line, e.g. a deposited cell line or a commonly available cell line.

[0019] The term "nucleic acid molecule" or “nucleotide sequence” as used herein refers to a polymeric form of nucleotides (i.e. polynucleotide) which are usually linked from one deoxyribose or ribose to another. The term "nucleic acid molecule" preferably includes single and double stranded forms of DNA or RNA. A nucleic acid molecule may include both sense and antisense strands of RNA (containing ribonucleotides), cDNA, genomic DNA, and synthetic forms and mixed polymers of the above. They may be modified chemically or biochemically or may contain non-natural or derivatized nucleotide bases, as will be readily appreciated by those of skill in the art. Such modifications include, for example, labels, methylation, substitution of one or more of the naturally occurring nucleotides with an analog, internucleotide modifications such as uncharged linkages (e.g., methyl phosphonates, phosphotriesters, phosphoramidates, carbamates, etc.), charged linkages (e.g., phosphorothioates, phosphorodithioates, etc.), pendent moieties (e.g., polypeptides), intercalators (e.g., acridine, psoralen, etc.), chelators, alkylators, and modified linkages (e.g., alpha anomeric nucleic acids, etc.) Also included are synthetic molecules that mimic polynucleotides in their ability to bind to a designated sequence via hydrogen bonding and other chemical interactions. Such molecules are known in the art and include, for example, those in which peptide linkages substitute for phosphate linkages in the backbone of the molecule. In a preferred embodiment the term “nucleic acid molecule” to be introduced into a cell refers to DNA and even more preferred to double stranded DNA, whereas a nucleic acid being an expression product is preferably a RNA.

[0020] The term “selection marker”, “selectable marker” or “marker” are used interchangeably herein and refer to a gene introduced into a cell that confers a trait suitable for selection of cells when being expressed, for e.g. successful transfection or a specific genetic modification of a cell. A selection marker preferably provides the cell with a phenotype that is optically detectable via FACS, flow cytometry or fluorescence microscopy, such as e.g. fluorescent proteins.

[0021] The term “indicating” and its grammatical variants, such as “indicative for” when used in the context of a selection marker indicating homologous or heterologous recombination,

respectively, does not mean that the selection marker is indicative that a homologous or heterologous recombination indeed occurred. Rather, said term means that the selection marker provides a skilled artisan with a reasonable likelihood/probability that homologous or heterologous recombination, respectively, occurred. Put differently, the selection marker is an indicator for a homologous or heterologous recombination, respectively, but is not a proof for homologous or heterologous recombination, respectively.

[0022] A selection marker indicating homologous recombination when integrated in the sequence of interest comprised in a eukaryotic cell is thus indicative that homologous recombination occurred, while a selection marker indicating heterologous recombination when not integrated in the sequence of interest comprised in a eukaryotic cell is indicative to detect and exclude recombination events outside of the sequence of interest comprised by a eukaryotic cell.

[0023] The term "homologous recombination" as used herein refers to homology-directed repair (HDR) which is a template-dependent pathway for DNA double-strand break repair. By supplying a homology-containing donor template, preferably along with a site-specific nuclease, HDR faithfully inserts the donor molecule at the targeted locus. This approach enables the insertion of single or multiple transgenes, as well as single nucleotide substitutions. Thus, the present invention preferably employs homologous recombination for site-specific genetic modification of the nucleic acid sequence of interest comprised by the eukaryotic cell by integration of the nucleic acid molecule of the invention. To this end, the nucleic acid molecule of the invention comprises nucleotide sequences that are homologous to nucleotide sequences of a nucleic acid sequence of interest comprised by the eukaryotic cell. The homologous nucleotide sequences comprised by the nucleic acid molecule of the invention flank the selection marker which indicates homologous recombination 5' and 3' and are thus called "homology arms". The homology arms direct the nucleic acid molecule of the invention to the desired nucleotide sequence of interest comprised by the eukaryotic cell and thus mediate the site specific integration. As the homology arms are integrated upon homologous recombination, the sequence flanked by the homology arms (i.e. the sequence situated between the homology arms), e.g. the selection marker indicating homologous recombination or any other nucleotide sequence, will also be integrated. The homology arms do preferably not comprise any repetitive element. Without being bound by theory, excluding repetitive elements from the homology arms increases homology directed repair efficiency and decreases the rate of random integration. However, the homology arms can also comprise one or more mismatches compared to the nucleic acid sequence of interest comprised by the eukaryotic cell, as long as such mismatches do not prevent homologous recombination. Such a mismatch in the homology arms may be employed in order to

introduce mutations in the nucleic acid sequence of interest and/or to avoid a target sequence of a nuclease used for inducing homologous recombination in the homology arms.

[0024] The term "heterologous recombination" as used herein refers to the integration of the nucleic acid molecule of the invention in a nucleic acid sequence comprised by the eukaryotic cell which is not homologous to the nucleotide sequence of the homology arms of the nucleic acid molecule of the invention, i.e. random integration. Therefore, heterologous recombination is not site-specific and results in an integration of the nucleic acid molecule of the invention in an undesired sequence comprised by the eukaryotic cell or off-site. The selection marker indicating heterologous recombination is not flanked by the homology arms and is thus not situated between the homology arms. Without being bound by theory, the present inventors assume that in the event of heterologous recombination the part of the nucleic acid molecule of the invention which is integrated in the nucleic acid sequence comprised by the eukaryotic cell is different compared to the part of the nucleic acid molecule of the invention which is integrated in the nucleic acid sequence comprised by the eukaryotic cell upon homologous recombination. More precisely, in case of homologous recombination it is assumed that only the nucleic acid sequence of the nucleic acid molecule of the invention comprising the homology arms and the nucleic acid sequence flanked by the homology arms (e.g. selection marker indicating homologous recombination) is integrated in the sequence of interest comprised by the eukaryotic cell, whereas in case of heterologous recombination also nucleic acid sequences of the nucleic acid molecule of the invention may be integrated in the nucleic acid sequence comprised by the eukaryotic cell which are not comprised by the nucleic acid sequence comprising the homology arms and the sequence flanked by the homology arms, e.g. the complete nucleic acid molecule of the invention. Therefore in case of heterologous recombination also the second selection marker indicating heterologous recombination may be integrated in the nucleic acid sequence comprised by the eukaryotic cell and is therefore indicative of an unwanted off-site integration or random integration event.

[0025] As described herein, the presence or absence of any one of the described selection markers is indicative of a specific genetic modification of the nucleic acid sequence comprised by the eukaryotic cell. However, the presence or absence of the described selection markers provides no guarantee for a specific genetic modification of the nucleic acid sequence comprised by the eukaryotic cell. Therefore, a further verification, e.g. sequencing, may be used for verification of the genetic modification as described herein.

[0026] The term "nucleic acid sequence of interest" as used herein refers to any nucleic acid sequence comprised by a eukaryotic cell, such as a plant or eukaryotic cell which is intended to be genetically modified.

[0027] In a preferred embodiment the nucleic acid sequence of interest comprised by said eukaryotic cells, e.g. plant or mammalian cell is in the genome of said eukaryotic cell.

[0028] The term "genome" as used herein includes the cellular genome, mitochondrial genome and/or chloroplast genome. The latter, if the eukaryotic cell is a plant cell. For eukaryotic cells, said term includes the cellular genome and/or mitochondrial genome.

[0029] In a further preferred embodiment of the invention the nucleotide sequence encoding a selection marker indicating homologous recombination when integrated in the sequence of interest and said selection marker indicating heterologous recombination when not integrated in the sequence of interest each comprises a promoter driving expression of said selection markers. Also envisioned herein is that the gene encoding the selection marker indicating homologous recombination and the gene encoding the selection marker indicating heterologous recombination are comprised in an expression cassette.

[0030] The term "promoter" as used herein is a non-coding expression control sequence preferably inserted nearby the start of the coding sequence of the expression cassette and regulates its expression. Put into a simplistic yet basically correct way, it is the interplay of the promoter with various specialized proteins called transcription factors that determine whether or not a given coding sequence may be transcribed and eventually translated into the actual protein encoded by the gene. It will be recognized by a person skilled in the art that any compatible promoter can be used for recombinant expression in host cells. The promoter itself may be preceded by an upstream activating sequence, an enhancer sequence or combination thereof. These sequences are known in the art as being any DNA sequence exhibiting a strong transcriptional activity in a cell and being derived from a gene encoding an extracellular or intracellular protein. It will also be recognized by a person skilled in the art that termination and polyadenylation sequences may suitably be derived from the same sources as the promoter. Tthe promoter may be constitutive or inducible.

[0031] Expression cassettes as used herein contain transcriptional control elements suitable to drive transcription such as e.g. promoters, enhancers, polyadenylation signals, transcription pausing or termination signals. For proper expression of the polypeptides, suitable translational control elements are preferably included, such as e.g. 5' untranslated regions leading to 5' cap structures suitable for recruiting ribosomes and stop codons to terminate the translation process.

[0032] The terms "inducible" or "inducible promoter" as used herein refer to a promoter that regulate the expression of an operably linked gene in response to the presence or absence of an endogenous or exogenous stimulus. Such stimuli can be but are not limited to chemical compounds or environmental signals. This is in contrast to a constitutive promoter which does not require any stimulus to induce expression of an operably linked gene but constitutively drives the expression of said gene.

[0033] In an even further preferred embodiment of the invention the nucleotide sequence encoding a selection marker indicating homologous recombination comprises 5' and 3' nucleotide sequences (i.e. excision elements) which allow excision of said nucleotide sequence encoding said selection marker.

[0034] The excision elements comprised by the nucleic acid molecule of the invention preferably flank the selection marker indicating homologous recombination 5' and 3'. Thus, in a preferred embodiment of the invention the nucleic acid sequence comprised by the nucleic acid molecule of the invention comprising the selection marker indicating homologous recombination is arranged as follows:

homology arm – excision element – selection marker indicating homologous recombination operably linked to a promoter – poly A – excision element – homology arm.

In case two of said nucleic acid molecules comprising a different nucleotide sequence encoding a selection marker indicating homologous recombination are used, one or both alleles can be targeted, e.g. in order to introduce a point mutation. Subsequently, the selection markers may be excised. By way of example, such a genetically modified cell may be a suitable model system for a disease allowing to test and identify novel therapeutic agents.

[0035] In a preferred embodiment the nucleotide sequences which allow excision of the nucleotide sequence encoding the selection marker indicating homologous recombination are selected from loxP sequences, derivatives of loxP sequences, such as Lox511, Lox5171, Lox2272, M2, M3, M7, M11, Lox71 or Lox66 sequences, Cre recombinase binding sites, FRT sequences, derivatives of FRT sequences, such as FRT-G, FRT-H or FRT-F3, FLP recombinase binding sites, terminal repeats, transposase binding sites, derivatives of transposase binding sites, such as terminal repeats, internal terminal repeats, direct repeats, inverted repeats or palindromic repeats, piggybac transposon binding sites, sleeping beauty transposon binding sites, piggybat binding sites, binding site of transposons fused to estrogen receptor, estrogen binding sites or mutational derivatives, binding site of transposons fused to estrogen receptor tamoxifen binding sites, RNA-guided nuclease

binding site, Cas9 binding sites, Cpf binding site, nuclease binding sites, transcription activator like effector nuclease (TALEN or TALEN-Fok1) binding sites, zinc finger nuclease (ZFN) binding sites or RNA-guided nuclease binding sites.

[0036] The nucleotide sequence encoding a selection marker indicating homologous recombination may be removed by excision or recombination or cleavage after depositing a modification into the genome. The removal of the nucleotide sequence encoding a selection marker indicating homologous recombination may be performed by the use of a recombinase, transposase, RNA guided nuclease or nuclease. The excision, recombination or cleavage of the nucleotide sequence encoding a selection marker indicating homologous recombination may be induced by the expression of a recombinase, transposase, RNA guided nuclease or nuclease. Such enzyme can be delivered by electroporation or transfection of a double stranded DNA, transfection of a pre transcribed mRNA or pre translated protein. When such enzyme is fused to a nuclear receptor domain (e.g. estrogen receptor) it can be translocated into the nucleus by the supplementation of tamoxifen, to induce ER domain (or nuclear receptor translocation domains) mediated nuclear translocation. Such enzyme may also be induced by the supplementation of doxycycline to the media, inducing the tetracycline-controlled transcriptional activation of its gene. Cells that have undergone removal of the nucleotide sequence encoding a selection marker indicating homologous recombination may further be enriched by the selection of cells that lost the fluorescence signal by FACS or fluorescence microscopy. After the removal of the positive selection module homozygous gene corrected edited lines, homozygous mutant genome edited lines, heterozygous mutant genome edited lines or heterozygous gene corrected edited lines can be subcloned or used for phenotypic characterization, drug screening or cell therapy.

[0037] In a further preferred embodiment the nucleic acid molecule of the invention comprises a chemical resistance selection marker selected from neomycin resistance, hygromycin resistance, HPRT1, puromycin resistance, puromycin N-acetyl-transferase, blasticidin resistance, G418 resistance, phleomycin resistance, nourseothricin resistance or chloramphenicol resistance, puromycin resistance being preferred.

[0038] It is envisioned herein that the chemical resistance selection marker is associated or not associated with the selection marker indicating homologous recombination. Accordingly, the chemical resistance selection marker may be associated with the selection marker indicating homologous recombination via a linking element, e.g. P2A, T2A, E2A, F2A or and internal ribosome entry site (IRES), T2A being preferred. Thus, in a preferred embodiment of

the invention the genetic element comprised by the nucleic acid molecule of the invention comprising the selection marker indicating homologous recombination is arranged as follows:

homology arm – excision element – selection marker indicating homologous recombination operably linked to a promoter – linking element – chemical resistance marker – poly A – excision element – homology arm.

[0039] In a preferred embodiment of the invention the nucleotide sequences that are homologous (homology arms) to nucleotide sequences of a nucleic acid sequence of interest comprised by said eukaryotic cell allow homologous recombination with nucleotide sequences of a nucleic acid sequence of interest comprised by said eukaryotic cell. However, as described elsewhere herein the homology arms may comprise one or more mismatches compared to the nucleic acid sequence of interest comprised by the eukaryotic cell, as long as such mismatches do not prevent homologous recombination. Such a mismatch in the homology arms may be employed in order to introduce mutations in the nucleic acid sequence of interest.

[0040] Accordingly, in a preferred embodiment the present invention employs homologous recombination for depositing a modification into the genome, said modification is selected from a single nucleotide polymorphism (SNP), phosphomimetic mutation, phospho null mutation, missense mutation, nonsense mutation, synonymous mutation, insertion, deletion, knock-out or knock-in.

[0041] A preferred SNP that may be introduced into the alpha synuclein gene or an othologue thereof of a eukaryotic cell, preferably of a human induced pluripotent stem cell is one which results in the following mutation A30P, A53T, E46K, G51D or H50Q. Of course, any preferred SNP can be introduced in any preferred gene of any eukaryotic cell, since techniques for introducing SNPs or knocking-in or knocking-out genes by means and methods facilitating homologous recombination are well known in the art and exemplarily described herein, such as CRISPR/Cas.

[0042] The modification may be deposited in the genome of the cell preferably by a mismatch in the homology arms of the nucleic acid molecule, which is integrated in the genome of the cell upon homologous recombination, compared to the homologous nucleotide sequences of a nucleic acid sequence of interest. However, a modification may also be deposited by inserting a nucleic acid sequence or modification to be deposited in the genome of the cell between the homology arms in the nucleic acid molecule of the invention.

[0043] In a preferred embodiment the homologous recombination occurs at one allele (mono allelic) or at both alleles (bi-allelic) of said nucleic acid sequence of interest comprised by said eukaryotic cell.

[0044] In a further preferred embodiment homologous recombination is mediated by TALENs, ZFNs, meganucleases, or CRISPR/Cas. Homologous recombination of the nucleic acid molecule of the invention with the nucleic acid sequence of interest comprised by said eukaryotic cell is a rare event. It is known in the art that inducing a DNA double-strand break in nucleic acid sequences comprised by a cell induces cellular DNA repair mechanisms, such as homologous recombination. Thus, the induction of a site specific DNA double-strand break in the nucleic acid sequence of interest increases homologous recombination with the nucleic acid molecule of the invention, being as well directed to the nucleic acid sequence of interest via the homology arms. Such a DNA double-strand break may be induced by employing TALENs, ZFNs, meganucleases, or CRISPR/Cas, or any other nuclease being directed to the nucleic acid sequence of interest comprised by the eukaryotic cell.

[0045] The term "TALEN" as used herein refers to transcription activator-like effector nucleases which are fusions of the FokI cleavage domain and DNA-binding domains derived from TALE proteins. As the FokI cleavage domain is only active as a dimer, two TALENs have to be used which bring the FokI cleavage domains in close proximity upon binding to their target sequence resulting in the induction of a DNA double-strand break. TALEs contain multiple 33–35-amino-acid repeat domains that each recognizes a single base pair with the so-called repeat variable di-residue (RVD) which are two variable amino acids determining the binding specificity one single repeat. Like ZFNs, TALENs induce targeted DSBs that activate DNA damage response pathways and enable custom alterations. However, TALENs may also be modified such that one of the FokI cleavage domains is inactivated. Such modified TALENs cause only single-strand breaks and are thus nickases.

[0046] The term "ZFN" or "zinc-finger nuclease" as used herein refers to fusions of the nonspecific DNA cleavage domain from the FokI restriction endonuclease with zinc-finger proteins. ZFN dimers induce targeted DNA DSBs that stimulate DNA damage response pathways. The binding specificity of the designed zinc-finger domain directs the ZFN to a specific genomic site. However, also zinc-finger nickases (ZFNickases) may be used. Zinc-finger nickases are ZFNs that contain inactivating mutations in one of the two FokI cleavage domains. ZFNickases make only single-strand DNA breaks and induce HDR without activating the mutagenic NHEJ pathway.

[0047] The term "meganuclease" as used herein refers to a family of endonucleases, also called homing endonucleases that can be divided into five families based on sequence and

structure motifs: LAGLIDADG, GIY-YIG, HNH, His-Cys box and PD-(D/E)XK characterized by a large recognition site (double-stranded DNA sequences of 12 to 40 base pairs). The most well studied family is that of the LAGLIDADG proteins, including I-SceI, I-CreI and I-DmoI which are most widely used in research and genome engineering. The best known LAGLIDADG endonucleases are homodimers (I-CreI) or internally symmetrical monomers (I-SceI). The DNA binding site, which contains the catalytic domain, is composed of two parts on either side of the cutting point. The half-binding sites can be extremely similar and bind to a palindromic or semi-palindromic DNA sequence (I-CreI), or they can be non-palindromic (I-SceI).

[0048] The term "CRISPR/Cas" as used herein relates to the Clustered Regularly Interspaced Short Palindromic Repeats (CRISPR) Type II system which is a bacterial immune system that has been modified for genome engineering. CRISPR consists of two components: a "guide" RNA (gRNA) and a non-specific CRISPR-associated endonuclease (Cas9). The gRNA is a short synthetic RNA composed of a "scaffold" sequence necessary for Cas9-binding and a user-defined ~20 nucleotide "spacer" or "targeting" sequence which defines the genomic target to be modified. Thus, one can change the genomic target of Cas9 by simply changing the targeting sequence present in the gRNA. CRISPR/Cas can be used for gene engineering by co-expressing a gRNA specific to the sequence to be targeted and the endonuclease Cas9. The genomic target can be any ~20 nucleotide DNA sequence, provided the sequence is unique compared to the rest of the genome and the target is present immediately upstream of a Protospacer Adjacent Motif (PAM).The PAM sequence is absolutely necessary for target binding and the exact sequence is dependent upon the species of Cas9.

[0049] In a further preferred embodiment of the invention the nucleotide sequences that are homologous (homology arms) to nucleotide sequences of a nucleic acid sequence of interest comprised by the eukaryotic cell do not comprise a target sequence for TALENs, ZFNs, meganucleases, or CRISPR/Cas or any other nuclease which mediate homologous recombination.

[0050] As nucleotide sequences that are homologous (homology arms) to nucleotide sequences of a nucleic acid sequence of interest are intended to be integrated in the nucleic acid sequence of interest comprised by the eukaryotic cell or the cellular genome, cleavage by the nuclease used to mediate homologous recombination is to be avoided. Thus, it is envisioned that the homology arms do not comprise a target sequence for a nuclease used to mediate homologous recombination. In order to avoid a target sequence within the homology arms the nucleic acid sequence of the homology arms may be modified such that

the nuclease does not recognize it as a target sequence or the binding affinity of the nuclease is reduced. Thus the nuclease used to mediate homologous recombination can only induce a DNA double-strand break in the nucleotide sequence of interest comprised by the cell but not in the integrated nucleic acid molecule of the invention or the non-integrated nucleic acid molecule of the invention comprised by the eukaryotic cell. However, the target sequence of the nuclease may also be splitted in the nucleic acid molecule of the invention by the selection marker indicating homologous recombination such that the nuclease cannot recognize it as a target sequence or the binding affinity of the nuclease is reduced. Without being bound by theory, such an unwanted DNA double-strand break could induce the error prone DNA repair mechanism non-homologous end joining and would thus introduce unwanted mutations in the nucleic acid molecule of the invention or in the nucleic acid molecule of the invention integrated in the cellular genome. Accordingly, using two nucleic acid molecules comprising different nucleotide sequences encoding different selection markers advantageously indicate that two homologous recombination events have occurred in cells being double positive for both markers and consequently no unwanted mutations have been introduced via non-homologous end joining in any one of the targeted alleles.

[0051] The term “non-homologous end joining” as used herein refers to a DNA repair pathway that ligates or joins two broken ends together. NHEJ does not use a homologous template for repair and thus typically leads to the introduction of small insertions and deletions at the site of the break, often inducing frame-shifts that knockout gene function.

[0052] In another preferred embodiment the nucleic acid molecule of the invention is a vector.

[0053] The term "vector" as used herein refers to a nucleic acid molecule into which the nucleic acid molecule of the invention may be inserted or cloned. The vector may encodes a further antibiotic resistance gene. The vector may be an expression vector. The vector may be capable of autonomous replication in a host cell (e. g., vectors having an origin of replication which functions in the host cell). The vector may have a linear, circular, or supercoiled configuration and may be complexed with other vectors or other material for certain purposes.

[0054] One type of vector is a plasmid, which refers to a circular double stranded DNA loop into which additional DNA segments may be introduced via ligation or by means of restriction-free cloning. Other vectors include cosmids, bacterial artificial chromosomes (BAC), yeast artificial chromosomes (YAC) or mini-chromosomes. Another type of vector is a viral vector, wherein additional DNA segments may be ligated into the viral genome.

[0055] In a preferred embodiment of the invention the vector is circular or linearized.

[0056] In yet another preferred embodiment of the invention the optical discriminability is different emission wavelength, e.g. different emission wavelength in the fluorescence range.

[0057] The term "optically discriminable" as used herein preferably relates to a difference in emission wavelength, e.g. different colors such that the selection marker indicating homologous recombination and the selection marker indicating heterologous recombination can be distinguished upon detection, e.g. using FACS, fluorescence microscopy or flow cytometry.

[0058] In a preferred embodiment of the invention the selection marker indicating homologous recombination and the selection marker indicating heterologous recombination is a fluorescent protein. The fluorescent protein is preferably selected from Sirius, SBFP2, Azurite, EBFP2, mKalama1, mTagBFP2, Aquamarine, ECFP, Cerulean, mCerulean3, SCFP3A, mTurquoise2, CyPet, AmCyan1, mTFP1, MiCy, iLOV, AcGFP1, sfGFP, mEmerald, EGFP, mAzamiGreen, cfSGFP2, ZsGreen, mWasabi, SGFP2, Clover, mClover2, EYFP, mTopaz, mVenus, SYFP2, mCitrine, YPet, ZsYellow1, mPapaya1, mKO, mOrange, mOrange2, mKO2, TurboRFP, mRuby2, eqFP611, DsRed2, mApple, mStrawberry, FusionRed, mRFP1, mCherry, mCherry2, dTOMATO, tdTOMATO, tagBFP, photoactivatable or photoswitchable fluorescent protein.

[0059] The fluorescent proteins applied in the different nucleic acid molecules of the present invention are advantageously chosen such that they are optically discriminable from each other. A pair of fluorescent proteins applied in connection with the selection marker indicating homologous recombination is optically discriminable from each other and is optically discriminable from the fluorescent protein applied in connection with the selection marker indicating heterologous recombination.

[0060] Exemplary combinations of fluorescent proteins are as follows:

selection marker indicating heterologous recombination	selection marker indicating homologous recombination (nucleic acid molecule 1)	selection marker indicating homologous recombination (nucleic acid molecule 2)
tagBFP	EGFP	dTOMATO
tagBFP	EGFP	EBFP2
tagBFP	EGFP	Cerulean
tagBFP	EGFP	SYFP2
tagBFP	EGFP	mRFP1

EGFP	tagBFP	dTOMATO
dTOMATO	EGFP	tagBFP

[0061] In another preferred embodiment the invention provides a composition of matter comprising a mixture of at least two different nucleic acid molecules of the invention, each comprising a different nucleotide sequence encoding a selection marker indicating homologous recombination in said eukaryotic cell.

[0062] Such a composition of matter, comprises different nucleic acid molecules of the invention, differing in the nucleotide sequence encoding a selection marker indicating homologous recombination in the eukaryotic cell such that the selection markers when being expressed are optically discriminable as described herein. Such a composition of matter is advantageous in detecting cells in which both alleles have been successfully genetically modified as the presence of both selection markers in the eukaryotic cell are indicative of two homologous recombination events and thus genetic modification of both alleles. By way of example, one nucleic acid molecule comprises a selection marker gene indicating homologous recombination encoding for EGFP, whereas the second nucleic acid molecule comprises a selection marker gene indicating homologous recombination encoding for dTomato. Thus, without being bound by theory a cell being positive for EGFP and dTomato (and being negative for the selection marker indicating heterologous recombination) has two site specific integrations of the nucleic acid molecules of the invention and has therefore the genetic modification in both alleles. Such a cell may be positive for EGFP and dTomato or may also be yellow, due to the presence of green and red, when subjected to FACS analysis or fluorescence microscopy. The discrimination between the two nucleic acid molecules differing in the nucleotide sequence encoding a selection marker indicating homologous recombination in the eukaryotic cell further allows to detect cells in which both alleles have different genetic modifications. By way of example, the first nucleic acid molecules may comprise a wild type sequence and an EGFP selection marker indicating homologous recombination, whereas the second nucleic acid molecules may comprise a pathologic mutation and a dTomato selection marker indicating homologous recombination. Thus, a cell being EGFP and dTomato positive (or yellow) when subjected to FACS analysis or fluorescence microscopy has both nucleic acid molecules integrated and is thus heterozygous with respect to the genetically modified sequence of interest. However, it is also envisioned to discriminate cells which are only positive for a single selection marker by way of the expression level of the selection marker gene, e.g. brightness of the fluorescence due to the expression of a fluorescent protein. Without being bound by theory, it is expected that cells having two integrations of the nucleic acid molecule of the invention encoding e.g. a

fluorescent protein are brighter when subjected to FACS analysis or fluorescence microscopy and thus have both alleles genetically modified.

[0063] In a further preferred embodiment the invention provides an *in vitro* method for enriching eukaryotic cells which are modified by homologous recombination, comprising

(a) subjecting a population of cells transformed with a nucleic acid molecule or a composition of the invention to means for selecting for said marker indicating heterologous recombination and separate transformed cells expressing said selection marker indicating heterologous recombination in said eukaryotic cell; and

(b) subjecting the non-separated cells to means for selecting for said marker indicating homologous recombination in order to enrich transformed cells comprising said homologous recombination.

[0064] The *in vitro* methods of the invention make use of the discriminable selection markers by separating in a first step (a) cells which comprise the selection marker indicating heterologous recombination and therefore an unspecific and/or off-site integration of the nucleic acid molecule or the composition of the invention in the eukaryotic cell. In the second selection step (b) non-separated cells (cells which are not positive for the selection marker indicating heterologous recombination) are selected for said marker indicating homologous recombination indicating a site-specific integration of the nucleic acid molecule or the composition of the invention. Said second selection step separates cells which do not comprise the selection marker, indicating that said cells were not successfully transformed. In case a composition of the invention is used in the *in vitro* methods of the invention two different selection markers may be detected, as the nucleic acid molecules of the composition differ in the nucleotide sequence encoding a selection marker indicating homologous recombination. Thus, in case nucleic acid molecule one comprises marker 1 and nucleic acid molecule two comprises marker 2 a cell may comprise the following combinations of selection markers with respect to two alleles of the nucleic acid sequence of interest: marker 1, marker 2, marker 1 and marker 1, marker 2 and marker 2, and marker 1 and marker 2 (or marker 2 and marker 1). Said combinations of selection markers provide further information on the genetic modification of the cell. In case a cell is single positive for marker 1 or marker 2 this indicates a single integration of one nucleic acid molecule of the invention and therefor the modification of one allele, only. In case a cell is double positive for marker 1 or marker 2 (i.e. marker 1 and marker 1 or marker 2 and marker 2) this indicates two integrations of the same nucleic acid molecule of the invention. Thus, both alleles of the cell are likely to be modified and the cell is likely to be homozygous with respect to the modified allele (sequence of interest). Without being bound by theory, such a cell appears more positive when subjected to detection means suitable to detect the marker (e.g. brighter

in color in case of fluorescent proteins). In case a cell is positive for marker 1 and marker 2 this indicates two integrations (one integration of each nucleic acid molecule of the invention). Thus, both alleles of the cell are likely to be modified. As the combination of two different markers, which are discriminable, preferably optical discriminable, such as different fluorescent proteins differing in emission wavelength, are easily detectable by a person skilled in the art, such a cell is preferred. In case the two different nucleic acid molecules of the invention further differ in the genetic modification introduced upon homologous recombination in the eukaryotic cell, such a cell would be likely heterozygous with respect to the modified allele (sequence of interest).

[0065] By way of example, Figure 2 shows possible outcomes for nucleic acid molecules with different combinations of fluorescent markers and homology arms with or without mismatches. The upper panel shows a possible scenario in which the fluorescent marker EGFP is combined with homology arms without mismatches in the first nucleic acid molecule and the fluorescent marker dTomato is combined with homology arms with a single mismatch in the second nucleic acid molecule. Consequently, a target cell being double positive of EGFP and d Tomato will be heterozygous with one wild type allele and one mutated allele comprising a SNP. The middle panel shows a possible scenario in which the fluorescent marker EGFP is combined with homology arms without mismatches in the first nucleic acid molecule and the fluorescent marker dTomato is also combined with homology arms without mismatches in the second nucleic acid molecule. Consequently, a target cell being double positive of EGFP and dTomato will be homozygous with two wild type alleles. The lower panel shows a possible scenario in which the fluorescent marker EGFP is combined with homology arms with a single mismatch in the first nucleic acid molecule and the fluorescent marker dTomato is also combined with homology arms with a single mismatch in the second nucleic acid molecule. Consequently, a target cell being double positive of EGFP and d Tomato will be homozygous with two mutated alleles comprising a SNP.

[0066] The above described single and double integrations of one marker also applies *mutatis mutandis* to the use of one nucleic acid molecule of the invention. However, in case the nucleic acid molecule or the nucleic acid molecules comprised by the composition of matter further comprise a chemical resistance marker, the cells may be subjected to chemical selection prior to subjecting to selection for the marker indicating heterologous recombination and the marker indicating homologous recombination.

[0067] The selection process described for the *in vitro* methods of the invention may also be performed more than one time, such as 2, 3, 4, 5, 6, 7, 8, 9 or more times to further enrich the eukaryotic cell comprising the desired homologous recombination or mutation.

[0068] The term “enriching” as used herein also refers to “selecting” and “obtaining” eukaryotic cells which are modified by homologous recombination.

[0069] The term “means for selecting” as used herein refers to means which are suitable to detect the selectable marker. In case of an optically detectable marker, e.g. a fluorescent protein, such means may be but are not limited to FACS, fluorescent guided capture, e.g. colony/clone picking by detecting fluorescent colonies/clones, flow cytometry or fluorescence microscopy.

[0070] The term “transformed” or “transformation” as use herein refers to any method suitable to deliver or transport nucleic acid to the cell, such as transformation, transfection, transduction, electroporation, magnetofection, lipofection and the like, electroporation being preferred.

[0071] In a further preferred embodiment of the invention the *in vitro* method for enriching eukaryotic cells which are modified by homologous recombination further comprises (c) subjecting said enriched cells to sequencing.

[0072] The term "sequencing" as used herein refers to obtaining sequence information from a nucleic acid strand, typically by determining the identity of at least some nucleotides (including their nucleobase components) within the nucleic acid molecule. While in some embodiments, "sequencing" a given region of a nucleic acid molecule includes identifying each and every nucleotide within the region that is sequenced, in some embodiments "sequencing" comprises methods whereby the identity of only some of the nucleotides in the region is determined, while the identity of some nucleotides remains undetermined or incorrectly determined. “Sequencing” may refer to obtaining sequence information of a region or of the whole genome of the cell. Any suitable method of sequencing may be used, such as label-free or ion based sequencing methods, labeled or dye-containing nucleotide or fluorescent based nucleotide sequencing methods, or cluster-based sequencing or bridge sequencing methods.

[0073] In a further preferred embodiment of the invention the *in vitro* method for enriching eukaryotic cells which are modified by homologous recombination further comprises removing the nucleotide sequence encoding said marker indicating homologous

recombination. Said marker indicating homologous recombination is preferably removed by excision as described herein.

[0074] In another preferred embodiment the invention provides an in vitro method for producing eukaryotic cells comprising a modification in its genome introduced by homologous recombination, comprising

(a) subjecting a population of cells transformed with a nucleic acid molecule of the invention or a composition of the invention to means for selecting for said marker indicating heterologous recombination and separate transformed cells expressing said selection marker indicating heterologous recombination in said eukaryotic cell;

(b) subjecting the non-separated cells to means for selecting for said marker indicating homologous recombination in order to enrich transformed cells comprising said homologous recombination; and

(c) sequencing said enriched transformed cells in order to determine whether said enriched transformed cells comprise the desired modification.

[0075] In a further preferred embodiment of the invention the *in vitro* method for producing eukaryotic cells comprising a modification in its genome introduced by homologous recombination further comprises removing the nucleotide sequence encoding said marker indicating homologous recombination. Said marker indicating homologous recombination is preferably removed by excision as described herein.

[0076] The present invention also provides the use of a nucleic acid molecule as described herein or a composition as described herein for enriching eukaryotic cells which are modified by homologous recombination.

[0077] Furthermore, the present invention provides the use of a nucleic acid as described herein or a composition as described herein for producing eukaryotic cells comprising a modification in its genome introduced by homologous recombination.

[0078] The present invention allows to discriminate between different nucleic acid molecules of the invention, due to different selection markers, wherein the nucleic acid molecules target the same sequence of interest. The different nucleic acid molecules may further deposit different modifications into the genome of the cell. Thus a cell being positive for both markers is likely to be heterozygous with respect to the sequence of interest. Such a cell may comprise a mutation in one allele, whereas the other allele comprises the wild type nucleic acid sequence giving rise to bi-allelically targeted homozygotes and heterozygote cell populations at will. This allows the generation of cell lines which are homozygous gene

corrected edited lines, homozygous mutant genome edited lines, heterozygous mutant genome edited lines or heterozygous gene corrected edited lines which may be subcloned or used for phenotypic characterization, drug screening or cell therapy.

FIGURES

[0079] Fig. 1: Examples of nucleic acid molecules of the invention and selection process.

A) Representation of a standard donor vector containing a fluorescent positive selection module expressing EGFP or dTOMATO and a negative selection module expressing tagBFP

B) Expected outcomes for the derived population as designed with each dsDNA donor.

C) Workflow of Fluorescence Assisted Genome Editing (FAGE). Is shown the gating structure to exclude random integration tagBFP positive cells and include herozygotes-homozygotes combinations for each modification.

D) One specific genotype is sorted based on the fluorescence combination. Representative heterozygous EGFP and dTOMATO positive single cell and colonies after sorting.

E) The selected population is expanded and transfected with transposase to remove the positive selection module restoring the native structure of the locus. The polyclonal populations is sequenced optionally subcloned.

[0080] Fig. 2: Known outcomes of biallelic targeting .

Possible outcomes according to different combinations of fluorescent markers and homology arms with or without mismatches (this is without considering the silent mismatches introduced for avoiding the recognition of the nuclease). 1A) The fluorescent marker EGFP is combined with homology arms without mismatches and the fluorescent marker dTomato is combined with homology arms with a single mismatch, composition necessary for producing an heterozygous knock in of a desired mutation. 1B) The fluorescent marker EGFP is combined with homology arms without mismatches and the fluorescent marker dTomato is combined with homology arms without mismatches as well, composition necessary for producing an homozygous knock in with two wild type alleles. 1C) The fluorescent marker EGFP is combined with homology arms with a desired mismatch and the fluorescent marker dTomato is combined with homology arms with a desired mismatch as well, composition necessary for producing an homozygous knock in with two mutated alleles comprising a SNP.

[0081] Fig. 3: Further examples of nucleic acid molecules of the invention and selection process.

A) Representation of a standard donor vector containing a fluorescent positive selection module expressing EGFP or dTOMATO and a negative selection module expressing tagBFP

B) Expected outcomes for the derived population as designed with each dsDNA donor (in this case represented with a composition to produce a homozygous modification)

C) Workflow of Fluorescence Assisted Genome Editing (FAGE).

D) Gating structure to exclude random integration tagBFP positive cells and include herozygotes-homozygotes combinations for each modification.

E) One specific genotype is sorted based on the fluorescence combination. Representative heterozygous EGFP and dTOMATO positive single cell and colonies after sorting.

F) Purification step to obtain an entire population with the desired genotype, with the presence of both fluorescences

G) The selected population is expanded and transfected with transposase to remove the positive selection module restoring the native structure of the locus.

EXAMPLES

The following Examples illustrate the invention, but are not to be construed as limiting the scope of the invention.

Example 1: Designing of the donor constructs.

[0082] Desired nucleotide modifications are added into the homology arms targeting a specific sequence in the genome by site directed mutagenesis. When used CRISPR-Cas9 a point mutation in the PAM sequence is introduced. The homology arms are cloned into the donor scaffold by Gibson assembly as shown in Figure 1A and 3A. Two donor vectors are created to introduce a biallelic knock in of the donor DNA and giving rise to homozygote or heterozygote edited cells as described in Figure 1B and 3B. A fluorescent reporter (distinct from the one used in the positive selection cassette) is inserted externally to the homology arms and the positive selection cassette to exclude cells that present random integration events as shown in Figure 1A and 1C and Figure 3A and 3D.

Example 2: Cell culture conditions and transfection.

[0083] Human induced pluripotent stem cell lines derived by episomal, mRNA or retroviral methods were used. Lines were cultured on Essential 8 media (Life Technologies) on laminin 521 or 511. For electroporation and normal passage cell lines are detached with Acutase (Life Technologies). Human induced pluripotent stem cell lines were transformed with both donor vectors and nuclease coding vector with an Amaxa nucleofector 4D kit (Lonza) and plated in media containing Rho Kinase inhibitor.

Example 3: Enrichment of on target edited cells.

[0084] After electroporation cells are cultured on 0.5ug/mL of puromicyn and expanded for up to 3 days and sorted in BD ARIAII FACS. Random integration events are evidenced by the expression of the negative selection reporter tagBFP and are discarded (Figure 1C and Figure 3D). Based on the fluorescent pattern, only the population presenting biallelic integration of both positive selection modules is selected by FACS or microscopy guided capture of the cells (Figure 1D and 1E and Figure 3E and 3F).

Example 4: Removal of the positive selection cassette and QC.

[0085] Homogeneous biallelic populations coexpressing both positive selection module reporters are transfected with IVT mRNA (Applied Biosystems) coding codon optimized hyper transposase using Stemfect (Stemgent) according to manufacturer instruction. Two days after transfection the cells are sorted in BD ARIAII for the removal of the fluorescent reporters indicative of the excision of the positive selection module and restoration of the endogenous locus. The quality of homogenously edited polyclonal population is assessed by MiSeq deep sequencing including the analysis of nuclease off targets and random integration.

Example 5: Knock in of Parkinson disease associated SNPs using FAGE.

[0086] Parkinson disease is a multifactorial neurodegenerative disorder with a limited number of mendelian linked genetic variants. Parkinson patients with mutations in the alpha synuclein gene carry the heterozygote mutations A30P, A53T, E46K, G51D or H50Q. Fast enrichment of the desired populations was achieved by the use of two donors containing the fluorescent protein EGFP or dTOMATO and a drug selection resistant gene (Figure 1A and Figure 3A). In order to load the genotypic combinations into wild type human induced pluripotent stem cell (hiPSC) lines for SNCA (Figure 1B and Figure 3B) dsDNA donors were used. In order to enhance the homology directed repair (HDR) efficiency and decrease the rate of random integration any repetitive element was excluded from the homology arms used in the dsDNA donors. Random integration events were excluded by the selection of tagBFP negative cells (Figure 1A and 1C and Figure 3A and 3D). The efficiency of biallelic knock in for SNCA was 5%. Stepwise enrichment of the double positive population ranged 5%-10% in the first sorting, 95-98 in the second to 99.9-99.9% in the third for all the mutants analyzed.

Example 6: Enrichment of bi-allele targeted cells

The positive selection module coupled to fluorescent protein markers allows the genotyping by FACS or fluorescence microscopy for the enrichment or fluorescence guided capture of gene edited lines (such as, homozygous gene corrected edited lines, homozygous mutant genome edited lines, heterozygous mutant genome edited lines and heterozygous gene corrected edited lines but not exclusively).

By the use of double stranded DNA donors (nucleic acid molecules of the invention) with homology arms carrying both (homozygous) or only one (heterozygous) specific sequence and positive selection cassettes containing fluorescent selection modules, the enrichment of

gene corrected lines from a population of genome targeted cells is possible based on the fluorescence expression pattern. Examples for editing specific disease patient lines or for creating isogenic control lines for in vitro disease modelling are mentioned below.

Enrichment of non-random integration edited lines

By the use of a fluorescent reporter or a chemical selection located in a different area of the positive selection cassette of the donor, enrichment of cells not carrying this reporter will be avoided since the fluorescent positive cells in this case represent incorrect gene edited lines.

Enrichment of homozygous gene edited lines.

By the use of double stranded DNA donors with homology arms carrying both a specific sequence and positive selection cassette containing fluorescent selection modules, the enrichment of gene corrected lines from a population of genome targeted cells is possible based on the fluorescence expression pattern.

Enrichment of homozygous gene corrected edited lines.

By the use of double stranded DNA donors with homology arms carrying wild type alleles and positive selection cassette containing fluorescent selection modules, the enrichment of gene corrected lines from a population of genome targeted cells is possible based on the fluorescence expression pattern.

Enrichment of heterozygous gene edited lines.

By the use of double stranded DNA donors with homology arms carrying different specific sequences and positive selection cassette containing fluorescent selection modules, the enrichment of gene corrected lines from a population of genome targeted cells is possible based on the fluorescence expression pattern.

Enrichment of heterozygous mutant genome edited lines.

By the use of double stranded DNA donors with homology arms carrying one of them a mutant allele and the other a wild type allele and both carrying positive selection cassette containing fluorescent selection modules the enrichment of gene heterozygote mutant lines from a population of genome targeted cells is possible based on the fluorescence expression pattern.

Enrichment of homozygous mutant genome edited lines

By the use of double stranded DNA donors with homology arms carrying mutant alleles and positive selection cassette containing fluorescent selection modules the enrichment of gene homozygous mutant lines from a population of genome targeted cells is possible based on the fluorescence expression pattern.

ITEMS

1. A nucleic acid molecule comprising at least one nucleotide sequence encoding a selection marker indicating homologous recombination when integrated in the sequence of interest comprised in a eukaryotic cell and at least one nucleotide sequence encoding a selection marker indicating heterologous recombination when not integrated in the sequence of interest comprised in said eukaryotic cell, wherein the selection markers when being expressed are optically discriminable, e.g. in FACS or any fluorescence guided capture, and wherein the nucleotide sequence encoding a selection marker indicating homologous recombination in a eukaryotic cell is flanked 5' and 3' by nucleotide sequences that are homologous to nucleotide sequences of a nucleic acid sequence of interest comprised by the eukaryotic cell.

2. The nucleic acid molecule of item 1, wherein said nucleic acid sequence of interest comprised by said eukaryotic cell is in the genome of said eukaryotic cell.

3. The nucleic acid molecule of any one of the preceding items, wherein said nucleotide sequence encoding a selection marker indicating homologous recombination and said selection marker indicating heterologous recombination comprises a promoter driving expression of said selection markers.

4. The nucleic acid molecule of item 3, wherein said promoter is constitutive or inducible.

5. The nucleic acid molecule of any one of the preceding items, wherein said nucleotide sequence encoding a selection marker indicating homologous recombination comprises 5' and 3' nucleotide sequences which allow excision of said nucleotide sequence encoding said selection marker.

6. The nucleic acid molecule of item 5, wherein said nucleotide sequences which allow excision of said nucleotide sequence encoding said selection marker are selected from loxP sequences, derivatives of loxP sequences, such as Lox511, Lox5171, Lox2272, M2, M3, M7, M11, Lox71 or Lox66 sequences, Cre recombinase binding sites, FRT sequences, derivatives of FRT sequences, such as FRT-G, FRT-H or FRT-F3, FLP recombinase binding sites, terminal repeats, transposase binding sites, derivatives of transposase binding sites, such as terminal repeats, internal terminal repeats, direct repeats, inverted repeats or palindromic repeats, piggybac transposon binding sites, sleeping beauty transposon binding sites, piggybat binding sites, binding site of transposons fused to estrogen receptor, estrogen binding sites or mutational derivatives, binding site of transposons fused to estrogen receptor tamoxifen binding sites, RNA-guided nuclease binding site, Cas9 binding sites, Cpf

binding site, nuclease binding sites, TALEN-Fok1 binding sites, zinc finger binding sites or RNA-guided nuclease binding sites.

7. The nucleic acid molecule of any one of the preceding items, wherein said nucleic acid molecule comprises a chemical resistance selection marker selected from neomycin resistance, hygromycin resistance, HPRT1, puromycin resistance, puromycin N-acetyl-transferase, blasticidin resistance, G418 resistance, phleomycin resistance, nourseothricin resistance or chloramphenicol resistance.

8. The nucleic acid molecule of item 7, wherein said chemical resistance selection marker is associated or not associated with said selection marker indicating homologous recombination.

9. The nucleic acid molecule of any one of the preceding items, wherein said nucleotide sequences that are homologous to nucleotide sequences of a nucleic acid sequence of interest comprised by said eukaryotic cell allow homologous recombination with nucleotide sequences of a nucleic acid sequence of interest comprised by said eukaryotic cell.

10. The nucleic acid molecule of item 9, wherein homologous recombination allows depositing a modification into the genome, said modification is selected from a single nucleotide polymorphism, phosphomimetic mutation, phospho null mutation, missense mutation, nonsense mutation, synonymous mutation, insertion, deletion, knock-out or knock-in.

11. The nucleic acid molecule of item 9 or 10, wherein homologous recombination occurs at one allele or at both alleles of said nucleic acid sequence of interest comprised by said eukaryotic cell.

12. The nucleic acid molecule of any one of the preceding items, wherein homologous recombination is induced by TALENs, ZFNs, meganucleases, or CRISPR/Cas.

13. The nucleic acid molecule of item 12, wherein said nucleotide sequences that are homologous to nucleotide sequences of a nucleic acid sequence of interest comprised by said eukaryotic cell do not comprise a target sequence for TALENs, ZFNs, meganucleases, or CRISPR/Cas which mediate homologous recombination.

14. The nucleic acid molecule of any one of the preceding items, wherein said nucleic acid molecule is a vector.

15. The nucleic acid molecule of item 14, wherein said vector is circular or linearized.

16. The nucleic acid molecule of any one of the preceding items, wherein said optical discriminability is different emission wavelength.

17. The nucleic acid molecule of any one of the preceding items, wherein said selection marker indicating homologous recombination and said selection marker indicating heterologous recombination is a fluorescent protein.

18. The nucleic acid molecule of item 17, wherein said fluorescent protein is selected from Sirius, SBFP2, Azurite, EBFP2, mKalama1, mTagBFP2, Aquamarine, ECFP, Cerulean, mCerulean3, SCFP3A, mTurquoise2, CyPet, AmCyan1, mTFP1, MiCy, iLOV, AcGFP1, sfGFP, mEmerald, EGFP, mAzamiGreen, cfSGFP2, ZsGreen, mWasabi, SGFP2, Clover, mClover2, EYFP, mTopaz, mVenus, SYFP2, mCitrine, YPet, ZsYellow1, mPapaya1, mKO, mOrange, mOrange2, mKO2, TurboRFP, mRuby2, eqFP611, DsRed2, mApple, mStrawberry, FusionRed, mRFP1, mCherry, mCherry2, dTOMATO, tdTOMATO, tagBFP, photoactivatable or photoswitchable fluorescent protein.

19. A composition of matter comprising a mixture of at least two different nucleic acid molecules of any one of items 1 to 18, each comprising a different nucleotide sequence encoding a selection marker indicating homologous recombination in said eukaryotic cell.

20. An *in vitro* method for enriching eukaryotic cells which are modified by homologous recombination, comprising

    (a) subjecting a population of cells transformed with a nucleic acid molecule of any one of items 1 to 18 or a composition of item 19 to means for selecting for said marker indicating heterologous recombination and separate transformed cells expressing said selection marker indicating heterologous recombination in said eukaryotic cell; and

    (b) subjecting the non-separated cells to means for selecting for said marker indicating homologous recombination in order to enrich transformed cells comprising said homologous recombination.

21. The method of item 20, further comprising (c) subjecting said enriched cells to sequencing.

22. The method of item 20 or 21, further comprising removing the nucleotide sequence encoding said marker indicating homologous recombination.

23. An *in vitro* method for producing eukaryotic cells comprising a modification in its genome introduced by homologous recombination, comprising

    (a) subjecting a population of cells transformed with a nucleic acid molecule of any one of items 1 to 18 or a composition of item 19 to means for selecting for

said marker indicating heterologous recombination and separate transformed cells expressing said selection marker indicating heterologous recombination in said eukaryotic cell;

(b) subjecting the non-separated cells to means for selecting for said marker indicating homologous recombination in order to enrich transformed cells comprising said homologous recombination; and

(c) sequencing said enriched transformed cells in order to determine whether said enriched transformed cells comprise the desired modification.

24. The method of item 23, further comprising removing the nucleotide sequence encoding said marker indicating homologous recombination.

25. Use of a nucleic acid molecule of any one of items 1 to 18 or a composition of item 19 for enriching eukaryotic cells which are modified by homologous recombination.

26. Use of a nucleic acid molecule of any one of items 1 to 18 or a composition of item 19 for producing eukaryotic cells comprising a modification in its genome introduced by homologous recombination.

CLAIMS

1. A composition of matter comprising a mixture of at least two different nucleic acid molecules, each nucleic acid molecule comprising at least one nucleotide sequence encoding a selection marker indicating homologous recombination when integrated in the sequence of interest comprised in a eukaryotic cell and at least one nucleotide sequence encoding a selection marker indicating heterologous recombination when not integrated in the sequence of interest comprised in said eukaryotic cell, wherein the selection markers when being expressed are optically discriminable, e.g. in FACS or any fluorescence guided capture, and wherein the nucleotide sequence encoding a selection marker indicating homologous recombination in a eukaryotic cell is flanked 5' and 3' by nucleotide sequences that are homologous to nucleotide sequences of a nucleic acid sequence of interest comprised by the eukaryotic cell, each of the at least two different nucleic acid molecules comprising a different nucleotide sequence encoding a selection marker indicating homologous recombination in said eukaryotic cell.

2. The composition of claim 1, wherein said nucleic acid sequence of interest comprised by said eukaryotic cell is in the genome of said eukaryotic cell.

3. The composition of any one of the preceding claims, wherein said nucleotide sequence encoding a selection marker indicating homologous recombination and said selection marker indicating heterologous recombination each comprises a promoter driving expression of said selection markers.

4. The composition of claim 3, wherein said promoter is constitutive or inducible.

5. The composition of any one of the preceding claims, wherein said nucleotide sequence encoding a selection marker indicating homologous recombination comprises 5' and 3' nucleotide sequences which allow excision of said nucleotide sequence encoding said selection marker.

6. The composition of claim 5, wherein said nucleotide sequences which allow excision of said nucleotide sequence encoding said selection marker are selected from loxP sequences, derivatives of loxP sequences, such as Lox511, Lox5171, Lox2272, M2, M3, M7, M11, Lox71 or Lox66 sequences, Cre recombinase binding sites, FRT sequences, derivatives of FRT sequences, such as FRT-G, FRT-H or FRT-F3, FLP recombinase binding sites, terminal repeats, transposase binding sites, derivatives of transposase binding sites, such as terminal repeats, internal terminal repeats, direct repeats, inverted repeats or palindromic repeats, piggybac transposon binding sites,

sleeping beauty transposon binding sites, piggybat binding sites, binding site of transposons fused to estrogen receptor, estrogen binding sites or mutational derivatives, binding site of transposons fused to estrogen receptor tamoxifen binding sites, RNA-guided nuclease binding site, Cas9 binding sites, Cpf binding site, nuclease binding sites, TALEN-Fok1 binding sites, zinc finger binding sites or RNA-guided nuclease binding sites.

7. The composition of any one of the preceding claims, wherein said nucleic acid molecule comprises a chemical resistance selection marker selected from neomycin resistance, hygromycin resistance, HPRT1, puromycin resistance, puromycin N-acetyl-transferase, blasticidin resistance, G418 resistance, phleomycin resistance, nourseothricin resistance or chloramphenicol resistance.

8. The composition of claim 7, wherein said chemical resistance selection marker is associated or not associated with said selection marker indicating homologous recombination.

9. The composition of any one of the preceding claims, wherein said nucleotide sequences that are homologous to nucleotide sequences of a nucleic acid sequence of interest comprised by said eukaryotic cell allow homologous recombination with nucleotide sequences of a nucleic acid sequence of interest comprised by said eukaryotic cell.

10. The composition of claim 9, wherein homologous recombination allows depositing a modification into the genome, said modification is selected from a single nucleotide polymorphism, phosphomimetic mutation, phospho null mutation, missense mutation, nonsense mutation, synonymous mutation, insertion, deletion, knock-out or knock-in.

11. The composition of claim 9 or 10, wherein homologous recombination occurs at one allele or at both alleles of said nucleic acid sequence of interest comprised by said eukaryotic cell.

12. The composition of any one of the preceding claims, wherein homologous recombination is induced by TALENs, ZFNs, meganucleases, or CRISPR/Cas.

13. The composition of matter of claim 12, wherein said nucleotide sequences that are homologous to nucleotide sequences of a nucleic acid sequence of interest comprised by said eukaryotic cell do not comprise a target sequence for TALENs, ZFNs, meganucleases, or CRISPR/Cas which mediate homologous recombination.

14. The composition of any one of the preceding claims, wherein said nucleic acid molecule is a vector.

15. The composition of claim 14, wherein said vector is circular or linearized.

16. The composition of any one of the preceding claims, wherein said optical discriminability is different emission wavelength.

17. The composition of any one of the preceding claims, wherein said selection marker indicating homologous recombination and said selection marker indicating heterologous recombination is a fluorescent protein.

18. The composition of claim 17, wherein said fluorescent protein is selected from Sirius, SBFP2, Azurite, EBFP2, mKalama1, mTagBFP2, Aquamarine, ECFP, Cerulean, mCerulean3, SCFP3A, mTurquoise2, CyPet, AmCyan1, mTFP1, MiCy, iLOV, AcGFP1, sfGFP, mEmerald, EGFP, mAzamiGreen, cfSGFP2, ZsGreen, mWasabi, SGFP2, Clover, mClover2, EYFP, mTopaz, mVenus, SYFP2, mCitrine, YPet, ZsYellow1, mPapaya1, mKO, mOrange, mOrange2, mKO2, TurboRFP, mRuby2, eqFP611, DsRed2, mApple, mStrawberry, FusionRed, mRFP1, mCherry, mCherry2, dTOMATO, tdTOMATO, tagBFP, photoactivatable or photoswitchable fluorescent protein.

19. An *in vitro* method for enriching eukaryotic cells which are modified by homologous recombination, comprising

    (a) subjecting a population of cells transformed with a composition of any one of claims 1 to 18 to means for selecting for said marker indicating heterologous recombination and separate transformed cells expressing said selection marker indicating heterologous recombination in said eukaryotic cell; and

    (b) subjecting the non-separated cells to means for selecting for said marker indicating homologous recombination in order to enrich transformed cells comprising said homologous recombination.

20. The method of claim 19, further comprising (c) subjecting said enriched cells to sequencing.

21. The method of claim 19 or 20, further comprising removing the nucleotide sequence encoding said marker indicating homologous recombination.

22. An *in vitro* method for producing eukaryotic cells comprising a modification in its genome introduced by homologous recombination, comprising

    (a) subjecting a population of cells transformed with a composition of any one of claims 1 to 18 to means for selecting for said marker indicating heterologous recombination and separate transformed cells expressing said selection marker indicating heterologous recombination in said eukaryotic cell;

(b) subjecting the non-separated cells to means for selecting for said marker indicating homologous recombination in order to enrich transformed cells comprising said homologous recombination; and

(c) sequencing said enriched transformed cells in order to determine whether said enriched transformed cells comprise the desired modification.

23. The method of claim 22, further comprising removing the nucleotide sequence encoding said marker indicating homologous recombination.

24. Use of a composition of any one of claims 1 to 18 for enriching eukaryotic cells which are modified by homologous recombination.

25. Use of a composition of any one of claims 1 to 18 for producing eukaryotic cells comprising a modification in its genome introduced by homologous recombination.

1 / 11

Figure 1

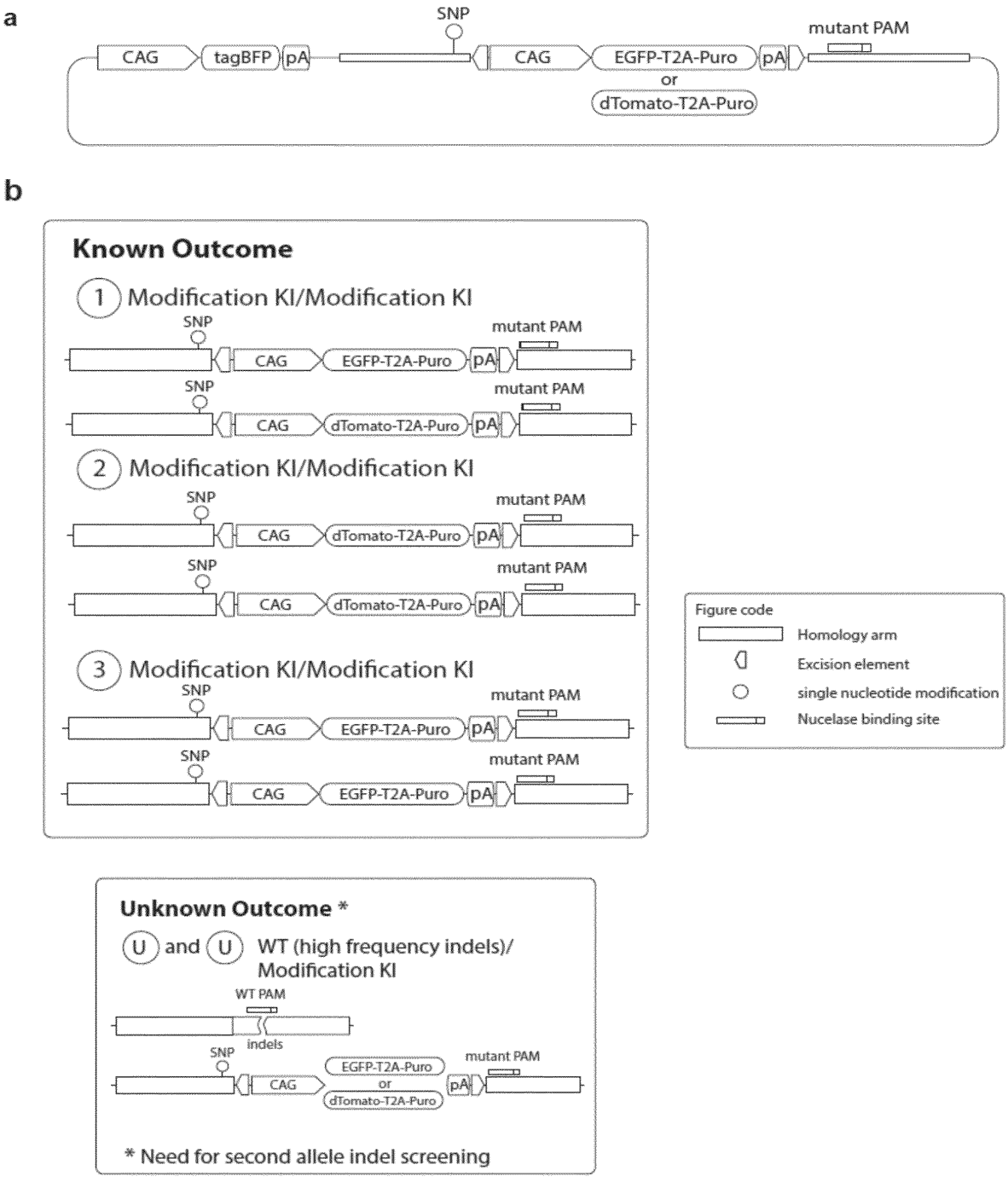

SUBSTITUTE SHEET (RULE 26)

Figure 1 (cont'd)

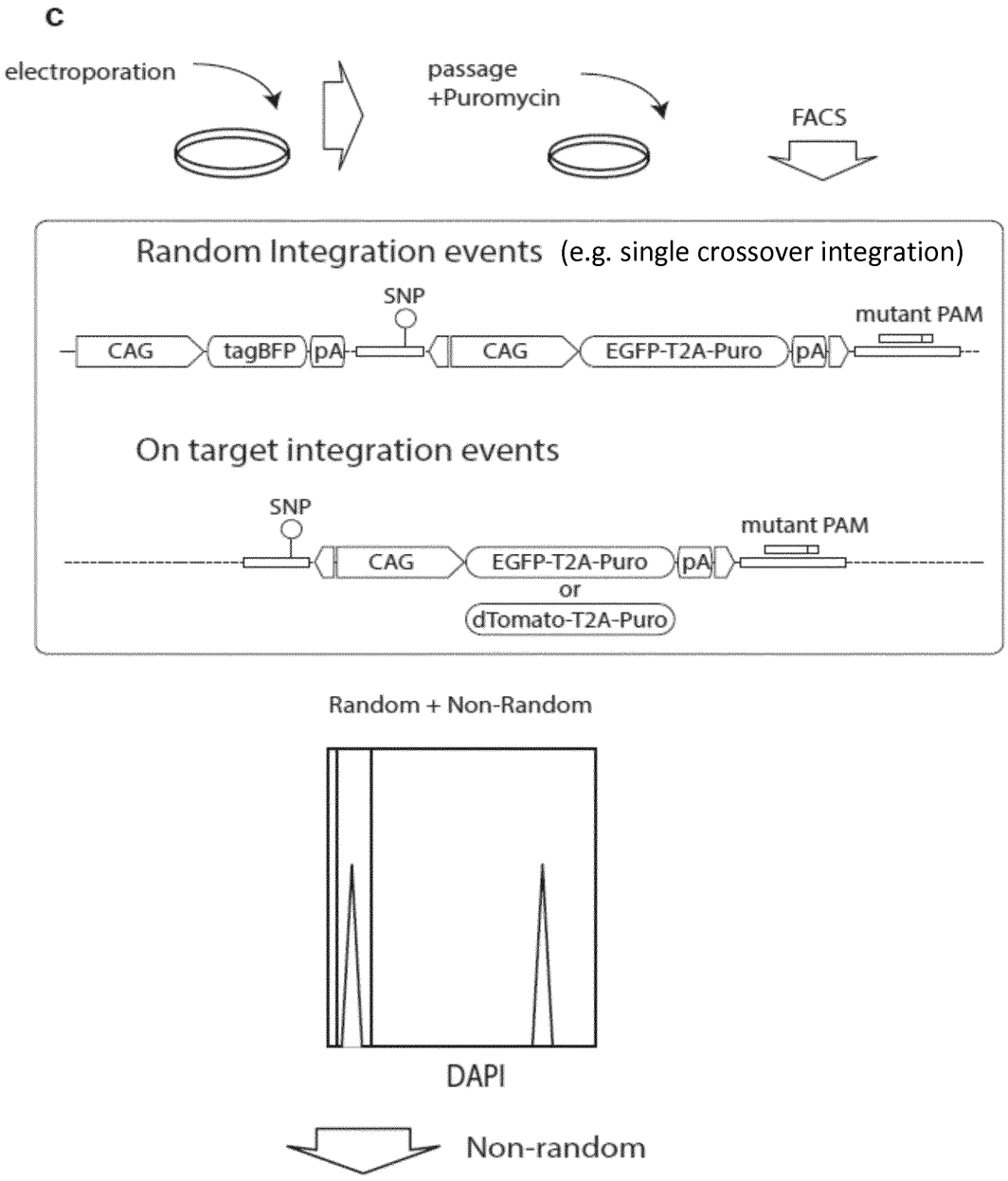

3 / 11

Figure 1 (con t'd)

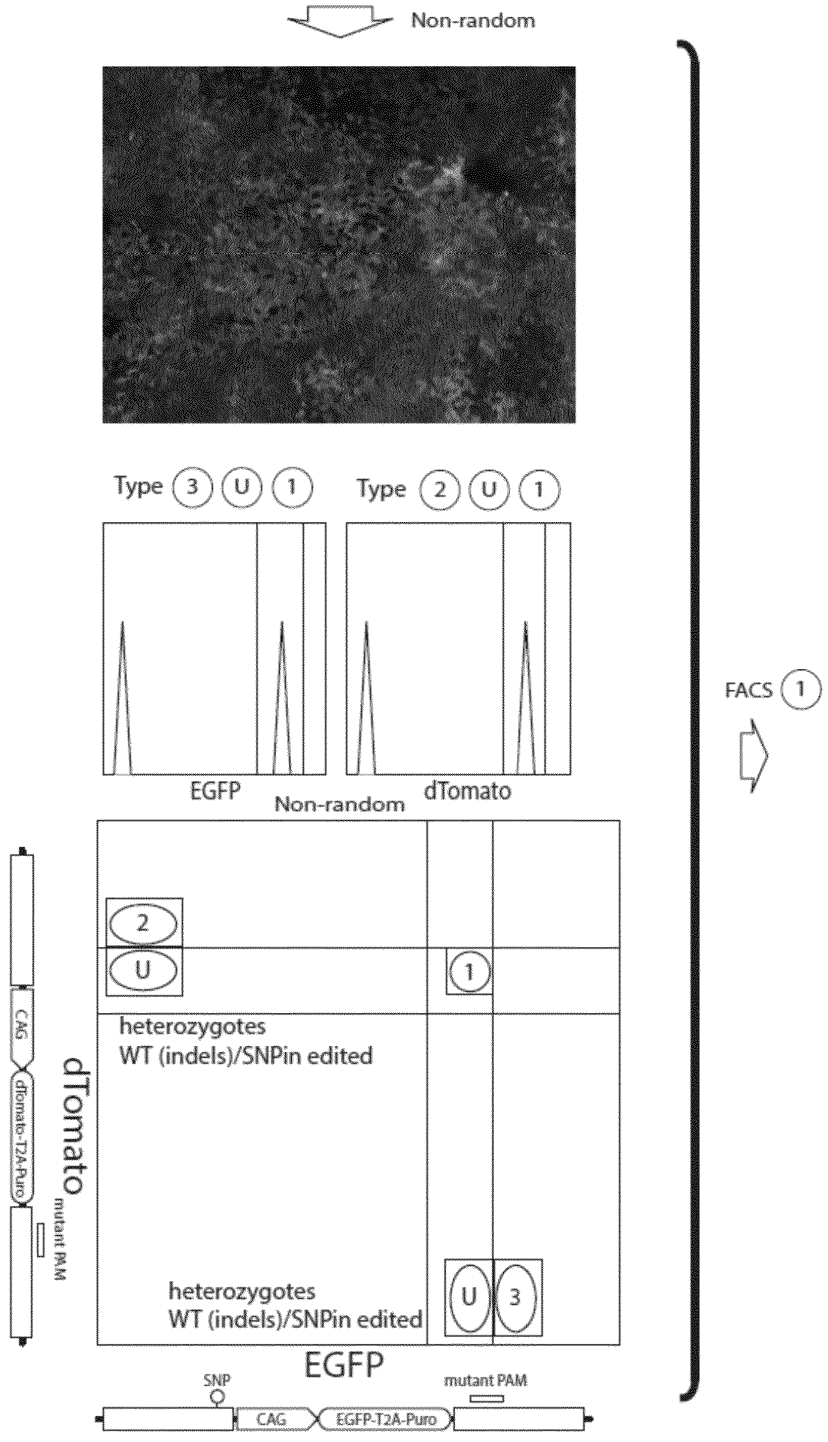

SUBSTITUTE SHEET (RULE 26)

Figure 1 (con t'd)

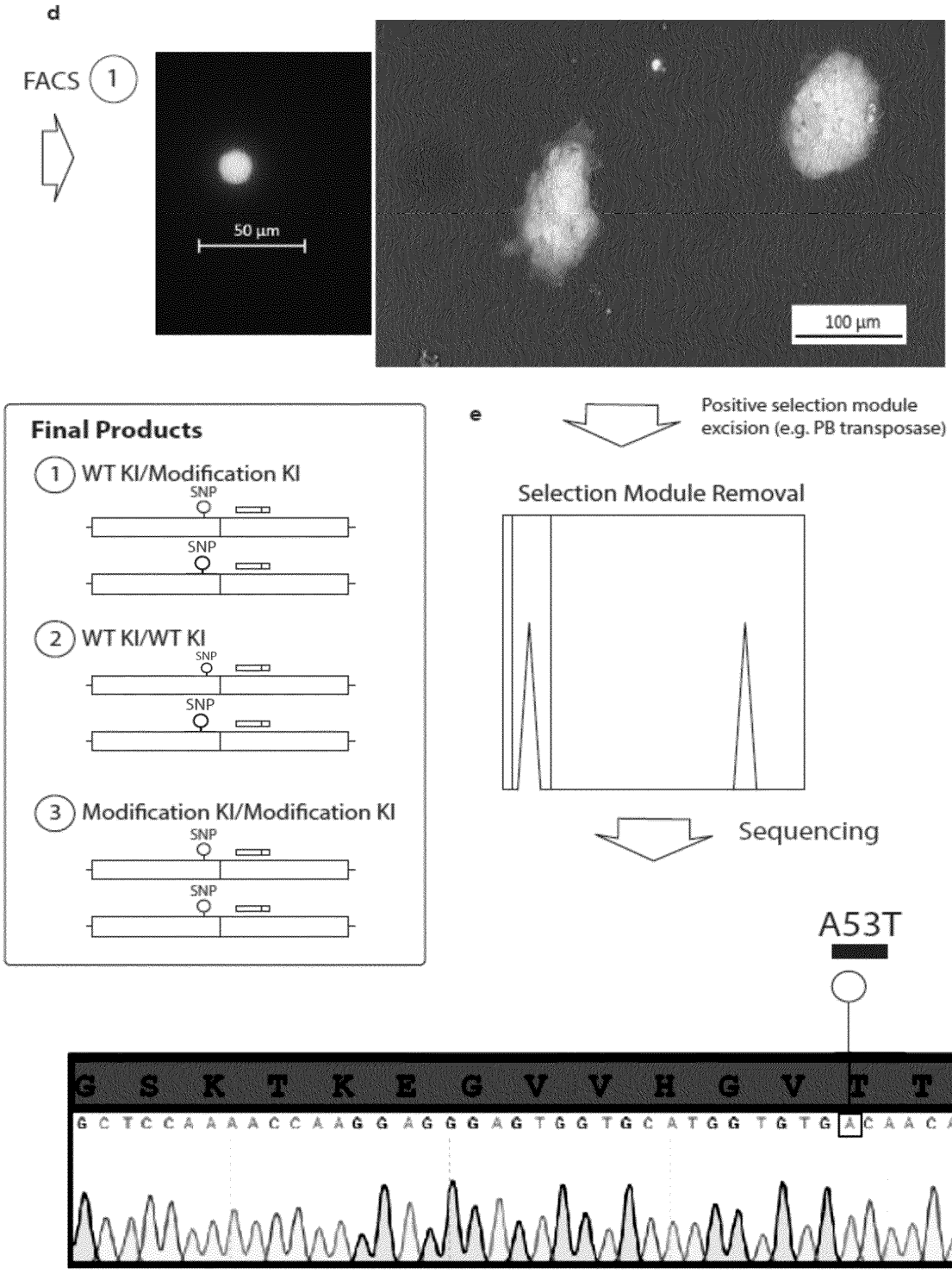

Figure 2

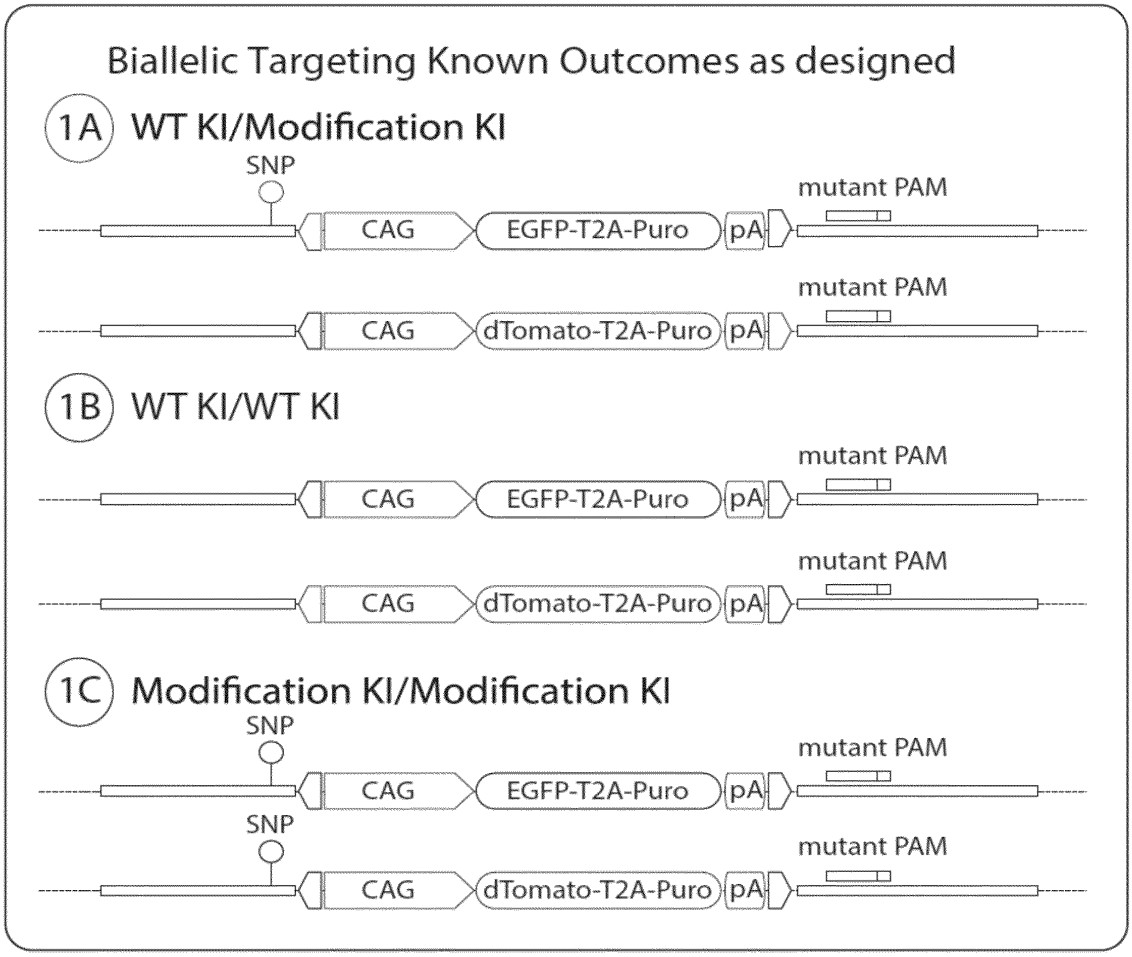
Biallelic Targeting Known Outcomes as designed
1A WT KI/Modification KI
SNP
mutant PAM
CAG
EGFP-T2A-Puro
pA
mutant PAM
CAG
dTomato-T2A-Puro
pA
1B WT KI/WT KI
mutant PAM
CAG
EGFP-T2A-Puro
pA
mutant PAM
CAG
dTomato-T2A-Puro
pA
1C Modification KI/Modification KI
SNP
mutant PAM
CAG
EGFP-T2A-Puro
pA
SNP
mutant PAM
CAG
dTomato-T2A-Puro
pA

6 / 11

Figure 3

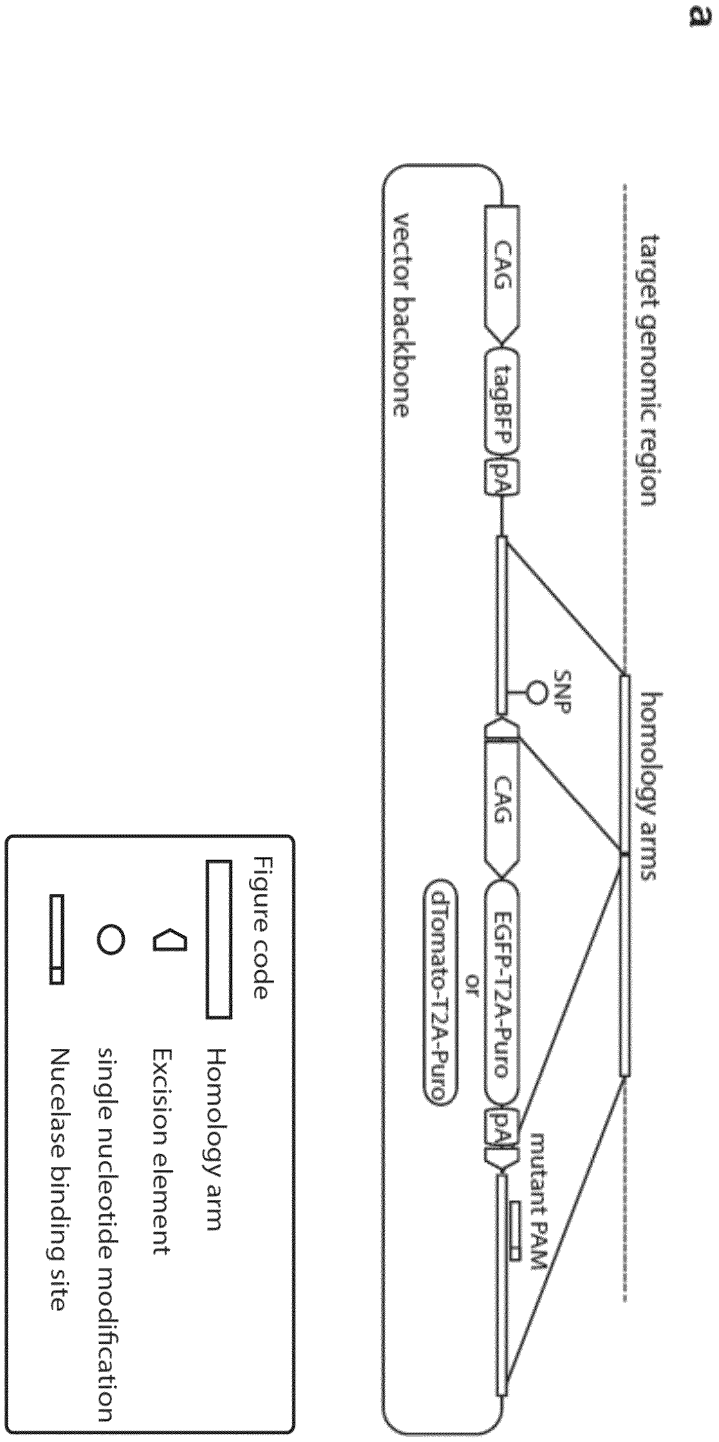
a
target genomic region
homology arms
vector backbone
CAG
tagBFP
pA
SNP
CAG
EGFP-T2A-Puro
or
dTomato-T2A-Puro
pA
mutant PAM
Figure code
Homology arm
Excision element
single nucleotide modification
Nuclease binding site

Figure 3 (con t'd)

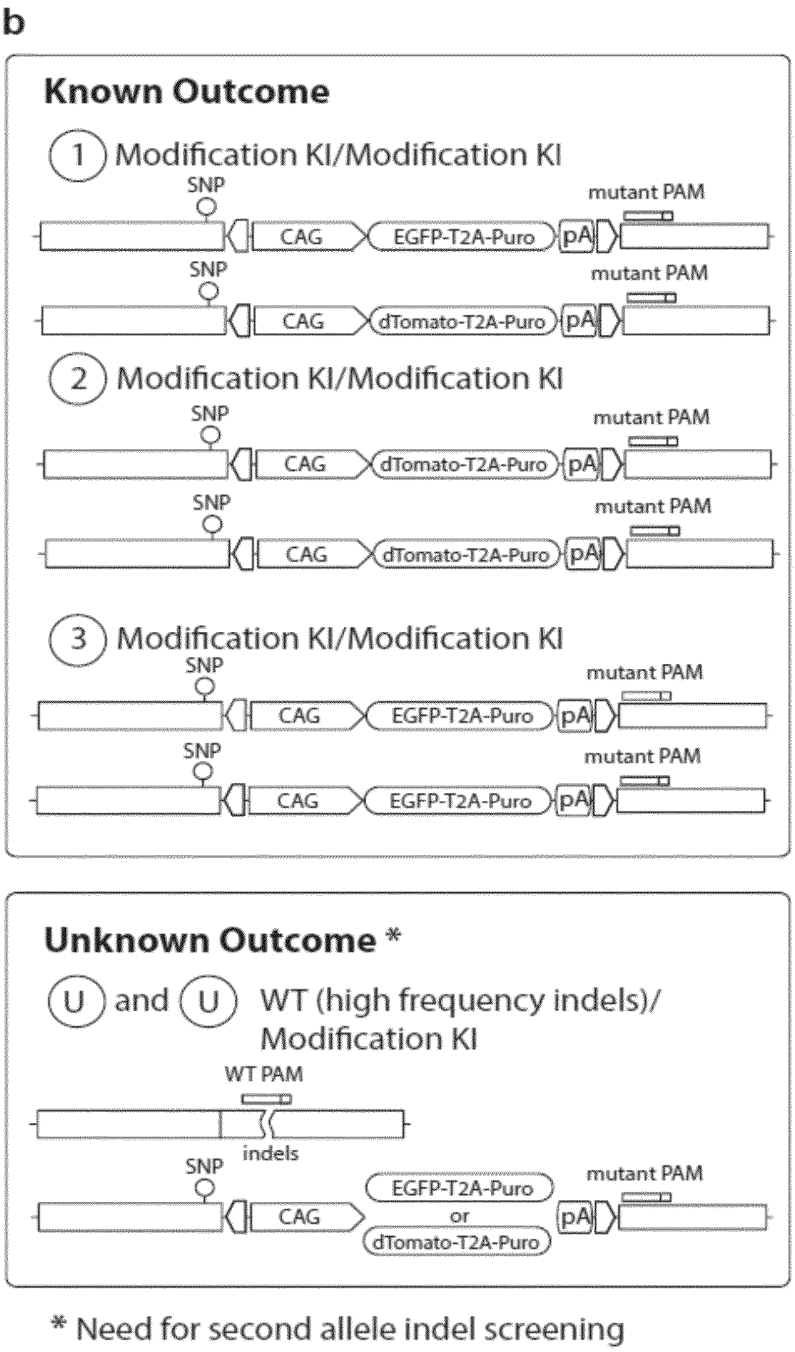

8 / 11

Figure 3 (con t'd)

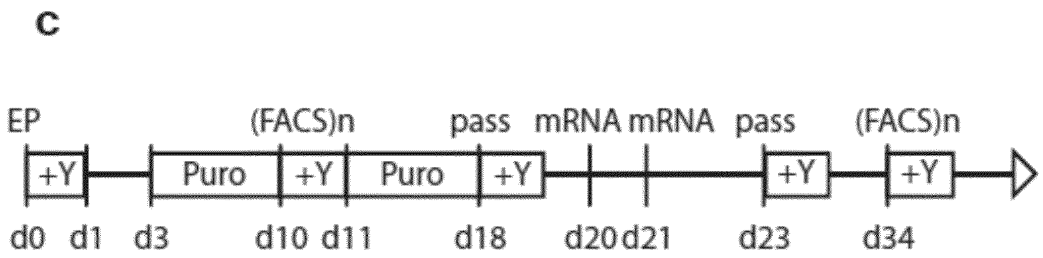

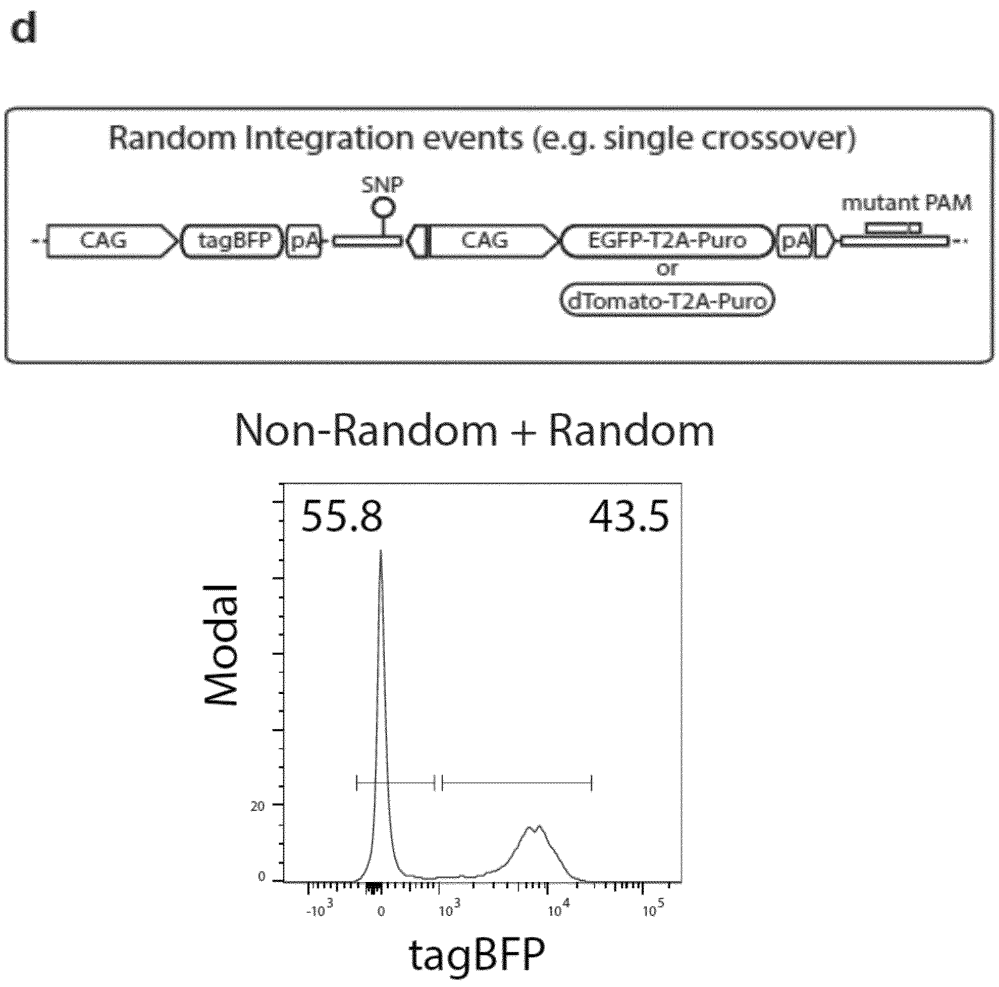

SUBSTITUTE SHEET (RULE 26)

Figure 3 (con t'd)

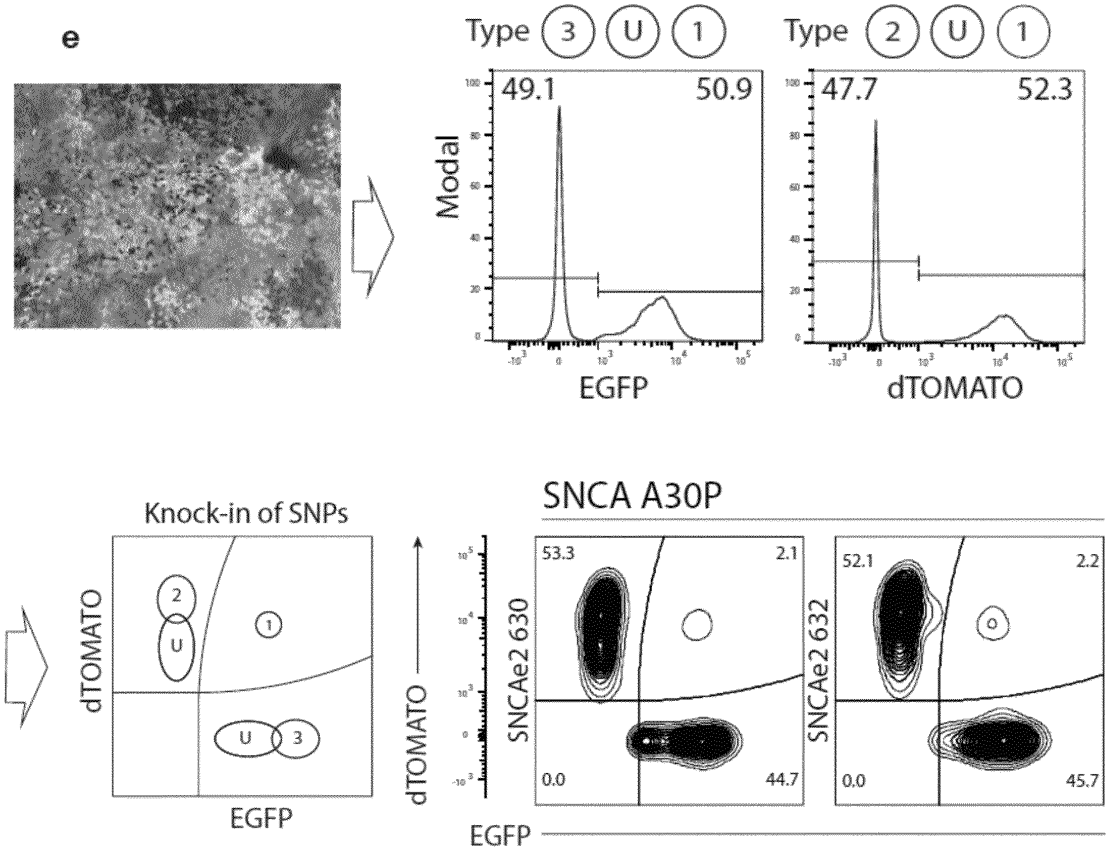

Figure 3 (con t'd)

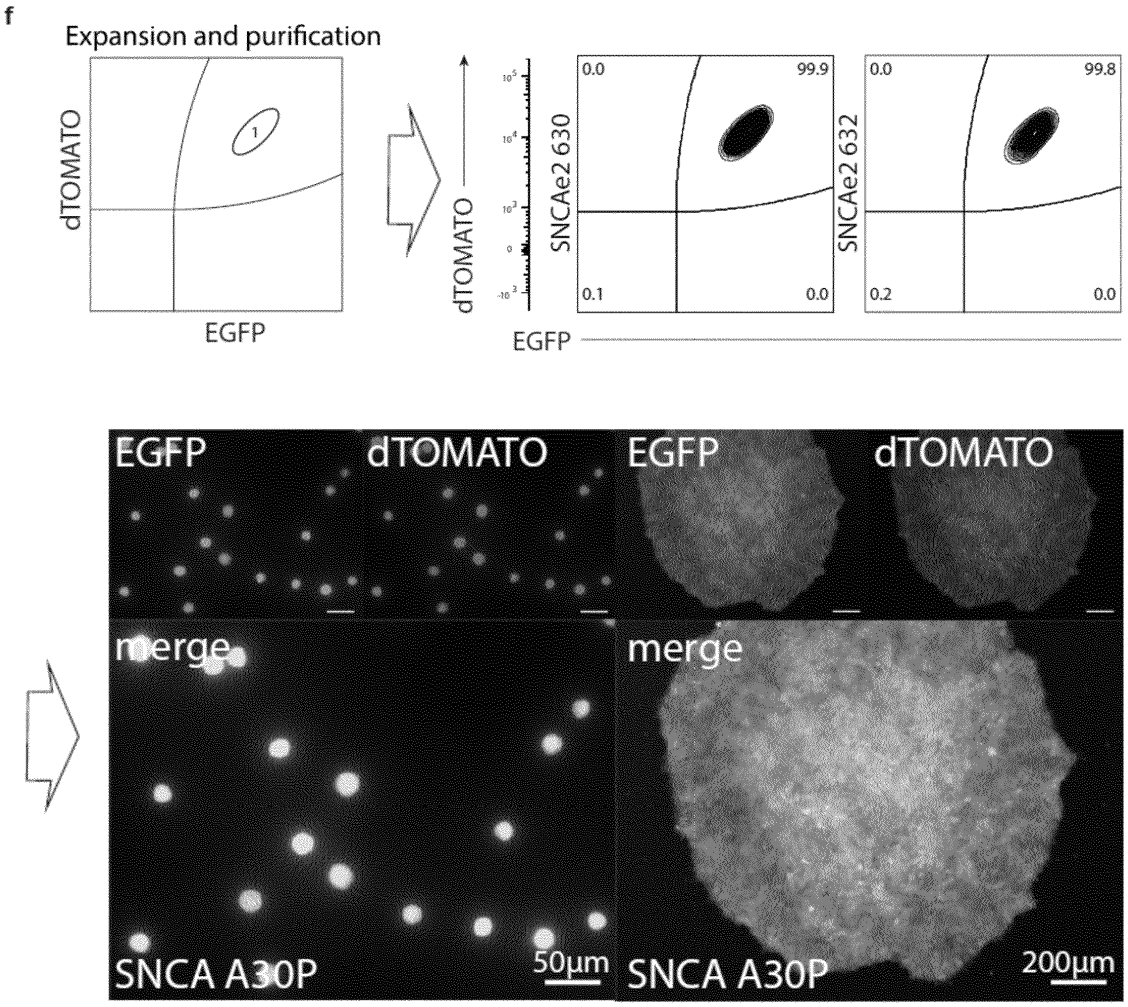

11 / 11

Figure 3 (con t'd)

g

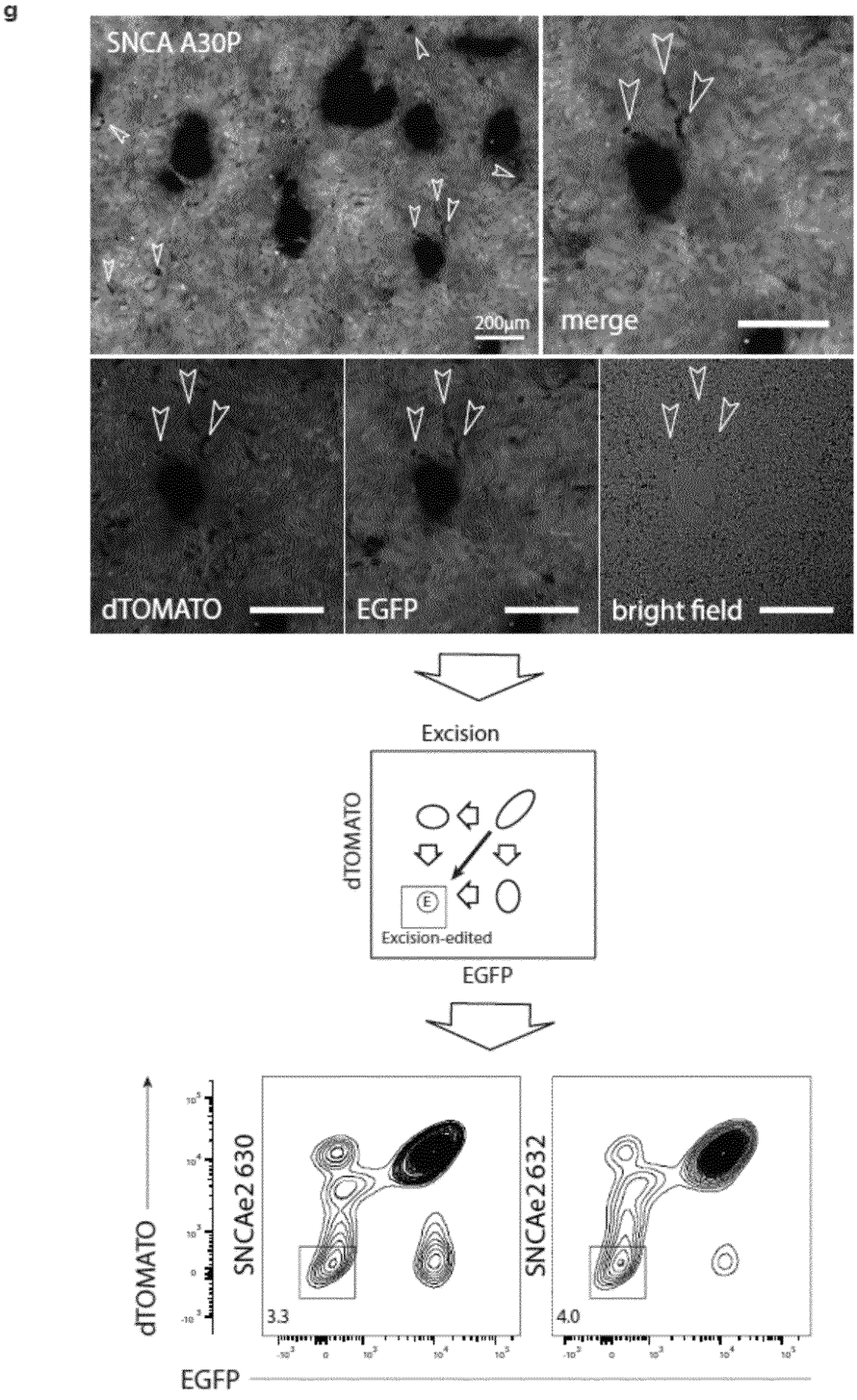

SUBSTITUTE SHEET (RULE 26)

INTERNATIONAL SEARCH REPORT

International application No
PCT/EP2017/051889

A. CLASSIFICATION OF SUBJECT MATTER
INV. C12N15/65 C12N15/90
ADD.

According to International Patent Classification (IPC) or to both national classification and IPC

B. FIELDS SEARCHED

Minimum documentation searched (classification system followed by classification symbols)
C12N

Documentation searched other than minimum documentation to the extent that such documents are included in the fields searched

Electronic data base consulted during the international search (name of data base and, where practicable, search terms used)
EPO-Internal, BIOSIS, EMBASE, WPI Data

C. DOCUMENTS CONSIDERED TO BE RELEVANT

Category*	Citation of document, with indication, where appropriate, of the relevant passages	Relevant to claim No.
X	US 2005/118648 A1 (LI LIMIN [US]) 2 June 2005 (2005-06-02) Whole doc., in partic. para. [0009-0017], Fig.1, 5 -----	1-25
X	CN 1 647 624 A (UNIV ZHONGSHAN [CN]) 3 August 2005 (2005-08-03) Whole doc., in partic. Fig.3 -----	1-25
X	MANDAR DEEPAK MUZUMDAR ET AL: "A global double-fluorescent Cre reporter mouse", GENESIS, vol. 45, no. 9, 1 September 2007 (2007-09-01), pages 593-605, XP055011399, ISSN: 1526-954X, DOI: 10.1002/dvg.20335 Whole doc., in partic. p.598 onwards; Fig.1 -----	1-25
	-/--	

[X] Further documents are listed in the continuation of Box C. [X] See patent family annex.

* Special categories of cited documents :

"A" document defining the general state of the art which is not considered to be of particular relevance

"E" earlier application or patent but published on or after the international filing date

"L" document which may throw doubts on priority claim(s) or which is cited to establish the publication date of another citation or other special reason (as specified)

"O" document referring to an oral disclosure, use, exhibition or other means

"P" document published prior to the international filing date but later than the priority date claimed

"T" later document published after the international filing date or priority date and not in conflict with the application but cited to understand the principle or theory underlying the invention

"X" document of particular relevance; the claimed invention cannot be considered novel or cannot be considered to involve an inventive step when the document is taken alone

"Y" document of particular relevance; the claimed invention cannot be considered to involve an inventive step when the document is combined with one or more other such documents, such combination being obvious to a person skilled in the art

"&" document member of the same patent family

Date of the actual completion of the international search	Date of mailing of the international search report
3 March 2017	13/03/2017

Name and mailing address of the ISA/	Authorized officer
European Patent Office, P.B. 5818 Patentlaan 2 NL - 2280 HV Rijswijk Tel. (+31-70) 340-2040, Fax: (+31-70) 340-3016	Roscoe, Richard

1

Form PCT/ISA/210 (second sheet) (April 2005)

page 1 of 2

INTERNATIONAL SEARCH REPORT

International application No
PCT/EP2017/051889

C(Continuation). DOCUMENTS CONSIDERED TO BE RELEVANT

Category*	Citation of document, with indication, where appropriate, of the relevant passages	Relevant to claim No.
A	US 7 402 728 B2 (CHAN ANDREW C [US] ET AL) 22 July 2008 (2008-07-22) Whole doc., in partic. col.16	1-25
A	LEI SHI ET AL: "Combination of FACS and Homologous Recombination for the Generation of Stable and High-Expression Engineered Cell Lines", PLOS ONE, vol. 9, no. 3, 19 March 2014 (2014-03-19), page e91712, XP055279563, DOI: 10.1371/journal.pone.0091712 the whole document	1-25
A	ERIKA A O'DONNELL ET AL: "Multiparameter Flow Cytometry: Advances in High Resolution Analysis", IMMUNE NETWORK, vol. 13, no. 2, 1 January 2013 (2013-01-01), page 43, XP055351323, ISSN: 1598-2629, DOI: 10.4110/in.2013.13.2.43 sentence spanning p.50-51	1-25
A	WANG YANLIANG ET AL: "Highly efficient generation of biallelic reporter gene knock-in mice via CRISPR-mediated genome editing of ESCs", PROTEIN & CELL, SPRINGER ASIA, BEIJING, CN, vol. 7, no. 2, 10 December 2015 (2015-12-10), pages 152-156, XP035966463, ISSN: 1674-800X, DOI: 10.1007/S13238-015-0228-3 [retrieved on 2015-12-10] p.154, col.2, sentence starting 10 lines from bottom.	1-25

1

Form PCT/ISA/210 (continuation of second sheet) (April 2005)

page 2 of 2

INTERNATIONAL SEARCH REPORT

Information on patent family members

International application No
PCT/EP2017/051889

Patent document cited in search report	Publication date	Patent family member(s)	Publication date
US 2005118648 A1	02-06-2005	AU 2002337769 A1	07-04-2003
		US 2005118648 A1	02-06-2005
		WO 03027261 A2	03-04-2003
CN 1647624 A	03-08-2005	NONE	
US 7402728 B2	22-07-2008	AT 401787 T	15-08-2008
		AU 2003297012 A1	29-07-2004
		AU 2003297023 A1	29-07-2004
		CA 2507880 A1	22-07-2004
		CA 2507882 A1	22-07-2004
		EP 1573313 A2	14-09-2005
		EP 1573314 A2	14-09-2005
		JP 2006513725 A	27-04-2006
		JP 2006517096 A	20-07-2006
		KR 20050084317 A	26-08-2005
		KR 20050084318 A	26-08-2005
		US 2006179501 A1	10-08-2006
		US 2006218655 A1	28-09-2006
		WO 2004060052 A2	22-07-2004
		WO 2004060053 A2	22-07-2004

Form PCT/ISA/210 (patent family annex) (April 2005)

7. Affidavit

I hereby confirm that the PhD thesis entitled “The Parkinson’s Disease Associated Pink1-Parkin Pathway in Pathology and Development” has been written independently and without any other sources than cited.

Javier JARAZO

Luxembourg, 20/4/2018